SOLUTION OF SOIL-STRUCTURE INTERACTION PROBLEMS BY COUPLED BOUNDARY ELEMENT-FINITE ELEMENT METHOD

by

Mark Albert Zarco

Dissertation submitted to the Faculty of the
Virginia Polytechnic Institute and State University
in partial fulfillment of the requirements
for the degree

of

DOCTOR OF PHILOSOPHY

in

Civil Engineering

APPROVED:

T. Kuppusamy, Chairman

J. M. Duncan

T. L. Brandon

J. R. Martin, II

O. H. Griffin, Jr.

July 1993
Blacksburg, VA

ABSTRACT

Soil-structure interaction problems involve the solution of boundary value problems consisting of two domains: A near field finite domain representing the structure and adjacent soil, and a semi-infinite far-field domain representing the soil distant from the structure. Currently, the most used numerical method for solving such problems, the finite element method, considers only the near field, and neglects the effects of the far field. Depending on the domain size considered, this results in significant errors in the computed displacements and stress compared to closed form solutions.

This research develops a numerical method in which both the near and far-field are considered. In this numerical procedure, the far field is assumed to be a homogenous elastic half-plane is modeled using boundary elements based on the Melan fundamental solution. A technique, called the *substructure method,* for coupling the boundary element method with finite element method is developed. Unlike other coupling techniques, the *substructure method* preserves the bandedness and symmetry of the system of equations resulting from the finite element method. The *substructure method* is implemented into a computer for program BEFEC for solving linear elastic and elasto-plastic plane strain problems. The proposed coupling technique is also incorporated into an existing finite element program SOILSTRUCT to perform soil-structure interaction analysis on U-frame lock structures.

A series of analyses performed on the elastic strip footing problem indicate that significant errors occur in the predicted displacements and stresses when the effects of the the far field are ignored. These errors are unaffected by the boundary conditions assumed or the type of finite element used. The analyses demonstrated that the displacements and

stresses obtained using the coupled BEM-FEM solution agree well with closed form solutions.

Results of the soil-structure interaction analyses performed on U-frame lock structures indicates that neglecting the effects of the far field domain results in a significant underprediciton of the vertical displacements. These analyses also showed that there are significant differences in the computed shear stress and lateral pressures when the effects of the far field are considered.

Results of the bearing capacity analyses of strip footing on elasto-plastic soils indicate that when the effects of the far field are taken into consideration, initial yield takes place at a higher load level. This in turn results is smaller plastic deformations as compared to the case when the far field is ignored. These analyses also shown that taking into consideration the far field results in significant differences in the computed stresses. These differences are diminished when the effects of self-weight are taken into consideration. The analyses performed on the Rankine earth pressure problem indicate that while the far field does not significantly affect the computed Rankine forces or lateral pressure distribution, much larger wall movements are required to reach both the active or passive states.

ACKNOWLEDGMENTS

I am most grateful to my academic and thesis adviser, Prof. Thangavelu. Kuppusamy, for his support and guidance in my graduate studies and throughout the course of this research, for sharing from the wealth of his engineering knowledge, for patiently and thoroughly reviewing the manuscript, and for his warm friendship.

My gratitude also goes to Professors James Michael Duncan, Thomas L. Brandon, James R. Martin II, and Odis Hayden Griffin Jr. for their willingness to be involved in my research. Their contributions are greatly appreciated.

Academic funding was provided by a Fulbright-Hayes grant through the Institute of International Education. Research funding was provided by the US Army Corps of Engineers. I am deeply grateful to Dr. Bob Ebeling and Dr. Reed Mosher for their support of the project.

My gratitude also goes to my classmates and friends at VPI, for sharing their ideas comments and suggestions.

Many thanks to the Filipino community in Blacksburg for their company and friendship, and for making my stay a pleasant and memorable one.

The support from numerous people in Blacksburg Christian Fellowship has been a constant source of strength and encouragement for me. I am particularly thankful to Greg and Tomoko Foliente, Donna Cassell, and my roomate, Walter Rhodes for their constant support and encouragement.

Finally, I thank the Almighty God for his faithfulness in my life, and granting me the wisdom and ability to pursue, and finish my graduate studies. It is to his greater glory that I dedicate this work.

TABLE OF CONTENTS

CHAPTER 1 - Introduction 1
Statement of Purpose 1
Methodology 1
Structure of Presentation 4

CHAPTER 2 - Theoretical Background 5
2.1 Introduction 5
2.2 Finite Element Fomulation 5
2.3 Boundary Element Formulation 6
- Direct Boundary Element Method 6
- Fundamental Solutions 12
- Linear Boundary Elements 13
- Symmetry Conditions 16
2.4 Summary 19

CHAPTER 3 Development and Implementation of the Substructure Method 20
3.1 Introduction 20
3.2 Previous Work 20
3.3 Formulation of Substructure Method 31
3.4 Development of the Transformation Matrix 36
3.5 Nonlinear Case 40
3.6 Implementation of Substructure Method 41
- Solution Phase 42
- Finite Element Computations 43
- Incompressible Formulation 46
- Stress Computations 46
- Stress-Strain Matrix Computations 48
- Boundary Element Computations 50
- Element Assembly 52
- Equation Solving Routines 53
3.7 Summary 60

CHAPTER 4 - Solution of Strip Footing Problems 63
4.1 Introduction 63
4.2 Strip Footing Problem 64
4.3 Effects of Domain Size 66
4.4 Effects of Element Type 74
4.5 Effects of Infinite Boundary 83
4.6 Solution of Non-Homogenous Linear Problems 95
4.7 Solution of Nonlinear Problems 103
4.8 Summary 112

CHAPTER 5 - Solution of U-Frame Lock Problems 115
5.1 Introduction 115
5.2 SOILSTRUCT Implementation 115
5.3 Description of the Problem 117
5.4 One-Step Linear Analysis 120
5.5 Linear Analysis with Construction Simulation 130
5.6 Nonlinear Analysis with Construction Simulation 137
5.7 Summary 149

CHAPTER 6 - Solution of Elasto-Plastic Problems 153
6.1 Introduction 153
6.2 Bearing Capacity of Strip Footings 153
6.3 Problem 1: Weightless Soils with $\phi = 0$ 154
6.4 Problem 2: Weightless Soils with $\phi > 0$ 172
6.5 Problem 3: Soils with $\phi > 0$ and Self-Weight 194
6.6 Rankine Passive Pressure Problem 212
6.7 Rankine Active Pressure Problems 218
6.8 Summary 226

CHAPTER 7 Conclusions and Recommendations 228
Conclusions 228
Recommendations 231

REFERENCES 232

APPENDIX A - Fundamental Solutions 236

APPNEXIX B - BEFEC User's Guide 243

APPENDIX C - Analytical Solutions to Strip Footing Problem 254

VITA 257

LIST OF FIGURES

Figure 1.1 A typical soil-structure interaction problem 2

Figure 2.1 Geometry of linear boundary elements in cartersina and local coordinates 14
Figure 2.2 Symmetry conditions of boundary element system 17

Figure 3.1 Coupled finite element - boundary element system (Brebbia and Georgiou, 1979) 25
Figure 3.2 Coupled finite element - boundary element system (Vallabhan, Sivakumar and Radhakrishnan, 1984) 27
Figure 3.3 Propose coupled finite element - boundary element system 32
Figure 3.4 Coupled finite element - boundary element system 37
Figure 3.5 Nodal force-traction transformation for a general coupled system 39
Figure 3.6 Flowchart for Solution Phase 44
Figure 3.7 Flowchart for Subroutine STIFQ4 45
Figure 3.8 Flowchart for Subroutine BEMSTF 51
Figure 3.9 Illustrative Example 54
Figure 3.10 ID Array 55
Figure 3.11 IEN, LM, IX and LMBEM Array for example mesh 56
Figure 3.12 Storage of system of equations for fully symmetric case 57
Figure 3.13 Storage of system of equations for fully unsymmetric case 59
Figure 3.14 Storage of system of equations for partially unsymmetric case 61

Figure 4.1 Geomtery of the Stip Footing Problem 65
Figure 4.2 Finite element mesh assuming roller support conditions 67
Figure 4.3 Finite element mesh assuming fixed support conditions 67
Figure 4.4 Effect of domain size and boundary conditions on vertical displacements along centerline 69
Figure 4.5 Effect of domain size and boundary conditions on vertical displacements along surface 70

Figure 4.6 Effect of domain size and boundary conditions on σ_{xx} along diagonal elements 72
Figure 4.7 Effect of domain size and boundary conditions on σ_{xy} along diagonal elements 73
Figure 4.8 Effect of domain size and boundary conditions on σ_{yy} along diagonal elements 75
Figure 4.9 Effect of element type and boundary conditions on vertical displacements along centerline 77
Figure 4.10 Effect of element type and boundary conditions on vertical displacements along surface 78
Figure 4.11 Effect of element type and boundary conditions on σ_{xx} along diagonal elements 80
Figure 4.12 Effect of element type and boundary conditions on σ_{xy} along diagonal elements 81
Figure 4.13 Effect of element type and boundary conditions on σ_{yy} along diagonal elements 82
Figure 4.14 Effect of infinite boundary on vertical displacements along centerline 86
Figure 4.15 Effect of infinite boundary on vertical displacements along surface 88
Figure 4.16 Effect of infinite boundary on σ_{xx} 90
Figure 4.17 Effect of infinite boundary on σ_{xy} 91
Figure 4.18 Effect of infinite boundary on σ_{yy} 92
Figure 4.19 Vertical displacements along centerline for G=my 97
Figure 4.20 Vertical displacements along y/a = 1.0 for G=my 99
Figure 4.21 σ_{xx} along diagonal elements for G=my 100
Figure 4.22 σ_{xy} along diagonal elements for G=my 101
Figure 4.23 σ_{yy} along diagonal elements for G=my 102
Figure 4.24 Vertical displacements along centerline - nonlinear case 106
Figure 4.25 Vertical displacements along surface - nonlinear case 108
Figure 4.26 σ_{xx} along diagonal elements for - nonlinear case 109
Figure 4.27 σ_{xy} along diagonal elements for - nonlinear case 110
Figure 4.28 σ_{yy} along diagonal elements for - nonlinear case 111

Figure 5.1 Flowchart of SOILSTRUCT 116
Figure 5.2 Flowchart of STRSTF 118

Figure 5.3 U-Frame Lock Problem 119
Figure 5.4 Finite Element Mesh used in Linear Analyses 122
Figure 5.5 Finite Element - Boundary Element Mesh used in Linear Analyses 123
Figure 5.6 Vertical Displacements Along Foundation Centerline .....
(Linear One-Step Analysis) 124
Figure 5.7 Vertical Displacements Along Foundation Surface
(Linear One-Step Analysis) 126
Figure 5.8 Lateral Pressure Against Lock Wall (Linear One-Step Analysis) 127
Figure 5.9 σ_{xy} Along Base of Embankment (Linear One-Step Analysis) 129
Figure 5.10 σ_{yy} Along Base of Embankment (Linear One-Step Analysis) 131
Figure 5.11 Vertical Displacements Along Foundation Centerline
(Linear Analysis withConstruction Simulation) 133
Figure 5.12 Vertical Displacements Along Foundation Surface .....
(Linear Analysis with Construction Simulation) 134
Figure 5.13 Lateral Pressure Against Lock Wall
(Linear Analysis with Construction Simulation) 136
Figure 5.14 σ_{xy} Along Base of Embankment (Linear Analysis with Construction
Simulation) 138
Figure 5.15 σ_{yy} Along Base of Embankment (Linear Analysis with Construction
Simulation) 139
Figure 5.16 Finite Element Mesh used in Nonlinear Analysis 141
Figure 5.17 Finite Element - Boundary Element Mesh used in Nonlinear Analysis .. 142
Figure 5.18 Vertical Displacements Along Foundation Centerline
(Nonlinear Analysis with Construction Simulation) 145
Figure 5.19 Vertical Displacements Along Foundation Surface
(Nonlinear Analysis with Construction Simulation) 146
Figure 5.20 Lateral Pressure Against Lock Wall
(Nonlinear Analysis with Construction Simulation) 147
Figure 5.21 σ_{xy} Along Base of Embankment
(Nonlinear Analysis with Construction Simulation) 148
Figure 5.22 σ_{yy} Along Base of Embankment
(Nonlinear Analysis with Construction Simulation) 150

Figure 6.1 Finite element mesh for elasto-plastic footing problem 155
Figure 6.2 Coupled finite element - boundary element mesh for elasto-plastic footing problem 156
Figure 6.3 Load-Displacement Curve for elasto-plastic footing problem 1..... 158
Figure 6.4 Vertical displacements along centerline with *w/c* = 4.0 for elasto-plastic footing problem 1 160
Figure 6.5 Vertical displacements along surface with *w/c* = 4.0 for elasto-plastic footing problem 1 161
Figure 6.6 σ_{xx} along diagonal elements with w/c = 4.0 for elasto-plastic footing problem 1 163
Figure 6.7 σ_{xy} along diagonal elements with w/c = 4.0 for elasto-plastic footing problem 1 164
Figure 6.8 σ_{yy} along diagonal elements with w/c = 4.0 for elasto-plastic footing problem 1 166
Figure 6.9 Vertical displacements along centerline with *w/c* = 5.2 for elasto-plastic footing problem 1 167
Figure 6.10 Vertical displacements along surface with *w/c* = 5.2 for elasto-plastic footing problem 1 169
Figure 6.11 σ_{xx} along diagonal elements with w/c = 5.2 for elasto-plastic footing problem 1 170
Figure 6.12 σ_{xy} along diagonal elements with w/c = 5.2 for elasto-plastic footing problem 1 171
Figure 6.13 σ_{yy} along diagonal elements with w/c = 5.2 for elasto-plastic footing problem 1 173
Figure 6.14 Spread of plastic zones for elasto-plastic footing problem 1 using the finite element method alone..... 174
Figure 6.15 Spread of plastic zones for elasto-plastic footing problem 1 using the coupled finite element boundary element solution..... 175
Figure 6.16 Load-Displacement Curve for elasto-plastic footing problem 2..... 177
Figure 6.17 Vertical displacements along centerline with *w/c* = 8.0 for elasto-plastic footing problem 2 179
Figure 6.18 Vertical displacements along surface with *w/c* = 8.0 for elasto-plastic footing problem 2 180

Figure 6.19 σ_{xx} along diagonal elements with w/c = 8.0 for elasto-plastic footing problem 2 182
Figure 6.20 σ_{xy} along diagonal elements with w/c = 8.0 for elasto-plastic footing problem 2 183
Figure 6.21 σ_{yy} along diagonal elements with w/c = 8.0 for elasto-plastic footing problem 2 184
Figure 6.22 Vertical displacements along centerline with *w/c* = 14.0 for elasto-plastic footing problem 2 185
Figure 6.23 Vertical displacements along surface with *w/c* = 14.0 for elasto-plastic footing problem 2 187
Figure 6.24 σ_{xx} along diagonal elements with w/c = 14.0 for elasto-plastic footing problem 2 188
Figure 6.25 σ_{xy} along diagonal elements with w/c = 14.0 for elasto-plastic footing problem 2 190
Figure 6.26 σ_{yy} along diagonal elements with w/c = 14.0 for elasto-plastic footing problem 2 191
Figure 6.27 Spread of plastic zones for elasto-plastic footing problem 2 using the finite element method alone 192
Figure 6.28 Spread of plastic zones for elasto-plastic footing problem 2 using the coupled finite element-boundary element solution 193
Figure 6.29 Load-Displacement Curve for elasto-plastic footing problem 3 195
Figure 6.30 Vertical displacements along centerline with *w/c* = 10.0 for elasto-plastic footing problem 3 197
Figure 6.31 Vertical displacements along surface with *w/c* = 10.0 for elasto-plastic footing problem 3 198
Figure 6.32 σ_{xx} along diagonal elements with w/c = 10.0 for elasto-plastic footing problem 3 200
Figure 6.33 σ_{xy} along diagonal elements with w/c = 10.0 for elasto-plastic footing problem 3 201
Figure 6.34 σ_{yy} along diagonal elements with w/c = 10.0 for elasto-plastic footing problem 3 202
Figure 6.35 Vertical displacements along centerline with *w/c* = 16.0 for elasto-plastic footing problem 3 203

Figure 6.36 Vertical displacements along surface with w/c = 16.0 for elasto-plastic footing problem 3 205
Figure 6.37 σ_{xx} along diagonal elements with w/c = 16.0 for elasto-plastic footing problem 3 206
Figure 6.38 σ_{xy} along diagonal elements with w/c = 16.0 for elasto-plastic footing problem 3 208
Figure 6.39 σ_{yy} along diagonal elements with w/c = 16.0 for elasto-plastic footing problem 3 209
Figure 6.40 Spread of plastic zones for elasto-plastic footing problem 3 using the finite element method alone 210
Figure 6.41 Spread of plastic zones for elasto-plastic footing problem 3 using the coupled finite element-boundary element solution 211
Figure 6.42 Finite element mesh used in Passive Rankine Analysis 213
Figure 6.43 Coupled boundary element-finite element mesh used in Rakine Passive Analysis 214
Figure 6.44 Passive force in Rankine Passive Pressure Problem 216
Figure 6.45 Lateral earth pressure distribution at failure for Rankine Passive Pressure Problem 217
Figure 6.46 Plastic zone at failure in finite element solution for Rankine Passive Pressure Problem 219
Figure 6.47 Plastic zone at failure in coupled BEM-FEM solution for Rankine Passive Pressure Problem 220
Figure 6.48 Active force in Rankine Active Pressure Problem 222
Figure 6.49 Lateral earth pressure distribution at failure for Rankine Active Pressure Problem 223
Figure 6.50 Plastic zone at failure in finite element solution for Rankine Active Pressure Problem 224
Figure 6.51 Plastic zone at failure in coupled BEM-FEM solution for Rankine Active Pressure Problem 225

Figure A.1 Kelvin Fundamental Solution 238
Figure A.2 Mealn Fundamental Solution 238
Figure A.3 Geometry of quantities used in the Melan complementary solution 242

Figure B.1 Bilinear generation of nodal coordinate data (NUMGP=4) 246
Figure B.2 Biquadratic serendipity generation of nodal coordinate data (NUMGP=8) 246
Figure B.3 Schematic representation of the generation algorithm for element nodal data 249

Figure C.1 Distances and angles from enpoints of strip 256

LIST OF TABLES

Table 4.1 Parameters for Linear Elastic Strip Footing Problem 64

Table 4.2 Parameters for Nonhomogenous Strip Footing Problem 96

Table 4.3 Parameters for Nonlinear Elastic Strip Footing Problem 104

Table 5.1 Material Parameters of U-Frame Lock Problem (Linear Case) 120

Table 5.2 Material Parameters for soils in U-Frame lock Problem (Non-linear case) 140

Table 5.3 Material Parameters for Interface Elements in Nonlinear U-Frame Lock problem 143

Chapter 1

INTRODUCTION

Statement of Purpose

Soil-structure interaction problems in geotechnical engineering involve the solution of boundary value problems consisting of two-domains: A near-field finite domain representing the structure and the adjacent soil and a semi-infinite far-field domain representing the soil far distant from the structure. Figure 1 illustrates a typical soil-structure interaction problem. Such problems often are solved numerically because of their complexity. Currently, the most used numerical method, the finite element method, considers only the near field, and neglects the effects of the far-field domain. In order to obtain reasonable results, the finite element mesh used must include a very large domain and hence a very large number of elements. Depending upon the domain size considered, the error resulting in both the displacement and stress prediction may be very large compared to the closed form solution. The objective of this dissertation is to develop a numerical method for solving soil-structure interaction problems in which both the near and far-field are considered and minimize the error so that only a reasonable size of the near-field is included.

Methodology

The finite element method is widely used as the numerical technique for obtaining solutions to boundary value problems. The main advantage of this method is the capability to solve nonlinear and non-homogenous problems involving arbitrary geometry, various types of boundary conditions and constitutive properties which is typical of most soil-structure interaction problems. A solution strategy based on the Newton-Raphson method

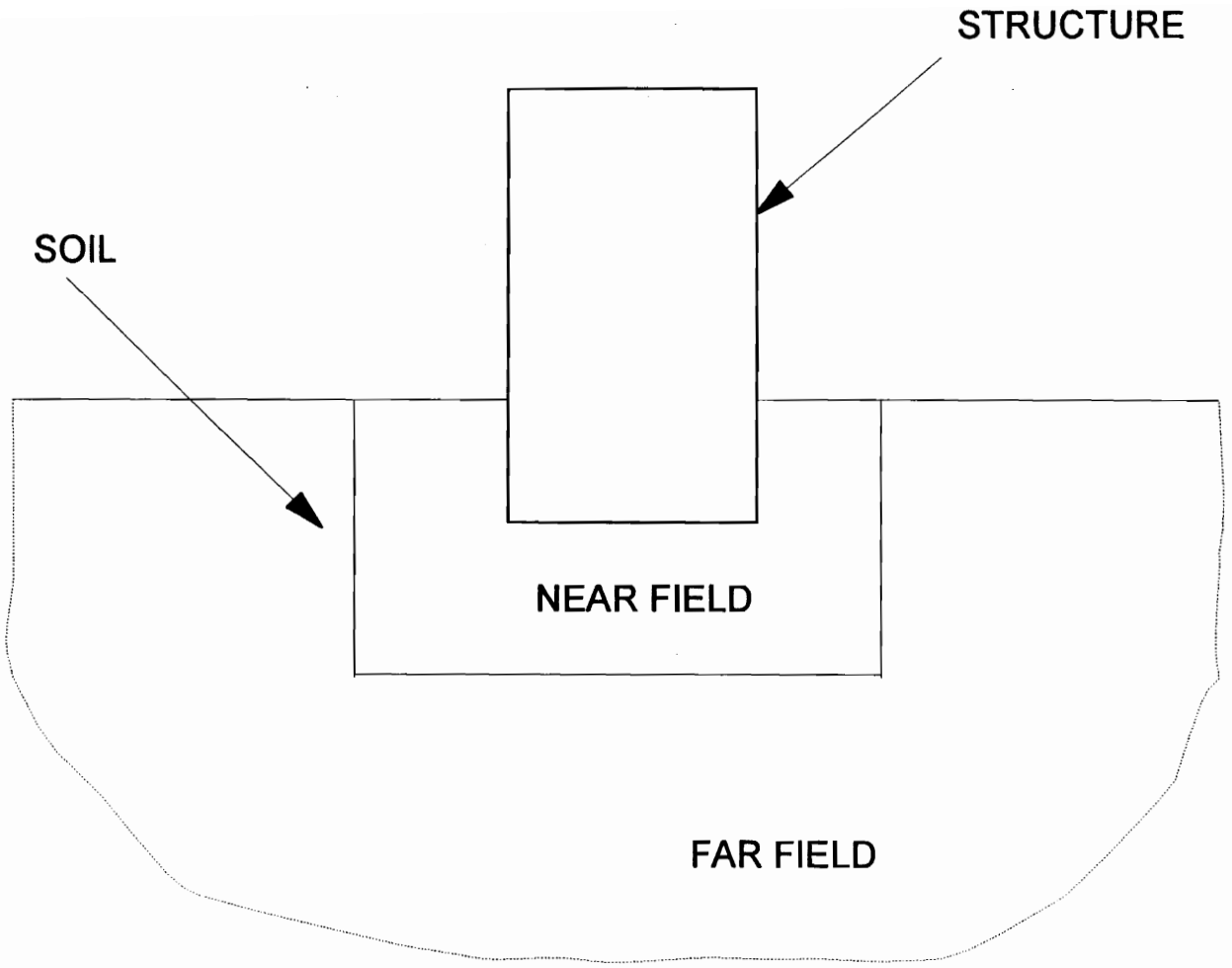

Figure 1. A typical soil-structure interaction problem.

is usually adopted to solve the non-linear system of equations resulting from the finite element method. The near field is modeled by the finite element method in this research.

The far-field domain is assumed in this research to be a linearly elastic and homogenous half-plane. The effects of the far field domain are modeled by the boundary element method and then coupled to the finite element method. The boundary element formulation adopted is based on an elastic half-plane solution. A coupling technique called the *substructure method* is developed to couple the boundary element and finite element method. This technique treats the entire boundary element system as a substructure and preserves the bandedness and symmetry of the system of equations resulting from the finite element method.

The numerical procedure described above is implemented into a coupled finite element/boundary element computer program called BEFEC. This program has the capability of analyzing elasto-plastic plane strain soil-structure interaction problems. The proposed method is also incorporated into another existing computer program called SOILSTRUCT. This program is a general purpose finite element program used to analyze soil-structure interaction problems and has the added capability of modeling nonlinear stress-strain behavior and simulating incremental construction.

To investigate the validity of the proposed coupling procedure, BEFEC is used to perform parametric studies on the solution of the classical strip footing problem. Numerical results are evaluated on the basis of their agreement with analytical solutions. The effects of the far-field on the solution of nonlinear soil-structure interaction problems such as bearing capacity, lateral earth pressure and U-lock construction problems are investigated.

Structure of Presentation

Chapter 2 presents the theoretical background behind the finite element and boundary element method. A review of the work done in boundary element - finite element coupling is also presented.

Chapter 3 presents the development of the substructure technique used to couple the boundary element and finite element method. The chapter also describes how the proposed coupling technique is implemented into the program BEFEC.

Chapter 4 deals with the verification of the substructure technique. The validity of the coupling technique is evaluated by solving a strip footing problem and comparing the result with the known analytical solution. Also, the effects of the element type, domain size and boundary conditions on the solution are examined.

Chapter 5 investigates the effects of far field on the solution of soil-structure interaction problems. The solution of U-lock problem is presented.

Chapter 6 investigates the effects of the far field on the solution of elasto-plastic limit equilibrium problems. The solution to elasto-plastic bearing capacity and lateral earth pressure problems is presented.

Chapter 7 summarizes the work and presents the salient conclusions derived. Recommendations are made for improvement of both the coupling technique and the computer program.

Chapter 2

THEORETICAL BACKGROUND

2.1 Introduction

The objective of this chapter is to present the theory behind numerical techniques used in solving nonlinear soil-structure problems. These include the finite and boundary element methods. For the finite element method, only a brief summary of the formulations used in this dissertation is presented. A detailed discussion of the direct boundary element method is included. Specifically, the formulation of linear boundary elements based on a half-plane fundamental solution is given.

2.2 Finite Element Formulation

The **finite element method** is a well known numerical technique for solving boundary-value problems. It involves dividing the domain of the problem into a finite number of subdomains or elements, and using variational or other principles the solution procedure is arrived. This method has the capability of solving problems involving complex geometry, boundary conditions and constitutive properties. Because the theory behind the finite element method is well discussed in literature, it is not repeated here. Reddy (1984) and Hughes (1987) give an excellent introduction of the theory and application of the finite element method to the solution of linear problems. A general discussion of the application of the finite element method to the nonlinear analysis of solids is given by Bathe (1982). For the application of the finite element method to the solution of plasticity problems, a comprehensive discussion is given by Owen and Hinton (1980)

In chapter 4, the solution of a half-plane problems is obtained using various types of elements. These include the 4-node quadrilateral element (Taig, 1961), 9-node lagrangian element (Irons, 1966), the 5-node QM5 element (Doherty, Wilson and Taylor, 1969), and the 8-node hybrid stress element (Pian and Tong, 1969). Also, the infinite element developed by Beer and Meek (1977) is used to model the far field domain.

2.3 Boundary Element Formulation

The **boundary element method** is a numerical technique for solving boundary value problems. It involves dividing the boundary into a finite number of elements over which the solution is approximated using variational principles. The boundary element method is most useful in solving boundary value problems involving infinite or semi-infinite domains. A major advantage of this method over other numerical techniques is the reduction in dimensionality of the problem by one. Because of this, two-dimensional problems can be solved using line elements. This results in a system of equations which in general tends to be smaller as compared to other numerical techniques such as the finite element and finite difference method. However, the resulting system of equations is generally both fully-populated and unsymmetric.

Direct Boundary Element Method

Boundary element formulations fall into two classes namely: indirect and direct. In the indirect approach, the resulting equations involve fictitious quantities which do not have any direct physical significance. Once determined, these quantities can be used to determine the stresses and displacements both on the boundary and within the problem's domain. The direct formulation results in a system of equations which when solved immediately yield the stresses and displacements on the boundary. This feature makes the

direct boundary element method more suitable over the indirect approach for coupling with the finite element method and is used here.

In the direct formulation, the governing differential equations are converted into an equivalent integral statement by successively applying integration by parts. This integral statement, known as the *boundary integral equation*, for an elastostatic problem is given by (Brebbia 1984)

$$C_{ij}(s)u_j + \oint_\Gamma p^*_{ij}(s,q)u_j(q)d\Gamma = \oint_\Gamma u^*_{ij}(s,q)u_j(q)d\Gamma \qquad (2.1)$$

for i,j = 1,2 which correspond to the x and y directions respectively. Γ is the boundary of the problem while s and q are points on Γ. The quantities $u_j(q)$ and $p_j(q)$ are the jth component of the displacement and tractions at point q of the problems being solved. These are either prescribed as boundary conditions, or unknowns which are to be solved for. The quantities $u^*_{ij}(s,q)$ and $p^*_{ij}(s,q)$ are the jth component of displacement and traction respectively at point q, resulting from a point load applied in the ith direction at point s. This quantity is often referred to in most boundary element literature as the *fundamental solution* of the boundary element formulation. $C_{ij}(s)$ is a 2×2 matrix which is a function of the point s.

The basic steps involved in the boundary element method are:

1. The boundary Γ is discretized into a series of elements of which displacements and tractions are chosen to be piecewise interpolated between the element nodal points.
2. The boundary integral equation is applied in discretized form to each nodal point s on the boundary Γ and the integrals are computed over each boundary element. In most cases, the integration must be performed numerically because of the complexity of the integrand. A system of $2N$ linear algebraic equations involving the set of N nodal displacements is therefore obtained.

3. Boundary conditions are imposed and consequently $2N$ nodal values are prescribed. These correspond to the traction and displacements in each direction per node. The system of $2N$ equations can therefore be solved by standard methods to obtain the remaining boundary conditions.

For the discretization of the boundary integral equation, an arbitrary number of interpolation points referred to as nodes are selected along the boundary Γ. Between these points, Γ is approximated by a series of elements Γ_j. These element consists of either straight lines or curves depending on the degree of interpolation of the coordinates within each element. For an element with M nodes, the Cartesian coordinates (x,y) of points located within the element are expressed in terms of the lagrangian interpolating functions ψ_j of order $(M\text{-}1)$ and the nodal coordinates (x_j,y_j) of the element by the relation

$$\left.\begin{aligned} x &= \sum_{j=1}^{N} x_j \psi_j \\ y &= \sum_{j=1}^{N} y_j \psi_j \end{aligned}\right\} \tag{2.2}$$

where x_j and y_j are the x and y coordinates at the jth node. Similarly, for an element with M nodes, the boundary displacements and tractions are approximated within the element in terms of the lagrangian interpolating functions ψ_j of order $(M\text{-}1)$ in the following relations

$$\left.\begin{aligned} u_i &= \sum_{j=1}^{N} U_{ij} \psi_j \\ p_i &= \sum_{j=1}^{N} P_{ij} \psi_j \end{aligned}\right\} \tag{2.3}$$

where u_i and p_i are the jth component of the displacement and traction along the element and U_{ij} and P_{ij} are the jth component of the displacement and traction at node j.

If the boundary Γ is discretized into a system consisting of L elements Γ_j and N nodes, the substitution of the approximation in equations (2.2) and (2.3) into equation (2.1) results in

$$\left.\begin{aligned} C_{ij}(s)u_j(s) + \sum_{l=1}^{L}\sum_{k=1}^{M}\left(\oint_{\Gamma_l} p_{ij}^*(s,q_k)U_{jk}(q_k)\psi d\Gamma\right) \\ = \sum_{l=1}^{L}\sum_{k=1}^{M}\left(\oint_{\Gamma_l} u_{ij}^*(s,q_k)P_{jk}(q_k)\psi d\Gamma\right) \end{aligned}\right\} \tag{2.4}$$

where i,j = 1,2, k = 1...N and q_k corresponds to the kth node of the lth element. From equation (2.4), the resulting system will involve $4N$ nodal quantities consisting of a boundary displacement and tractions in each direction for every node. In a well posed problem, half of these equations are prescribed as boundary conditions. This results in a total of $2N$ unknowns. The $2N$ equations needed to solve the $2N$ unknown nodal quantities can be obtained by evaluating equation (2.4) at each of the N nodal points. The results of this is a system of equations of the form:

$$\left.\begin{aligned} C_{ij}(s_n)u_j(s_n) + \sum_{l=1}^{L}\sum_{k=1}^{M}\left(\oint_{\Gamma_l} p_{ij}^*(s_n,q_k)U_{jk}(q_k)\psi d\Gamma\right) \\ = \sum_{l=1}^{L}\sum_{k=1}^{M}\left(\oint_{\Gamma_l} u_{ij}^*(s_n,q_k)P_{jk}(q_k)\psi d\Gamma\right) \end{aligned}\right\} \tag{2.5}$$

or in matrix form:

$$(C+H)U = \hat{H}U = GP \tag{2.6}$$

where

$$C = C_{ij}(s_n)u_j(s_n) \tag{2.7}$$

$$H = \sum_{l=1}^{L}\sum_{k=1}^{M}\left(\oint_{\Gamma_l} p_{ij}^*(s_n,q_k)U_{ik}(q_k)\psi d\Gamma\right) \tag{2.8}$$

$$G = \sum_{l=1}^{L}\sum_{k=1}^{M}\left(\oint_{\Gamma_l} u_{ij}^{*}(s_n, q_k) P_{ik}(q_k)\psi d\Gamma\right) \tag{2.9}$$

In most cases, equations (2.8) and (2.9) can be evaluated numerically. However, for the case when the singular nodes s_n lies within element Γ_j, because of the singularity in both p^* and q^*,the integral becomes improper and must either be integrated analytically or by means of a special numerical quadrature.

For the case when the singular point is outside the element, equations (2.8) and (2.9) can readily be evaluated using the standard Gaussian quadrature (Stroud and Secrest 1966) which is of the form:

$$\left.\begin{aligned}\oint_{\Gamma_j} p_{ij}^{*}(s_n, q_n)\psi(q)d\Gamma &= \int_{-1}^{1} p_{ij}^{*}(s_n, q_n)\psi(q)|J|d\xi \\ &= \sum_{k=1}^{K} p^{*}(s_n, q_k)\psi(q_k)|J|_k W_k\end{aligned}\right\} \tag{2.10}$$

$$\left.\begin{aligned}\oint_{\Gamma_j} u_{ij}^{*}(s_n, q_n)\psi(q)d\Gamma &= \int_{-1}^{1} u_{ij}^{*}(s_n, q_n)\psi(q)|J|d\xi \\ &= \sum_{k=1}^{K} u^{*}(s_n, q_k)\psi(q_k)|J|_k W_k\end{aligned}\right\} \tag{2.11}$$

where K is the number of Gaussian integration points, W_k is the weighting factor associated with the kth Gaussian point q_k. ξ is the local coordinate along the length of the element and $|J|$ is the determinant of the jacobian corresponding to the transformation in equation (2.2) given by

$$|J| = \sqrt{\left(\frac{dx}{d\xi}\right)^2 + \left(\frac{dy}{d\xi}\right)^2} \tag{2.12}$$

The functions u^* and p^* in equations (2.10) and (2.11) must be evaluated using the x and y coordinates of point q_k corresponding to the local coordinate ξ_k of the kth Gaussian point.

For the special case when the singular point s_n is one of the nodal points of the element, the right-handside term involving u^* in equation (2.9) cannot be accurately integrated using standard Gaussian quadrature due to the presence of a singular logarithm term. For constant elements or linear elements, equation (2.9) can be integrated analytically (Brebbia 1978, Crouch 1983). For higher order elements, a numerical quadrature specifically formulated for singular logarithmic integrals is used (Cristescu and Loubignac, 1978). Integrals involving p^* in equation (2.10), which correspond to the leading diagonal submatrices in $\hat{H}$, need not be explicitly evaluated. Instead, they can be calculated by imposing to the matrix equation the condition that rigid body translations result in zero tractions. Thus, the diagonal submatrices in $\hat{H}$ can be calculated using the relations (Brebbia 1978).

$$\hat{H}_{\alpha\alpha} = -\sum_{\substack{q=1 \\ q\neq\alpha}}^{N} \hat{H}_{\alpha q} \tag{2.13}$$

for finite bodies, and

$$\hat{H}_{\alpha\alpha} = I - \sum_{\substack{q=1 \\ q\neq\alpha}}^{N} \hat{H} \tag{2.14}$$

for infinite bodies and semi-infinite domains. In the above expression $\hat{H}_{ij}$ refers to a 2×2 submatrix corresponding to the evaluation of the fundamental solution at point j due to a load at i. I is a 2×2 identity matrix.

Fundamental Solutions

The most important component of any boundary element formulation is the fundamental solution. This is because the fundamental solution dictates type of problem the boundary element formulation can be applied to. For general plane strain problems, the fundamental solution most commonly used in the direct boundary element formulation is the Kelvin solution (Timshenko, 1970). This solution gives the displacements and stresses at a point q inside an infinite elastic plane due to the application of a point load at the point s. Appendix A.1 gives the complete set of expressions for the displacements u^* and stresses σ^* as well as the geometry of the Kelvin solution. To obtain the tractions along the boundary Γ necessary for evaluating equations (2.8) and (2.9), the following relation is used.

$$\left.\begin{aligned} p_x &= n_x\sigma_{xx} + n_y\sigma_{xy} \\ p_y &= n_x\sigma_{xy} + n_y\sigma_{yy} \end{aligned}\right\} \tag{2.15}$$

where (n_x,n_y) are the components of the unit vector n normal to the boundary Γ.

The Kelvin solution is suitable for solving both finite and infinite domain problems. However, for half-plane problems, the solution first developed by Melan (1932) is most suitable. This solution corresponds to the application of a point load within an elastic half-plane. Because the traction-free surface is an infinite boundary, a very large number of boundary elements are required to model this surface if the Kelvin fundamental solution is to be used. Also, using the Kelvin solution for solving half-plane problems introduces discretization errors. These errors result from the approximate modeling of the infinite boundary with a finite number of boundary elements. In the Melan fundamental solution, no boundary elements are need to model the traction free surface because it is automatically incorporated into the fundamental solution. Thus, compared to the Kelvin

approach, the Melan formulation requires fewer elements to model the problem. Also, no disretization errors occur due to the faithful modeling of the traction free boundary.

It should be pointed out that while the Melan solution has existed for sometime, it is only recently that it has been used with the boundary element method for solving half-plane problems. This is due to the fact that in the original work there seems to be errors. which were pointed out only recently by Telles (1981). The complete solution involves superposing a complementary solution $()_c^*$ on to the Kelvin solution $()_K^*$. Thus the solution can be written in the form:

$$u^* = u_c^* + u_K^* \tag{2.16}$$

$$\sigma^* = \sigma_c^* + \sigma_K^* \tag{2.17}$$

Again, the boundary tractions can be obtained from the stresses using equation (2.11). The complete and correct expression for the displacement and stresses as the geometry of Melan complementary solution is given in Appendix A.2.

Linear Boundary Elements

Among the different types of elements that can be employed in the numerical discretization of the boundary integral equation, the linear element has been found to give acceptable accuracy without requiring much computer effort for the solution of plane strain elastostatic problems. The geometry of the element as shown in Figure (2.1) is represented by a straight line of length l and thus $|J| = \frac{1}{2}$ throughout the entire element. Nodes are numbered such that the normal to the element always points towards the domain of the boundary element system. The interpolation functions are given by

$$\left.\begin{aligned} \psi_1(\xi) &= \frac{1-\xi}{2} \\ \psi_2(\xi) &= \frac{1+\xi}{2} \end{aligned}\right\} \tag{2.18}$$

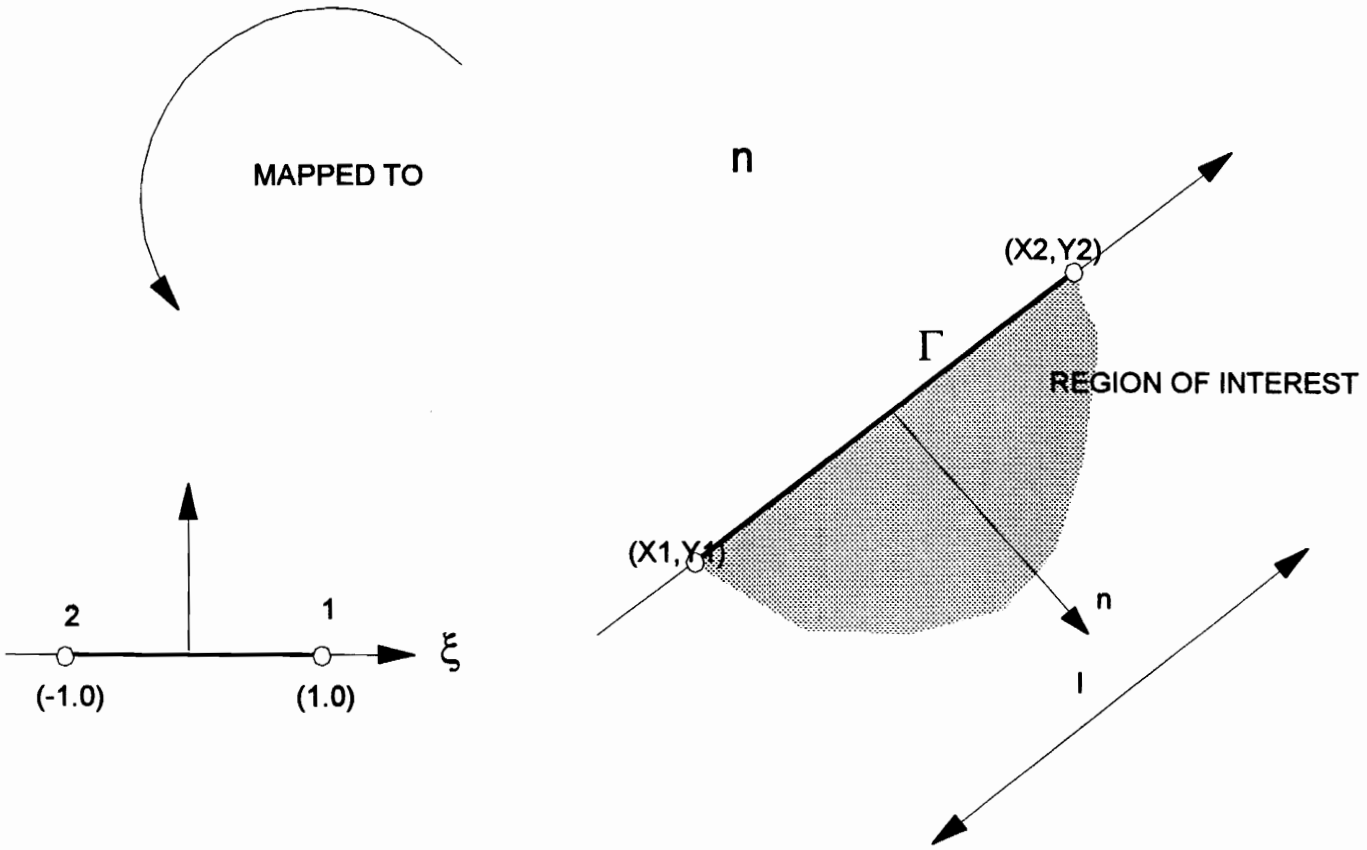

Figure 2.1. Geometry of linear boundary element in cartesian and local coordinates.

The discretization of the boundary integral equation gives rise to two 2 × 4 element matrix h and g respectively of the following form:

$$h = \begin{bmatrix} \int_{-1}^{1} p_{xx}\psi_1 |J| d\xi & \int_{-1}^{1} p_{xy}\psi_1 |J| d\xi & \int_{-1}^{1} p_{xx}\psi_2 |J| d\xi & \int_{-1}^{1} p_{xy}\psi_2 |J| d\xi \\ \int_{-1}^{1} p_{yx}\psi_1 |J| d\xi & \int_{-1}^{1} p_{yy}\psi_1 |J| d\xi & \int_{-1}^{1} p_{yx}\psi_2 |J| d\xi & \int_{-1}^{1} p_{yy}\psi_2 |J| d\xi \end{bmatrix} \tag{2.19}$$

$$g = \begin{bmatrix} \int_{-1}^{1} u_{xx}\psi_1 |J| d\xi & \int_{-1}^{1} u_{xy}\psi_1 |J| d\xi & \int_{-1}^{1} u_{xx}\psi_2 |J| d\xi & \int_{-1}^{1} u_{xy}\psi_2 |J| d\xi \\ \int_{-1}^{1} u_{yx}\psi_1 |J| d\xi & \int_{-1}^{1} u_{yy}\psi_1 |J| d\xi & \int_{-1}^{1} u_{yx}\psi_2 |J| d\xi & \int_{-1}^{1} u_{yy}\psi_2 |J| d\xi \end{bmatrix} \tag{2.20}$$

For the special case when the singular node is coincident with one of the end nodes of the element, the coefficients of the g matrix can be computed analytically to avoid significant errors introduced by the numerical integration of the improper integral. Integrating equation (2.20) for elements containing singular nodes results in the following indicial expression:

$$g_{ij}^{kn} = \frac{1}{[16\pi(1-\nu)G]}\left\{(3-4\nu)[\delta_{kn} + 0.5 - \ln(l)] + \frac{l_i l_j}{l}\right\} \qquad i,j = 1,2 \tag{2.21}$$

for the Kelvin solution and

$$g_{ij}^{kn} = \frac{1}{4\pi G}\left\{2(1-\nu)[\delta_{kn} + 0.5 - \ln(l)]\delta_{ij} + \frac{l_i l_j}{l} + \alpha(1-\delta_{ij})l\theta(1-2\nu)\right\} \qquad i,j = 1,2 \tag{2.22}$$

for the half-plane solution. The subscripts i and j indicate the position of the coefficient in the 2 × 2 submatrix k of g and n indicates which nodes in the element is singular. Also

$$\delta_{ij} = \begin{cases} 0, i \neq j \\ 1, i = j \end{cases} \tag{2.23}$$

$$\alpha = \begin{cases} -1, & j = 1 \\ 1, & j = 2 \end{cases} \tag{2.24}$$

$$\theta = \arctan\left(\frac{l_2}{l_1}\right), \quad (-\pi/2 \leq \theta \leq \pi/2) \tag{2.25}$$

and where l_i is the jth components of the element length.

Once the element matrices have been computed, they are assembled together to form the global matrices G and H. For a boundary element system consisting of n boundary elements

$$G = \sum_{i=1}^{n} g^{(i)} \tag{2.26}$$

$$H = \sum_{i=1}^{n} h^{(i)} \tag{2.27}$$

where $g^{(i)}$ and $h^{(i)}$ are the g and h matrices for element i.

Symmetry Conditions

One technique of taking into consideration symmetry in a problem is by considering only half of the domain. At the boundary located along the axis of symmetry, the normal displacements and tangential tractions are assumed to be zero. This approach is commonly used in the finite element method and results in half as many elements. However, for the boundary element method, this approach is inefficient because it does not reduce the number of boundary elements by half. Furthermore, this approach is not applicable for infinite or semi-infinite domains. For this reason, a technique known as the *method of images* is used. In order to illustrate this technique, only the case where the problem is symmetric about the axis $x = x^*$ shall be considered. The geometry of the problem is illustrated in Figure (2.2) Given a boundary element with endpoints

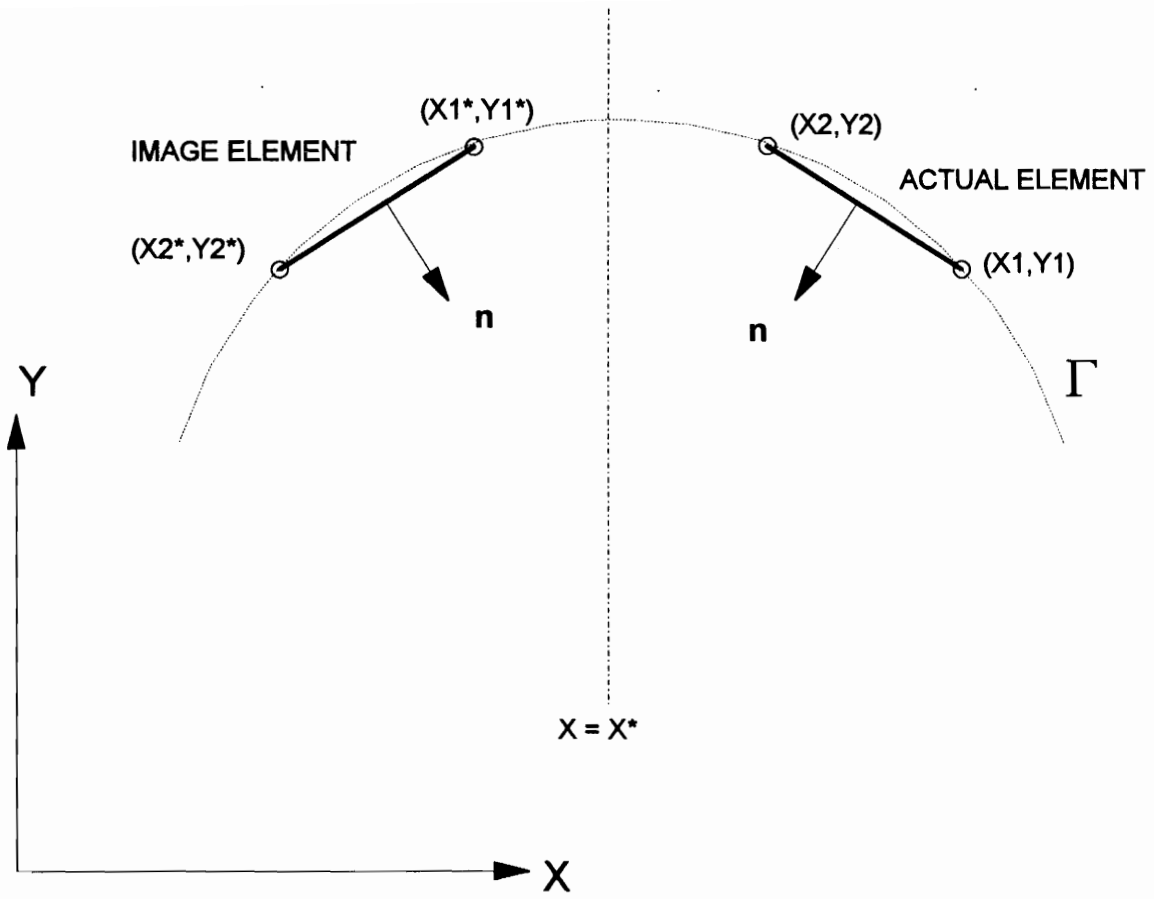

Figure 2.2. Symmetry conditions of boundary element system.

$\{(x_1,y_1),(x_2,y_2)\}$ where x_1 and x_2 are both greater than x^*, there exists an image element with end points $\{(x^*\text{-}x_1,y_1),(x^*\text{-}x_2,y_2)\}$. Because of the symmetry conditions, the displacements $\mathbf{u}^I=\{u_x^I,u_y^I\}$ and tractions $\mathbf{p}^I=\{p_x^I,p_y^I\}$ in the image element are related to the displacement $\mathbf{u}^A=\{u_x^A,u_x^A\}$ and tractions $\mathbf{p}^A=\{p_x^A,p_y^A\}$ in the actual element as follows:

$$\left.\begin{aligned} u_x^I &= -u_x^A \\ u_y^I &= u_y^A \end{aligned}\right\} \tag{2.28}$$

$$\left.\begin{aligned} p_x^A &= -p_x^I \\ p_y^A &= p_y^I \end{aligned}\right\} \tag{2.29}$$

Considering an entire system of boundary elements subdivided into the actual elements and their images, the system described in equation (2.6) can be written as:

$$(C_{AA}+H_{AA})u^A + H_{AI}u^I = G_{AA}p^A + G_{AI}p^I \tag{2.30}$$

$$H_{IA}u^A + (C_{II}+H_{II})u^I = G_{IA}p^A + G_{II}p^I \tag{2.31}$$

In a symmetric problem, equations (2.118) and (2.119) are equivalent. Using the conditions in equations (2.116) and (2.117), equation (2.118), can be written:

$$(C_{AA}+H_{AA}+\tilde{H}_{AI})u_A = (G_{AA}+\tilde{G}_{AI})p_A \tag{2.32}$$

where

$$\tilde{H}_{AI} = \sum_{i=1}^{n} \tilde{h}^{(i)} \tag{2.33}$$

$$\tilde{G}_{AI} = \sum_{i=1}^{n} \tilde{g}^{(i)} \tag{2.34}$$

The matrices of influence coefficients for the source points are obtained as follows

$$\tilde{h} = \begin{bmatrix} -\int_{-1}^{1} p_{xx}\psi_1|J|d\xi & -\int_{-1}^{1} p_{xy}\psi_1|J|d\xi & -\int_{-1}^{1} p_{xx}\psi_2|J|d\xi & -\int_{-1}^{1} p_{xy}\psi_2|J|d\xi \\ \int_{-1}^{1} p_{yx}\psi_1|J|d\xi & \int_{-1}^{1} p_{yy}\psi_1|J|d\xi & \int_{-1}^{1} p_{yx}\psi_2|J|d\xi & \int_{-1}^{1} p_{yy}\psi_2|J|d\xi \end{bmatrix} \tag{2.35}$$

$$\tilde{g} = \begin{bmatrix} -\int_{-1}^{1} u_{xx}\psi_1|J|d\xi & -\int_{-1}^{1} u_{xy}\psi_1|J|d\xi & -\int_{-1}^{1} u_{xx}\psi_2|J|d\xi & -\int_{-1}^{1} u_{xy}\psi_2|J|d\xi \\ \int_{-1}^{1} u_{yx}\psi_1|J|d\xi & \int_{-1}^{1} u_{yy}\psi_1|J|d\xi & \int_{-1}^{1} u_{yx}\psi_2|J|d\xi & \int_{-1}^{1} u_{yy}\psi_2|J|d\xi \end{bmatrix} \tag{2.36}$$

where the fundamental solution $u(s,q)$ and $p(s,q)$ integrated over the actual elements using the source point $s = (x^*\text{-}x,y)$. It should be pointed that for all image elements, no singularity takes place and thus all matrices corresponding to these elements can be computed numerically.

2.4 Summary

In this chapter, a theoretical background of the numerical techniques for solving soil-structure interaction problems is given. Only a brief summary of the various finite element formulations used in this research is included. The general theory of the direct boundary element method is presented in greater detail. The formulation of linear boundary elements based on a half-plane fundamental solution is presented. A method for incorporating symmetry into the boundary element method for solving half-plane problems is discussed.

Chapter 3

DEVELOPMENT AND IMPLEMENTATION OF THE SUBSTRUCTURE METHOD

3.1 Introduction

This chapter consists of three parts. Part A summarizes the work previously done in the area of coupling the boundary element and finite element for solving soil-structure interaction problems. In part B, a method for coupling the boundary element and finite element method called the *substructure method* is developed. Unlike previous methods, the *substructure method* uses boundary elements based on a half-plane fundamental solution to model the infinite far field region of a soil-structure interaction problem. Part C presents the implementation of the *substructure method* into the computer program BEFEC.

PART A

3.2 Previous Work

The concept of combining the boundary element method with other solution techniques was first introduced by Greenspan and Werner (1966). Latchat and Watson (1976) described how the boundary element method in combination with the finite element method could be used to efficiently solved infinite domain problems. This concept was further developed by Zienkiewicz, Kelly and Bettes (1977) and later on by Johnson and Nedelec (1980).

The coupling of the finite element and boundary element method for solving soil-structure interaction problems was first introduced by Brebbia and Georgiou (1979). In this work, the authors suggested two approaches for coupling the boundary element and

finite element method. In the first approach, the boundary element system is converted into an equivalent finite element and assembled with finite element system. Using the second approach, the system of finite elements is converted into an equivalent boundary element system and linked to the boundary element system.

For stress analysis problems, the finite element method results in a system of equations of the form:

$$KU = F \tag{3.1}$$

where K is the global stiffness matrix, U is the vector of nodal displacements, and F is the vector of nodal forces. From chapter two, it was pointed out that the boundary element method results in a system of equations of the form:

$$\hat{H}^K \hat{U} = G^K \hat{P} \tag{3.2}$$

where $\hat{H}^K$ and G^K are the matrices of influence coefficients evaluated using the Kelvin solution, $\hat{U}$ is the vector of nodal boundary displacements, and $\hat{P}$ is the vector of nodal boundary tractions. Solving for $\hat{P}$ in equation (3.2) gives:

$$\left(G^K\right)^{-1} \hat{H}^K \hat{U} = \hat{P} \tag{3.3}$$

So as to be consistent with the finite element system described in equation (3.1), the nodal boundary tractions $\hat{P}$ must be converted into nodal boundary forces $\hat{F}$. This is accomplished by a transformation of the form:

$$\hat{F} = M\hat{P} \tag{3.4}$$

where M is a matrix due to the weighting of the boundary tractions by the displacement interpolation functions. Premultiplying equation (3.3) with the matrix M results in:

$$M\left(G^K\right)^{-1} \hat{H}^K \hat{U} = M\hat{P} \tag{3.5}$$

which can be rewritten in the form:

$$\hat{K}\hat{U} = \hat{F} \tag{3.6}$$

where

$$\hat{K} = M\left(G^{K}\right)^{-1}\hat{H}^{K} \tag{3.7}$$

where $\hat{K}$ is the equivalent stiffness matrix corresponding to the boundary element system. Being of the same form as equation (3.1), the boundary element system as described in equation (3.6) can readily be assembled into the finite element system. This is accomplished by imposing along the boundary Γ_b the conditions of compatibility of displacements:

$$U = \hat{U} \tag{3.8}$$

and equilibrium of forces:

$$F + \hat{F} = 0 \tag{3.9}$$

It should be noted that while the matrix K resulting from the finite element method is symmetric, the equivalent stiffness matrix $\hat{K}$ resulting from the boundary element method is both unsymmetric and fully populated. However, $\hat{K}$ can be approximated by a symmetric matrix $\hat{K}^{s}$ obtained by minimizing the square of the errors ϖ_{ij} between the individual elements of $\hat{K}$ and $\hat{K}^{s}$ given by

$$\varpi_{ij} = \tfrac{1}{2}\left[\left(\hat{k}^{s}_{ij} - \hat{k}_{ij}\right) + \left(\hat{k}^{s}_{ij} - \hat{k}_{ji}\right)\right] \tag{3.10}$$

where $\hat{k}_{ij}$ is the (i,j)th element of the stiffness matrix $\hat{K}$, and $\hat{k}^{s}_{ij}$ is the (i,j)th element of the symmetric stiffness matrix $\hat{K}$. Minimizing the square of this error:

$$\frac{\partial}{\partial k^{s}_{ij}}\left(\varpi^{2}_{ij}\right) = \left(2\hat{k}^{s}_{ij} - \hat{k}_{ij} - \hat{k}_{ji}\right) = 0 \tag{3.11}$$

yields:

$$\hat{k}^{s}_{ij} = \tfrac{1}{2}\left(\hat{k}_{ij} + \hat{k}_{ji}\right) \tag{3.12}$$

According to Brebbia and Georgiou, the error introduced by this approximation is small.

It must also be emphasized that while the stiffness matrix K resulting from finite element method is normally sparse and banded, the matrix $\hat{K}$ is always fully populated. This significantly increases the bandwidth of the system.

Conversely, the finite element system can be converted into an equivalent boundary element system. This can easily be done by simply substituting

$$F = MP \tag{3.13}$$

into equation (3.1) resulting in

$$KU = MP \tag{3.14}$$

which can be considered as an equivalent boundary element system. To assemble this system and the boundary element system together, assume equation (3.14) can be partitioned as follows:

$$\left[\begin{array}{c|c} K_{FF} & K_{FI} \\ \hline K_{IF} & K_{II} \end{array}\right]\left\{\begin{array}{c} U_F \\ \hline U_F^I \end{array}\right\} = \left[\begin{array}{c|c} M_{BB} & M_{BI} \\ \hline M_{IB} & M_{II} \end{array}\right]\left\{\begin{array}{c} P_F \\ \hline P_F^I \end{array}\right\} \tag{3.15}$$

where U_F and P_F are the nodal displacements and forces exclusive to the boundary of the finite element system, while U_F^I and P_F^I are the nodal displacements and forces located on the boundary Γ_b. Similarly, the boundary element system can be partitioned in the following manner:

$$\left[\begin{array}{c|c} \hat{H}_{BB}^K & \hat{H}_{BI}^K \\ \hline \hat{H}_{IB}^K & \hat{H}_{II}^K \end{array}\right]\left\{\begin{array}{c} U_B \\ \hline U_B^I \end{array}\right\} = \left[\begin{array}{c|c} G_{BB}^K & G_{BI}^K \\ \hline G_{IB}^K & G_{II}^K \end{array}\right]\left\{\begin{array}{c} P_B \\ \hline P_B^I \end{array}\right\} \tag{3.16}$$

where U_B and P_F are the nodal displacements and forces exclusive to the boundary of the boundary element system, while U_B^I and P_B^I are the nodal displacements and forces located on the boundary Γ_b. Imposing the conditions of compatibility of displacements

$$U_B^I = U_F^I = U^I \tag{3.17}$$

and force equilibrium

$$F_B^I + F_F^I \tag{3.18}$$

along the boundary Γ_b the system

$$\begin{bmatrix} \hat{H}_{BB}^K & \hat{H}_{BI}^K & 0 \\ \hat{H}_{IB}^K & \hat{H}_{II}^K + K_{II} & K_{IF} \\ 0 & K_{FI} & K_{FF} \end{bmatrix} \begin{bmatrix} U_B \\ U_I \\ U_I \end{bmatrix} = \begin{bmatrix} G_{BB}^K & G_{BI}^K & 0 \\ G_{IB}^K & G_{II}^K + M_{II} & M_{IF} \\ 0 & M_{FI} & M_{FF} \end{bmatrix} \begin{bmatrix} P_B \\ P_I \\ P_I \end{bmatrix} \tag{3.19}$$

Consequently, the displacement and tractions must be re-ordered such that those which are unknown are kept on the left side while those that are prescribed are place on the right side and multiplied with their corresponding influence coefficient. One advantage of this approach over the previous one is that no inversion is necessary.

Between the two approaches, the former is more widely used. This is mainly because there exists a much larger number of computer programs for the finite element method as compared to boundary element method. Also, the second approach requires the linking to two dissimilar boundary element systems of which very few existing boundary element programs are capable of doing. In contrast, most finite element programs have the capacity to assemble together dissimilar element types.

Figure (3.1) illustrates the coupled system used by Brebbia and Georgiou for solving soil-structure interaction problems. In this model, the structure Ω_B is modeled using quadratic finite elements while the entire soil domain Ω_S is modeled using constant boundary elements. The boundary elements used are based on the Kelvin fundamental solution. As was previously mentioned, Ω_S is normally an infinite half-plane. However, because the Kelvin solution is used, Ω_S must be approximated by a significantly large finite domain. The argument of Brebbia and Georgiou is that using boundary elements as opposed to finite elements for modeling this domain significantly reduces the size of the problem.

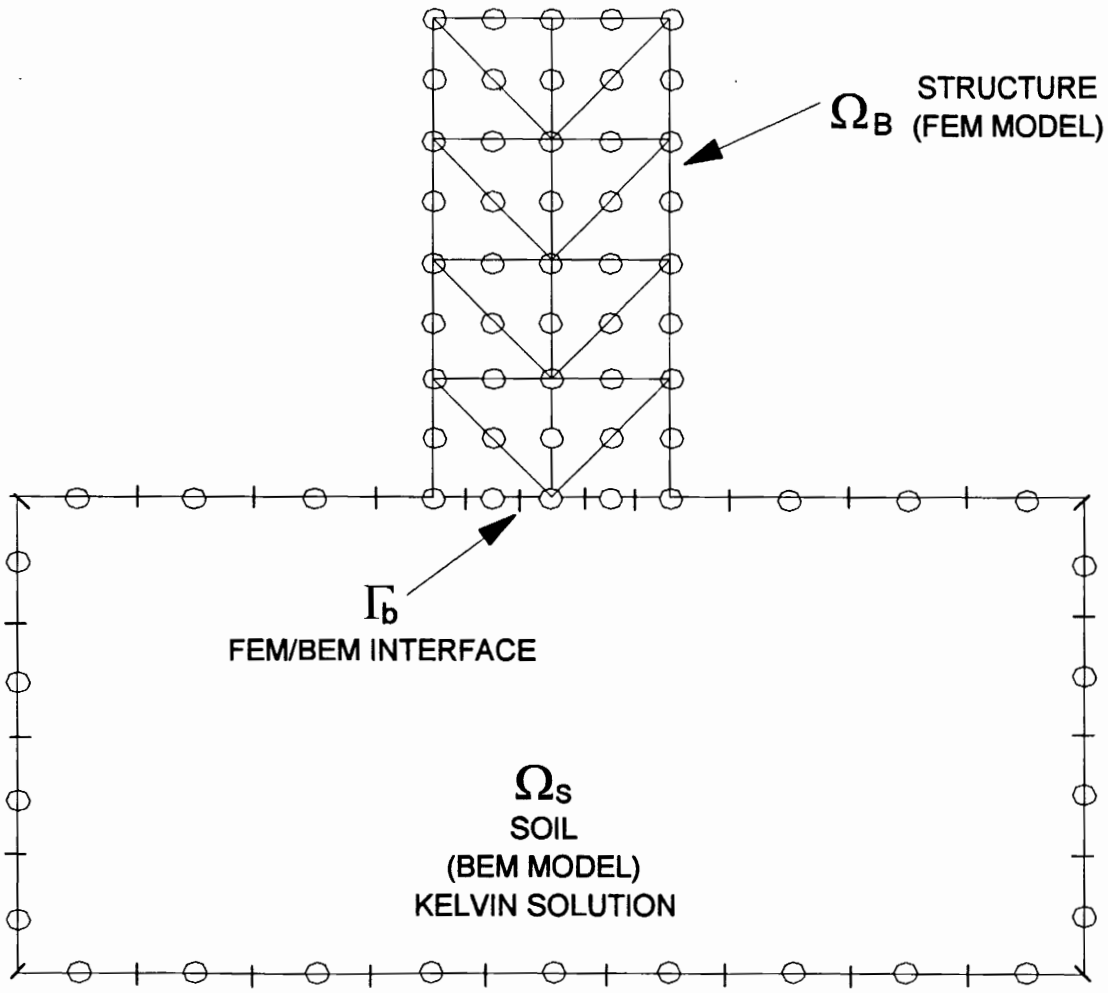

Figure 3.1. Coupled finite element - boundary element system (Brebbia and Georgiou, 1979)

Vallabhan, Sivakumar and Radhakrishnan (1984) applied the coupling of the boundary element and finite element method to the solution of U-frame lock problems. The model used by these, as illustrated in Figure (3.2), is similar to that used by Brebbia and Georgiou. Quadrilateral finite elements are used to model the U-frame lock structure while the entire soil domain is modeled using constant boundary elements based on the Kelvin solution. One difference between in the boundary element model used in this model over the previous one is the capability to take into consideration different soil layers. However this capability is limited to a maximum of three soils types. This because above this number, it becomes more efficient to model the soil domain using finite elements. The boundary element solution for problems where several layers of different materials are involved is described by Brebbia (1978).

In the Vallabhan model, the structure and soil domain are connected at the interface Γ_b. Along this interface, the displacements U_b and tractions P_b are unknown. Along the other boundaries of the soil domain, the following boundary conditions are prescribed:

$$\left.\begin{aligned} P_x &= 0 \\ U_y &= 0 \end{aligned}\right\} \text{ on } \Gamma_1$$

$$\left.\begin{aligned} U_x &= 0 \\ P_y &= 0 \end{aligned}\right\} \text{ on } \Gamma_2$$

$$\left.\begin{aligned} P_x &= 0 \\ P_y &= q \end{aligned}\right\} \text{ on } \Gamma_3 \text{ where } q \text{ is a prescribed traction}$$

$$\left.\begin{aligned} U_x &= 0 \\ P_y &= 0 \end{aligned}\right\} \text{ on } \Gamma_4$$

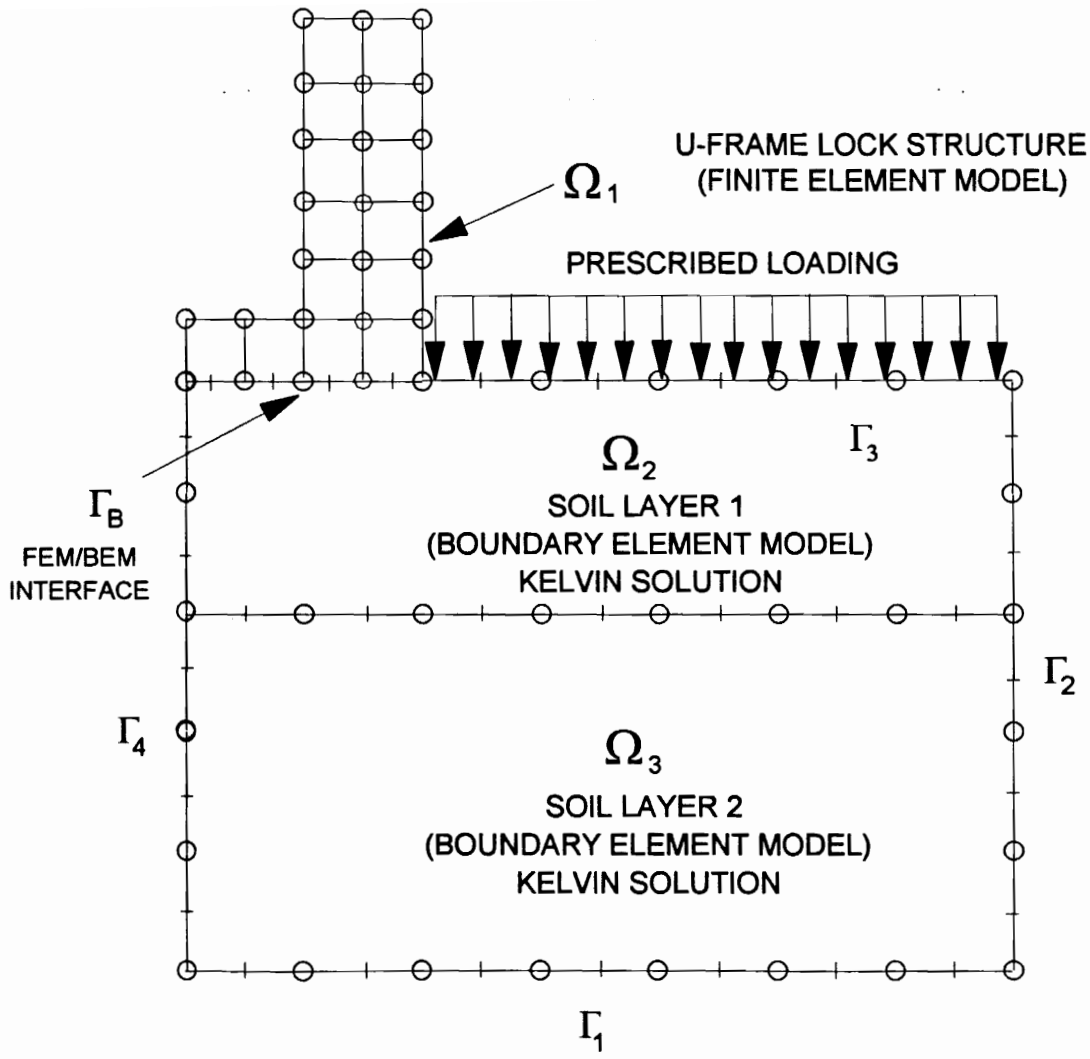

Figure 3.2. Coupled finite element - boundary element system (Vallabhan, Sivkumar and Radhakrishnan, 1984)

After the soils layers Ω_2 and Ω_3 are linked together, the degrees of freedom corresponding to nodes along the interface between Ω_2 and Ω_3 are eliminated using a static condensation procedure (Wilson, 1974). The resulting system can be partitioned in the following form:

$$\left[\begin{array}{c|c|c} \hat{H}_{11}^{K} & \hat{H}_{12}^{K} & \hat{H}_{13}^{K} \\ \hline \hat{H}_{21}^{K} & \hat{H}_{22}^{K} & \hat{H}_{23}^{K} \\ \hline \hat{H}_{31}^{K} & \hat{H}_{32}^{K} & \hat{H}_{33}^{K} \end{array}\right]\left[\begin{array}{c} U_B \\ \hline U_P \\ \hline U_U \end{array}\right] = \left[\begin{array}{c|c|c} G_{11}^{K} & G_{12}^{K} & G_{13}^{K} \\ \hline G_{21}^{K} & G_{22}^{K} & G_{23}^{K} \\ \hline G_{31}^{K} & G_{32}^{K} & G_{33}^{K} \end{array}\right]\left[\begin{array}{c} P_B \\ \hline P_P \\ \hline P_U \end{array}\right] \tag{3.20}$$

where U_F and P_F are the displacements and tractions respectively along the boundary Γ_b. U_P and P_P correspond to the prescribed displacements and tractions along boundaries Γ_1, Γ_2, Γ_3, and Γ_4. U_U and P_U correspond to the unknown displacements and tractions along boundaries Γ_1, Γ_2, Γ_3, and Γ_4. Using the Gauss-Jordan elimination procedure (James et al. 1967) equation (3.20) is transformed into a system of the form:

$$\left[\begin{array}{c|c|c} \hat{H}_{11}^{*} & \hat{H}_{12}^{*} & 0 \\ \hline \hat{H}_{21}^{*} & \hat{H}_{22}^{*} & 0 \\ \hline \hat{H}_{31}^{*} & \hat{H}_{32}^{*} & I \end{array}\right]\left[\begin{array}{c} U_B \\ \hline U_P \\ \hline U_U \end{array}\right] = \left[\begin{array}{c|c|c} G_{11}^{*} & G_{12}^{*} & G_{13}^{*} \\ \hline G_{21}^{*} & G_{22}^{*} & G_{23}^{*} \\ \hline G_{31}^{*} & G_{32}^{*} & G_{33}^{*} \end{array}\right]\left[\begin{array}{c} P_B \\ \hline P_P \\ \hline P_U \end{array}\right] \tag{3.21}$$

Taking the first two submatrix equations yields:

$$\left[\begin{array}{c|c} \hat{H}_{11}^{*} & \hat{H}_{12}^{*} \\ \hline \hat{H}_{21}^{*} & \hat{H}_{22}^{*} \end{array}\right]\left[\begin{array}{c} U_B \\ \hline U_P \end{array}\right] = \left[\begin{array}{c|c} G_{11}^{*} & G_{12}^{*} \\ \hline G_{21}^{*} & G_{22}^{*} \end{array}\right]\left[\begin{array}{c} P_B \\ \hline P_U \end{array}\right] + \left[\begin{array}{c} G_{13}^{*} \\ \hline G_{23}^{*} \end{array}\right] P_p \tag{3.22}$$

Using the Gauss-Jordan elimination procedure, equation (3.22) is transformed into a system of the form:

$$\left[\begin{array}{c|c} H_{11}^{**} & H_{12}^{**} \\ \hline H_{21}^{**} & H_{22}^{**} \end{array}\right]\left[\begin{array}{c} U_B \\ \hline U_P \end{array}\right] = \left[\begin{array}{c|c} G_{11}^{**} & 0 \\ \hline G_{21}^{**} & I \end{array}\right]\left[\begin{array}{c} P_B \\ \hline P_U \end{array}\right] + \left[\begin{array}{c} G_{13}^{**} \\ \hline G_{23}^{**} \end{array}\right] P_P \tag{3.23}$$

Expanding the first submatrix equation yields:

$$H_{11}^{**} U_B = G_{11}^{**} P_B - H_{12}^{**} U_P + G_{13}^{**} P_p \tag{3.24}$$

Premultiplying by the transformation matrix M described in equation (3.11) gives:

$$M\left(G_{11}^{**}\right)^{-1} H_{11}^{**} U_B = MP_B - M\left(G_{11}^{**}\right)^{-1}\left(H_{12}^{**} U_P + G_{13}^{**} P_p\right) \tag{3.25}$$

which can be rewritten as

$$\tilde{K} U_B = F_B - f_B \tag{3.26}$$

where

$$\tilde{K} = M\left(G_{11}^{**}\right)^{-1} H_{11}^{**} \tag{3.27}$$

$$F_B = MP_B \tag{3.28}$$

$$f_B = M\left(G_{11}^{**}\right)^{-1}\left(H_{12}^{**} U_p G_{12}^{**} P_P\right) \tag{3.29}$$

The equivalent stiffness matrix $\tilde{K}$ is then made symmetric using the technique proposed by Brebbia and Georgiou as described in equation (3.10).

One difference between the Vallabhan model and that proposed by Brebbia and Georgiou is the manner in which the constant boundary elements are connected to the finite elements. Constant boundary elements use only one node for interpolating both displacements and tractions. In the Brebbia-Georgiou model, this node is directly connected to the nodes in the adjoining finite elements. In the model used by Vallabhan et al. the endpoints of the constant boundary element are connect to nodes of the adjoining finite element. Thus, the nodes in the boundary element and finite element system do not coincide. To eliminate this inconsistency, matrix $\tilde{K}$ described in equation (3.27) is transformed into a stiffness matrix $\hat{K}$ which is compatible with the finite element system. This is done by performing a transformation of the following form:

$$U_b = TU_B \tag{3.30}$$

where U_B are the displacement at the center of the constant boundary elements and, U_b are the displacements at the ends of the element compatible with nodal displacements of the quadrilateral finite element. By the contragradient law,

$$F_B = T^t F_b \tag{3.31}$$

Applying equations (3.30) and (3.31) to (3.26) yields:

$$T^t \tilde{K} T U_b = T^t (F_B + f_B) \tag{3.32}$$

or

$$\hat{K} U_b = F_b + f_b \tag{3.33}$$

where

$$\hat{K} = T^t \tilde{K} T \tag{3.34}$$

$$f_b = T^t f_B \tag{3.35}$$

The equivalent finite element described in equation (3.32) can now be readily assembled into the finite element system.

Compared with the procedure previously presented by Brebbia and Georgiou, the Vallabhan procedure is computationally more intensive. However, the resulting stiffness matrix $\hat{K}$ is significantly smaller. This is because only those degrees of freedom necessary for assembling the boundary element system into the finite element system are included in $\hat{K}$. Consequently, the coupled system resulting from the Vallabhan procedure is significantly smaller as compared to that resulting from the procedure by Brebbia and Georgiou.

A smaller coupled system also results when solving problem with symmetric geometry and loading using the Vallabhan procedure are compared to the Brebbia-Gregiou procedure. In the Brebbia-Georgiou model, the endpoints of the boundary elements do not coincide with the corners of the finite elements along the interface Γ_b. Because of this, the problems domain cannot readily be halved along the line symmetry. Thus the entire domain of the problem must be considered even if the problem is symmetric. In the Vallabhan model, the endpoints of the boundary elements coincide with

the corners of the finite elements along the interface Γ_b. In this case, the half of the problems domain needs to be considered if the problem is symmetric.

PART B

3.3 Formulation of Substructure Method

This section presents a new procedure specifically suited for solving soil-structure interaction problems using a coupled boundary element-finite element system. In this procedure, both the near and far field of the soil domain are accounted for. The near field, consisting of the soil adjacent to the structure, is assumed to be a nonlinear and non homogenous finite domain. The far field, which consists of the soil distant from the structure, is assumed to be a homogenous and linear elastic infinite half-plane. Quadrilateral finite elements are used to model both the structure and the near field of the soil domain. Linear boundary elements based on the Melan fundamental solution are used to model the far field of the soil domain. The model used in the *substructure method* is illustrated in Figure (3.3)

The *substructure method* has several advantages over the two procedures described in part A. Because the soil in the near field is modeled using finite elements, the *substructure method* has the capability of solving problems involving nonlinear and non homogenous soils in the near field. In the Brebbia-Georgiou model, the entire soil domain must be both homogenous and linearly elastic. While the Vallabhan model allows the soil domain to have several layers of different soils, the number of layers is limited to three. In addition, all soils in the Vallabhan model must be linearly elastic. In the *substructure method*, there is no limit to the number of different soil layers the soil domain can have. Because the Melan solution is used instead of the Kelvin solution, there is no need to descretize the ground surface as well as the distant boundaries using boundary elements.

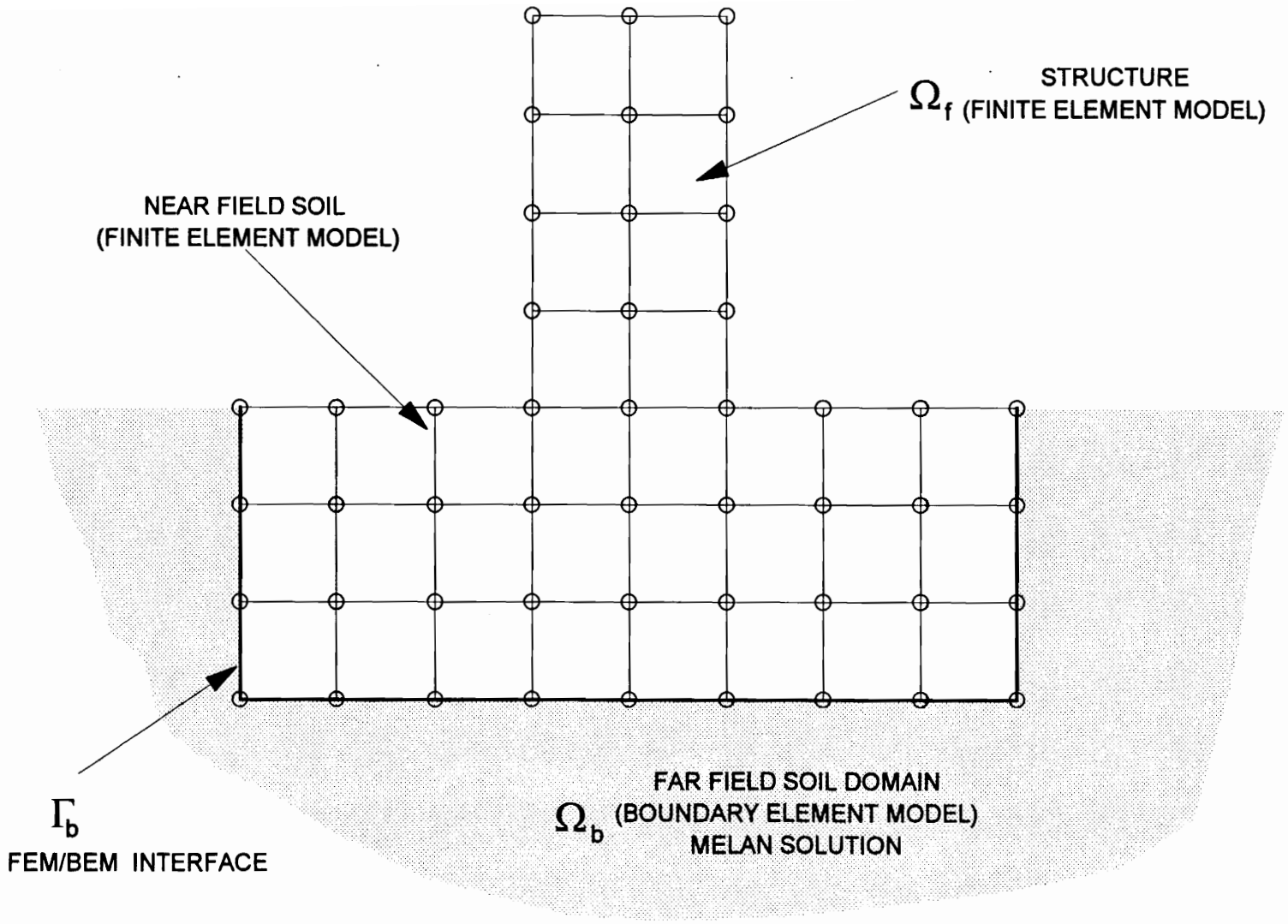

Figure 3.3. Proposed coupled finite element - boundary element system.

On the average, the system resulting from the Melan solution involves one-tenth the number of elements required if the Kelvin solution were used.

Compared with the finite element method, the *substructure method* results in a mesh which uses one-fifth the number of finite elements to model the soil domain. If the entire soil domain were model using finite elements, a mesh involving a very large domain hence very many elements need to be used in order to accurately model the soil domain. If this is not done, significant errors occur in both the predicted displacements and stresses when compared with the closed form solution. On the average, these errors can be as large as 60%. Using the *substructure method,* only the soil in the near field, where the nonlinearity is most pronounced, needs to be modeled using finite elements. The soil in the far field can be modeled using the Melan boundary elements. The number of boundary elements needed to model the far field is between 5% to 10% the number of finite elements needed to model the same domain.

In the *substructure method,* the equations (2.7) through (2.9) are evaluate using the Melan fundamental solution described in Appendix A. This results in a boundary element system of the form

$$\hat{H}^M \hat{U} = \hat{G}^M \hat{P} \tag{3.36}$$

where the matrices $\hat{H}^M$ and G^M are the matrices of influence coefficients evaluated using the Melan solution, and $\hat{U}$ and $\hat{P}$ are the nodal displacements and tractions along the boundary Γ_b. The boundary element system described in equation (3.36) is then converted to an equivalent finite element system using the procedure by Brebbia and Georgiou presented in Part A. This system is of the same form as equation (3.6) where the equivalent stiffness matrix $\hat{K}$ is given by:

$$\hat{K} = M\left(G^M\right)^{-1} \hat{H}^M \tag{3.37}$$

The stiffness matrix $\hat{K}$ can further be made symmetric using equation (3.12). It should be emphasized that the conclusion made by Brebbia and Georgiou as to the insignificance of the errors introduction by using equation (3.12) are only valid for the case where the boundary elements used are based on the Kelvin solution. In general, the errors resulting from the use of equation (3.12) may be significant. In chapter 4, the errors that resulting from use of equation (3.12) for case when boundary elements based on the Melan solution shall be studied.

As compared to the Kelvin solution, it is not necessary to use boundary element to model the free surface as well as the distant boundaries of the soil domain when using the Melan solution. Thus, the stiffness matrix $\hat{K}$ obtained using the *substructure method* is significantly smaller as compared to that obtained using the Brebbia-Georgiou procedure. The stiffness matrix $\hat{K}$ obtained using the Vallabhan procedure is of the same size as that obtained using the *substructure method.* However, *substructure method* does require the additional computations in the Vallabhan procedure necessary to eliminate the degrees of freedom not directly assembled into the finite element system.

The coupling of linear finite elements with linear boundary elements eliminates the need for the transformation described in equation (3.21) as required in the Vallabhan model. Also, problems involving symmetric geometry and loading can be solved by considering only half of the domain. In the Brebbia-Georgiou model, the entire domain needs to be considered even if the geometry of the problem is symmetric.

In the *substructure method,* the finite elements are assembled such that the resulting system is partitioned in the following manner:

$$\left[\begin{array}{c|c} K_{ff} & K_{fb} \\ \hline K_{bf} & K_{bb} \end{array}\right] \left\{\begin{array}{c} U_f \\ \hline U_b \end{array}\right\} = \left\{\begin{array}{c} F_f \\ \hline F_b \end{array}\right\} \tag{3.38}$$

where U_b and F_b are the nodal displacements and forces lying on Γ_b. U_f and F_f are the nodal displacements and forces respectively not located on the boundary Γ_b.

The boundary element system is assembled into the finite element system by imposing that the displacements in both the finite element and boundary element systems be compatible:

$$U_b = \hat{U} \tag{3.39}$$

Also, the sum of the nodal forces in the finite element and boundary element system equal zero along the boundary Γ_b:

$$F_b + \hat{F} = 0 \tag{3.40}$$

Thus, applying equations (3.6), (3.38), (3.39) and (3.40) to equation (3.37), results in a coupled system of the form:

$$\left[\begin{array}{c|c} K_{ff} & K_{fb} \\ \hline K_{bf} & K_{bb} + \hat{K} \end{array}\right] \left\{\begin{array}{c} U_f \\ \hline U_b \end{array}\right\} = \left\{\begin{array}{c} F_f \\ \hline 0 \end{array}\right\} \tag{3.41}$$

Arranging the equations as described in equation (3.41) has two major advantages. First, it isolates the elements of the fully populated matrix $\hat{K}$ and results in a minimum bandwidth for the coupled system. Also, only the part involving $\hat{K}$ becomes unsymmetric while the other parts of the system remain symmetric. Thus only the unsymmetric part of the lower portion, in addition to the entire upper triangular part, needs to be stored. Since $\hat{K}$ is very small compared to the entire stiffness matrix, the additional storage needed for the unsymmetric part of the stiffness matrix is very minimal. In Part C, the procedure for arranging the equations are described in equation (3.41) shall be presented. Also, the technique for storing and solving the "partially unsymmetric" system shall be described.

The coupling procedure can be summarized in the following steps:

STEP 1: From the problem geometry and material parameters given, form the $\hat{H}^M$, G^M matrices as described in chapter 2, and the transformation matrix M as shall be described in the following section.

STEP 2: Perform the matrix operations specified in equation (3.37) to obtain the boundary element stiffness matrix $\hat{K}$.

STEP 3: If only the symmetric part of $\hat{K}$ is to be used, used only the symmetric part as given in equation (3.12).

STEP 4: Assemble the stiffness matrix $\hat{K}$ into the global stiffness matrix as given in equation (3.41).

STEP 5: Solve the resulting system of equation as would be done for purely finite element system. However, if the unsymmetric $\hat{K}$ is used, the "partially unsymmetric" solution technique must be used.

STEP 6: Using displacements, compute the stresses as would be done in a purely finite element system.

3.4 Development of the Transformation Matrix

In this section, the transformation matrix M described in equation (3.4) shall now be derived for the special case when a quadrilateral element is coupled with a linear boundary element. Assume a single boundary element is assembled into a quadrilateral element over the boundary Γ^e as described in Figure (3.4).

From the finite element method, the equivalent nodal load f for a given traction distribution $p(x,y)$ over the boundary $\Gamma^e$of a finite element is given by

$$f_i^j = \int_{\Gamma^e} \psi_i(x,y) p_j(x,y) d\Gamma^e \tag{3.42}$$

where $p_i(x,y)$ is the ith traction component, $\psi_i(x,y)$ is the lagrangian interpolating function corresponding to the jth node. f_i^j is the ith component of the equivalent nodal force at

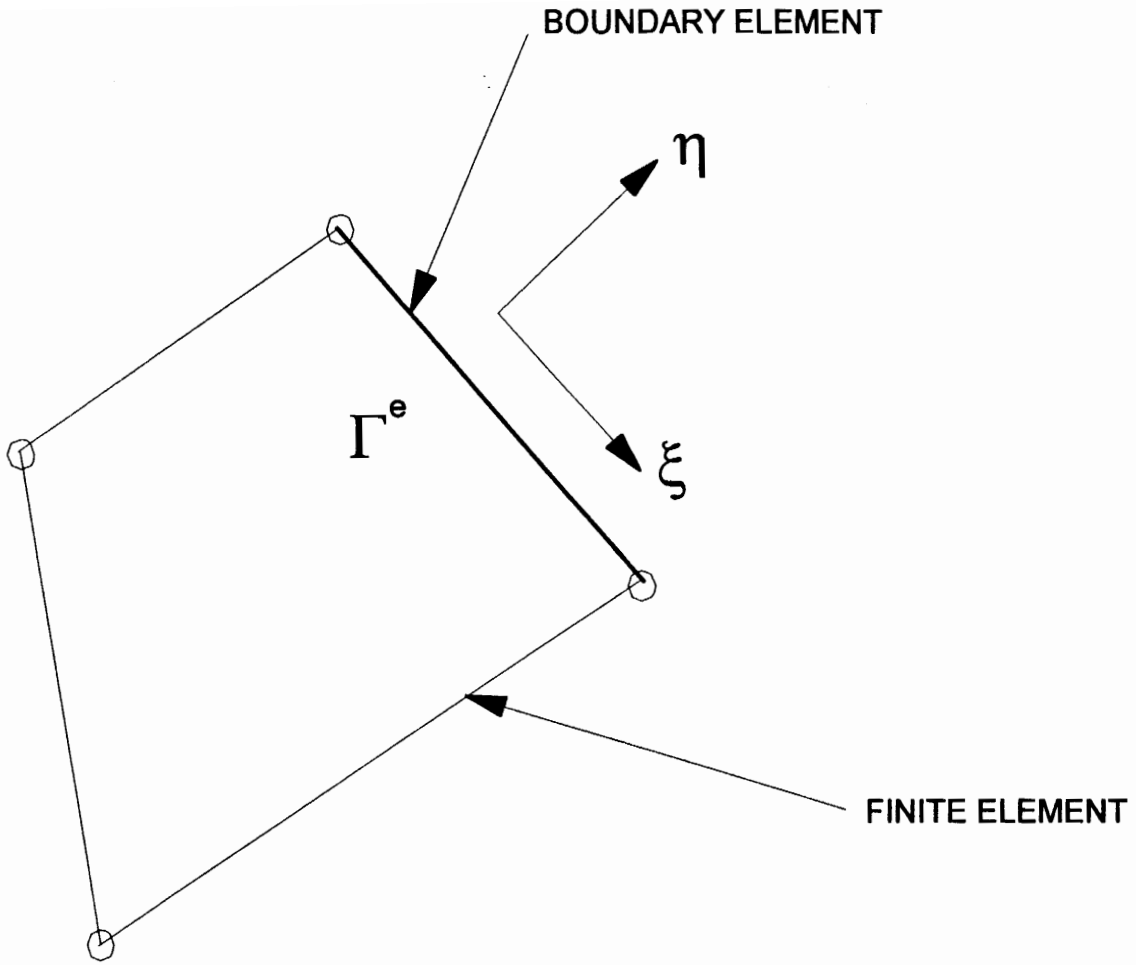

Figure 3.4. Coupled finite element - boundary element system.

node i. Because of the properties of the interpolating function, only those components corresponding to nodes on the boundary are non-zero. Furthermore, these non-vanishing components degenerate to function of one variable along the boundary. Thus, the above integral can be rewritten as

$$f_i^j = \int_{\Gamma^e} \psi_i(\xi) p_j(\xi) d\Gamma^e \tag{3.43}$$

where $i = 1,2$ and ξ is the local coordinate along the boundary Γ^e.

Similarly, for linear boundary elements, the tractions along a boundary element are assumed to vary in the following manner:

$$p_i(\xi) = \sum_{j=1}^{2} p_i^j \psi_j(\xi) \tag{3.44}$$

where i=1,2, and p_i^j is the ith component of traction at the jth node.

Thus, a relationship for transforming nodal traction in the boundary element system to equivalent nodal loads can be obtained by combining equations (3.43) and (3.44), the equivalent nodal load can be obtained by the relation

$$f_j^i = \sum_{k=1}^{2} M_{ik} p_k^j \tag{3.45}$$

where

$$M_{ij} = \int_{\Gamma^e} \psi_i(\xi) \psi_j(\xi) d\Gamma^e \tag{3.46}$$

and i=*1,2*.

For coupling between a quadrilateral finite element and linear boundary element, the quantity Γ^e equals the length of the boundary l, and the interpolating functions are given by equation (2.18). Thus, evaluating of equation (3.46) yields in matrix form:

$$\begin{Bmatrix} f_x^1 \\ f_y^1 \\ f_x^2 \\ f_y^2 \end{Bmatrix} = \frac{l}{6}\begin{bmatrix} 2 & 0 & 1 & 0 \\ 0 & 2 & 0 & 1 \\ 1 & 0 & 2 & 0 \\ 0 & 1 & 0 & 2 \end{bmatrix}\begin{Bmatrix} p_x^1 \\ p_y^1 \\ p_x^2 \\ p_y^2 \end{Bmatrix} \tag{3.47}$$

For the general case of a system consisting of m nodes and m-1 boundary elements, where element Γ^j of length l^j, equation (3.45) becomes

$$f_i^j = \sum_{k=1}^{m}\left[\sum_{l=1}^{m-1} M_{ki}^{(l)} p_k^j\right] \tag{3.48}$$

where f_i^j is the ith component of the nodal forces at the jth node, p_i^j is the ith component of the nodal traction at the jth node, and $M^{(l)}$ is the M matrix for the lth boundary element. Figure (3.5) shows equation (3.48) expanded in matrix form.

3.5 Nonlinear Case

The solution procedure described above can easily be applied to then solution of nonlinear soil-structure interaction problems with very little modification assuming the following assumptions are made. First, the nonlinear or non homogenous part of the problem is modeled using finite elements alone. The far field is assumed to be linearly elastic and homogenous. For the Newton-Raphson method, the tangent stiffness matrix of the boundary element system can be obtained by writing equation (3.6) in residual form

$$\hat{K}\hat{U} - \hat{F} = \hat{R} \tag{3.49}$$

where $\hat{R}$ is the residual for the boundary element system. Taking the derivative of the residual with respect to the displacements:

$$\frac{\partial}{\partial \hat{U}}\left(\hat{K}\hat{U}\right) = \frac{\partial \hat{K}}{\partial \hat{U}}\hat{U} + \hat{K} \tag{3.50}$$

$$
\begin{Bmatrix} f_x^1 \\ f_y^1 \\ f_x^2 \\ f_y^2 \\ f_x^3 \\ f_y^3 \\ \vdots \\ f_x^{m-1} \\ f_y^{m-1} \\ f_x^m \\ f_y^m \end{Bmatrix} =
\begin{bmatrix}
2l_1 & 0 & l_1 & & & & & & & & \\
0 & 2l_1 & 0 & l_2 & & & & & & & \\
l_1 & 0 & 2(l_1+l_2) & 0 & l_{21} & & & & & & \\
 & l_1 & 0 & 2(l_1+l_2) & 0 & l_2 & & & & & \\
 & & l_2 & 0 & 2(l_2+l_3) & 0 & \ddots & & & & \\
 & & & l_2 & 0 & 2(l_2+l_3) & 0 & l_{n-1} & & & \\
 & & & & \ddots & 0 & \ddots & 0 & l_{n-1} & & \\
 & & & & & l_{n-1} & 0 & 2(l_{n-1}+l_n) & 0 & l_n & \\
 & & & & & & l_{n-1} & 0 & 2(l_{n-1}+l_n) & 0 & l_n \\
 & & & & & & & l_n & 0 & l_n & 0 \\
 & & & & & & & & l_n & 0 & l_n
\end{bmatrix}
\begin{Bmatrix} p_x^1 \\ p_y^1 \\ p_x^2 \\ p_y^2 \\ p_x^3 \\ p_y^3 \\ \vdots \\ p_x^{m-1} \\ p_y^{m-1} \\ p_x^m \\ p_y^m \end{Bmatrix}
$$

Figure 3.5. Nodal force-traction transformation for a general coupled system.

Since for the linear elastic case, $\hat{K}$ is independent of the displacements $\hat{U}$, the first term vanishes and the tangent stiffness matrix is given by

$$\tilde{K}^{BEM} = \hat{K} \tag{3.51}$$

The residual vector used in the Newton-Raphson method can be computed using equation (3.49).

Based on these observations, it can be seen that for the nonlinear case, solving the coupled system is identical to solving a system involving finite elements only. It should be pointed out that the stiffness matrix corresponding to the boundary element system need only be formed once and stored so that it can be used to form the global stiffness matrix and residual vector during each iteration.

PART C

3.6 Implementation of Substructure Method

The substructure method which was developed in the preceding section is implemented in a computer program BEFEC. This program has the capability of solving elasto-plastic plane strain problems. BEFEC uses the four node isoparametric finite element and the linear boundary element using the half-plane fundamental solution. A non-associated plasticity model using the Drucker-Prager yield condition and Von Mises yield surface as a the plastic potential is used. This plasticity model has been widely preferred over the associated Drucker-Prager model for modeling geological materials. The reason for this is that the Von Mises surfaces tends to correct the often excessive dilitancy predicted by the Drucker Prager condition. Because of the modularized nature of the program, it is easy to add other elements and constitutive models. The integration of the stresses during elasto-plastic behavior are performed using a fully implicit Euler integration scheme.

The main algorithm is that of the Newton-Raphson method. The system of equations resulting during each iteration are solved using the LDU factorization technique. The program has the capability of solving both fully symmetric or unsymmetric systems of equations. In addition, a modification of the factorization technique is developed and implemented in BEFEC to handle the case of partially unsymmetric systems of equations resulting from the coupling of the finite element and boundary element systems.

The internal arrays are structured using dynamic allocation. This scheme makes the size of the internal memory grow with size of the problem being analyzed. Thus no core storage is wasted.

Execution of the program BEFEC for a given problems involves two phases: the input phase, and solution phase. In the input phase, data is read from an existing data file using free format rules. Data for the nodal coordinates, finite element connectivity, boundary element connectivity and boundary conditions can either be inputted individually or generated using various data generation subroutines. Details of these data generation schemes as well as the input format are described in the User's Manual given in Appendix B. In the solution phase, the problem is analyzed and resulting solution is printed out. If the "data-check-only" option is used, the solution phase is not executed. This option allows one to verify the correctness of data before any lengthy computations are performed.

Solution Phase

The solution phase is based on the Newton-Raphson method. The entire load is applied in a number of load steps. Within each load step, the solution iteratively solved using the current displacement and stresses. Each iteration consists of forming the tangent stiffness matrix and solving for the displacements. Formation of the tangent stiffness

matrix involve computing the individual finite element matrices and residual vector as well as the equivalent stiffness matrix and residual vector for the boundary element system. Before the system of equations is solved, the residual vector **R** is compared to the current vector of externally applied loads **F**. Convergence occurs when the following condition is satisfied:

$$\|\mathbf{R}\| = \frac{\sqrt{\sum_{j=1,n}(\mathbf{R}_j)^2}}{\sqrt{\sum_{j=1,n}(\mathbf{F}_j)^2}} \leq \varepsilon_{TOL} \tag{3.52}$$

where ε_{TOL} is an error tolerance specified in the input data. If the solution does not converge after a specified number of iterations NITER, the solution procedure is halted and the solution is printed out. After every load step, the displacements and stresses are printed. Only the displacements are printed out for each substep if the load sub increment option is used. A flowchart of the entire solution phase is given in Figure (3.6)

Finite Element Computations

The main driving routine for all finite element computations is subroutine STIFQ4. A flow chart of this subroutine is given in Figure (3.7). This subroutine forms the tangent stiffness matrix for a given finite element. Numerical integration is performed using a 2 × 2 gaussian quadrature. Prior to the integration loop, STIFQ4 call the subroutine SHAPE to compute the interpolation functions and their derivatives for four gaussian points. Within the integration loop, the strain-displacement matrix **B** is first computed for each gaussian point in the subroutine QBMAT. Using the strain-displacement matrix, the strain and stresses are computed in the subroutine STRQ4. These updated stresses are used to

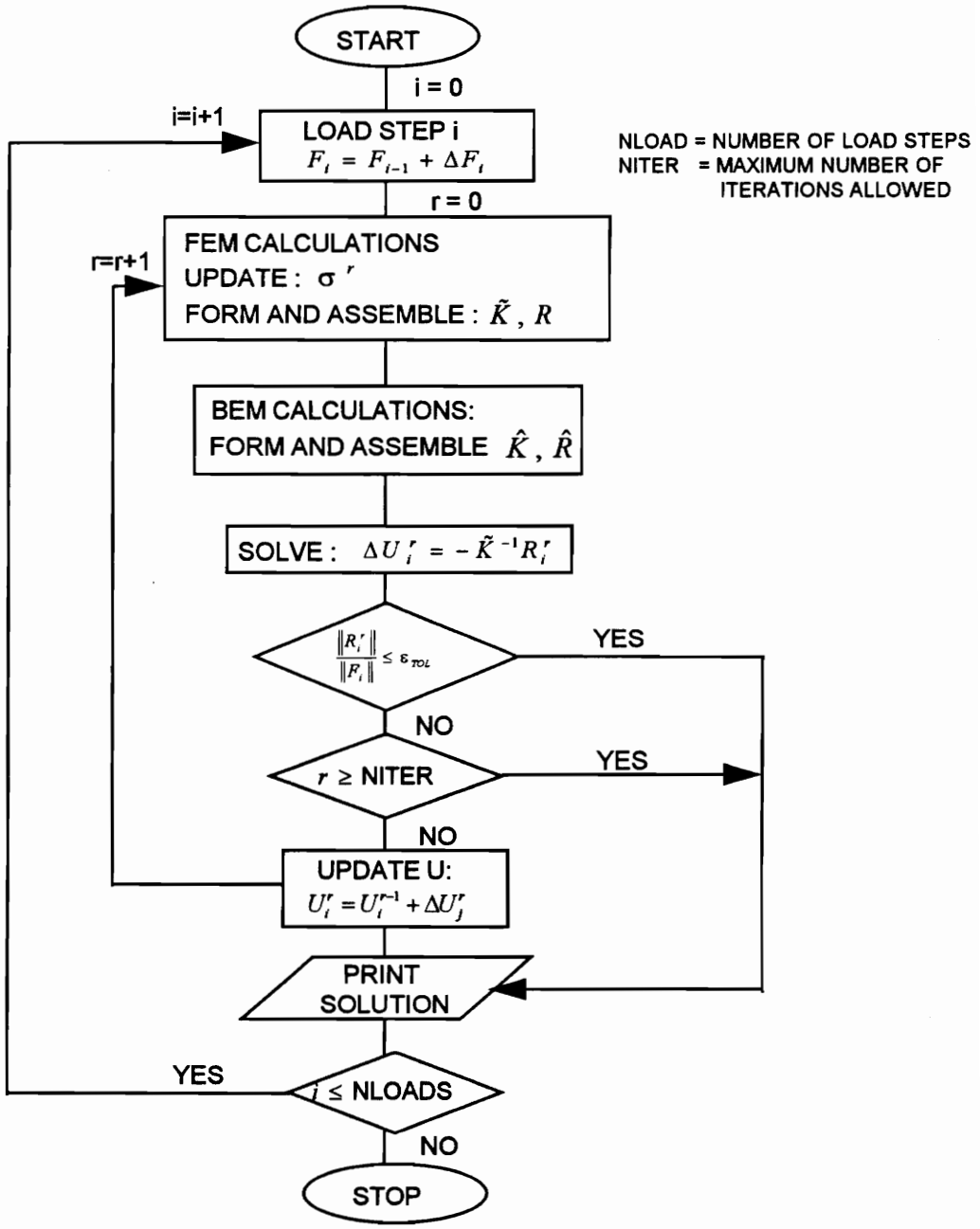

Figure 3.6. Flowchart of Solution Phase

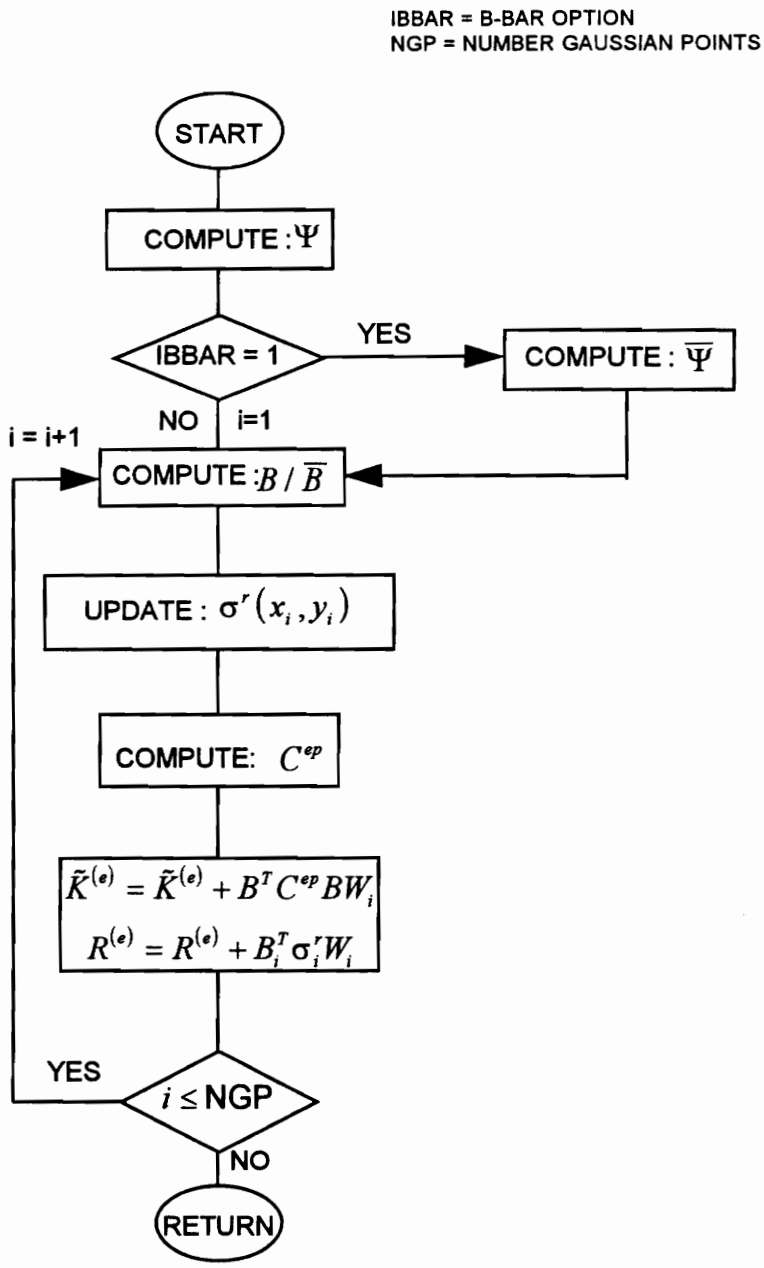

Figure 3.7. Flow Chart of Subroutine STIFQ4

compute the stress-strain matrix. The contribution to the tangent stiffness and residual vector are then computed.

Incompressible Formulation

It has often been observed that for elasto-plastic materials near the collapse load, the tangent stiffness finite element solution exhibits too stiff a response. Nagtegaal (1974) attributes this to the shear locking which occurs when the material is nearly incompressible. In this work, an approach known as the *mean dilatation* formulation is developed to alleviate this shear locking. In this formulation, the volumetrically stiff part of the strain-displacement matrix **B** is replaced by a improved strain-displacement matrix $\overline{\mathbf{B}}$. BEFEC uses this formulation for solving elasto-plastic problems. Details of the implementation of the *mean dilatation* formulation are presented by Hughes (1987).

Stress Computations

In BEFEC, the integration of elasto-plastic constitutive equations is performed using the fully implicit Euler method (Wilkins, 1964). In this method the trial stress is first computed assuming fully elastic behavior. If the stress states lies outside the yield surface, the stress state is projected radially back to the yield surface to obtain the correct final stress state. Unlike fully explicit integration schemes more commonly used, this method does not require the stress state at which the transition between the elastic and plastic range occurs to be known. A detailed description of how this technique is applied to the Drucker-Prager model is given by Loret and Prevost (1986). A summary of the procedure as applied to the non-associative case where the Drucker-Pragger criterion is used as the yield surface and the Von Mises yield function is used as the plastic potential is now presented.

The method starts with first solving for the strain increments using the relation

$$\Delta\varepsilon = \mathbf{B}\Delta\mathbf{d} \tag{3.53}$$

If the mean dilatation formulation is used, the strains are computed using $\overline{\mathbf{B}}$ instead. The strains are then decomposed into the volumetric (dilatation) ε_v and deviatoric components **e** respectively where

$$\Delta\varepsilon_v = \Delta\varepsilon_{xx} + \Delta\varepsilon_{yy} + \Delta\varepsilon_{zz} \tag{3.54}$$

$$\Delta e_{ij} = \Delta\varepsilon_{ij} - \tfrac{1}{3}\delta_{ij}\Delta\varepsilon_v \tag{3.55}$$

where δ_{ij} is the Dirac delta. Similarly, the previous stress state σ_{ij}^{r-1} is split into a volumetric part p^{r-1} and deviatoric part s_{ij}^{r-1}

$$p^{r-1} = \sigma_{xx}^{r-1} + \sigma_{yy}^{r-1} + \sigma_{zz}^{r-1} \tag{3.56}$$

$$s_{ij}^{r-1} = \sigma_{ij}^{r-1} - \tfrac{1}{3}\delta_{ij}p^{r-1} \tag{3.57}$$

The trial volumetric stress p and deviatoric stresses s_{ij} are computed using the linear stress-strain relations

$$\tilde{p}^r = p^{r-1} + K\Delta\varepsilon_v \tag{3.58}$$

$$\tilde{s}_{ij}^r = s_{ij}^{r-1} + 2G\Delta e_{ij} \tag{3.59}$$

where K is the bulk modulus and G is the shear modulus given by

$$K = \frac{E}{3(1-2\nu)} \tag{3.60}$$

$$G = \frac{E}{2(1+\nu)} \tag{3.61}$$

In the above constitutive relations, it should be pointed out that $2\varepsilon_{ij} = \gamma_{ij}$.

Using these stresses, the following condition is evaluated

$$3\alpha p + \sqrt{J_2(s)} - \kappa \le 0 \tag{3.62}$$

where α and κ are the parameters of the Drucker-Prager model, and $J_2(s)$ is the second invariant of the deviatoric stress s.

If the above condition is satisfied, the trial stress state becomes the final stress state. Otherwise, the stresses are in the plastic range. The parameter λ is computed as follows:

$$\lambda = \frac{\left[G \frac{s_{ij} \Delta e_{ij}}{\sqrt{J_2(s_{ij})}} + 3\alpha K \Delta \varepsilon_v \right]}{G} \tag{3.63}$$

The plastic strains are then computed by:

$$\left(\varepsilon^p\right)^r = \left(\varepsilon^p\right)^{r-1} + \lambda \frac{s_{ij}}{\sqrt{J_2(s_{ij})}} \tag{3.64}$$

The final volumetric and deviatoric stresses are given by:

$$p^r = \tilde{p}^r \tag{3.65}$$

$$s_{ij}^r = \hat{s}_{ij}^r - G\lambda \frac{s_{ij}}{\sqrt{J_2(s_{ij})}} \tag{3.66}$$

while the final total stresses are given by

$$\sigma_{ij}^r = p^r + s_{ij}^r \tag{3.67}$$

Stress-Strain Matrix Computations

It has often been observed that when the implicit Euler algorithm is used in conjunction with the elastoplatic tangent stiffness matrix derived directly from the theory of plasticity (Owen and Hinton, 1980), a loss in the quadratic rate of convergence of the Newton-Raphson method results. Simo and Taylor (1986) pointed out that this is a result of the inconsistency between stress integration algorithm and the elastoplastic stress-strain matrix C^{ep}. To preserve the quadratic rate of convergence, an elastoplatic stress- strain matrix consistent with the stress integration algorithm must be used. For the case where

the implicit Euler algorithm is applied to the non-associative Drucker-Prager model described in the previous section, the consistent elasto-plastic stress-strain matrix given by Simo and Taylor are follows:

$$C^{ep} = C^{e} - C^{p} \tag{3.68}$$

where

$$C^{e} = \begin{bmatrix} K+\frac{4}{3}\tilde{G} & K-\frac{2}{3}\tilde{G} & 0 & K-\frac{2}{3}\tilde{G} \\ K-\frac{2}{3}\tilde{G} & K+\frac{4}{3}\tilde{G} & 0 & K-\frac{2}{3}\tilde{G} \\ 0 & 0 & 2\tilde{G} & 0 \\ K-\frac{2}{3}\tilde{G} & K-\frac{2}{3}\tilde{G} & 0 & K+\frac{4}{3}\tilde{G} \end{bmatrix} \tag{3.69}$$

$$C^{p} = 3\alpha K \begin{bmatrix} n_1 & n_2 & 0 & n_3 \\ n_1 & n_2 & 0 & n_3 \\ 0 & 0 & 0 & 0 \\ n_1 & n_2 & 0 & n_3 \end{bmatrix} + 2\tilde{G} \begin{bmatrix} n_1 n_1 & n_1 n_2 & n_1 n_3 & n_1 n_4 \\ n_2 n_1 & n_2 n_2 & n_2 n_3 & n_2 n_4 \\ n_3 n_1 & n_3 n_2 & n_3 n_3 & n_3 n_4 \\ n_4 n_1 & n_4 n_2 & n_4 n_3 & n_4 n_4 \end{bmatrix} \tag{3.70}$$

$$n = \frac{1}{\sqrt{J_2(s)}} \begin{bmatrix} s_{xx} & s_{yy} & s_{xy} & s_{zz} \end{bmatrix} \tag{3.71}$$

$$\tilde{G} = \frac{\kappa + 3\alpha p}{\sqrt{J_2(\hat{s})}} G \tag{3.72}$$

If the conventional elasto-plastic stress-strain matrix, G is used in place of $\tilde{G}$. For the elastic case, the stress-strain matrix is given by taking only C^{e} with G used in place of $\tilde{G}$. It should be pointed out that C^{ep} is unsymmetric from the case when $\alpha \neq 0$. This results in a stiffness matrix which is unsymmetric and thus the full system of equations must be used.

Boundary Element Computations

The stiffness matrix $\hat{K}$ for the boundary is compute in the subroutine BEMSTF. The flow chart of this subroutine is given in Figure (3.8). The influence coefficient for the individual elements h and g are evaluated using equations (2.10) and (2.11). In evaluating these equations, the influence coefficients for the Kelvin and the complementary part of the Melan solution are evaluated separately and added together. For cases where the integrand is non-singular, evaluation of equation (2.10) and (2.11) are performed numerically. The integration quadrature used varies depending on the perpendicular distance of the source point s to the element. For a given element of length l, if the distance between s and the element is less than or equal to $1.5l$, a six-point quadrature is used. A four-point quadrature is used if the distance is between $1.5l$ and $5.5l$. Otherwise, a two-point rule is used. For the case where one of the two nodal of the element is a source point, the integrals are evaluated using equation (2.22). As the influence coefficients h and g are computed for each element, they are assembled into the global matrix $\hat{H}$ and G. For the case where the geometry of the problem is symmetric, the method of images is used.

The transformation matrix M is then computed, after which the inversion of the matrix G is performed by means of LDU decomposition. The stiffness matrix for the boundary element system is then computed by performing the matrix operation prescribed in equation (3.6).

If only the symmetric part of $\hat{K}$ is used, the skew-symmetric part is discarded using equation (3.12). The resulting stiffness matrix is stored in an array **A** with dimensions NN2 × NN2 where NN2 is twice the number of nodes in the boundary element system. Because the tangent stiffness $\hat{K}$ does not change, as was shown in equation (3.22), the above computations need only to be performed once. During the solution

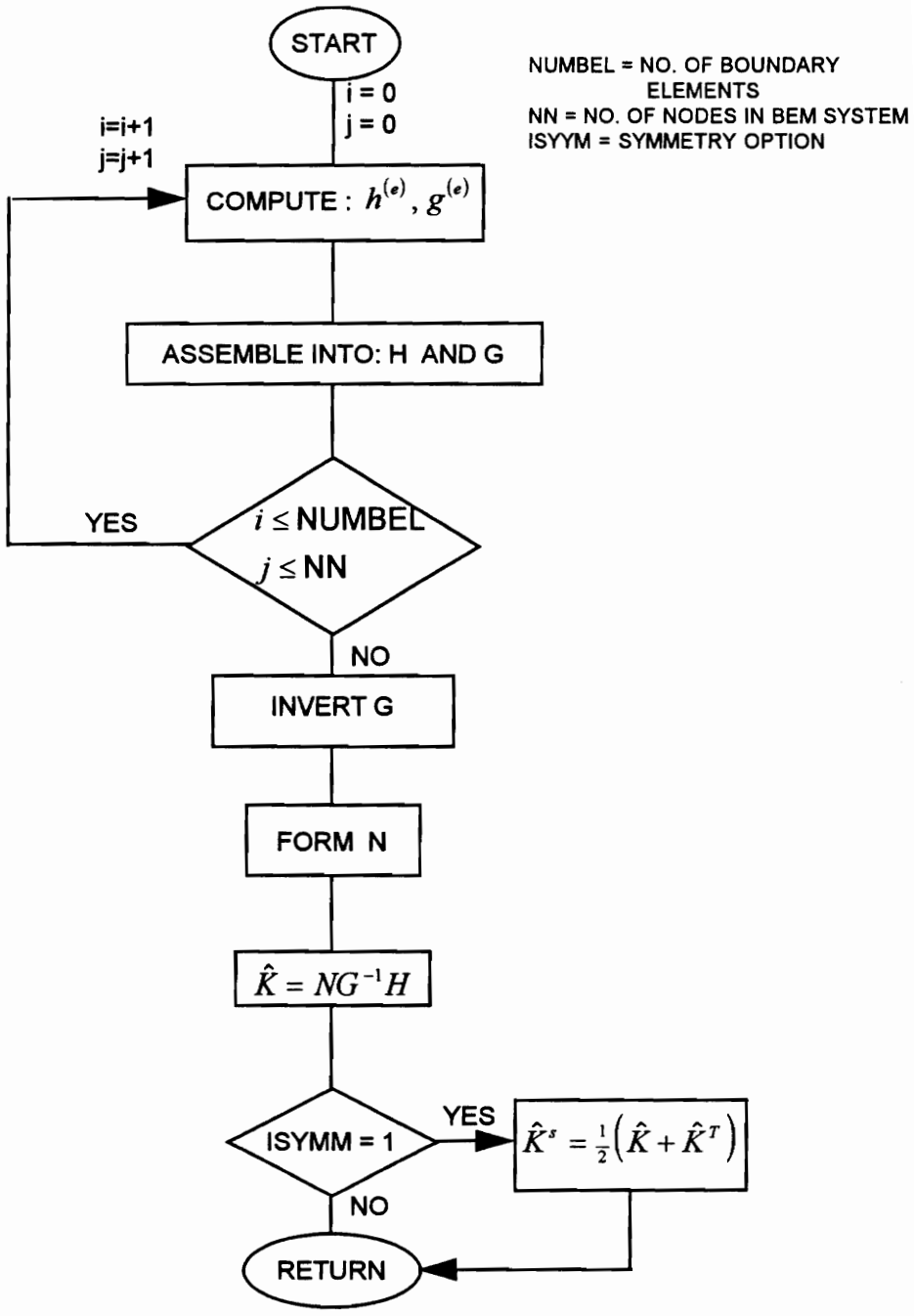

Figure 3.8. Flowchart for Subroutine BEMSTF

process, the stiffness matrix is used to compute the residual vector for the boundary element system using equation (3.20).

Element Assembly

As previously mention, minimizing the bandwidth of the coupled system requires that the degrees of freedom common to both the finite and boundary element system be located in the last equations. To accomplish this, a special assembly procedure is used. This assembly procedure makes use of a localization array LM to assign equation numbers to the degrees of freedom in the system. The LM array is formed using information from the element connectivity array IEN and the processed array ID using an algorithm proposed by Hughes (1987):

$$\mathrm{LM}(i,a,e) = \mathrm{ID}(i,\mathrm{IEN}(a,e))$$

where

i = Degree of freedom number, 1 in x-direction, 2 in y-direction

a = Local node number

e = Element number

Initially, the array ID stores the boundary condition codes which are inputted by the user. After processing, ID stores the equation numbers corresponding to the different nodes and degrees of freedom. The equation numbers are assigned in consecutive order, starting with the lowest node number, to degrees of freedom with unknown displacements. Degrees of freedom with known displacements are not assigned equations numbers and therefore are not assembled into the global stiffness matrix.

The stiffness matrix resulting from the boundary element system is assembled using a separate localization matrix LMBEM formed from the connectivity array IX and the array ID using the relation:

$$\mathrm{LMBEM}(i,a) = \mathrm{ID}(i,\mathrm{IX}(a))$$

where

i = Degree of freedom number

a = Local node number

In the original work by Hughes, the equations number are assigned to ID is one pass. In the assembly procedure proposed here, two passes are involved. In the first pass, the degrees of freedom exclusive to the finite element system are identified and assigned equation number is consecutive order. The second pass involves identifying the degrees of freedom common to both the finite element and boundary element systems and assigning the remaining equation numbers to them.

This process can be described better using the following example. Figure (3.9) shows a coupled finite element and boundary element system. The ID array initially and after each pass is given in Figure (3.10). The matrices IEN, IX, LM and LMBEM are given in Figure (3.11)

Equation Solving Routines

The global stiffness matrix is stored using a compact column storage scheme. For the symmetric case, the upper triangular portion of **K** is stored in a one-dimensional array, ALHS, column-wise beginning with the first non-zero element in each column and ending with the diagonal term. The locations of the diagonal terms are stored in an integer array IDIAG. The dimension of ALHS is NALHS, the sum of the *column heights.* The column height is the number of terms in a column beginning with the first non zero term and ending with the diagonal term. The heights of the columns are determined by subroutine COLHT from the element localization matrix LM. The column heights are initially stored in IDIAG. When the calculation of column heights is completed, subroutine DIAG determined the diagonal addresses and overwrites them into IDIAG. Figure (3.12) illustrates the matrix **K** matrix and the corresponding ALHS and IDIAG arrays.

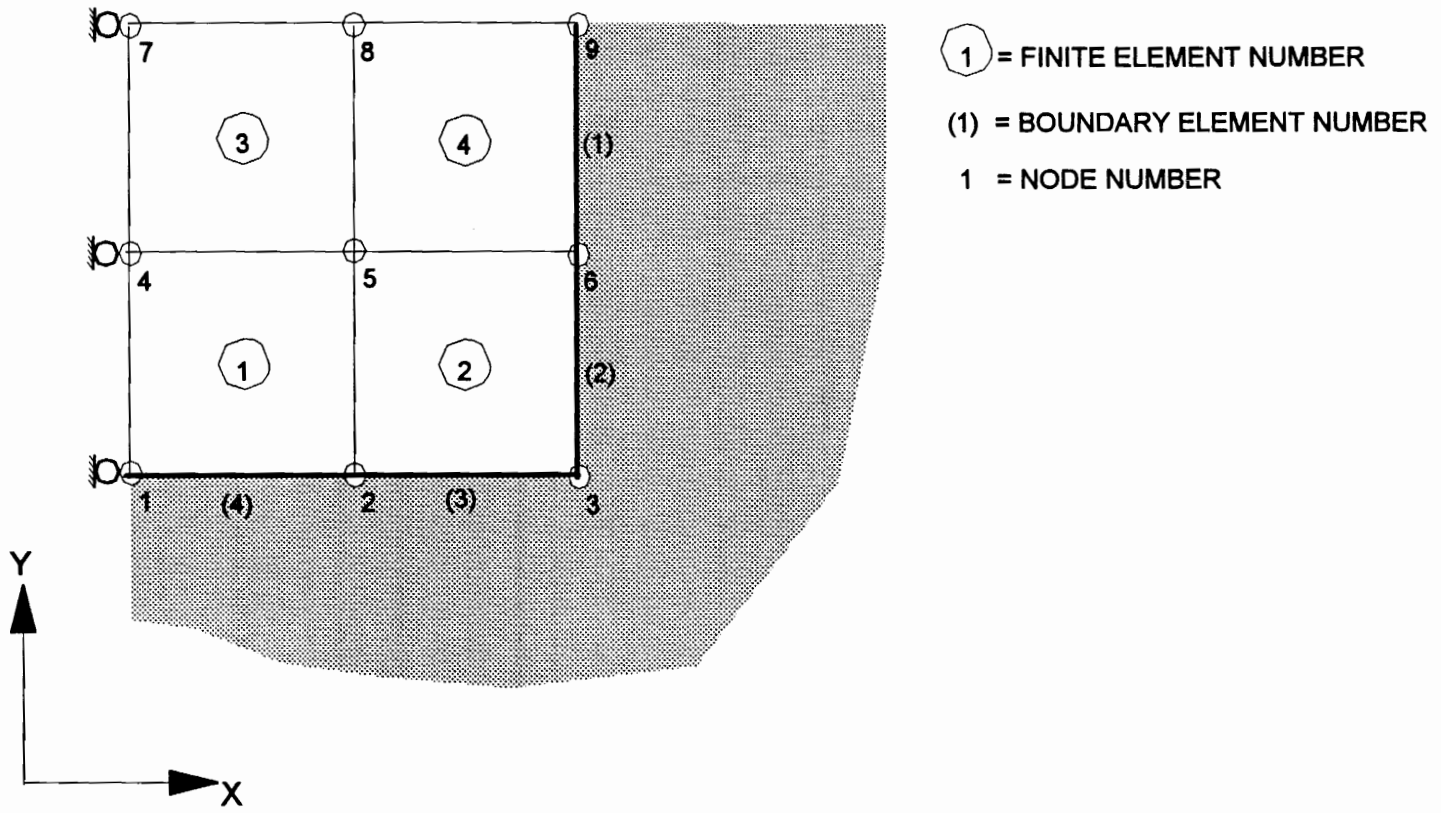

Figure 3.9. Illustrative Example

Initial ID array

Node Numbers (i)

DOF	1	2	3	4	5	6	7	8	9
1	1	2	2	1	0	2	1	0	2
2	2	2	2	0	0	2	0	0	2

0 = force known
1 = displacement known,
2 = force and displacement unknown

ID array after first pass

Node Numbers (i)

DOF	1	2	3	4	5	6	7	8	9
1	0	-1	-1	0	2	-1	0	5	-1
2	-1	-1	-1	1	3	-1	4	6	-1

< 0, temporary value
= 0, not assembled
> 0, assembled

ID array after second pass

Node Numbers (i)

DOF	1	2	3	4	5	6	7	8	9
1	0	8	10	0	2	12	0	5	14
2	7	9	11	1	3	13	4	6	15

= 0, not assembled
> 0, assembled

Figure 3.10. ID Array

IEN Array

Element	Local Node Number (a) 1	2	3	4
1	1	2	5	4
2	2	3	6	5
3	4	5	8	7
4	5	6	9	8

LM Array

Node No.	DOF	Local Node Number (a) 1	2	3	4
1	1	0	8	0	2
	2	7	9	1	3
2	1	8	10	2	12
	2	9	11	3	13
3	1	2	12	5	14
	2	3	13	6	15
4	1	0	2	0	5
	2	1	3	4	6

IX Array

Local NodeNumber 1	2	3	4	5
9	7	3	2	1

LMBEM Array

DOF	Local NodeNumber				
1	14	12	10	8	0
2	15	13	11	9	7

Figure 3.11. IEN, LM, IX and LMBEM Array for example mesh.

Stiffness Matrix **K**

K_{11}	K_{12}	K_{13}	0	K_{15}	0	0	0
	K_{22}	K_{23}	K_{24}	0	0	0	0
		K_{33}	0	K_{35}	0	K_{37}	0
			K_{44}	K_{45}	K_{46}	K_{47}	K_{48}
				K_{55}	K_{56}	K_{57}	K_{58}
SYMMETRIC					K66	K_{67}	K_{68}
						K_{77}	K_{78}
							K_{88}

ALHS Array

K_{11}	K_{12}	K_{22}	K_{13}	K_{23}	K_{33}	K_{24}	0	K_{44}	K_{15}	0	K_{35}	K_{45}	K_{55}

K_{46}	K_{56}	K_{66}	K_{37}	K_{47}	K_{57}	K_{67}	K_{77}	K_{48}	K_{58}	K_{68}	K_{78}	K_{88}

IDIAG Array

1	3	6	9	14	17	22	27

Figure 3.12. Storage of system of equations for fully symmetric case.

For the case when **K** is unsymmetric, an additional array ULHS is used to store the elements of **K** beneath the diagonal. Because of the manner in which the element arrays are assembled, the profile of ULHS is identical to ALHS. The diagonal addresses are obtained from the array IDIAG2. Because of the profile of ULHS and ALHS are identical, procedure for determining column heights is the same as the symmetric case. Figure (3.13) illustrates the matrix **K** matrix and the corresponding ALHS, ULHS and IDIAG arrays.

The solution of the equations involves factorization of the coefficient matrix using the Crout's elimination scheme as follows:

$$\mathbf{K} = \mathbf{LU} \tag{3.73}$$

where

L = lower triangular matrix

U = upper triangular matrix

In the case where **K** is symmetric, the Crout's elimination scheme reduces to:

$$\mathbf{K} = \mathbf{U}^T\mathbf{U} \tag{3.74}$$

Modified Method

In the coupling of the boundary element and finite element method, the resulting matrix equations are of the form:

$$\mathbf{K} = \left[\begin{array}{c|c} K_{AA} & K_{AB} \\ \hline K_{BA} & K_{BB} \end{array}\right] \tag{3.75}$$

such that

$$K_{AA} = K_{AA}^T \tag{3.76}$$

$$K_{BA} = K_{AB}^T \tag{3.77}$$

Stiffness Matrix **K** (NEQ = 8)

K_{11}	K_{12}	K_{13}	0	K_{15}	0	0	0
K_{21}	K_{22}	K_{23}	K_{24}	0	0	0	0
K_{31}	K_{32}	K_{33}	0	K_{35}	0	K_{37}	0
0	K_{42}	0	K_{44}	K_{45}	K_{46}	K_{47}	K_{48}
K_{51}	0	K_{53}	K_{54}	K_{55}	K_{56}	K_{57}	K_{58}
0	0	0	K_{64}	K_{65}	K_{66}	K_{67}	K_{68}
0	0	K_{73}	K_{74}	K_{75}	K_{76}	K_{77}	K_{78}
0	0	0	K_{84}	K_{85}	K_{86}	K_{87}	K_{88}

ALHS Array (NALHS=27)

K_{11}	K_{12}	K_{22}	K_{13}	K_{23}	K_{33}	K_{24}	0	K_{44}	K_{15}	0	K_{35}	K_{45}	K_{55}

K_{46}	K_{56}	K_{66}	K_{37}	K_{47}	K_{57}	K_{67}	K_{77}	K_{48}	K_{58}	K_{68}	K_{78}	K_{88}

IDIAG Array

1	3	6	9	14	17	22	27

ULHS Array (NULHS=19)

K_{21}	K_{31}	K_{32}	K_{42}	0	K_{51}	0	K_{53}	K_{54}	K_{64}	K_{65}	K_{73}	K_{74}	K_{75}

K_{76}	K_{84}	K_{85}	K_{86}	K_{87}

IDIAG2 Array

1	3	5	9	11	15	19

Figure 3.13. Storage of system of equations for fully unsymmetric case.

results because of the symmetry of the finite element method. K_{BB}, which is unsymmetric, is significantly smaller than the symmetric matrix K_{AA}. It can be shown by the principles of matrix algebra that Crout's elimination results in:

$$\left[\begin{array}{c|c} K_{AA} & K_{AB} \\ \hline K_{AB}^T & K_{BB} \end{array}\right] = \left[\begin{array}{c|c} U_{AA}^T & 0 \\ \hline U_{AB}^T & L_{BB} \end{array}\right] \left[\begin{array}{c|c} U_{AA} & U_{AB} \\ \hline 0 & U_{BB} \end{array}\right] \tag{3.78}$$

where

U_{AA}, U_{AB}, U_{BB} = upper triangular matrices

L_{BB} = lower triangular matrices

It should be pointed out that compared to the other matrices, L_{BB} is small. Thus, rearranging the equation in the manner suggested allows the coupled system to be treated as an unsymmetric system with minimal additional cost.

In the modified method, the upper triangular portion of the stiffness matrix is stored in the array ALHS while the lower unsymmetric portion is stored in the ULHS array. The diagonal addresses for ULHS are stored in the array IDIAG2. Again, the procedure for determining column heights is the same as the symmetric case. Figure (3.14) illustrates the matrix **K** matrix and the corresponding ALHS, ULHS, IDIAG and IDIAG2 arrays.

A option ISYMM is used to specify the type of system. ISYMM is equal to 0 for the symmetric case. The fully unsymmetric case is indicated by ISYMM equal to 1 while the partially unsymmetric case is indicated by ISYMM equal to 2.

3.6 Summary

In part A of this chapter, a summary of the work previously done with respect to the application of the coupled boundary element-finite element method to the solution of soil-structure interaction problems was presented. A new method for coupling the

Stiffness Matrix **K** (NEQ = 8)

K_{11}	K_{12}	K_{13}	0	K_{15}	0	0	0
	K_{22}	K_{23}	K_{24}	0	0	0	0
		K_{33}	0	K_{35}	0	K_{37}	0
			K_{44}	K_{45}	K_{46}	K_{47}	K_{48}
				K_{55}	K_{56}	K_{57}	K_{58}
SYMMETRIC				K_{65}	K_{66}	K_{67}	K_{68}
				K_{75}	K_{76}	K_{77}	K_{78}
				K_{85}	K_{86}	K_{87}	K_{88}

ALHS Array (NALHS=27)

K_{11}	K_{12}	K_{22}	K_{13}	K_{23}	K_{33}	K_{24}	0	K_{44}	K_{15}	0	K_{35}	K_{45}	K_{55}

K_{46}	K_{56}	K_{66}	K_{37}	K_{47}	K_{57}	K_{67}	K_{77}	K_{48}	K_{58}	K_{68}	K_{78}	K_{88}

IDIAG Array

1	3	6	9	14	17	22	27

ULHS Array (NULHS=6)

K_{65}	K_{75}	K_{76}	K_{85}	K_{86}	K_{87}

IDIAG2 Array

1	3	6

Figure 3.14. Storage of system of equations for partially unsymmetric case.

boundary element-finite element method specifically suited for solving soil structure interaction problems was presented in Part B. This method, called the *substructure method*, involves coupling linear finite element with linear boundary elements based on the Melan fundamental solution. In this procedure, the structure and near field soil domain are model using finite elements, while the infinite far field soil domain is modeled using boundary elements. This method is capable of solving nonlinear soil-structure interaction problem using a relatively few number of boundary and finite elements as compared to currently used methods. The *substructure method* is implemented into a computer program BEFEC. This computer program has the capacity to solve elastoplastic problems using the *substructure technique.*

Chapter 4

SOLUTION OF STRIP FOOTING PROBLEMS

4.1 Introduction

This chapter investigates the proposed substructure method as applied to the solution of problems involving infinite boundaries. This is done by solving various strip footing problems using the substructure method together with other techniques and comparing the solution obtained to analytical solutions.

Part A of this chapter investigates the solution of strip footing problems using only the finite element method. The objective is to evaluate the accuracy of finite element solutions with respect to closed form solutions. The effects of domain size, support conditions, and element type are studied. Element types used for this study include the 4-node isoparametric element (Taig, 1961), QM5 element (Doherty, Wilson and Taylor, 1969), 9-node isoparametric element (Irons, 1966), and the 8-node stress hybrid element (Pian and Tong, 1969).

In *Part B*, methods for incorporating the effects of the infinite boundary into the finite element method are studied. These include the use of infinite elements (Beer and Meek, 1977), analog spring elements, and the proposed use of boundary elements. The accuracy of these techniques is assessed by comparing the solutions obtained from them to the closed form solution. Also, the accuracy of the substructure method is assessed when a symmetric stiffness matrix for the boundary element system is used.

In *Part C*, the proposed substructure method is applied to the solution of non-homogenous linear elastic problems. The accuracy of the finite element method and the coupled boundary element - finite element method are compared with respect to the closed form solution. In particular, the accuracy of the solution obtained using the coupled

boundary element -finite element method when the non-homogenous far field domain is approximated by a homogenous domain is assessed.

Part D, the application of the proposed substructure method to of non-homogenous nonlinear problems is presented. The effects of the infinite boundary on the solution of nonlinear problems studied by comparing solution resulting from using only the finite element method and the solution obtained using the proposed substructure technique where the infinite boundary is accounted for.

PART A.

4.2 Strip Footing Problem

This problem consists of a uniformly distributed load w applied to a half-plane over a half-width of a as illustrated in Figure (4.1). The material in the half-plane is linearly elastic, homogenous and isotropic. The complete analytical solution to this problem is given in Appendix C. Table 4.1 gives the parameters assumed for the purpose of this study.

Table 4.1
Parameters for Linear Elastic Strip Footing Problem

Parameter	Name	Value
E	Young's Modulus	30.0 MPa
ν	Poison's Ratio	0.25
w	Distributed Load	1.0 KN/m
a	Load Half-width	1.0 m

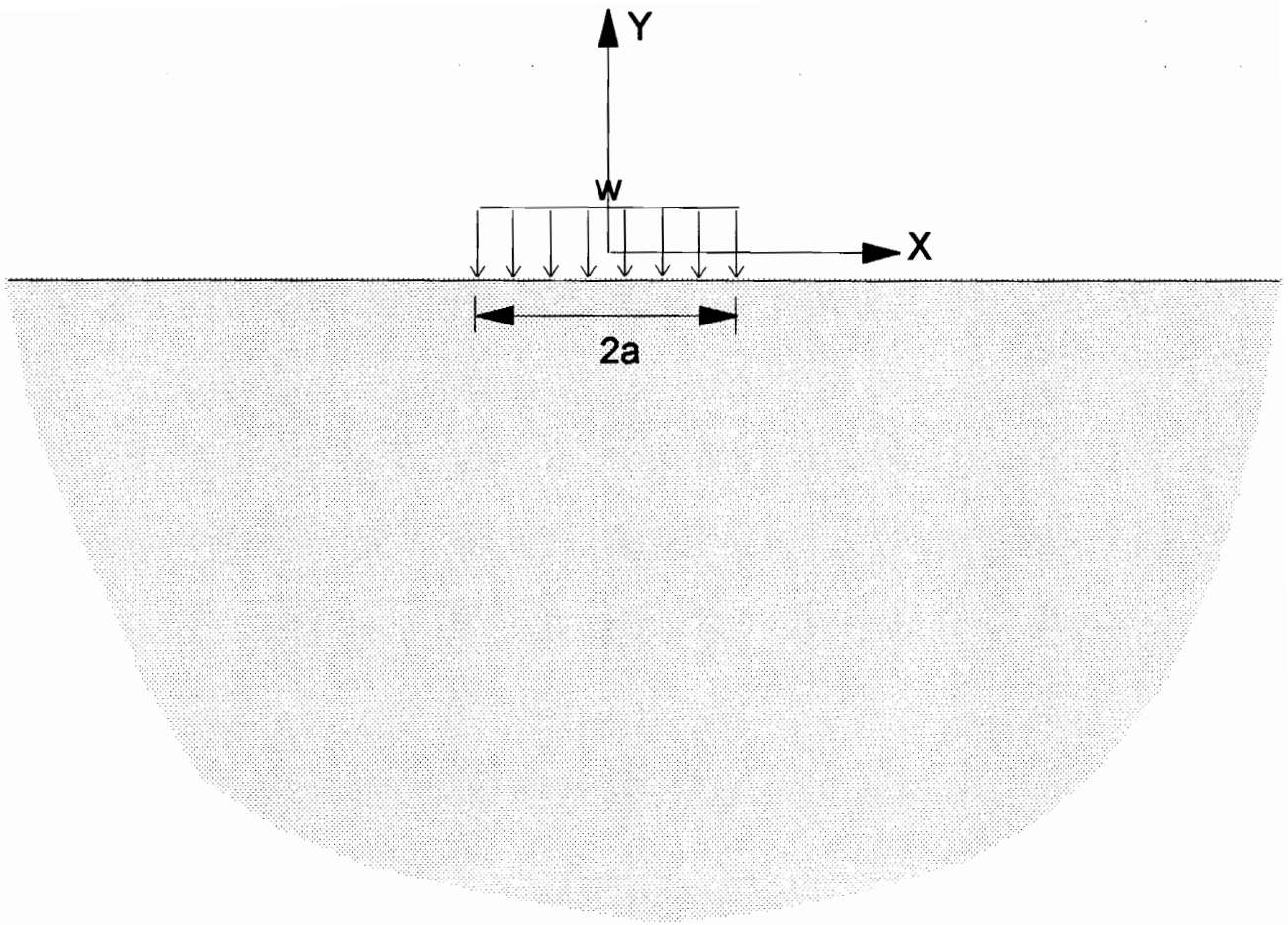

Figure 4.1. Geomtery of the Stip Footing Problem

4.3 Effects of Domain Size

In this section, the effects of the size of the domain used to model the half-plane in the strip footing problem are studied. The of objective of this study is to determine how much of the half-plane must be considered to be able to obtain reasonable results with respect to the closed form solution. Also studied in this section is the effects of the support conditions assumed on the solution.

To study the effects of domain size, the infinite half-plane was approximated using 4 different domain sizes namely: (1) a 10 m. × 10 m. mesh with 100 elements, (2) a 20 m. × 20 m. mesh with 144 elements, (3) a 50 m. × 50 m. mesh with 225 elements, and (4) a 100 m. × 100 m. mesh with 289 elements was used. Because of the symmetry of the problem, only half the actual domain was modeled. In all four cases, 4-node quadrilaterals elements were used. To study the effects of the assumed support conditions, two types of support conditions were assumed on the right-hand side boundary for each domain size. These included (1) roller support, and (2) fixed support conditions. Figures (4.2) and (4.3) illustrate the finite element mesh used assuming roller and support conditions respectively and a domain size of 10 m. × 10 m. The finite element mesh for the other analyses were obtained by adding more elements to the bottom and right-hand side boundary without changing the mesh in the original 10 m. × 10m. region.

Vertical Displacements: It should be pointed out that in the closed form solution of the strip footing problem given in Appendix C, the vertical displacement u_y is measured relative to an arbitrarily chosen reference point on the surface a distance L from the origin. In all analyses perform on the four different mesh sizes, all vertical displacement were measure relative to the point $L = 10.0$ on the surface of the half-plane.

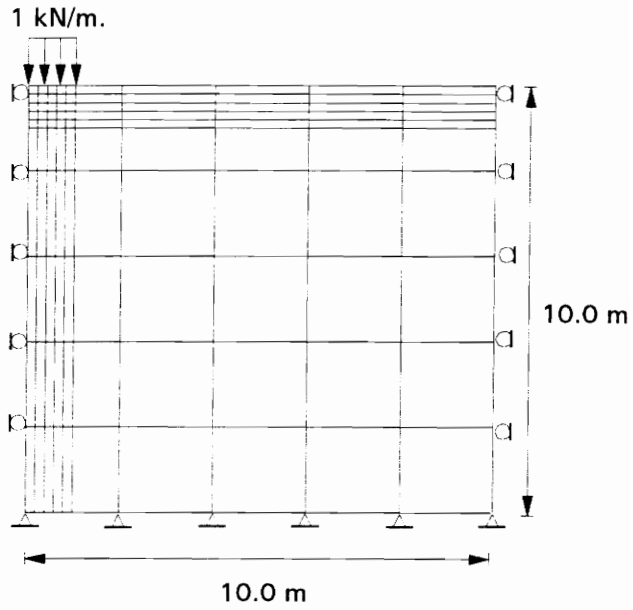

Figure 4.2. Finite element mesh assuming roller boundary conditions.

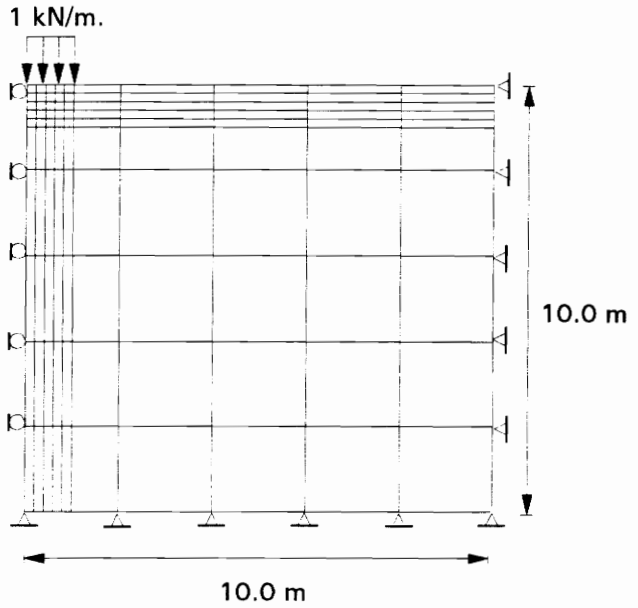

Figure 4.3. Finite element mesh assuming fixed boundary conditions.

The vertical displacements along the centerline relative to the point with coordinates (10.0,0) are normalized with respect to the loadings half-width a and plotted in Figure (4.4) with respect to the normalized coordinates $-y/L$. From Figure (4.4), it can be seen the vertical displacements obtained using the finite element method are always below the analytical solution by a constant amount. Increasing the domain reduces this underprediction. In the case of the 10 m. × 10 m. mesh., the underprediction in displacements with respect to the analytical solution ranges from 20% at the origin to 100% at $-y/L=1.0$. When the domain was increased to 20 m. × 20 m., the displacements were between 10%w at the origin to 50% at $-y/L=1.0$ below the analytical solution. Increasing the domain size to 50 m. × 50 m. resulted in the displacements within 10% of the analytical solution. Increasing the domain after this point did not result in any additional improvement in the solution.

In Figure (4.5), the normalized relative displacements along the surface of the half-plane are plotted with respect to the normalized coordinates x/L. This figure shows that displacements along the surface are always underpredicted as compared to analytical solution when using the finite element method. For the case of the 10 m. × 10 m., the underprediction ranges from 20% at the origin to 60% at $x/L = 0.6$. When a 20 m. × 20 m. mesh is used, the displacements range between 10% at the origin to 15% at $x/L = 0.4$ below the analytical solution. For the 50 m. × 50 m. mesh, the displacements were all within 10% of the analytical solution. Increasing the mesh size to 100 m. × 100 m. did not result in any observable reduction in the underprediction of the displacements as compared with the analytical solution. It was observed that underpredictions in the displacements along the surface were smaller in magnitude than those along the centerline.

Also, it was observed that the type of support conditions assumed on right-hand side boundary has no significant effect on the displacements computed along both the

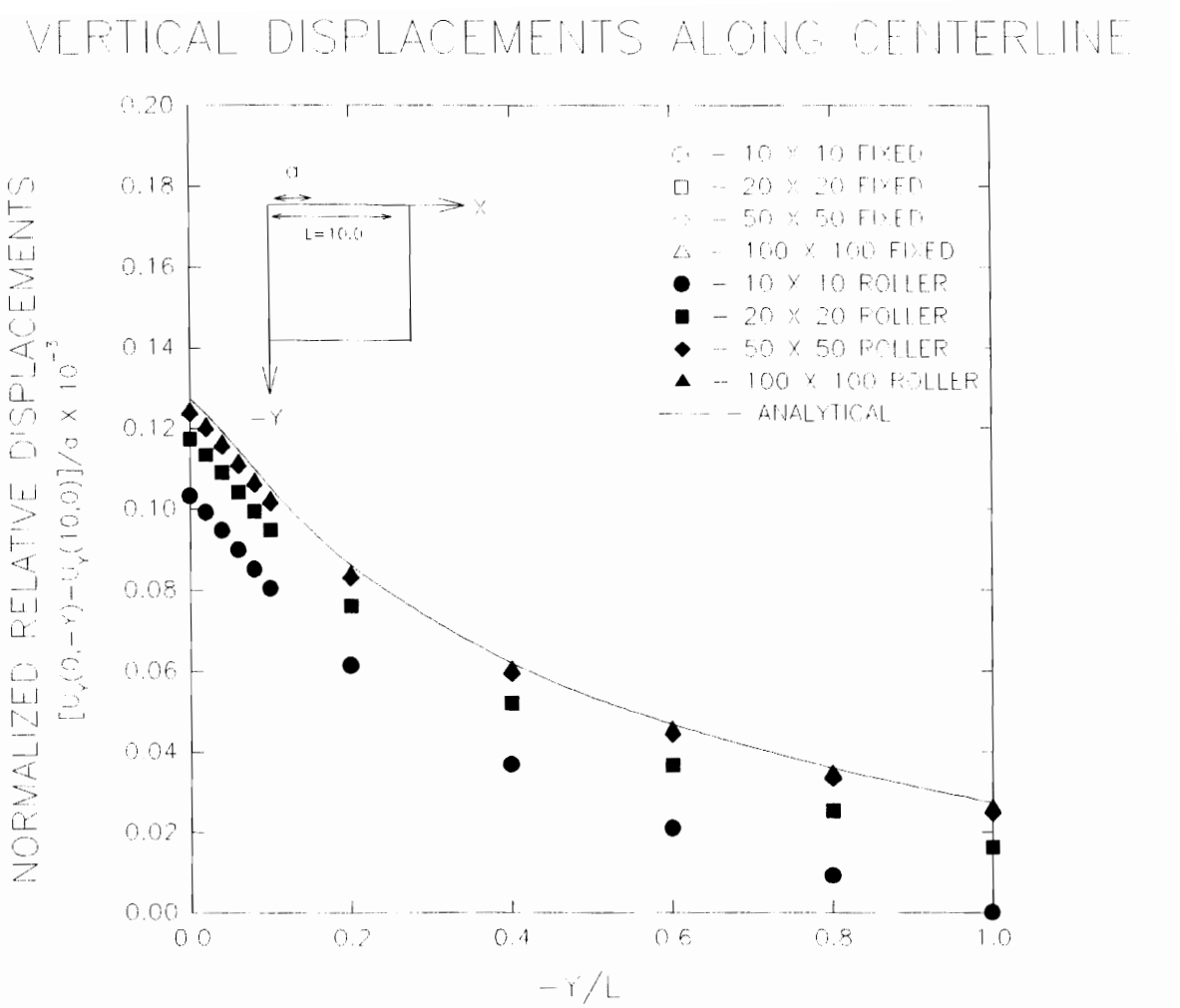

Figure 4.4 Effect of domain size and boundary conditions on vertical displacements along centerline.

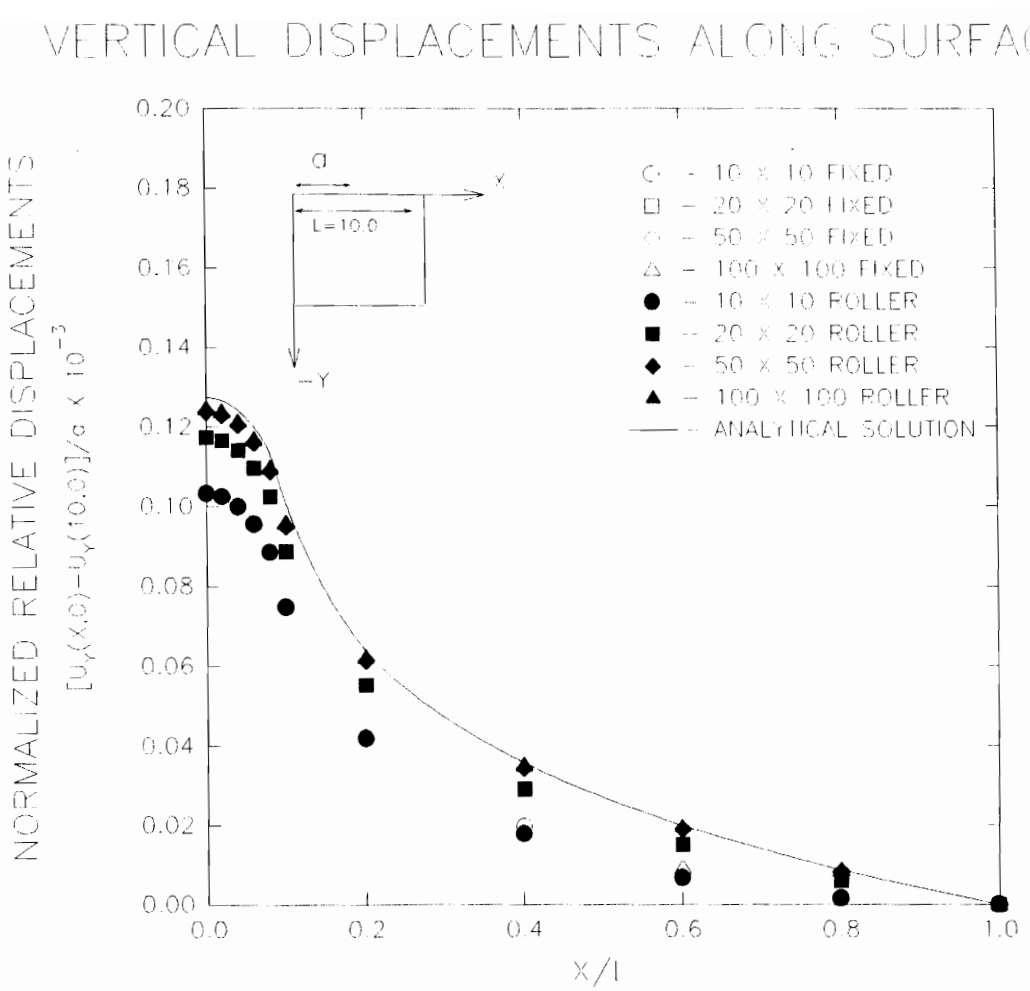

Figure 4.5 Effect of domain size and boundary conditions on vertical displacements along surface.

centerline and surface of the half-plane regardless of mesh size used. For all mesh sizes analyzed, the differences in the obtained vertical displacements between the two support conditions assumed were within 1%.

From the above observations, it can be concluded that the underprediction in the vertical displacements occurs mainly as a result of setting the vertical displacements u_y along the entire boundary to zero. As the domain size is increased and approaches the condition where the boundary is infinite, the boundary along which u_y becomes more distant from the region of interest and the effect of the assumed boundary conditions becomes less pronounced by virtue of Saint Venants principle (Timoshenko and Goodier, 1970).

Stress Along Diagonal Elements: In Figure (4.6), the normal stress in the *x*-direction σ_{xx} is plotted with respect to the normalized coordinates *x/R* in terms of the percentage error with the analytical solution. From this figure, it is observed that significant errors occur in the value of σ_{xx} computed. In addition, these errors tend to oscillate. These errors and the accompanying oscillation are most pronounced in the 10 m. × 10 m. mesh. In this mesh, errors of as large as 32% occur at the point (1.5,1.5). Increasing the domain reduces these error and the oscillation in the error. Nevertheless, these errors still remain significant. For example, after the domain was doubled in size to 20 m. × 20 m., the error was as large as 30% occurring at the point (3.0,3.0). For the 50 m. × 50 m. mesh, the error in σ_{xx} was as large as 25% occurring at the point (9.0,9.0). For the 100 m. × 100 m., the all values of σ_{xx} were within 10% of the analytical solution.

Figure (4.7) plots, with respect to the normalized coordinates *x/R*, the percentage error in the shear stress σ_{xy} with the analytical solution. From the analyses involving the 10 m. × 10 m. domain, errors of as large as 70% occur at the point (9.0,9.0). However, unlike σ_{xx}, these errors do not oscillate but steadily increase as points further away from

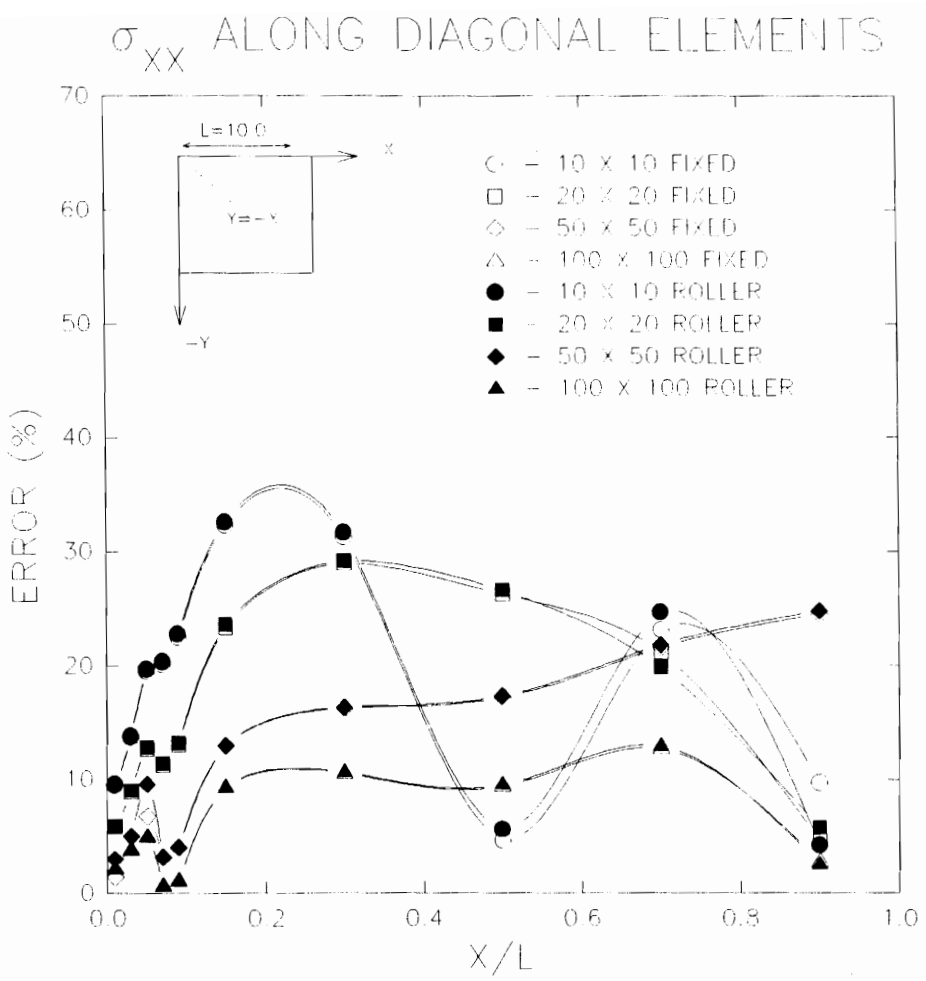

Figure 4.6 Effect of domain size and boundary conditions on σ_{xx} along diagonal elements.

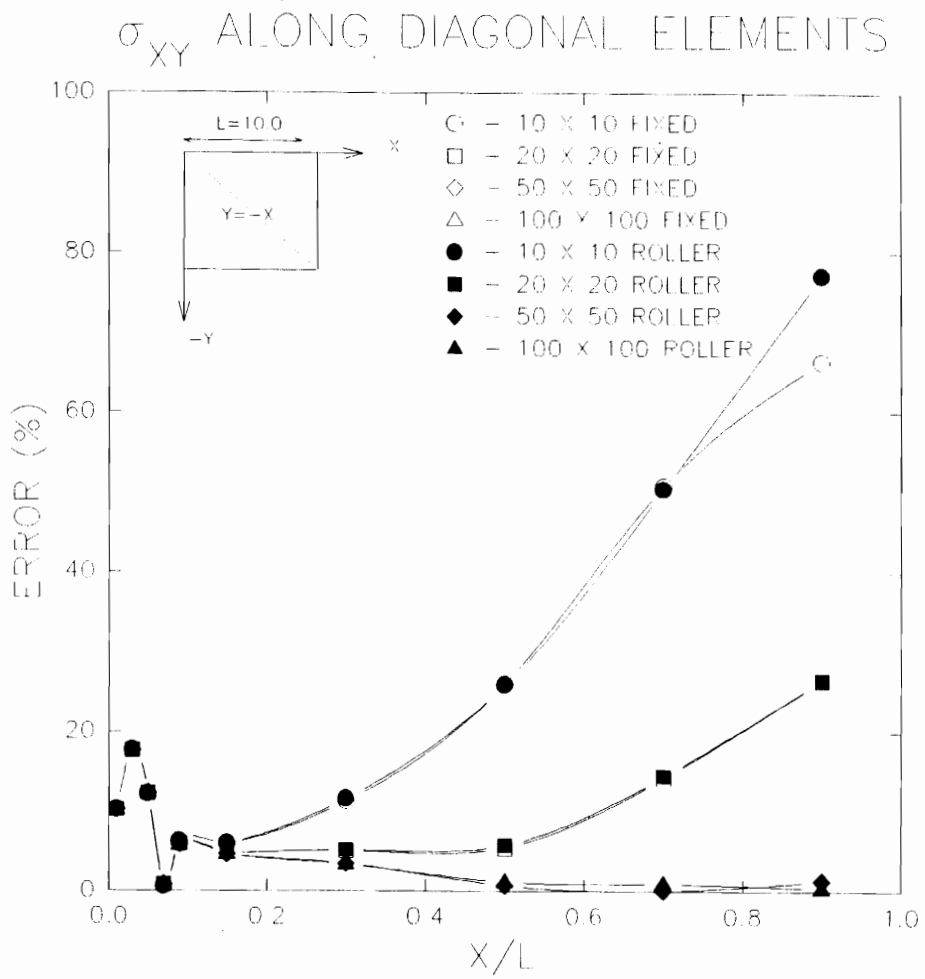

Figure 4.7 Effect of domain size and boundary conditions on σ_{xy} along diagonal elements.

the load are considered. As the domain size is increased, the error in the shear stresses decreases. For a 20 m. × 20 m. domain, the error in σ_{xy} was within 25% while for the 50 m. × 50 m. and 100 m. × 100 m. domain was within 5%.

Smaller errors, with respect to the analytical solution, were observed in normal stress in the y-direction σ_{yy} as shown by Figure (4.8). In the 10 m. × 10 m. domain, these errors were within 25% of the analytical solution. However like σ_{xx}, the errors oscillate. Increasing the domain size reduced both the magnitude and oscillation in the errors The 20 m. × 20 m., 50 m. × 50 m. and 100 m. × 100 m. mesh all yielded values of stress which were within 15% of the analytical solution.

In general, the assumed support conditions on the right-handside boundary have no significant effect on the calculated values of σ_{xx} and σ_{xy}. For the case of σ_{yy}, slightly smaller error result when the fixed support condition is assumed instead of the roller support conditions. However, this disparity is only observed in the 10 m. × 10 m. and 20 m. × 20 m. mesh. In the case of the 50 m. × 50 m. and 100 m. × 100m. mesh, the two support conditions give identical results.

From the above observation, it can be concluded that for the footing problem solved, a domain with a width and depth 50 times that of the half-width of the footing must be used to obtain vertical displacements within 10% of the analytical solution. To be able to obtain stresses within 10% of the analytical solution, a domain with a width and depth 100 times that of the half-width of the footing must be used.

4.4 Effects of Element Type

In this section, the effects of the type of element used to model the half-plane in the strip footing problem are studied. The objective of this study is determine if errors in the displacement and stresses with respect to the analytical solution observed in the previous section can be reduced using more sophisticated finite elements. In this section,

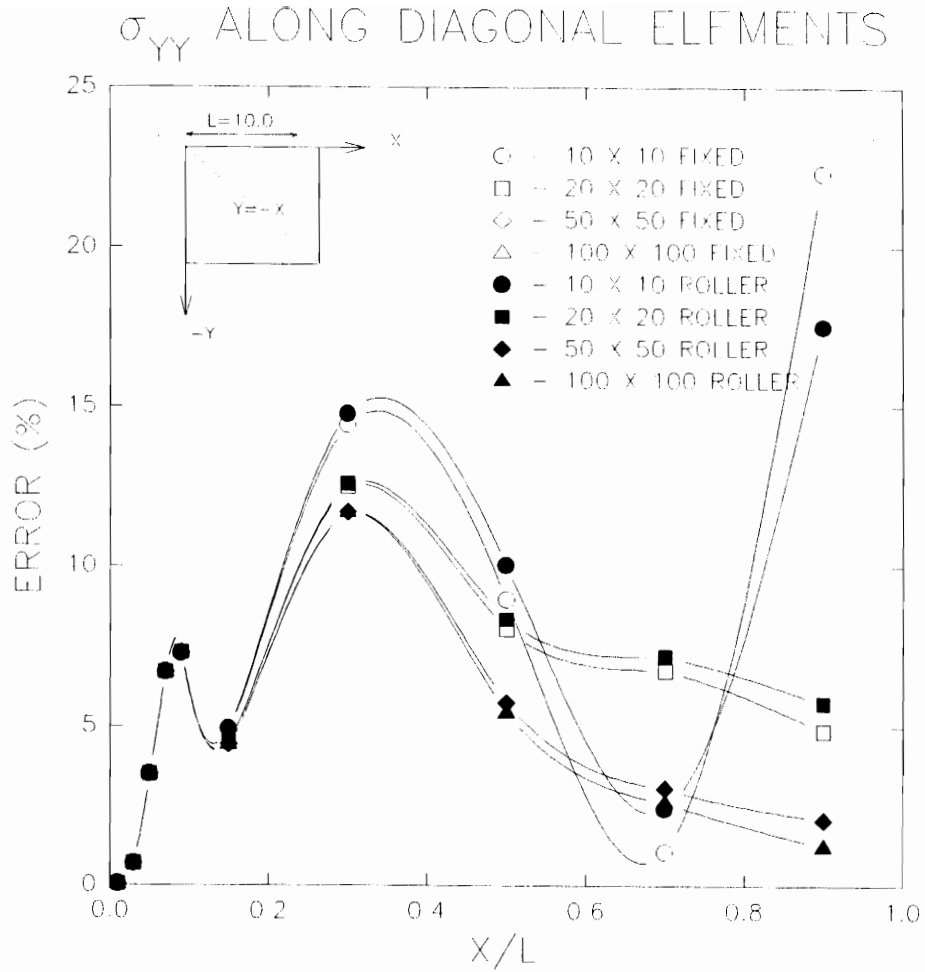

Figure 4.8 Effect of domain size and boundary conditions on σ_{yy} along diagonal elements.

four element types were considered namely: (1) 4-node quadrilateral element , (2) QM5 quadrilateral , (3) 8-node assumed stress hybrid , and (4) 9-node lagrangian element. For each element type, two support conditions were assumed on the right-hand boundary. Theses included (1) roller support, and (2) fixed support conditions. For all analysis, a 10 m. × 10 m. domain with 100 elements similar to that described in Figures (4.2) and (4.3) was used.

From the results of the above analyses, the following observations were made:

Vertical Displacement: Figure (4.9) shows the normalized relatives displacements along the centerline plotted with respect to the normalized coordinate $-y/R$ where R is the mesh size. It all analyses performed, the vertical displacements were measured relative to the point $L = 10.0$ on the surface of the half-plane. From Figure (4.9), the results obtained using the different element types are almost identical. For all element types used, the displacements were underpredicted with respect to the analytical solution. The underprediction ranged from 20% at the origin to 100% at the bottom of the mesh. On the average, the amount by which the vertical displacements were underpredicted was constant with depth along the centerline.

For both the displacements along the surface and centerline of the mesh, do difference was observed between the two support conditions assumed. This support the conclusion previously made that the underprediction in the vertical displacements is a results of the assumption that $u_y(x,-10.0) = 0$.

The similar observations with respect to the vertical displacement along the surface of the half-plane as shown in Figure (4.10). The displacements along the surface obtained using different type of finite elements were nearly identical. For element types, the vertical displacements along the surface were all underpredicted except at the point (10.0,0) since all displacements were taken relative to this point.

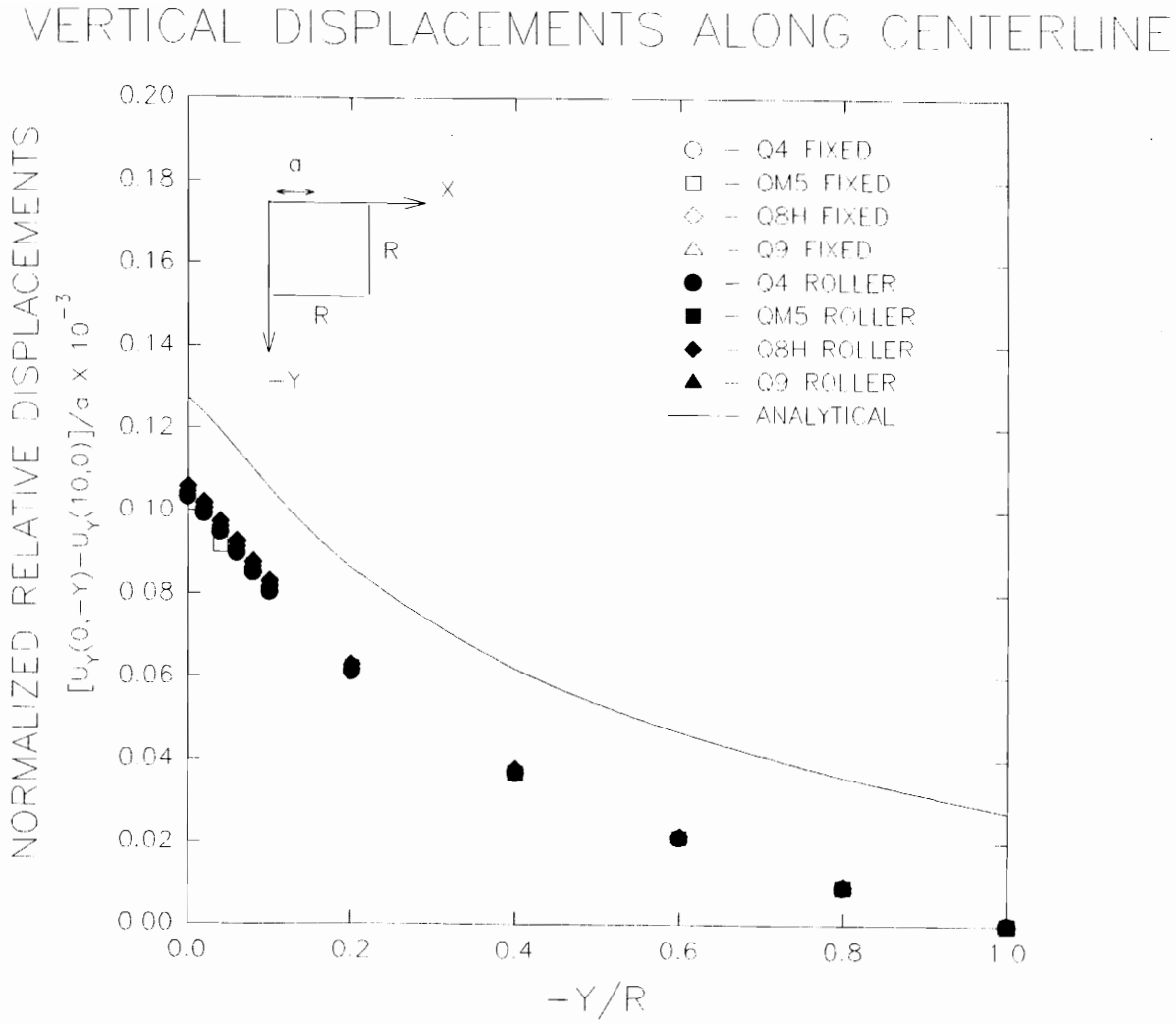

Figure 4.9 Effect of element type and boundary conditions on vertical displacements along centerline.

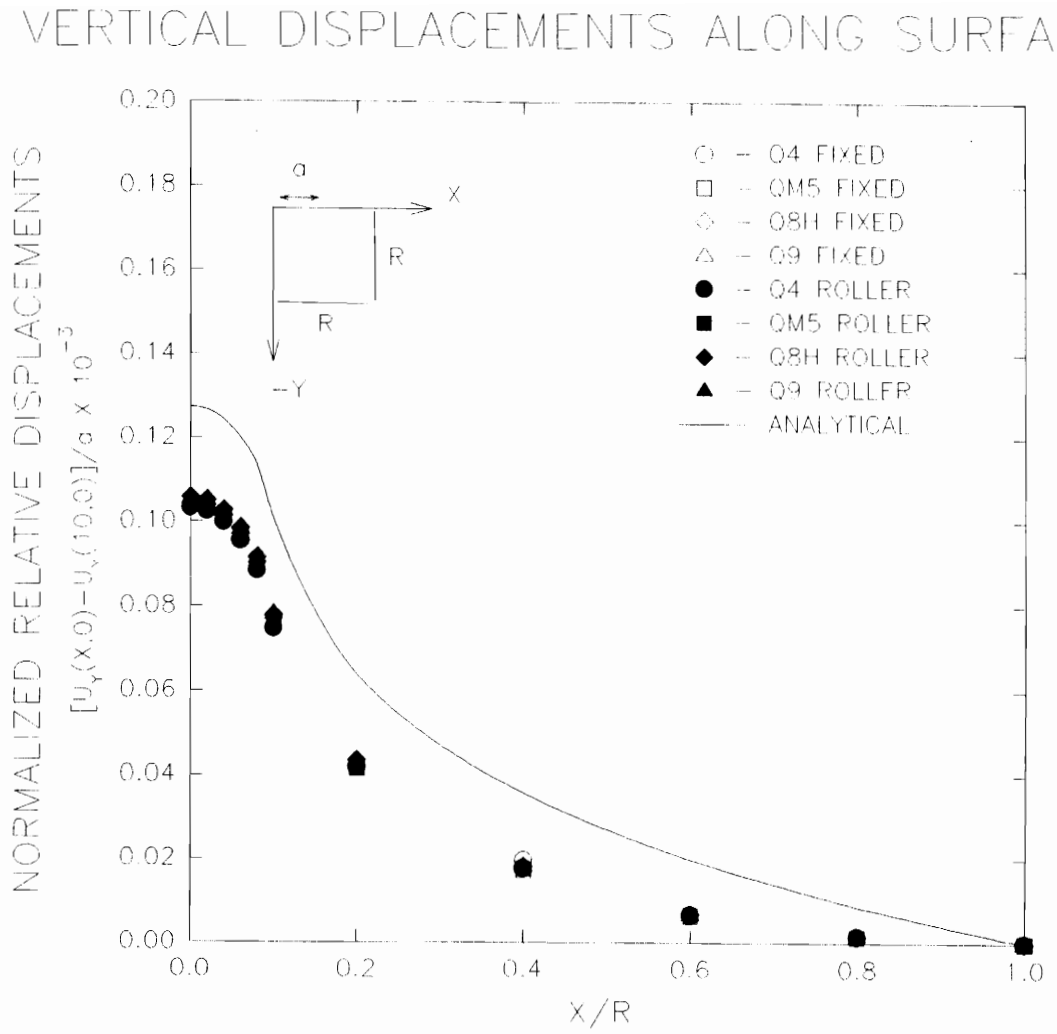

Figure 4.10 Effect of element type and boundary condtions on vertical displacements along surface.

It is apparent that the element type used in the analysis does not have any significant effect on the computed vertical displacements. Because elements of varying flexibility were used, this observation implies that the underprediction in the displacements is not caused by the lack of flexibility in the elements. Also, the type of support conditions assumed along the right-hand boundary does not have any significant effect on the displacements along right-hand side boundary regardless of the type of element used. These observations support the explanation previously given that the underprediction is mainly a result of fixing the displacement along the bottom boundary.

Stress Along Diagonal Elements: the percentage error in σ_{xx} along diagonal elements with respect to the analytical solution is plotted in Figure (4.11) It can be seen for either the 4-node lagrangian or the QM5 element, a error of as large as 35% at the point (5.0,-5.0) occurs in σ_{xx} Using the 9-node lagrangian element, the error in σ_{xx} for the same point increases to 37%. For the hybrid element, the error in σ_{xx} for the same point is reduced to 30%. It was also observed that, for all element types, the error in σ_{xx} tended to oscillate. Also, the type of support conditions assumed on the right-handside boundary did not have any significant effect on σ_{xx}.

The percentage error in the shear stress σ_{xy} along the diagonal elements is plotted in Figure (4.12). Between the different element types, similar errors occur in σ_{xz}. These errors were as large as 80% which occurred at the point (9.0,-9.0). As was previously observed, the error increased with increasing distance from the loaded area and did not oscillate as was the case in σ_{xx}. Except , the type of support conditions assumed on the right-hand side boundary did not have any significant effect on σ_{xy}. At the point (9.0,-9.0), the fixed support condition gave slightly better values of σ_{xy} over the roller support.

The percentage error with respect to the analytical solution in vertical normal stress σ_{yy} along diagonal elements is plotted in Figure (4.13). It can be seen that errors of

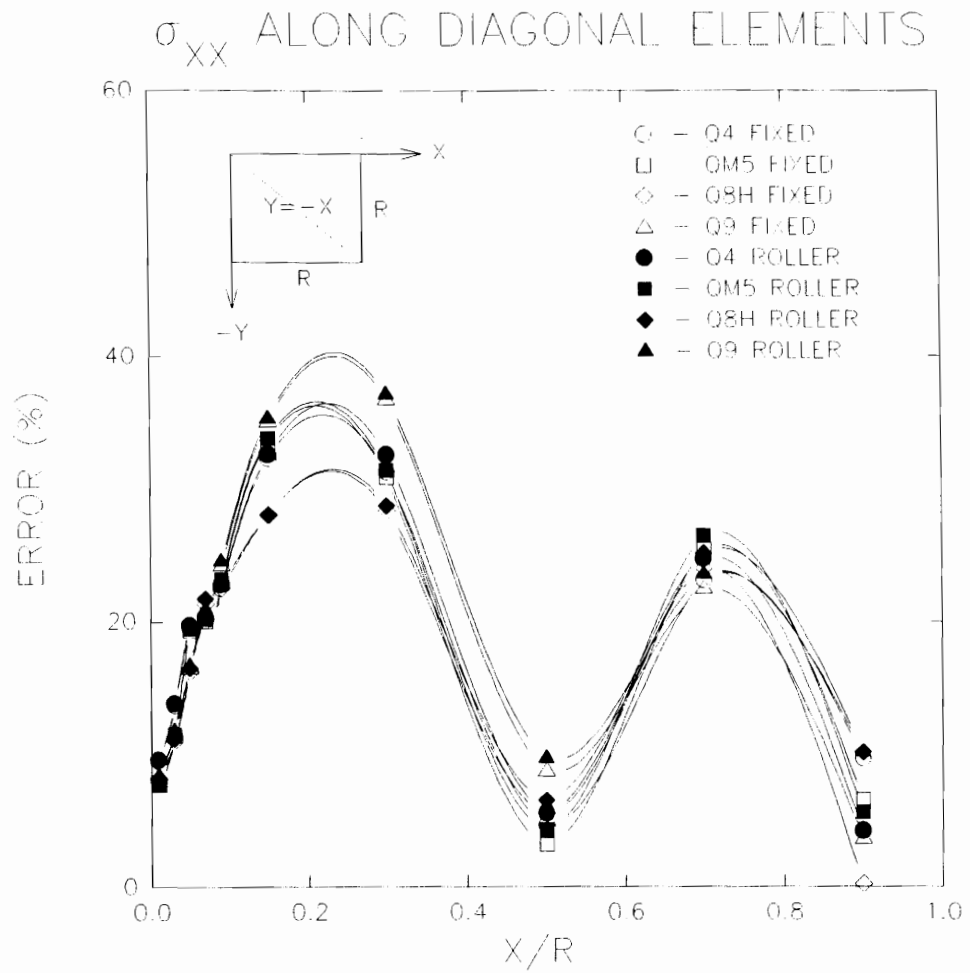

Figure 4.11 Effect of element type and boundary conditions on σ_{xx} along diagonal elements.

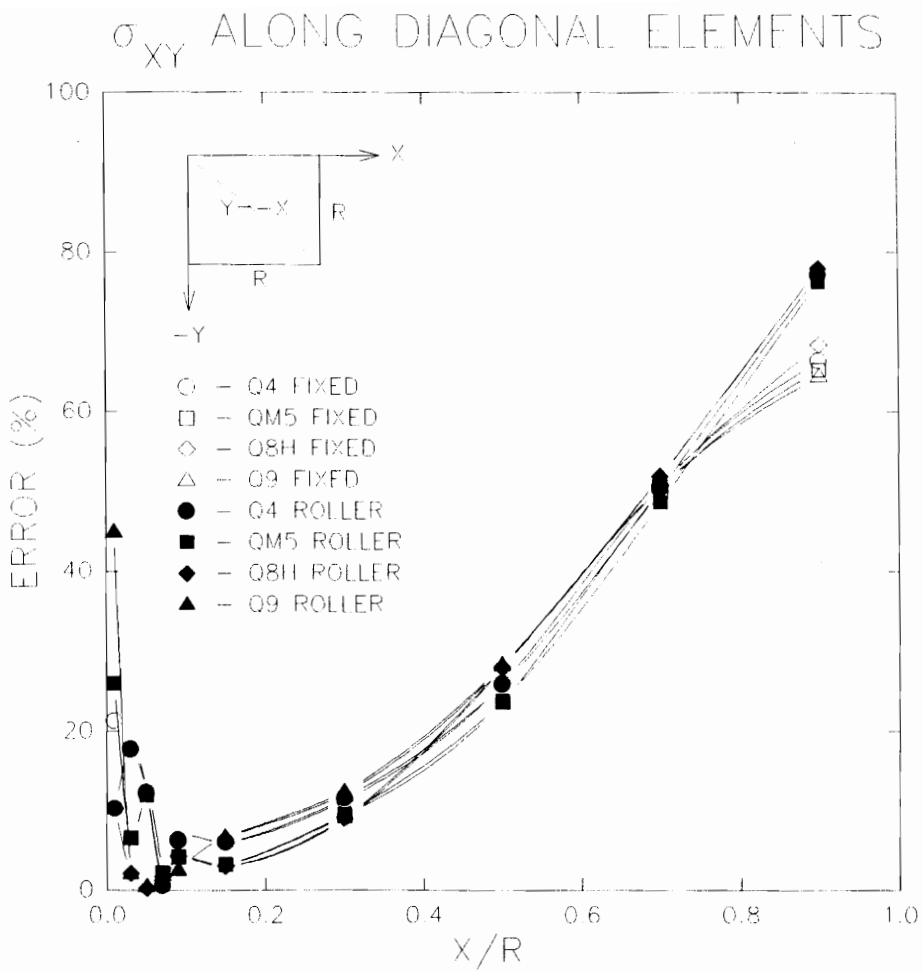

Figure 4.12 Effect of element type and boundary conditions on σ_{xy} along diagonal elements.

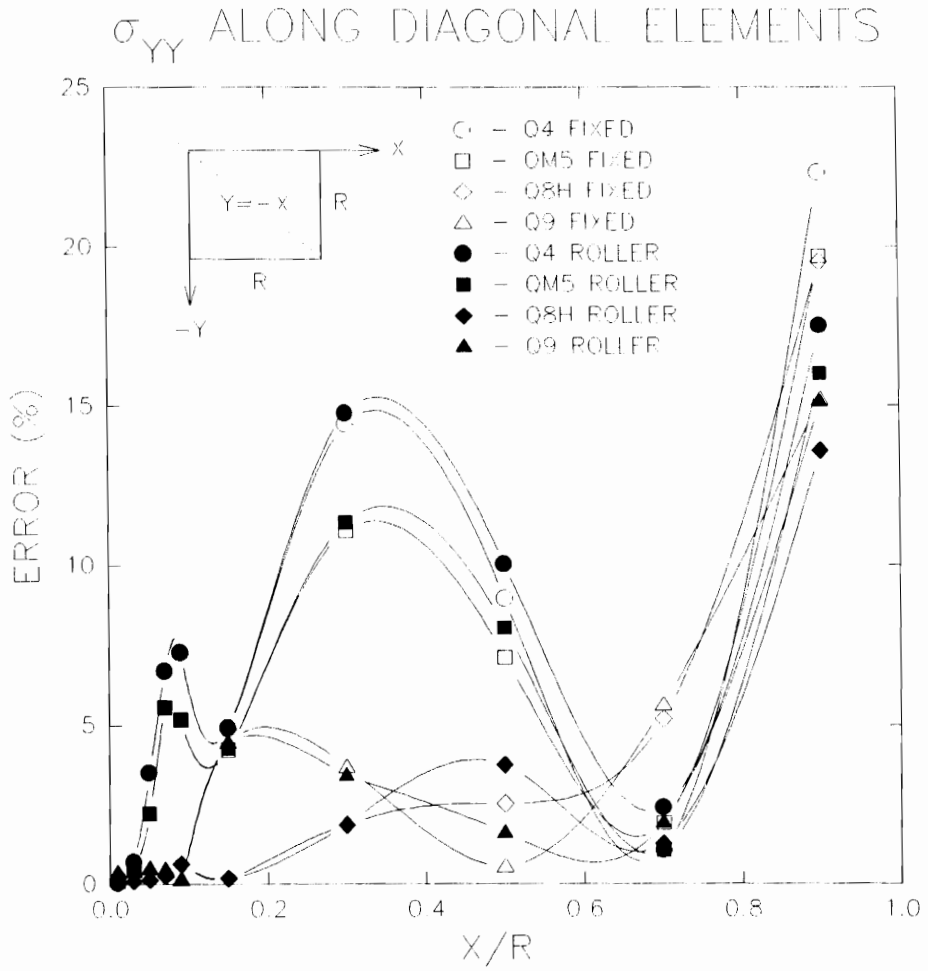

Figure 4.13 Effects of element type and boundary conditions on σ_{yy} along diagonal elements.

as large as 15% to 20% occurred. These error mostly occurred at the point (9.0,-9.0). Unlike σ_{xx} and σ_{xy}, significant differences occur between the different element types. The largest errors occurred in the 4-node lagrangian element, while the QM5 element gave slightly smaller errors. The 8-node hybrid and 9-node lagrangian element both gave values of σ_{yy} which are closest to the analytical solution. Except for the point (9.0,-9.0), errors in both these element types are within 7%.

These results indicate that the type of element used does not have any significant effect on the computed vertical displacements. In addition, the type of element used has little effect on the computed stresses. In most cases, the errors that occur in the stresses, particularly σ_{xx} and σ_{xy}, remain significant for all element types.

PART B.

4.5 Effects of Infinite Boundary.

It was pointed out in the previous sections that errors occur in both the displacements and stresses obtained using the finite element method due to the boundary conditions used to approximate the far field domain. In this section, different techniques for simulating the far field domain are considered. These include the use of (1) the analog spring model, (2) infinite elements (Beer and Meek, 1977), and (3) boundary elements based on the Melon fundamental solution. In the case of the coupled BEM/FEM solution, two analysis were performed to asses the effect of discarding the skew symmetric part of the BEM stiffness matrix. The strip footing problem described in section 4.2 is solved. A 10 m. × 10 m. domain with 100 quadrilateral elements similar to that shown in Figure (4.3) was used.

In the spring model, the stiffness of the infinite boundary is approximated using a series of springs. The additional flexibility of these springs is incorporated into the finite

element stiffness matrix by modifying the boundary conditions along the bottom and right-handside boundary. In the previous sections, it was assumed that the nodal displacements in the x-direction u_x and the y-direction u_y were equal to zero along the bottom and right-handside boundary for the fixed support case. In the case of roller supports, only u_x was set to zero along the right-handside boundary, while both components of displacements were set to zero at the bottom boundary. In the spring model, the following boundary conditions for every node along both the bottom and right-handside boundary are given by:

$$F_x = K_x u_x \qquad\qquad F_y = K_y u_y \tag{4.1}$$

where F_x and F_y are the nodal forces in the x and y direction. K_x and K_y are the corresponding spring constants in the x and y-direction respectively. Imposing these boundary conditions involves simply adding the spring constants K_x and K_y corresponding to the corresponding term along the diagonal in the global stiffness matrix.

The values used for the spring constants used in the analyses were based on the analog spring model proposed by Richart (Richart, Woods and Hall ,1970) and given by:

$$K_n = \frac{4Gr}{1-\nu} \qquad\qquad K_t = \frac{32(1-\nu)Gr}{7-8\nu} \tag{4.2}$$

where the subscripts n and t indicate the directions normal and tangent to the boundary. Thus for the bottom boundary, $K_x = K_t$ and $K_y = K_n$, while $K_y = K_t$ and $K_x = K_n$ along the right-hand side boundary. The quantity r is the effective radius. In this particular case the value of r was taken to be half the length of the boundary of the element over which the node was located. The quantities ν and G are the Poison's ratio and shear modulus which are the material properties.

The effects of the infinite boundary can also be simulated by infinite elements. This type of element is similar to the isoparametric 4-node element. However, this element uses

a different set of interpolation functions to map the Cartesian coordinates of the element into the local coordinates. This coordinate transformation allows one the side of the element to extend into infinity. Using this approach, the entire infinite domain in Cartesian coordinates is mapped into a finite domain in local coordinates. Unlike boundary elements, the displacement field assumed in this element does not satisfy the governing differential equation pointwise. The details regarding formulation and implementation of this element are given by Beer and Meek (1977). A total of 20 infinite elements were added to the right-handside and bottom boundary of the 10 × 10 finite element mesh using four node quadrilateral elements. The same values of E and ν used for the quadrilateral elements were used for the infinite elements.

In the coupled system, a total of 20 linear boundary elements were added to the right-handside and bottom boundary of the 10 × 10 finite element mesh using four node quadrilateral elements. Following the coupling procedure, the equivalent stiffness matrix for the boundary element system was computed and assembled into the global stiffness matrix. The same values of E and ν used for the finite elements were used for the boundary element system.

A comparison was made between the results obtained from the above analyses and the analysis involving a 10 m. × 10 m. domain with displacement at the bottom and right-hand side fixed, with the analytical solution. From these results the following observations can be made:

Vertical Displacements: The normalized relative vertical displacements along the centerline are shown in Figure (4.14). In all analyses, the vertical displacements are measure relative to the point on the surface 10 m. away from the centerline. As mentioned previously, for a 10 m. × 10 m. domain, when the effects of the infinite domain are not taken into consideration, an underprediction with respect to the analytical solution of the

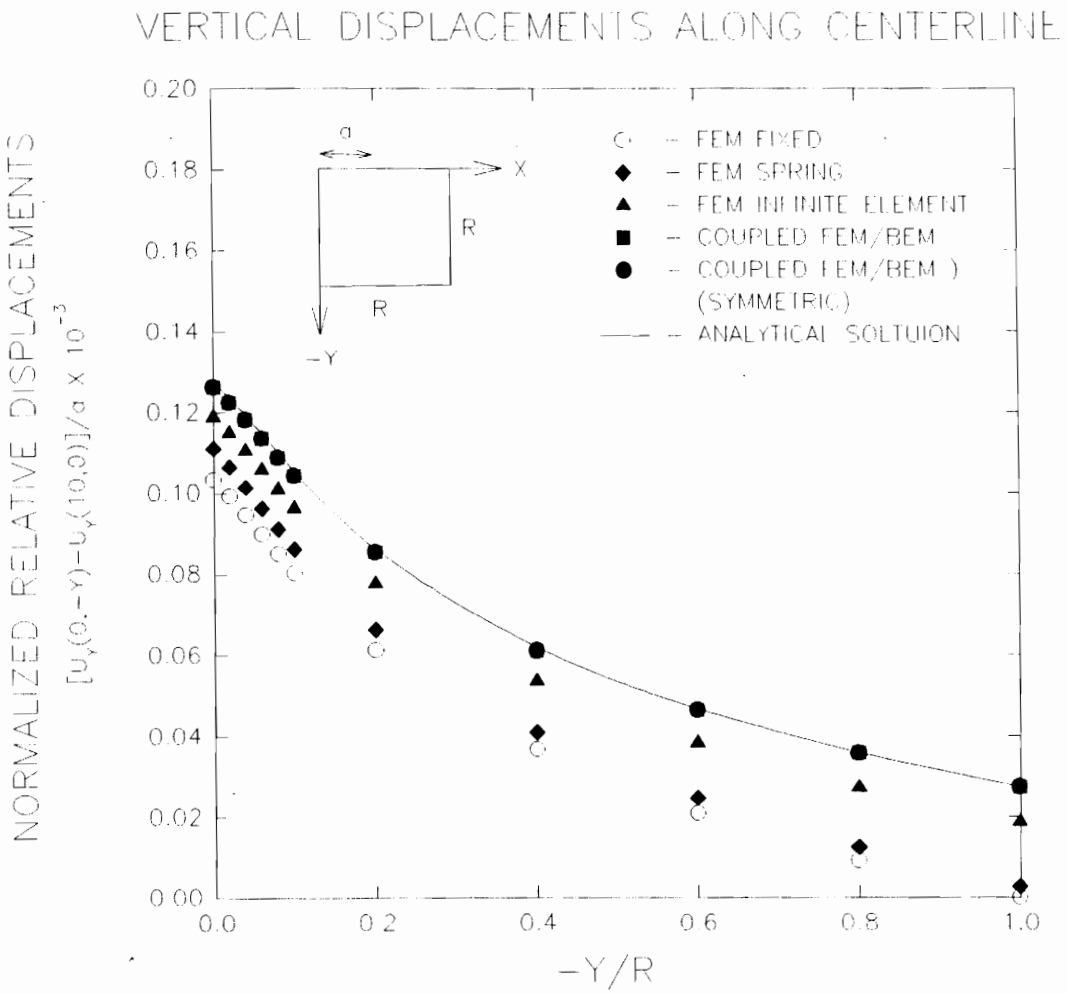

Figure 4.14 Effect of infinite boundary on vertical displacements along centerline.

vertical displacements occurs. The magnitude of the underprediction is least 20%, and can be as large as 100%. When analog springs are introduced along the top and right-handside boundaries of the 10 m. × 10 m. domain, a underprediction in vertical displacements is slightly reduced. However, the displacements are still at least 15% below the analytical solution. The use of infinite elements reduces this underprediction to between 5% at the origin and 30% at the point (9.0,-9.0). Using the proposed substructure method, the displacement are within 0.5% of the analytical solution.

The normalized relative displacements along the surface are plotted in Figure (4.15). Similarly, if the effects of the infinite boundary are neglected, underpredictions in the vertical displacements of between 20% occurring at the origin to 60% at the point (6.0,0.0) are observed for a domain size of 10 m. × 10 m. When the analog spring model is used, the underprediction of the vertical displacements is slightly reduced. However, the vertical displacements are significantly underpredicted. At the origin, the displacements are 20% below the analytical solution, while at the point (6.0,0) , the displacements are 50% below the analytical solution. When infinite element are used to account for the infinite boundary, the resulting vertical displacements are within 20% of the analytical solution. However, in this particular case, the largest underprediction occur within the proximity of the applied load. The proposed coupling method results in vertical displacements which are within 0.5% of the analytical solution.

It can be seen for both Figures (4.14) and (4.15), discarding the skew symmetric part of the boundary element stiffness matrix does not have any significant effect on the computed vertical displacements.

From the above observations, it can be concluded that the underprediction in the vertical displacements results from the manner in which the effects of the infinite boundary are accounted for. It was shown that as more sophisticated methods are used to account

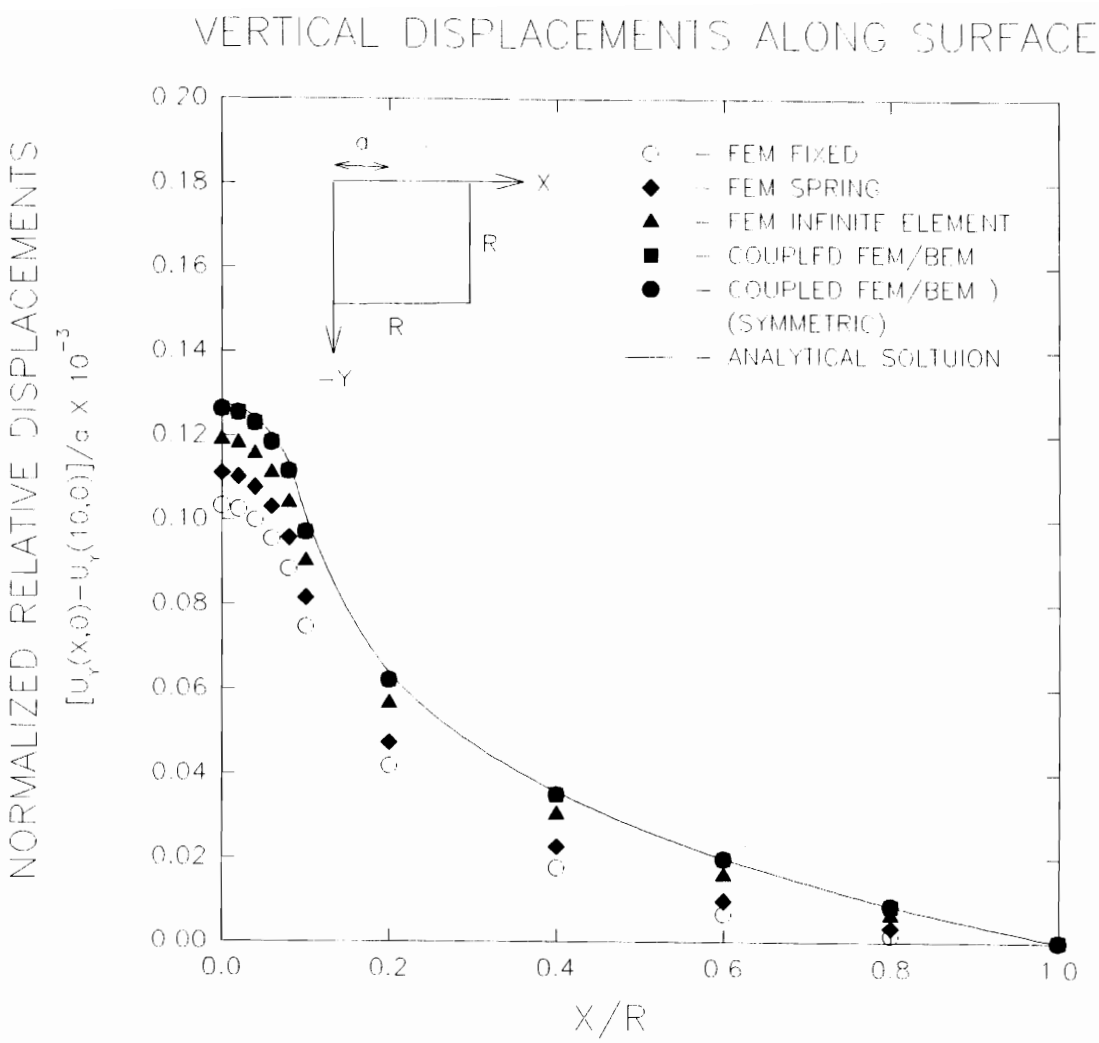

Figure 4.15 Effect of infinite boundary on vertical displacements along surface.

for the far field, the errors in the vertical displacements decrease. Since the boundary element method used is based on a half-plane fundamental solution, this approach is able to faithfully account for the effects of the far field domain. Because of this, very little error occurs.

Stresses Along Diagonal Elements: Figure (4.16) shows the percentage error in σ_{xx} with respect to the analytical solution along the diagonal elements. When the infinite boundary is neglected, the errors in σ_{xx} are as large as 32% which occurs the point (1.5,-1.5). Using the analog spring model, the maximum errors increases to 40%. This error occurs at the point (3.0,-3.0). When the infinite element is used, a maximum error of 68% occurs at the point (9.0,-9.0). However, errors occurring when the infinite element is used are on the average less than those that occur when the infinite boundary is neglected or model using the analog spring model. Also, the use of spring or infinite element does not eliminate the oscillation that occurs in the errors. Using the proposed substructure technique, σ_{xx} is within 5% of the analytical solution. In addition, the oscillation that occurs in the errors is eliminated.

Figure (4.17) shows the percentage error in the shear stresses σ_{xy} along the diagonal elements. It can be seen neglecting the effects of the infinite boundary results in errors of as large as 70% occurring at the point (9.0,-9.0) The maximum error which occurs at this same point is slightly reduced 50% when spring elements are used. The use of infinite elements results in shear stresses which are within 5% of the analytical solution. The proposed substructure technique gives shear stresses which are within 4% of the analytical solution.

The percentage errors in σ_{yy} along the diagonal elements is shown in Figure (4.18). Error of as large as 20% occur at the point (9.0,-9.0) when the effects of the infinite boundary are neglected. The maximum error which occurs at the same point increases to

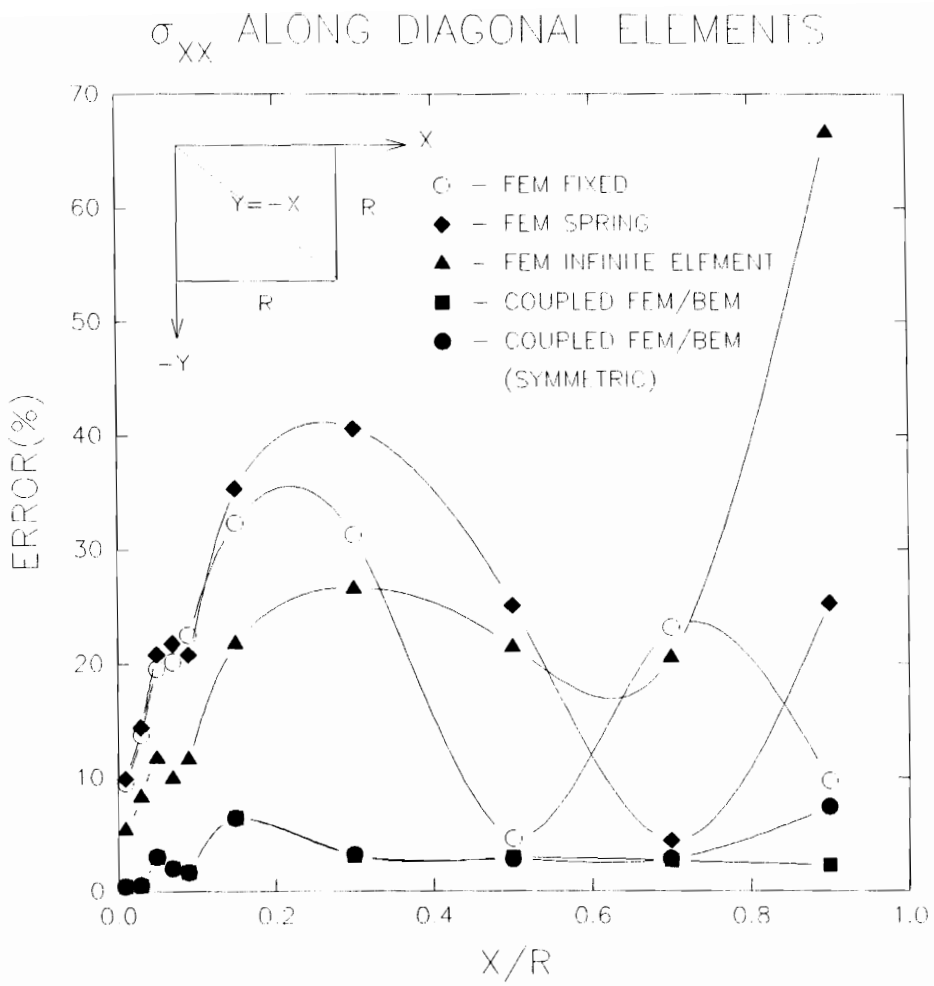

Figure 4.16 Effect of infinite boundary on σ_{xx}.

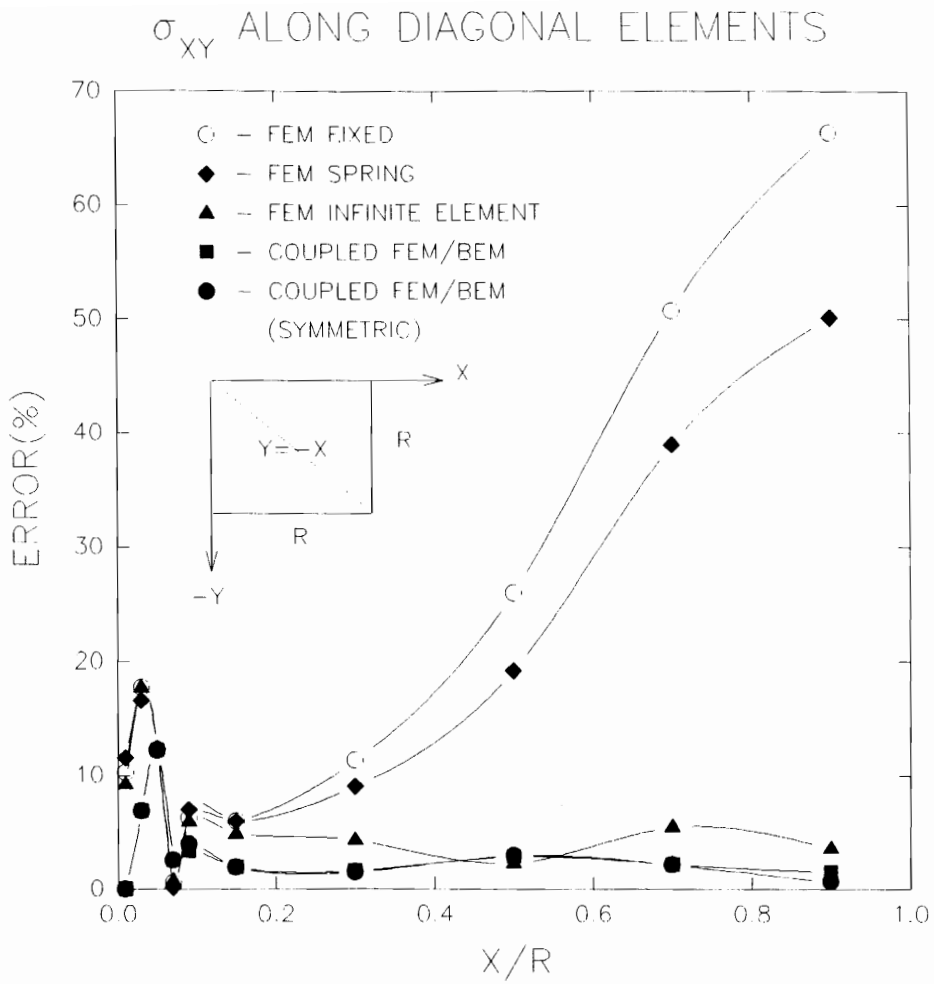

Figure 4.17 Effect of infinite boundary on σ_{xy}.

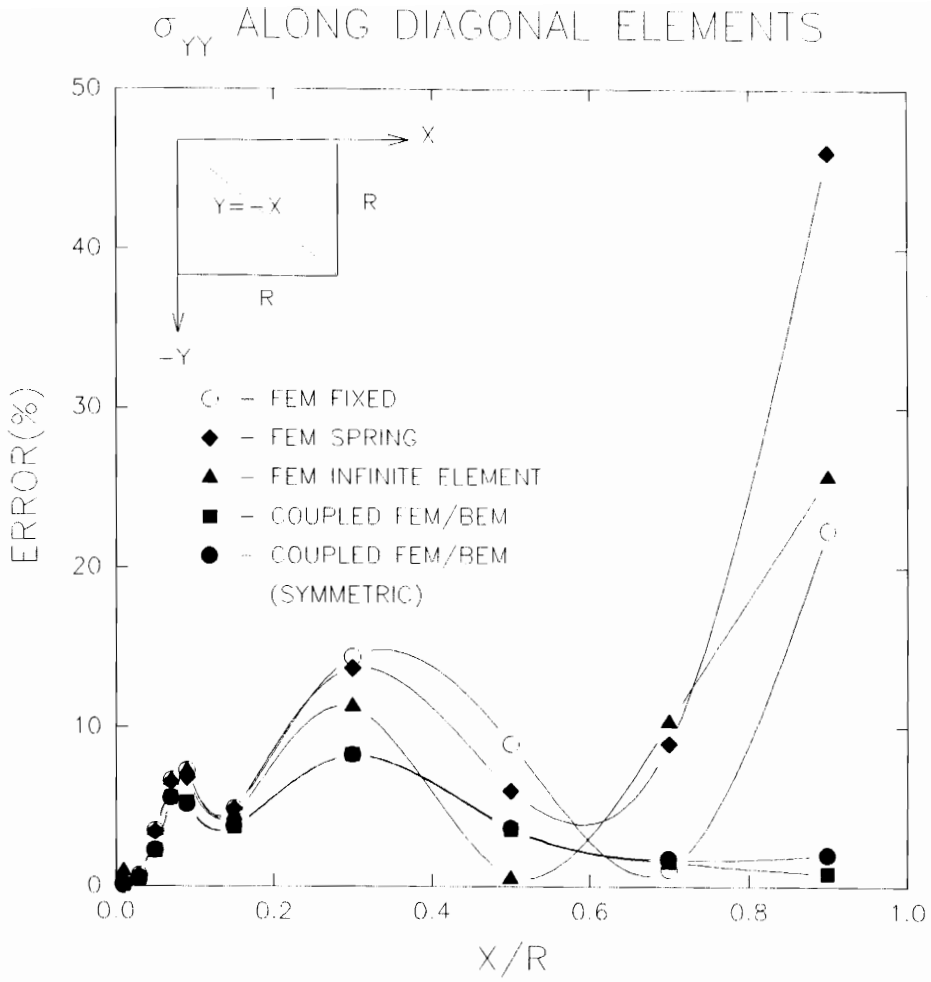

Figure 4.18 Effect of infinite boundary on σ_{yy}.

45% when spring elements are used. The use of infinite elements results in errors of as large as 25% which occur at the same point. However, the error in σ_{yy} using this method are less than the two previous methods. In all these three methods, very significant oscillations occur in the errors. Using the proposed coupling procedure, the values of σ_{yy} are within 8% of the analytical solution. In addition, the oscillation in error is eliminated.

Again, it can be observed from Figures (4.16), (4.17) and (4.18) that discarding the skew-symmetric part of the boundary element stiffness matrix does not have any significant effect on the computed stresses.

It can be seen from the observations made, while using springs may reduce the underprediction in the displacements, it results in less accurate stresses. In addition, the oscillation in the errors still remain. Infinite elements reduce underprediction in the vertical displacements. In addition, the stresses obtained using this technique are, on the average, more accurate compared to assuming fixed support conditions or using springs. However, the errors in σ_{xx} and σ_{yy} together with the oscillation that occurs is significant. The proposed substructure method seem to be the best option in that it gives displacements within 0.5%, and stresses within 8% of the analytical solution. In addition, the oscillation which occurs in the errors is eliminated.

As mentioned, when only the symmetric part of the boundary element stiffness matrix as used, the displacements and stresses obtained did not differ significantly from those obtained using the full stiffness matrix. From this observation, it can be concluded that the technique used by Brebbia and Georgiou in equation (3.12), for obtaining a symmetric boundary element stiffness matrix based on the Kelvin solution, is also valid when the Melon solution is used. Brebbia pointed out that in the boundary element stiffness matrix based the Kelvin solution $\hat{K}$, the difference in corresponding off diagonal terms compared with the diagonal term is insignificant:

$$\left|\frac{\hat{k}_{ij}-\hat{k}_{ji}}{\hat{k}_{ii}}\right| \le 0.002 \tag{4.3}$$

where $\hat{k}_{ij}$ is the (i,j)th element of the stiffness matrix $\hat{K}$. For the problems solved in this research where the Melon solution was used, it was observed that the difference in the off-diagonal terms of $\hat{K}$ compared to the diagonal term was slightly than in the Kelvin solution:

$$\left|\frac{\hat{k}_{ij}-\hat{k}_{ji}}{\hat{k}_{ii}}\right| \le 0.003 \tag{4.4}$$

When the geometry of the problem is symmetric and the method of images is used to incorporate this symmetry into the solution, the matrix $\hat{K}$ becomes more unsymmetric such that:

$$\left|\frac{\hat{k}_{ij}-\hat{k}_{ji}}{\hat{k}_{ii}}\right| \le 0.01 \tag{4.5}$$

However, in the stiffness matrix K resulting from assembling the boundary element stiffness matrix $\hat{K}$ into the finite element system:

$$\left|\frac{k_{ij}-k_{ji}}{k_{ii}}\right| \le 0.001 \tag{4.5}$$

This is due to the fact that the finite element stiffness matrix is symmetric and the terms along the diagonal are significantly larger than the off-diagonal terms. Thus when $\hat{K}$ is assembled into the finite element system, the effect of the asymmetry of $\hat{K}$ are significantly reduced.

PART C

4.6 Solution of Non-homogenous Linear Problems

It was shown previously that when the effects of the infinite boundary were accounted for using boundary elements, the resulting displacements were within 0.5% of the analytical solution. Also, this approach resulted in stresses which were within 5% of the analytical solution. However, one limitation of using boundary elements is that only one set of E and ν can be specified for the entire far field domain. For most soil-structure interaction problems, the soil modulus in both the near field and far field domain is not constant but is dependent on the confining pressure, and consequently varies with depth. The objective of this section is to determine what value of E used in the boundary element system to model a far field where the modulus increases with depth. Also, this section seeks to asses if this approximation introduces significant errors into the solution. To investigate these issues, the strip footing problem described in section 4.2 is modified by letting the shear modulus G vary with depth in the following manner:

$$G = my \tag{4.6}$$

where m is a constant and y is the distance from the surface of the half-plane. The solution to this problem for the case of $\upsilon = 0.5$ is given by Gibson (1967). Based on this analytical solution, the vertical displacement is given by:

$$u_y = \frac{w}{2\pi m}\left[\tan^{-1}\left(\frac{a+x}{y}\right)+\tan^{-1}\left(\frac{a-x}{y}\right)\right] \tag{4.7}$$

while the stresses are the same as the homogenous case. In equation (4.3), w is the magnitude of the uniformly distributed load applied over a half width of a. This problem was analyzed using the finite element method alone, and the proposed substructure method for coupling the boundary and finite element method. In the finite element method, fixed support conditions were assumed along the bottom and right-hand size boundary. In

the coupled BEM/FEM solution, 20 boundary elements were used to account for the infinite boundary. In both cases, a domain size of 10 m. × 10 m. modeled with 100 quadrilateral elements was used. The material parameters used in the analysis are given if table (4.2).

Table 4.2

Parameters for Linear Nonhomogenous Strip Footing Problem

Parameter	Name	Value
m	slope	100.0 MPa
ν	Poison's Ratio	0.495
w	Distributed Load	1.0 KN/m
a	Load Half-width	1.0 m

Because of the value of Poison's ratio used, the finite element formulation described in chapter 3 for nearly incompressible solids was used. It was previously observed that the displacements are most affected by the boundary conditions assumed on the bottom boundary of the mesh. Because of this, the modulus along the bottom of the mesh was assumed to be the modulus of the entire far field domain. For the finite element mesh, the modulus used for each element was computed by first getting the y-coordinate of the centroid of the element and evaluating equation (4.3) to obtain the shear modulus G. The modulus was then obtained noting that

$$E = 2(1+\nu)G \tag{4.8}$$

From the above analyses, the following observations can be made:

Vertical Displacements: The normalized vertical displacements along the centerline are presented in Figure (4.19). Underpredictions with respect to the analytical solution of between 10% at the origin and 100% at the bottom of the mesh occur when the finite element solution is used. The coupled BEM/FEM solution using the proposed

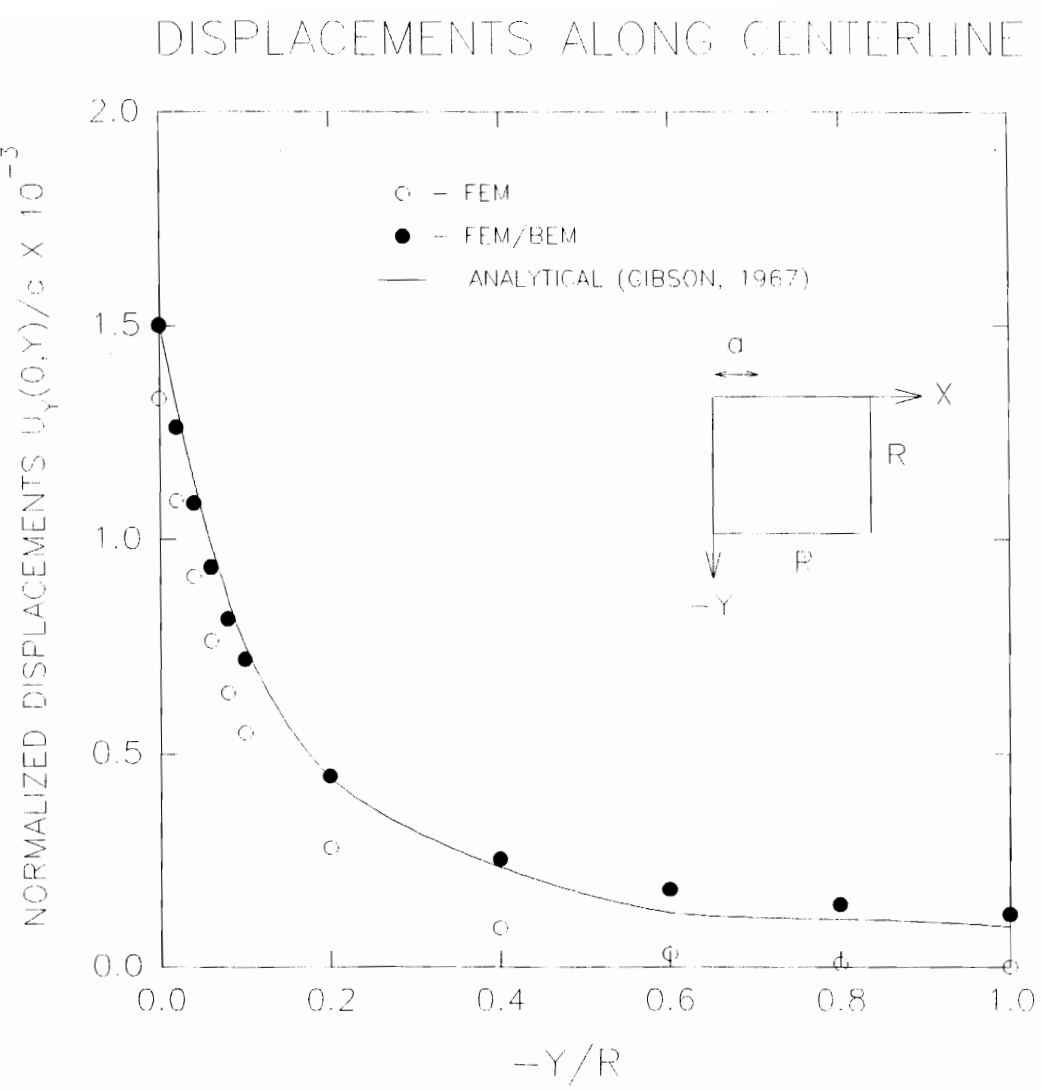

Figure 4.19 Vertical displacements along centerline for G=my.

substructure technique results in vertical displacements within 5% of the analytical solution.

Figure (4.20) shows the vertical displacements along y/a = -1.0. Here, the underpredictions in the vertical displacements are more pronounced. Displacements computed using the finite element method are at least 25% below the analytical solution. In particular, large errors in the finite element solution occur due to the erroneous prediction that heaving occurs beside the loaded area. Again, the proposed substructure technique results in displacements which are within 5% of the analytical solution.

Stresses Along Diagonal Elements: the error in σ_{xx} along diagonal elements is plotted in Figure (4.21). It can be seen that the finite element methods results in stresses which are in errors by as much as 240% occurring at the point (9.0,-9.0). These errors increase as points further away from the loaded area are considered. The proposed substructure method results in stresses which are within 25% of the analytical solution.

Figure (4.22) show the error in the shear stress σ_{xy} along diagonal elements. Errors of as large as 75% occur in the finite element analysis. With the exception of points very near the origin, shear stresses within 20% of the analytical solution result from the proposed substructure method.

Similar observation can be made with respect to error in σ_{yy} along diagonal elements as shown in Figure (4.23). Errors of as large as 200% occur at the point (9.0,-9.0) in finite element analysis. Similar to σ_{xx}, these errors increase with increasing distance from the loaded area. The substructure method results in values of σ_{yy} which are within 5% of the analytical solution.

In summary, based on the above observations, the following conclusions can be made:

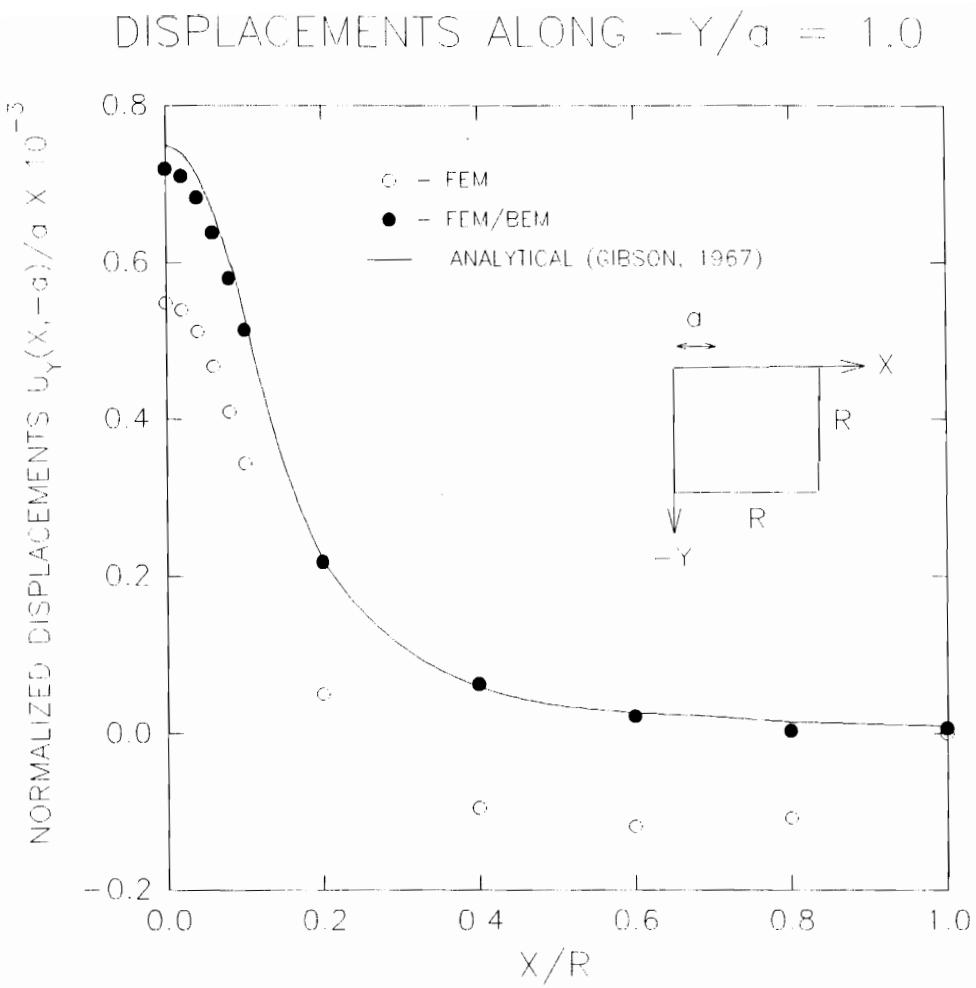

Figure 4.20 Vertical displacements along y/a = 1.0 for G=my.

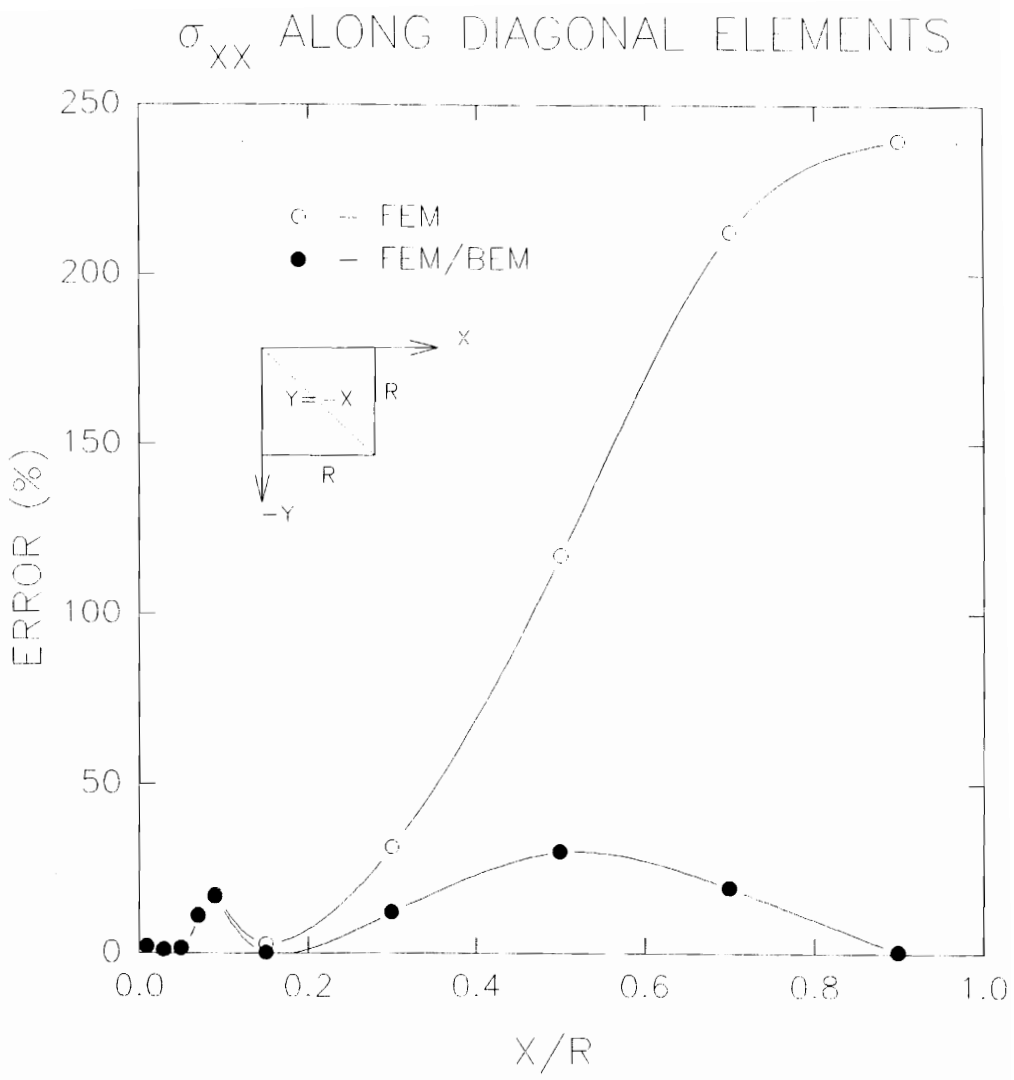

Figure 4.21 σ_{xx} along diagonal elements for G=my.

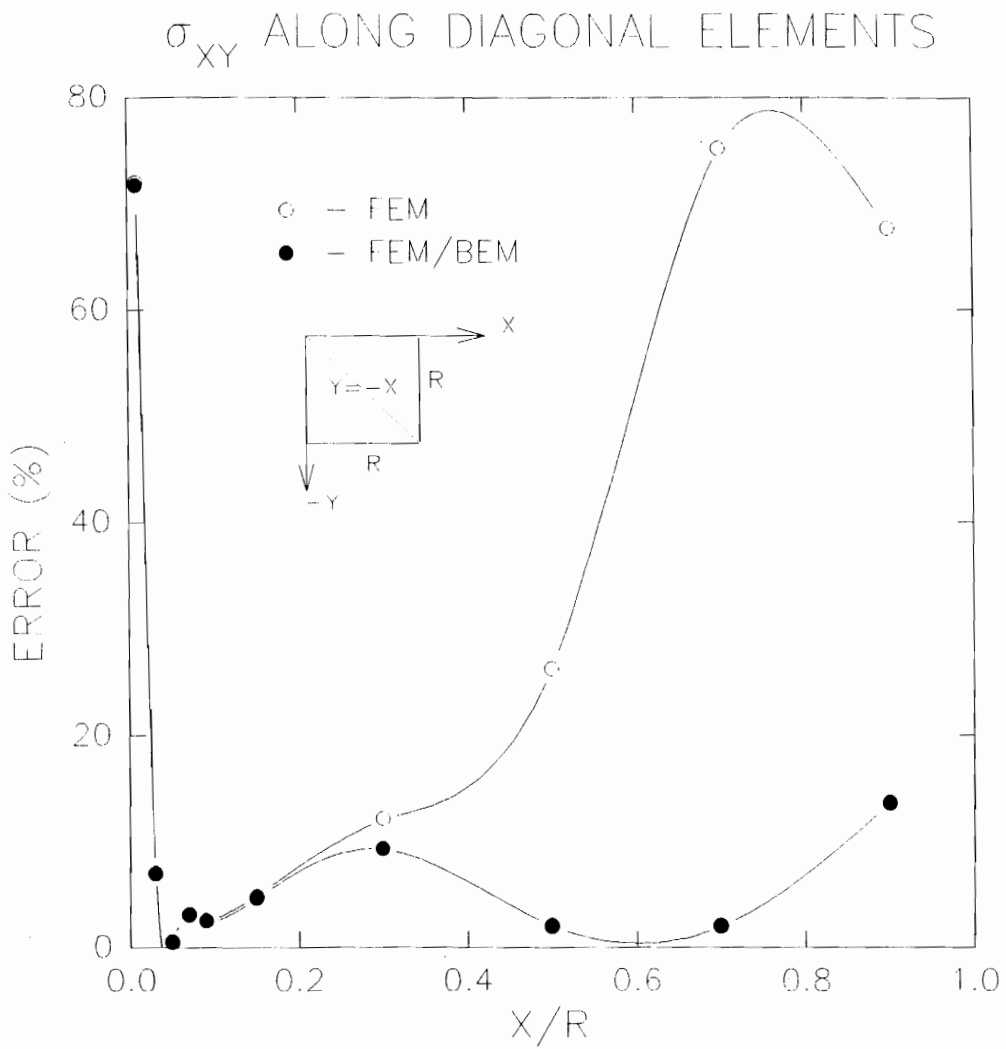

Figure 4.22 σ_{xy} along diagonal elements for G=my.

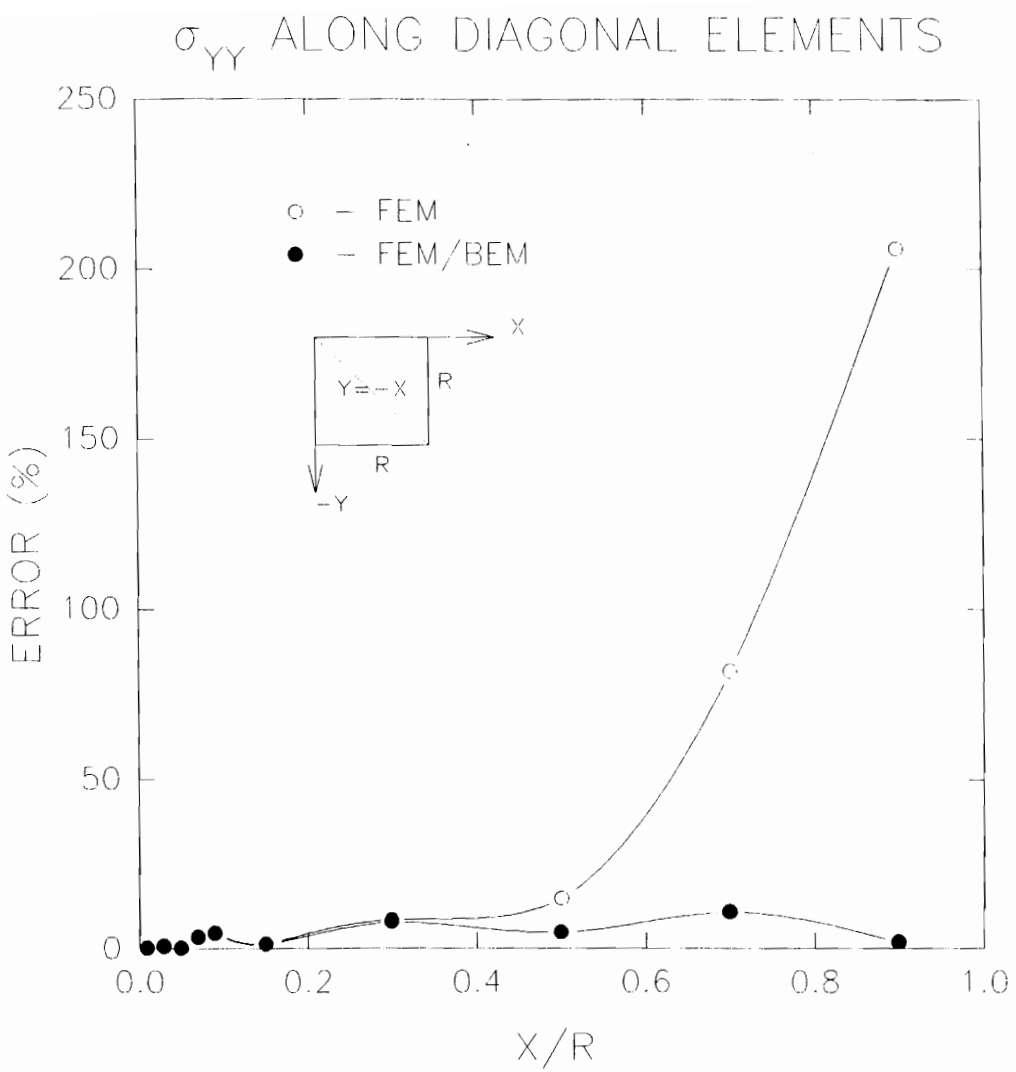

Figure 4.23 σ_{yy} along diagonal elements for G=my.

1. Significant underpredictions in vertical displacements as well as very large error in all components of stresses occur when the strip footing problem with increase modulus is solved using the finite element method. The underpredictions that occur in the displacements are slightly less than those that occur in the homogenous problem. However, errors as large as 80% or more occur in all components of stress.

2. The proposed substructure technique results in values of displacements and stresses which are significantly more accurate. Displacements obtained using this technique are within 5% of the analytical solution, while stresses are within 20% of the analytical solution.

3. While both the displacements and stresses obtained in this problem were less accurate with respect to the analytical solution as compared to those obtained in the homogenous case, it should be pointed that an approximation was made. This approximation involved replacing the non-homogenous far field with a homogenous far field. It was shown that when the modulus E at the base of the mesh is used for the entire far field domain, the resulting displacements and stresses were closer to the analytical solution as compared to fixing the displacements along the bottom and right-handside boundary.

PART D

4.7 Solution of Nonlinear Problems

In this section, the effects of the infinite boundary on the solution of nonlinear problems was investigated using the proposed substructure method for coupling the boundary element and finite element method. The strip footing problem described in section 4.2 was solved assuming a stress-strain behavior described by the hyperbolic

model (Duncan and Chang, 1969). In the hyperbolic model, the tangent modulus E_t is a function of the major and minor principal stresses (σ_1, σ_3) given by the equation:

$$E_t = \left[1 - \frac{R_f(1-\sin\phi)(\sigma_1 - \sigma_3)}{2c\cos\phi + \sigma_3 \sin\phi}\right] K P_a \left(\frac{\sigma_3}{P_a}\right)^n \tag{4.9}$$

where c is the cohesion intercept, ϕ is the internal angle of friction, R_f is the failure ratio, K is the modulus number, and n is the modulus exponent. The modulus number and modulus exponent are nondimensional numbers. The atmospheric pressure P_a is introduced to make conversion from one system of units to another easier. The units of E_t are the same as P_a.

The material parameters assumed for the hyperbolic model are given in table 4.3. In this particular case, the volume change behavior was assumed stress-independent resulting in a constant value of ν.

Table 4.3

Parameters for Nonlinear Elastic Strip Footing Problem

Parameter	Name	Value
K	Modulus number	340
n	Modulus exponent	0.5
R_f	Failure ratio	0.8
c	Cohesion intercept	900 psf
ϕ	Friction angle	15.0°
γ	Unit weight	125 pcf
ν	Poison's ratio	0.3

A uniformly distributed load was chosen so that none of the elements would have a stress ratio above 1.0. Using a value of w = 500 lb./ft, the highest stress ratio was just slightly below 1.0. Because of the nonlinear nature of the problem, the load was applied in five increments of 100 lb./ft. A domain of 100 ft. × 100 ft. and the finite element mesh illustrated in Figure (4.3) was used. Two analysis were performed using the computer program SOILSTRUCT, a general-purpose finite element program for two-dimensional analysis of soil-structure interaction problem. Details of the implementation of the substructure technique into this program are further explained in chapter 5.

The first analysis was done using the finite element method alone with the bottom and right-hand side boundary fixed. The coupled BEM/FEM solution using the proposed substructure method with the skew-symmetric part discarded was used in the second analysis. A value of $E = 6.0 \times 10^4$ psf was used as the modulus for the far field modeled by the boundary element method. This value was obtained by taking an average modulus at the bottom boundary over the five load steps performed in the first analysis. Comparing the results of these two analyses, the following observation can be made:

Vertical Displacements: In both analyses, all vertical displacements were measured relative to the point (10.0, 0.0) and were plotted against the coordinates normalized using the mesh size R = 10.0 m. Figure (4.24) shows the normalized relative vertical displacements along the centerline. It can be seen that the displacements obtained using the finite element method are smaller than those obtained using the coupled BEM/FEM solution. At the surface, the vertical displacement obtained using only the finite element method is 8% less than that obtained using the coupled BEM/FEM solution. This disparity increases steadily with depth to 100% at the bottom of the mesh. Like the

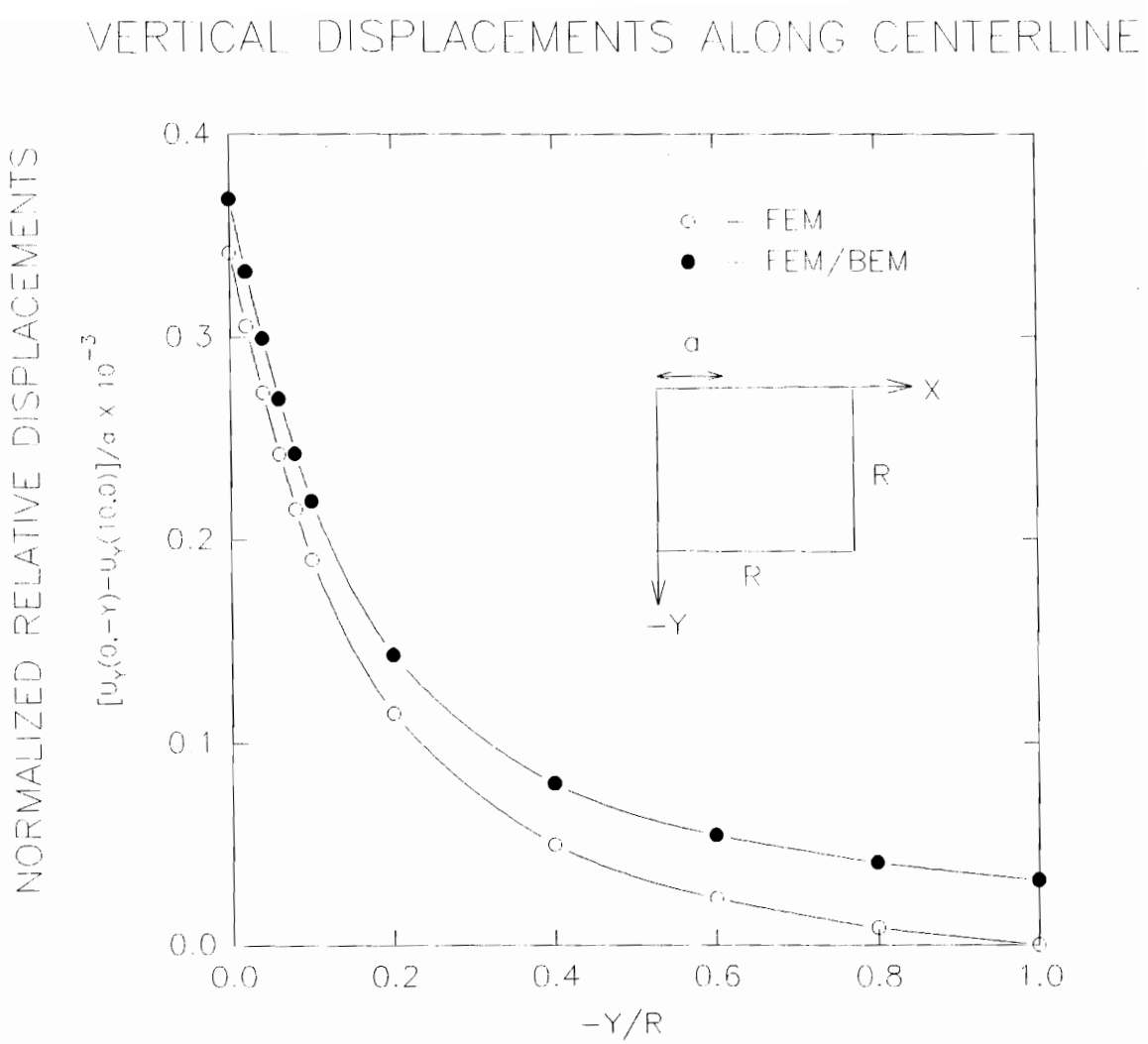

Figure 4.24 Vertical displacements along ceterline - nonlinear case.

linear case, the difference in the vertical displacements between the two solutions is roughly constant with depth.

The normalized relative displacement along the surface are plotted in Figure (4.25). It can be seen that vertical displacements obtained using the finite element method were less than those obtained using the coupled solution. These differences ranged from 8% at the origin to a maximum of 60% at $x/R = 0.6$.

As compared with the linear homogenous problem, the difference is displacements was smaller within the proximity of the load. However, as point further away from the load were considered, underpredictions similar to those obtained in the linear homogenous problem were observed.

Stresses along diagonal elements: Figure (4.26) shows the percentage difference between the two solution techniques in the value of σ_{xx} along the diagonal elements. It can be seen that errors of as large as 23% at point (7.0,-7.0) occur. An oscillation in the error ,similar to that observed in the linear problem, occurs in this problem.

Even larger differences as big as 150% at point (9.0,-9.0) occur in the shear stresses σ_{xy} along the diagonal elements as shown by Figure (4.27). As was observed in the linear case, the difference begins small are steadily increases as points further away from the loaded area are considered.

Figure (4.28) shows the percentage difference between the two solution techniques for σ_{yy} along diagonal elements. These two solution techniques result in values of σ_{yy} which differ by at most 10%.

From the above observation it can be seen that σ_{xx} and σ_{xy} are the stresses most affected by the boundary conditions while σ_{yy} does not seem to be greatly influenced. The difference between the two solutions for the shear stress σ_{xy} are double those in the linear case. For σ_{xx}, these differences are slightly smaller than those in the linear case.

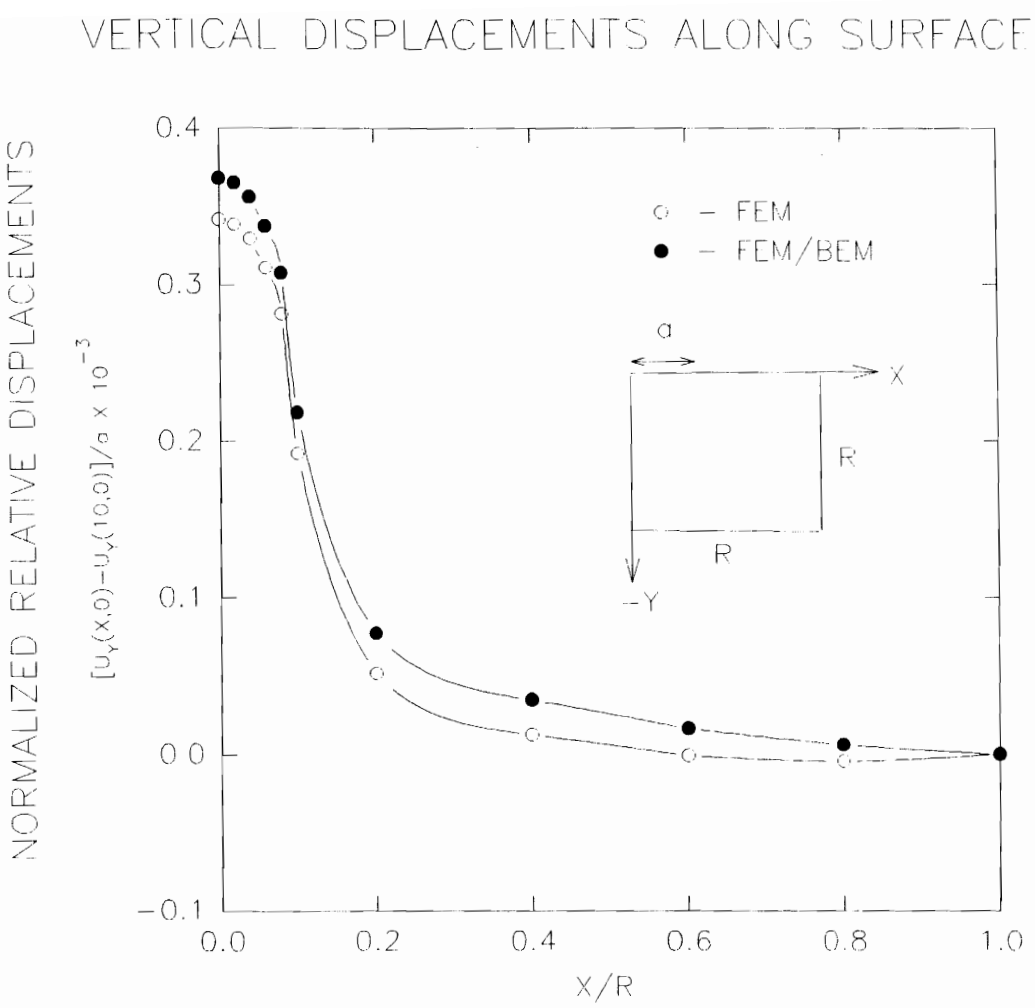

Figure 4.25 Vertical displacaments along the surface - nonlinear case.

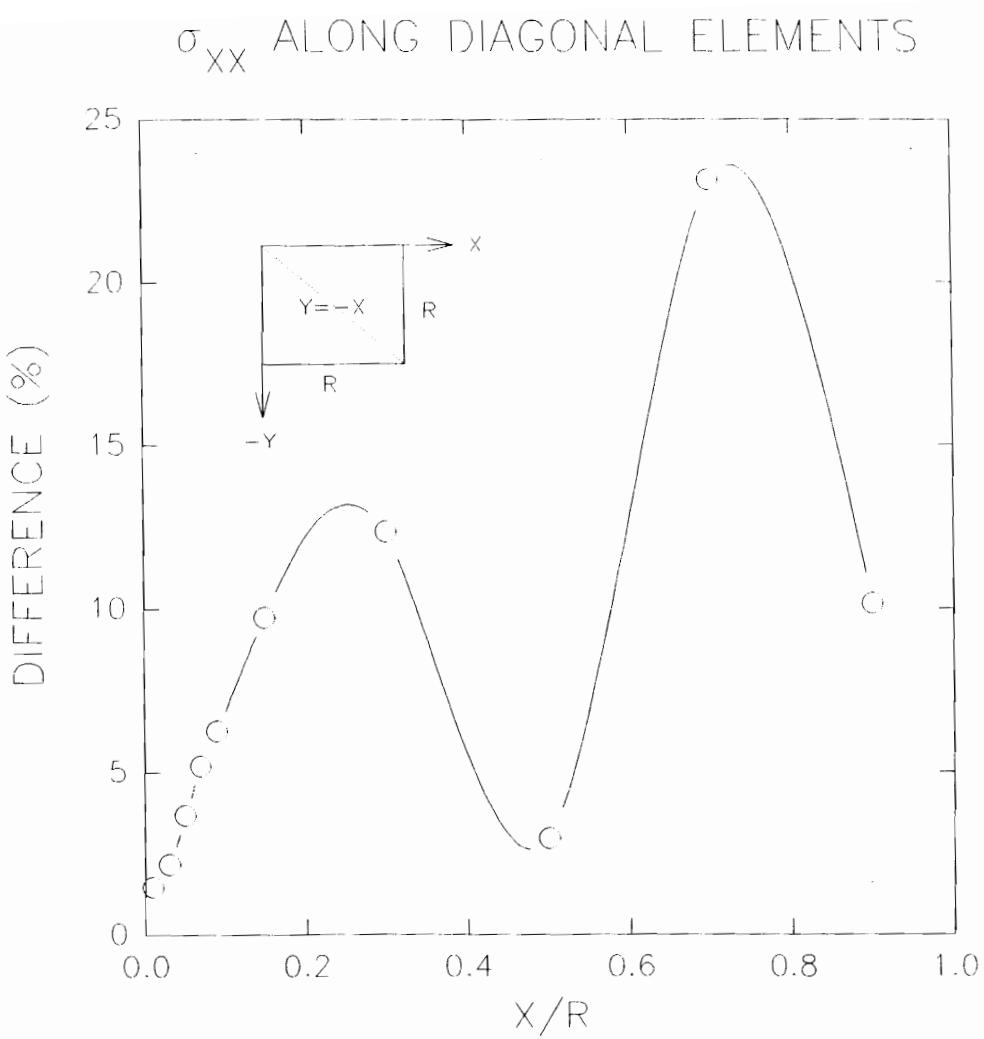

Figure 4.26 σ_{xx} along diagonal elements - nonlinear case.

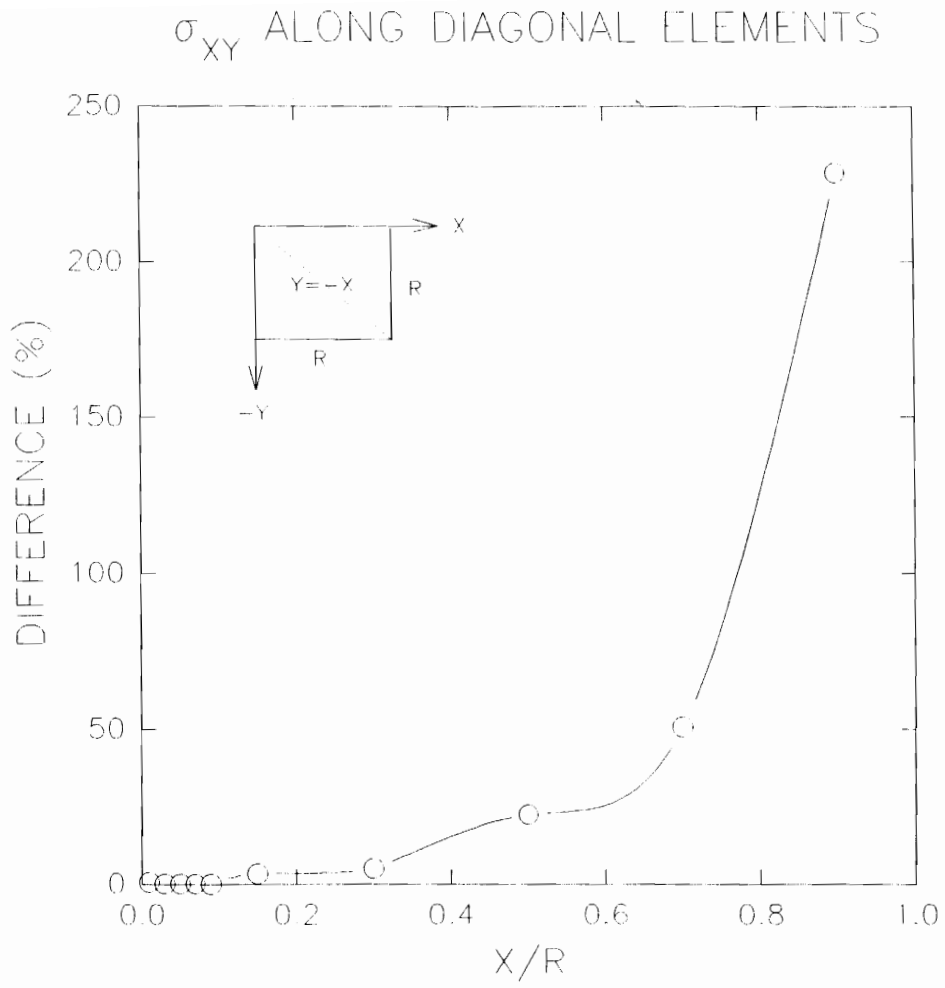

Figure 4.27 σ_{xy} along diagonal elements - nonlinear case.

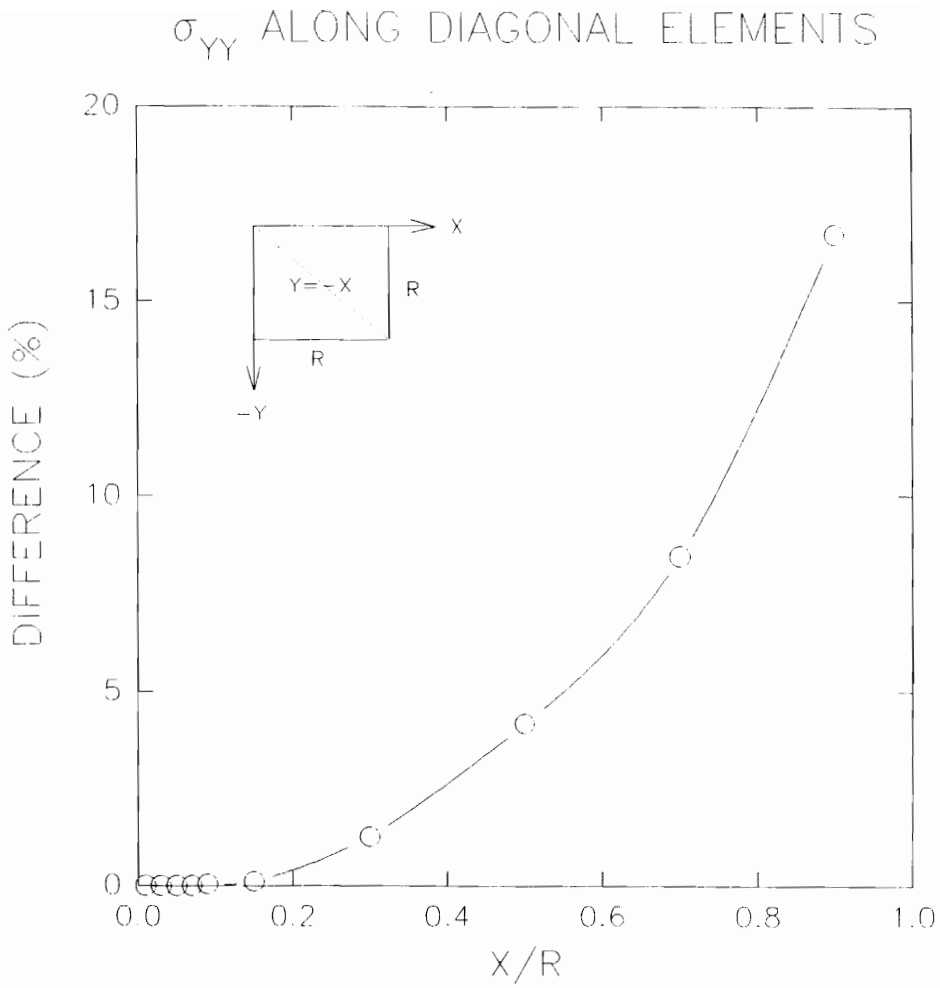

Figure 4.28 σ_{yy} along diagonal elements - nonlinear case.

4.8 Summary

In summary, from the results of the different analyses performed, the following conclusions were drawn.

1. Significant underpredictions of at least 25% in the vertical displacements, and errors of at least 30% in the horizontal normal stress σ_{xx} and shear stress σ_{xy} occur in the finite element method. In addition, oscillations occur in these errors. These result from the boundary conditions assumed along the bottom boundary. This is true for both the homogenous case as well as when the modulus increases with depth.

   Increasing the domain reduces the magnitude and oscillations of these errors. However, these errors remain significant even for considerably large domains.

2. Using higher order elements such as quadratic and stress hybrid elements slightly reduces the errors that occur in the stresses particularly, σ_{xx}. However, the these errors still remain significant. Also, no significant improvement is observed in the vertical displacements.

3. The underpredictions that occur in the vertical displacements as well as the errors that occur in the stresses are not affected by the type of support conditions assumed along the right-handside boundary. This is true regardless of domain size or element type.

4. The use of spring or infinite elements to model the far field reduces in the underpredictions that occur in the vertical displacements. For spring elements, the

vertical displacements are within 20% of the analytical solution while for infinite elements they are within 10%. However, the errors that occur in the stresses obtained using these techniques are significantly larger than those in the conventional finite element analysis.

5. The coupled BEM/FEM solution using the proposed substructure technique gives values of displacement which are within 0.5% of the analytical solution. This solution also gives values of stresses which are within 2% of the analytical solution. In addition, using this solution technique eliminates the oscillations that occur in the conventional finite element solution. This is true for both the homogenous case as well as when the modulus increases with depth.

It was also observed that discarding the unsymmetric part of the boundary element stiffness matrix has no observable effect on the displacements are stresses obtained.

6. For the non-homogenous problems, the far field domain can be approximated with a homogenous far field domain using average value of E at the bottom of the mesh. While slightly less accurate as compared to the homogenous case, the solution resulting from this approach is significantly more accurate than that when the infinite boundary is neglected.

7. For nonlinear problems, the coupled BEM/FEM solution results in displacements which are higher than those obtained using the finite element method only. The difference in the vertical displacement obtained using two solution techniques is on the average the same as that in the linear homogenous case. An exception to this is area near the applied load where the difference is roughly half that of the linear homogenous case. The values of normal stresses σ_{xx}

and σ_{yy}, obtained using the two solution procedure, differed by magnitude roughly equal to that in the linear homogenous case. However, the difference in shear stress σ_{xy} was double that of the linear homogenous case.

Chapter 5
SOLUTION OF U-FRAME LOCK PROBLEMS

5.1 Introduction

In this chapter, the proposed method for coupling the boundary element and finite element method is applied to the solution of a U-frame lock soil-structure interaction problem. The BEM-FEM coupling technique is incorporated into the program SOILSTRUCT (Clough and Duncan, 1969). The problem is analyzed for both linear elastic and nonlinear material behavior. In both analyses, the construction sequences are simulated. The displacements and stresses obtained using the coupled method are compared with those obtained using the finite element method alone.

5.2 SOILSTRUCT Implementation

For the purpose of solving the U-frame lock problem, the proposed coupling technique is incorporated into the computer program SOILSTRUCT. SOILSTRUCT is a general purpose finite element program for solving soil-structure interaction problems. It has the capability of analyzing problems involving incremental construction and nonlinear material behavior.

A flowchart of the main calling program is illustrated in Figure (5.1). After all data has been inputted, the subroutine DETNA is called to compute the profile of the system of equations and determine the diagonal addresses for use in the column storage. The initial stresses are computed using the subroutine INITAL, after which the load is applied in NC load steps. To keep track of the load steps, a counter MQ is used. Within each load step, NUMIT(MQ) iterations are performed. This number of iterations is specified in the data file and can vary between load steps. Each iteration consists of forming the tangent stiffness matrix, solving the resulting system of equations and calculating the stresses. The global tangent stiffness matrix is formed in the subroutine STRSTF. The subroutine

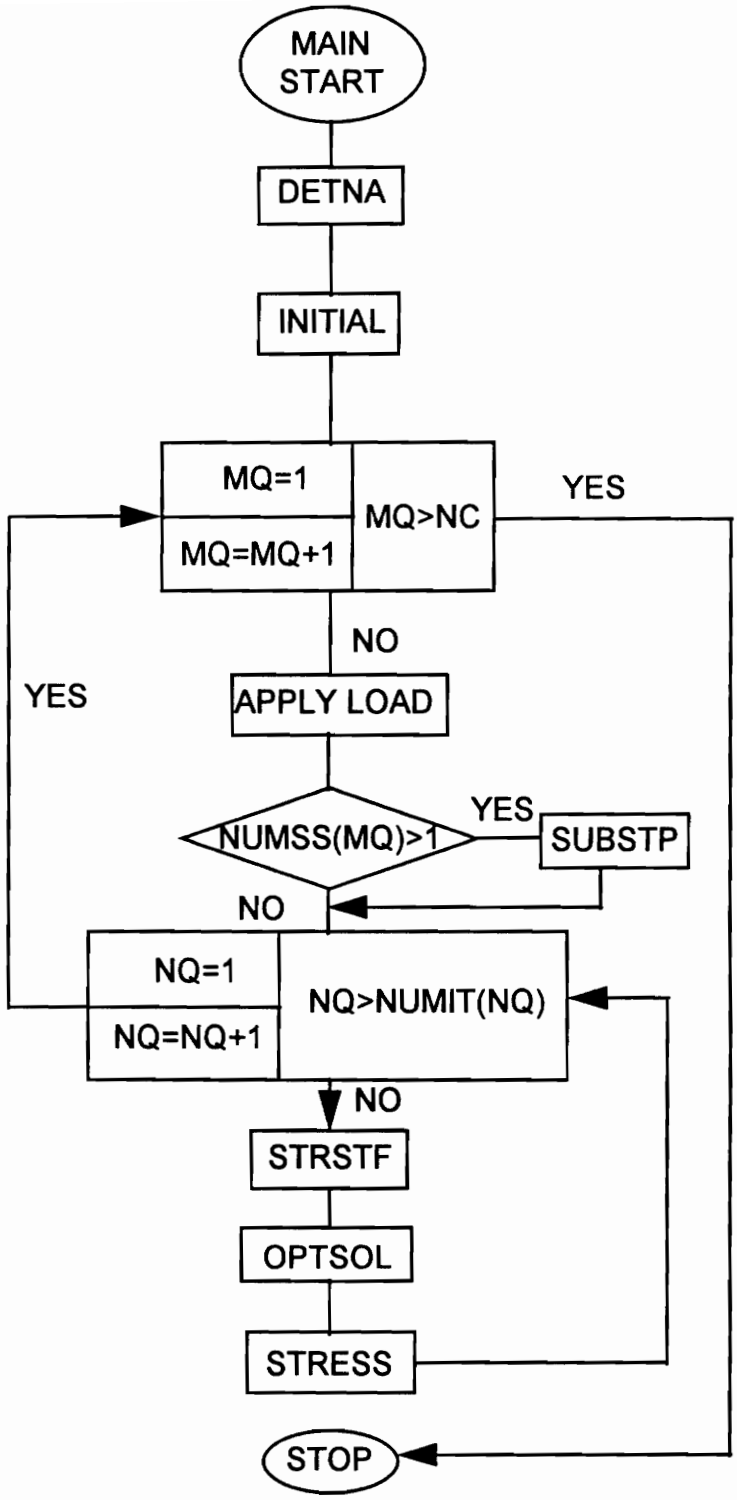

Figure 5.1. Flowchart of SOILSTRUCT

OPTSOL solves the symmetric system of equations and the stresses of two-dimensional and interface elements are calculated in subroutine STRESS and JSTRES respectively.

To incorporate the substructure technique into the SOILSTRUCT program, two modifications needed to be made. The subroutine DETNA was modified to compute the profile of the system taking into consideration the connectivity of the boundary element system in addition to the finite element system. Also, the subroutine STRSTF was modified to assemble the boundary element stiffness matrix into the global stiffness matrix as shown in Figure (5.2). Because the subroutines OPTSOL and STRSTF are limited to symmetric matrices, only symmetric portion of the boundary element stiffness matrix obtained using equation (3.12) is assembled in subroutine STRSTF. It was mentioned in chapter 4 that for linear problems, the displacements and stresses obtained using on the symmetric part of the boundary element stiffness matrix did not differ significantly from those obtained when the full stiffness matrix was used. Because SOILSTRUCT models the material nonlinearity using a series of linear analyses, using only the symmetric part of the boundary element stiffness matrix does not significantly affect the resulting displacements and stresses.

5.3 Description of the Problem

This problem consists of a concrete U-frame lock structure filled with water as illustrated in Figure (5.3). Beside the lock structure, a 20 ft. high embankment with a slope of 1:2.5 is built. The material properties assumed in this problem are given in table (5.1)

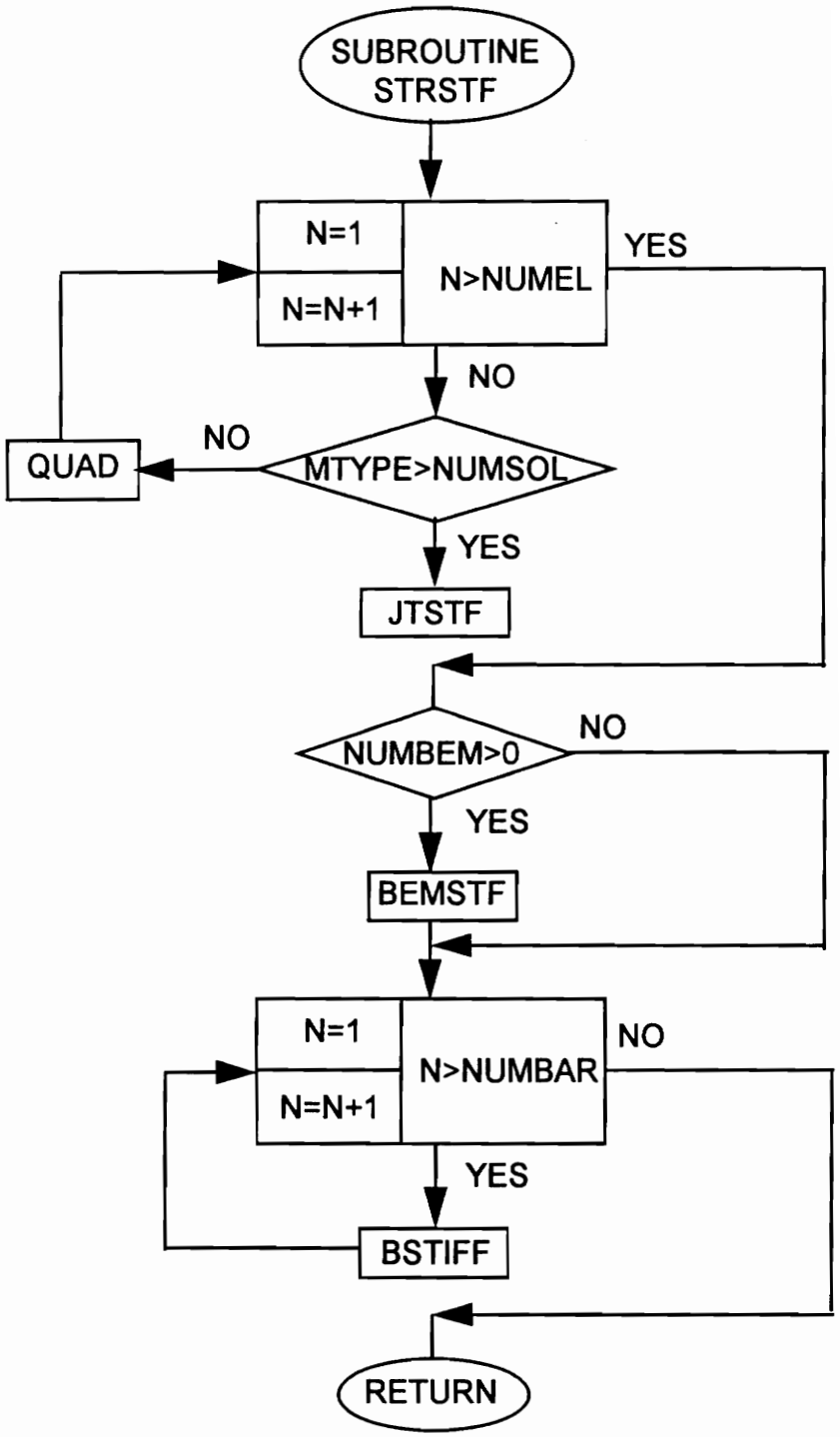

Figure 5.2. Flowchart of Subroutine STRSTF

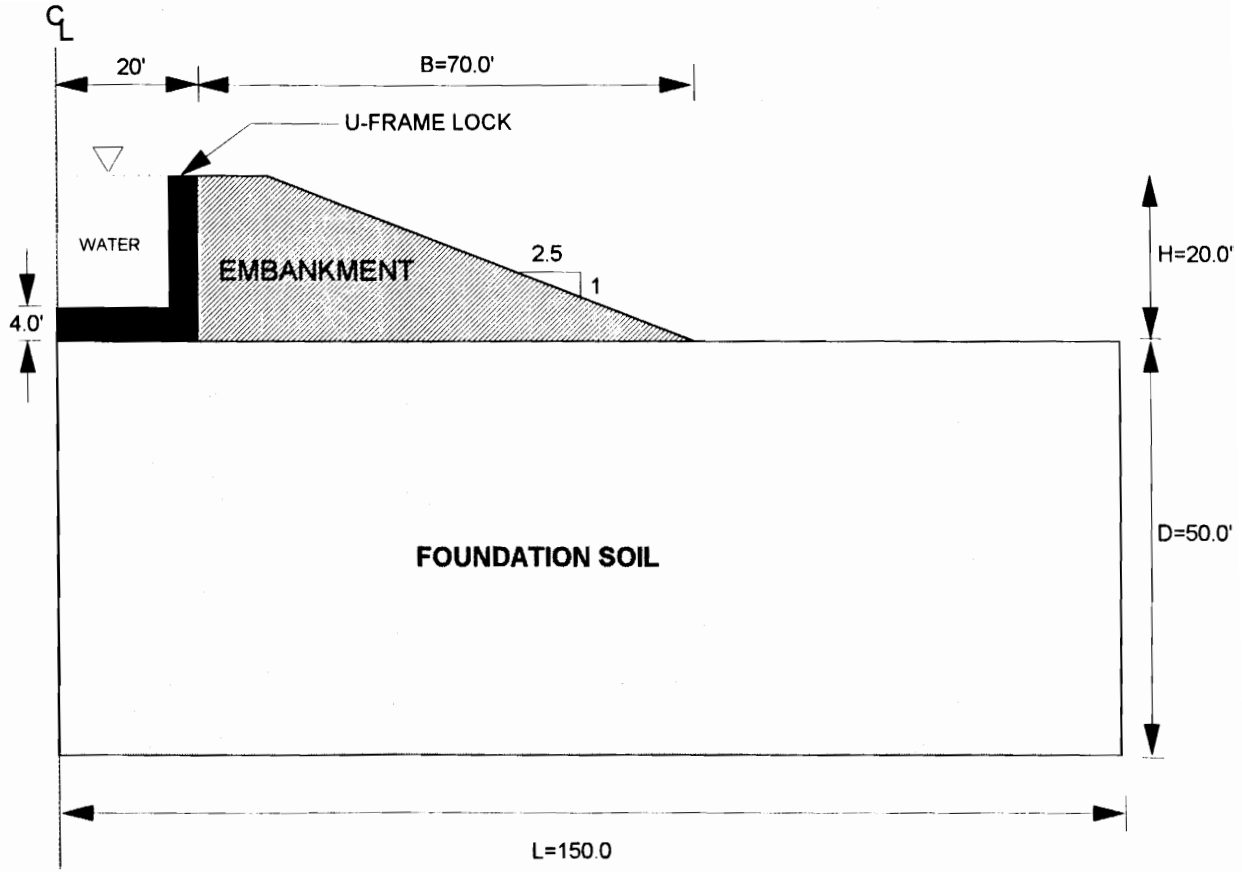

Figure 5.3. U-Frame Lock Problem

Table 5.1
Material Parameters of U-Frame Lock Problem (Linear Case)

Material Property	Soil	Concrete
Young's Modulus, E	4.5×10^7 psf	4.5×10^8 psf
Poison's Ratio, ν	0.2	0.2
Unit Weight, γ	120 pcf	150 pcf

The soil properties for both the foundation soil and the embankment were assumed the same. This problem is similar to that solved by Vallabhan et. al. (1984) in which the embankment was approximated by a series of equivalent nodal loads applied to the surface of the foundation soil and against the lock wall. In this work, the U-frame lock problem was solved using both the finite element method alone and the coupled boundary element-finite element model described in Chapter 3. In Vallabhan's study, it was concluded that the vertical displacements along the surface of the foundation soil obtained using coupled boundary element-finite element method did not significantly differ from those obtained using the finite element method alone.

5.4 One Step Linear Analysis

In the one-step linear analysis, the material behavior of the lock, embankment and soil foundation are assumed to be linearly elastic. The initial stresses in the foundation soil are computed at the centroid of each finite element assuming "at rest" conditions using the relationships:

$$\sigma_{yy} = \gamma y_c \qquad \sigma_{xx} = \frac{\nu}{1-\nu}\sigma_{yy} \qquad \sigma_{zz} = \nu\left(\sigma_{xx} + \sigma_{yy}\right) \qquad \tau_{xy} = 0 \qquad (5.1)$$

where y_c is the vertical distance from the surface of the foundation soil to the centroid of the finite element. All nodal displacements are initially set to zero. The weight of the lock and embankment as well as the hydrostatic pressure exerted by the water inside the lock structure are then converted into equivalent nodal loads and applied in a single load step. The individual stiffness matrices are computed using the corresponding elastic parameters given in table (5.1). The resulting system is solved for the nodal displacements. The stresses corresponding to these displacement are computed and added to the initial stress computed using equation (5.1) to give the final stresses.

To study the effects of the infinite boundary on the solution of the U-frame lock problem, two analysis are performed. In the first analysis, a total of 460 quadrilateral elements are used to model the lock, the embankment and the soil beneath as shown in Figure (5.4). Support conditions in this analysis are assumed fixed along both the bottom and right-handside boundary of the foundation soil. For the second analysis, the coupled BEM-FEM coupling technique is used. The finite element mesh used in the previous analysis is also used in this analysis. In addition, total 36 boundary elements are added along both the bottom and right-handside boundary of the foundation soil to model the infinite boundary as shown in Figure (5.5). Because of the symmetry of the problem, only half of the domain is considered in both analyses. Based on the results of these analyses, the following observations are made:

Vertical Displacements: In analyses performed in section, all vertical displacements are measured relative to a reference point and normalized with respect to the embankment height H. The reference chosen is located along the surface of the foundation at a distance of L=150.0' from the centerline. Figure (5.6) shows the normalized vertical displacements along the centerline of the foundation These normalized displacements are plotted versus the normalized coordinates y/D where y is the distance from the foundation surface and D = 50.0 ft. is the depth of the finite element

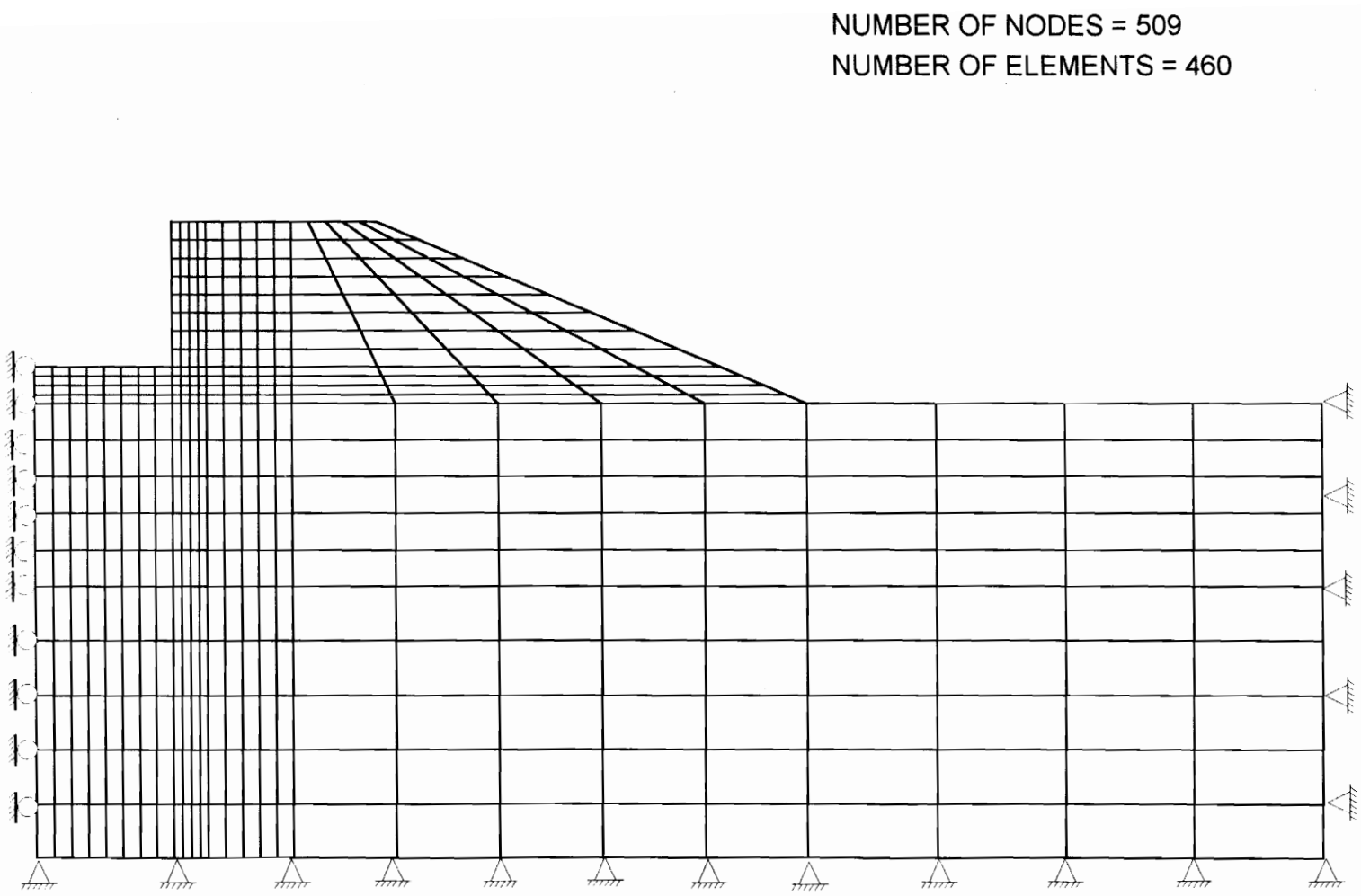

Figure 5.4 Finite Element Mesh used in Linear Analyses

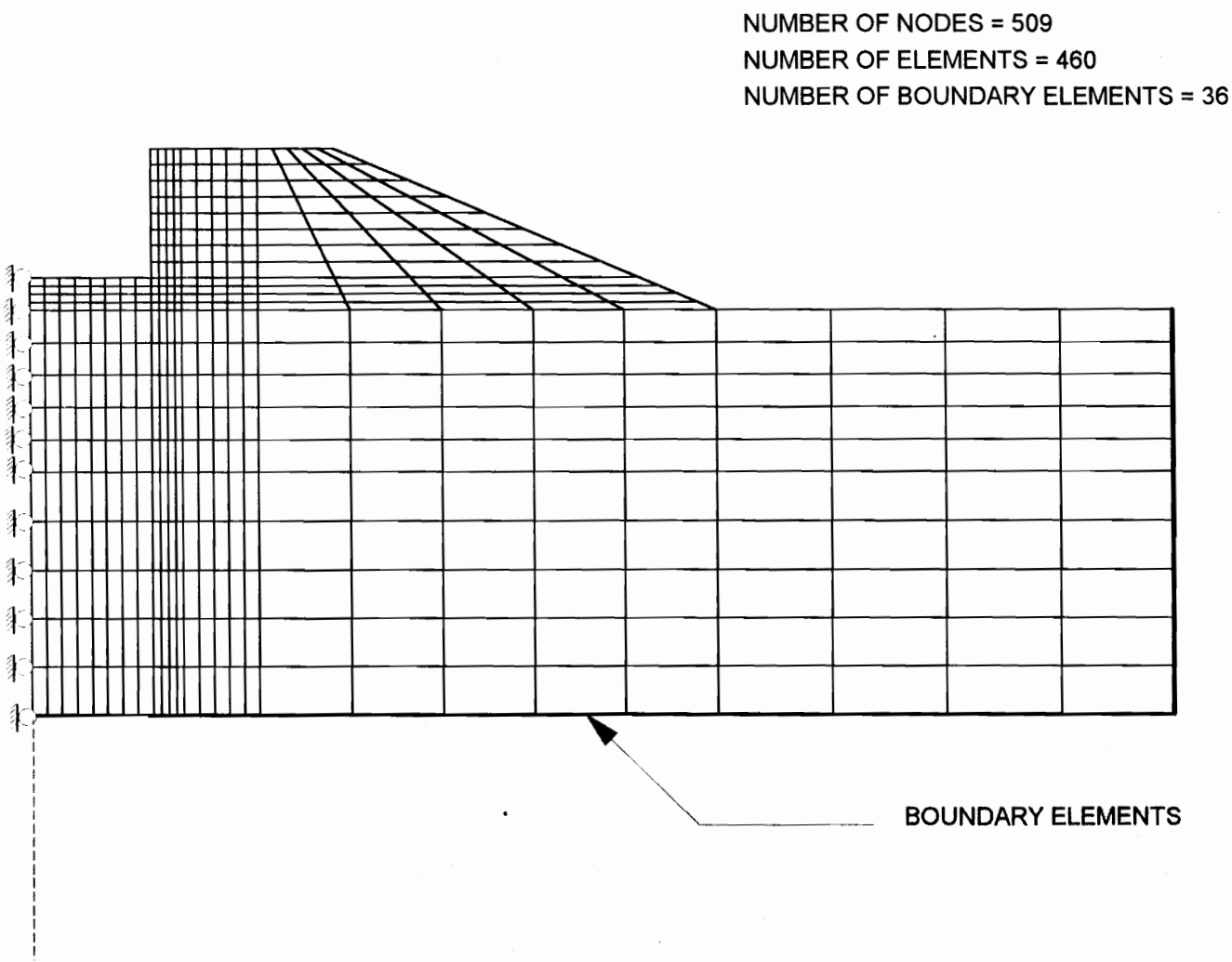

Figure 5.5 Finite Element - Boundary Element Mesh used in Linear Analyses

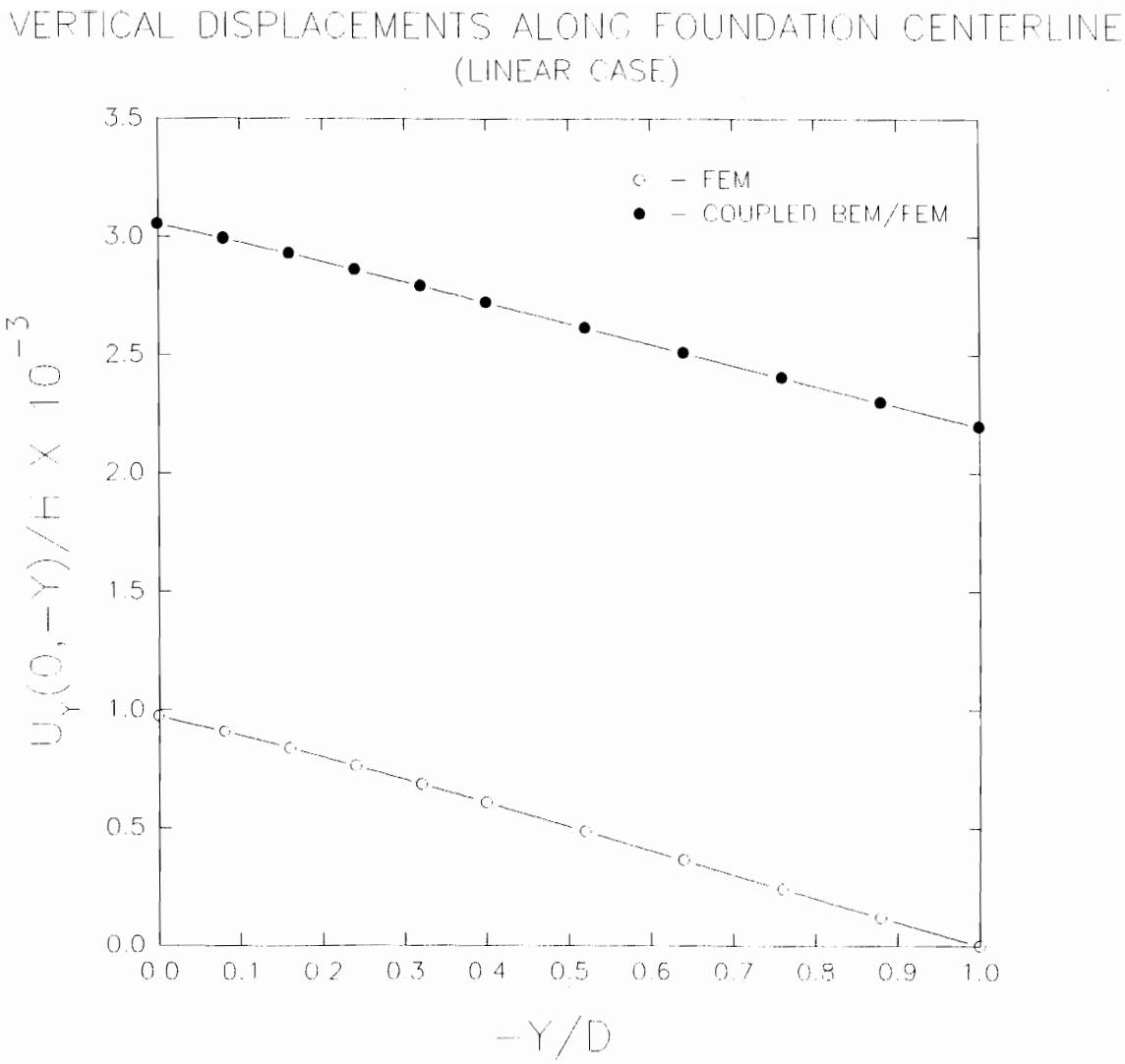

Figure 5.6. Vertical Displacements Along Foundation Centerline (Linear One-Step Analysis).

mesh used. It can be seen from this figure that at the foundation surface, the vertical displacement obtained using the coupled BEM-FEM solution is three times that obtained using only the finite element method. Like the strip footing problem, the disparity between the vertical displacements along the centerline obtained using the two solution procedures is constant.

Figure (5.7) shows the normalized vertical displacements along the foundation surface plotted versus the normalized coordinates x/L where x is the distance along the foundation surface from the centerline. In this figure, the vertical displacements are measured with respect to the point on the foundation surface located a distance L from the centerline. From this figure it can be seen that on the average, the displacements obtained using the coupled BEM-FEM method are three time those obtained using the finite element method alone. The disparity in the vertical displacement obtained using the two solution techniques decreases with increasing values of x/L. This is a result of the choice of reference point used for measuring the displacements. Again this pattern is very similar to that observed in the strip footing problem.

Compared to the strip footing problem, the disparity between the vertical displacements obtained using the two solution technique is very much greater in this problem. This can be attributed to the fact the soil domain considered in this problem is significantly smaller compared to that considered in the strip footing problem. Taking the loaded area to consist of the region beneath the lock and embankment, the loaded area would be 90 ft. long. With a foundation depth of 50 ft., the ratio of the loaded area versus foundation depth would be 1.8:1 which is very much smaller than the ratio of 1:10 used in the strip footing problem.

Lateral Pressures Against Lock Wall: Figure (5.8) shows the variation in the lateral pressure exerted by the embankment on the lock wall. In this figure the lateral pressure is normalized with respect to the quantity γH where γ is the unit weight of the

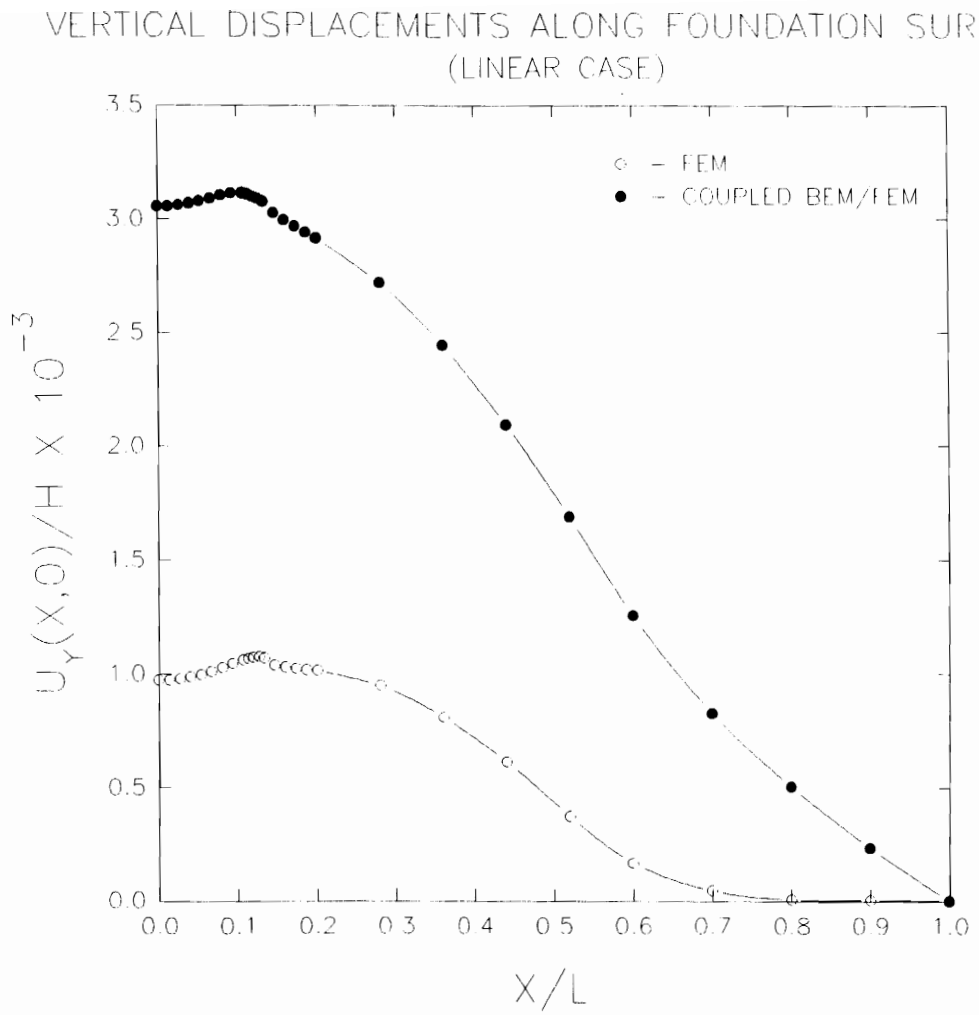

Figure 5.7. Vertical Displacements Along Foundation Surface (Linear One-Step Analysis).

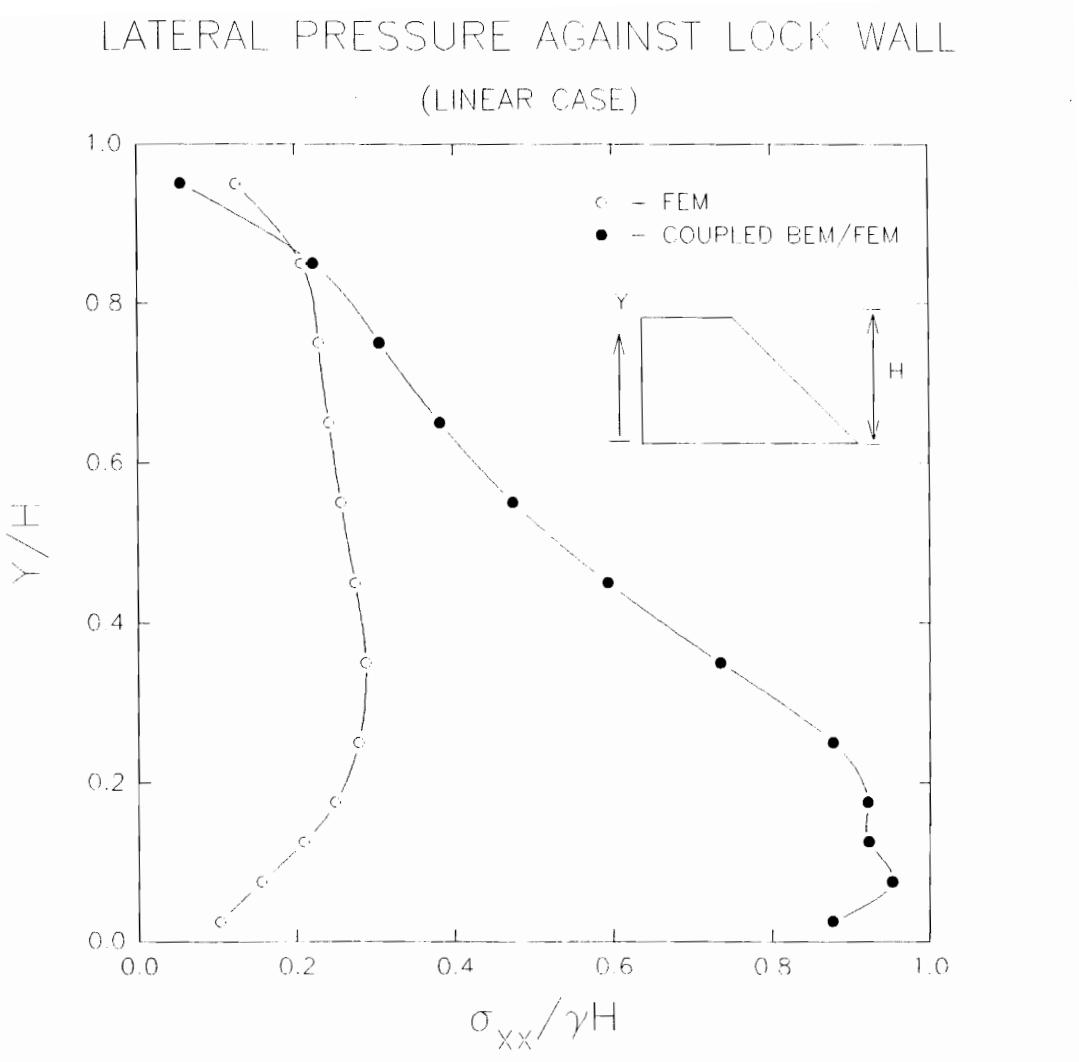

Figure 5.8. Lateral Pressure Against Lock Wall (Linear One Step Analysis).

embankment soil, and H = 20.0 ft is the height of the embankment. The lateral pressures are plotted versus the normalized coordinates Y/H where Y is the vertical distance from the base of the embankment. This figure shows that within 4.0 ft. from the top of the embankment, the lateral pressures predicted using the coupled BEM-FEM method are slightly smaller than those obtained using the finite element method alone. However, beneath this level, the coupled BEM-FEM method gives significantly larger lateral pressures compared to the finite element solution. The disparity between the two solution procedures is largest at the bottom of the embankment where the stresses obtained by the coupled BEM-FEM method are more than three times larger compared to those obtained using the finite element method. This disparity arises due to major differences in the shape of the pressure distribution along the lock wall. In finite element solution, the lateral pressure only increases in the first 4.0 from the top of the embankment. Beyond this point, the lateral pressure remains roughly constant until 4.0 ft from the base of the embankment where the lateral pressure starts to decrease. In comparison, coupled BEM-FEM method, the lateral pressures steadily increase with depth until 4.0 ft from the base of the embankment where the pressures are roughly constant.

Stresses Along Base of Embankment: Figure (5.9) shows the shear stresses along the base of the embankment. In this figure, the shear stresses are normalized with respect to the quantity γH and plotted versus the normalized coordinates x/B where x is the horizontal distance from the heal of the embankment, and B =70.0 ft. is the width of the base of the embankment. From this figure it can be observed that the coupled BEM-FEM method results values of shear stress which are greater than those obtained using the finite element method only. On the average, the shear stresses obtained using the coupled BEM-FEM method are double those obtained using the finite element method alone. However, the manner in which the shear stresses vary along the base of the embankment is

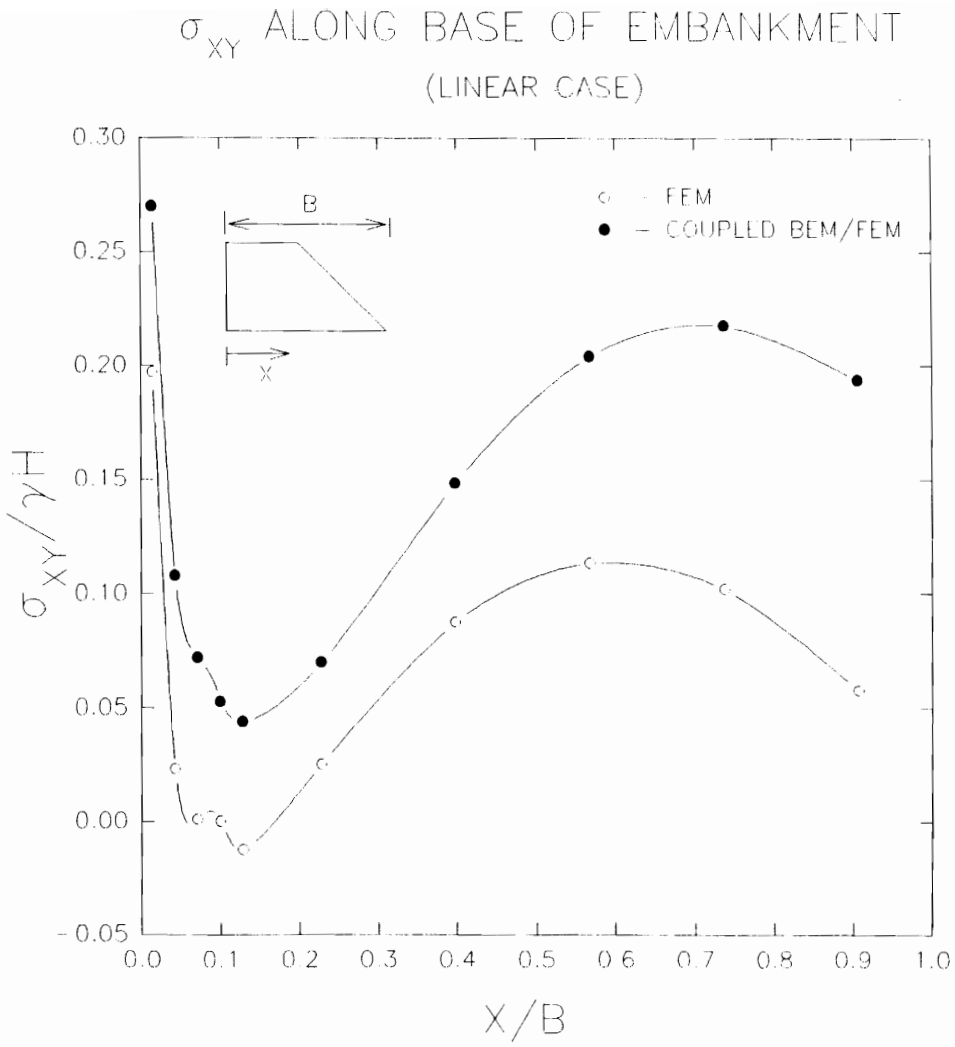

Figure 5.9. σ_{xy} Along Base of Embankment (Linear One-Step Analysis)

similar for both solution procedures. In particular, the occurrence of stress concentration is visible within the proximity of the interface between the lock wall and the embankment

The variation in σ_{yy} along the bottom of the embankment is illustrated in Figure (5.10). In this figure, σ_{yy} is normalized with respect to the quantity γH and plotted versus the normalized coordinates x/B. From this figure it can be seen that within 10 ft. from the interface between the lock wall and embankment corresponding to values of $x/B < 0.15$, the coupled BEM-FEM method results in values of σ_{yy} which on the average are 13% beneath those obtained using the finite element method alone. However, for larger values of x/B, the difference in the values of σ_{yy} obtained using the two solution procedures does not significantly differ.

5.5 Linear Analysis with Construction Simulation

In this section, the analysis of the U-frame lock problem described in previous section is repeated so as to simulate construction of the U-frame lock and embankment. Prior to the analysis, the initial stresses in the foundation are computed using equation (5.1). The construction sequence involves first building the U-frame lock, after which the embankment is incrementally constructed in lifts. Lastly, the lock is filled to capacity with water. The construction of the U-frame lock is performed in a single load step by first assigning properties of fluid concrete to the elements comprising the U-frame lock. In succeeding load steps, these elements are assigned the properties of hardened concrete to simulate the concrete setting. The embankment construction is performed using the "backfill placement" procedure. In this procedure, the elements comprising the embankment are assigned the properties of air. Within each load step, a lift is placed by changing the properties of the elements in that lift from those of air to those of soil. When the elements within each lift are first placed, they are assigned the properties of a dense fluid with a low modulus. In subsequent load steps, these elements are allowed to harden by assigning the modulus for soil to them. Applications of the "backfill placement"

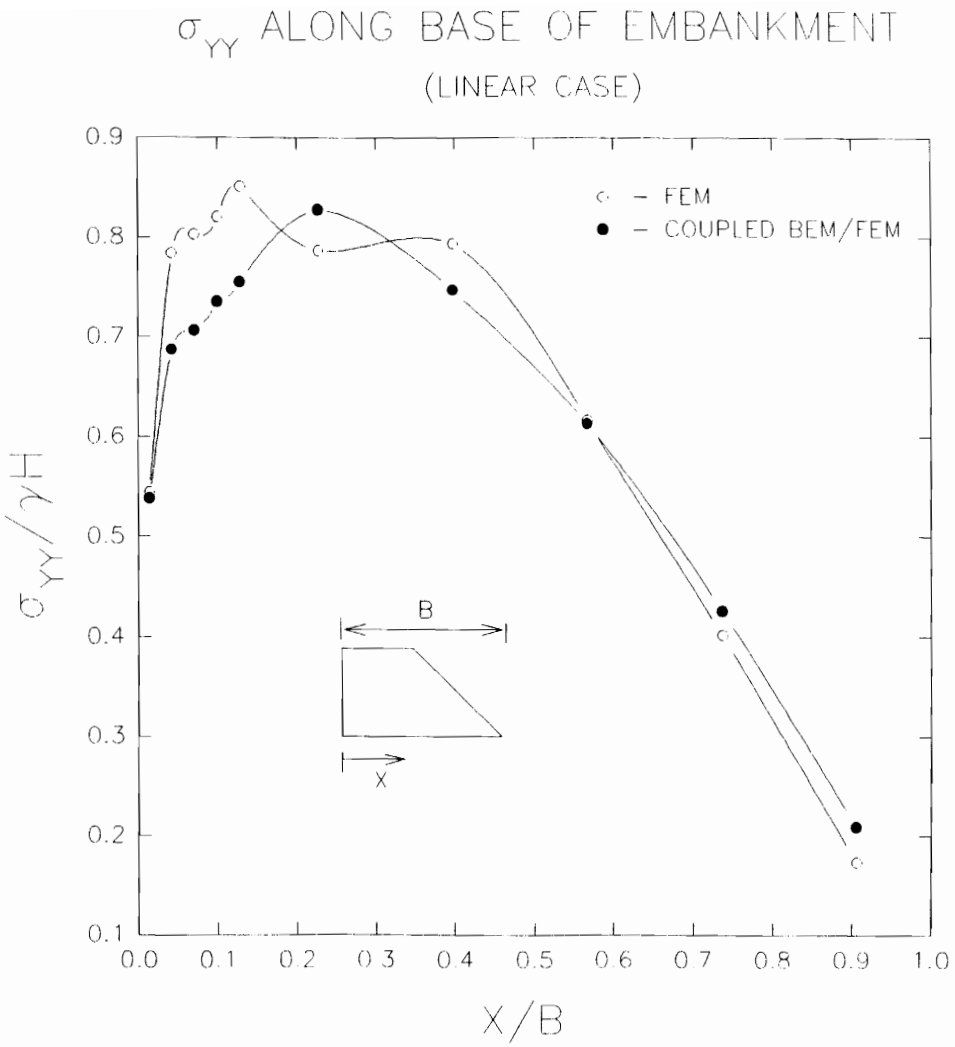

Figure 5.10. σ_{yy} Along Base of Embankment (Linear One-Step Analysis).

procedure to a variety of soil-structure interaction problems have shown the importance of modeling the construction process as closely as possible. Clough and Duncan (1969) showed that to achieve accurate results, a minimum of 8 lifts are required. In the analyses performed in this section, the construction of the embankment was simulated using ten 2-foot thick lifts. The filling of the lock with water is accomplished in the final load step. Altogether, a total of 12 load steps are use in the analyses.

As in the previous section, the effects of the infinite boundary are investigated by conducting two analyses. In the first analysis, the U-frame lock problem is analyzed using the finite element method alone. The problem is also analyzed using the coupled BEM-FEM method. The same set of meshes used in the previous section as illustrated in figures (5.4) and (5.5) are also used the analyses performed in this section. Based on the results of these analyses, the following observations are made:

Vertical Displacements: In analyses performed in section, all vertical displacements are measured relative to a reference point and normalized with respect to the embankment height H. The reference chosen is located along the surface of the foundation at a distance of L=150.0' from the centerline. Figure (5.11) shows the normalized vertical displacements along the centerline of the foundation soil plotted versus the normalized coordinates y/D. From this figure, the vertical displacement of the point y/D = 0.0 obtained using the coupled BEM-FEM method are 3.3 times that obtained using the finite element method alone. The difference in the vertical displacements obtained using the two solution procedures remains constants along the entire centerline.

Figure (5.12) shows the normalized vertical displacements along the foundation surface plotted versus the normalized coordinates x/L. The vertical displacements along the foundation surface obtained using the coupled BEM-FEM method are significantly greater than those obtained using the finite element method alone. This disparity is greatest underneath the lock and embankment where the displacements obtained using the

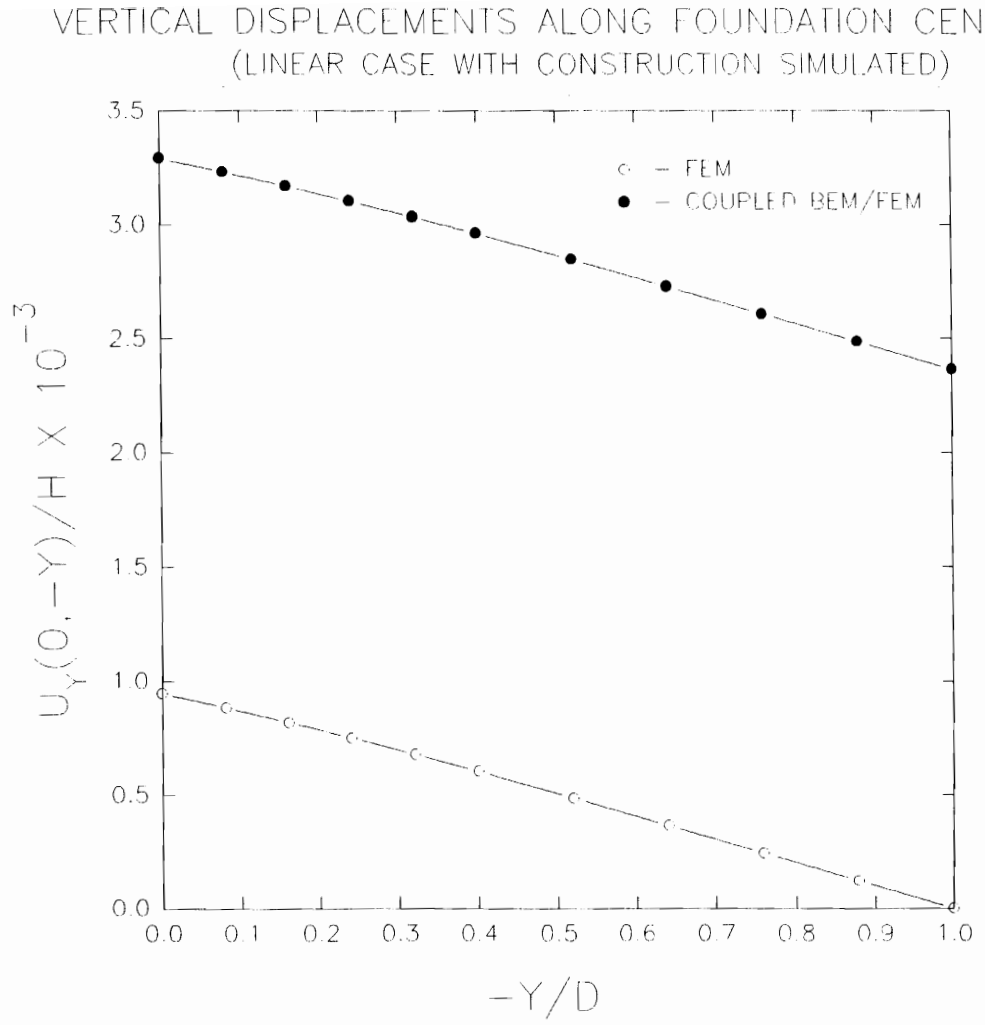

Figure 5.11. Vertical Displacements Along Foundation Centerline (Linear analysis with construction sequence simulation).

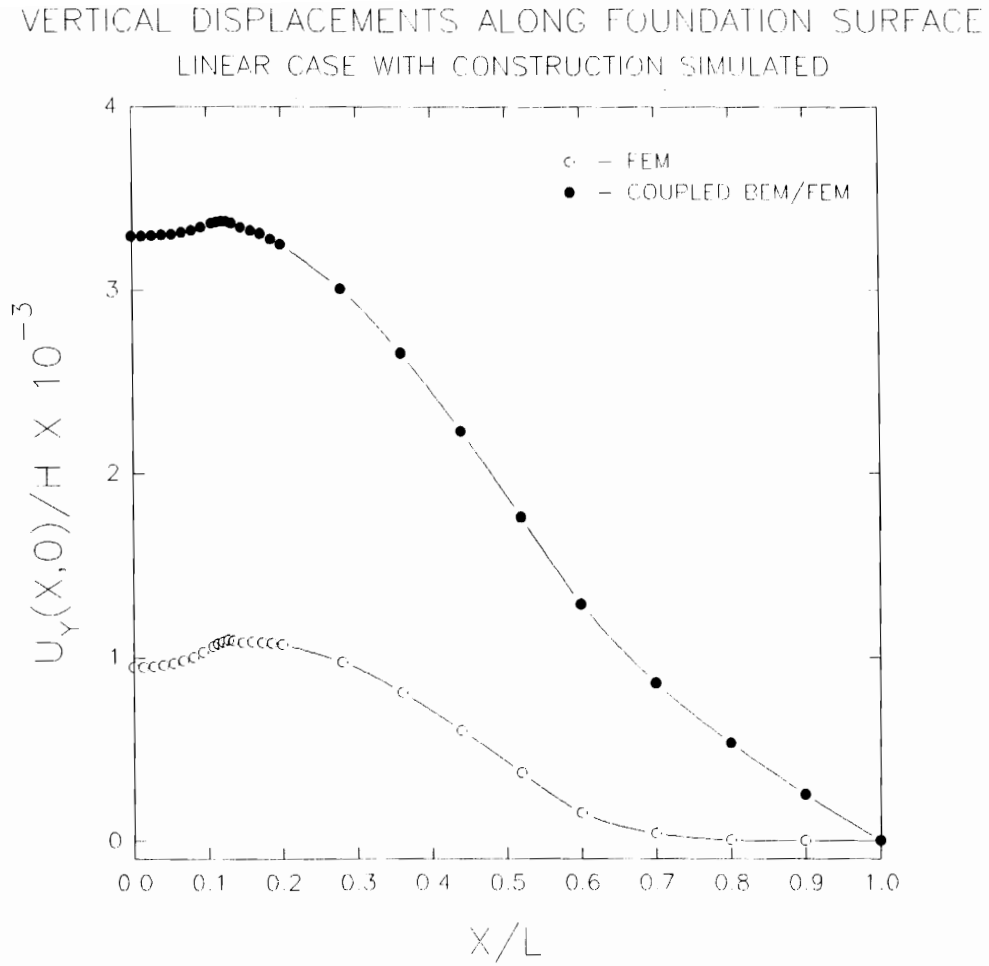

Figure 5.12. Vertical Displacements Along Foundation Surface (Linear analysis with construction sequence simulation).

coupled BEM-FEM method are 3.3 times greater than those obtained using the finite element method alone. As the value of x/L approaches 1.0, the disparity in the vertical displacement obtained using the two methods vanishes. This is due to the fact that all displacements are measured relative to the reference point located at $x/L = 1.0$.

From the above observations, simulation of the construction sequence had no effect on the vertical displacements obtained using the finite element method alone. However, for the coupled BEM-FEM solution, the simulation of the construction sequence resulted in a 10% increase in the vertical displacements obtained. It can also be concluded that the simulation of the construction sequence did not have any significant effect on the manner by which the vertical displacement obtained using the two solution procedures differ as compared to the one-step linear analysis.

Lateral Earth Pressures: Figure (5.13) shows the lateral pressures exerted by the embankment on the lock wall. In this figure, the lateral pressures are normalized with respect the quantity γH and plotted versus the normalized coordinates Y/H. Within the first 5.0 ft. from the top of the embankment corresponding to values of $0.75 \leq Y/H \leq 1.0$, there is very little difference between the lateral pressures compared using the two solution procedures. For values of $Y/H < 0.75$, the coupled BEM-FEM method gives values of lateral pressure which are higher than those obtained using the finite element method alone. The disparity largest near the bottom of the embankment (Y/H=0.025) where the lateral pressures obtained using the coupled BEM-FEM method are 4 times greater than those obtained using the finite element method.

In comparison with the one-step analysis, the lateral pressures obtained with the construction sequence simulated are significantly less for both solution procedures. For the coupled BEM-FEM method, the lateral pressures obtained with the construction sequence simulated are roughly one-third of those obtained in the one-step analysis. For the analysis involving only the finite element method, the lateral pressures obtained with the

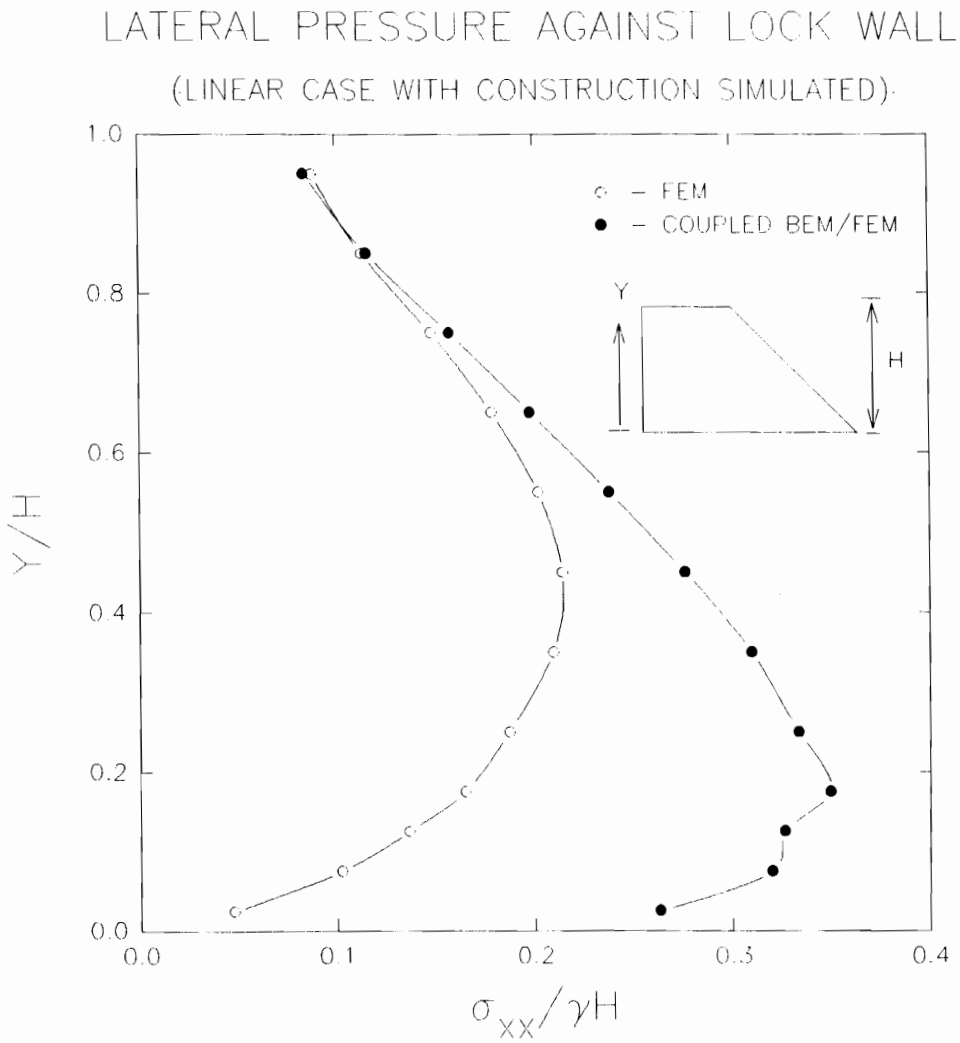

Figure 5.13. Lateral Pressure Against Lock Wall (Linear Analysis with construction sequence simulation).

construction sequence simulated are roughly 50% less of those obtained in the one-step analysis.

Stresses Along Base of Embankment: The shear stresses along the base of the embankment normalized with respect to the quantity γH and plotted versus the normalized coordinates x/B are shown in Figure (5.14). For both solution procedures, the shear stresses are positive for $x/B \leq 0.12$. Within in region, the shear stresses obtain using the coupled BEM-FEM method are on average 15% below those obtained using the finite element method alone. For points along the base of the embankment where $x/B \geq 0.12$, both solution procedures give shear stresses which are negative. Within this region, the coupled BEM-FEM method gives significantly larger values of shear stress as compared to those obtained using the finite element method alone. This difference is most pronounce for $0.35 \leq x/B \leq 0.75$ where the coupled BEM-FEM method gives values which are 30% greater than those obtained from the finite element method.

The normal stress σ_{yy} along the base of the embankment normalized with respect to the quantity γH and plotted versus the normalized coordinates x/B are shown in Figure (5.15). This figure shows that the difference in the values of σ_{yy} obtained using the two solution procedures are at most 2.0%. This is significantly less than the one-step analysis where, as mentioned previously, the difference in the values of σ_{yy} obtained using the two solution procedures was as much as 13.0%.

5.6 Nonlinear Analysis with Construction Simulation.

In the section, the analysis of the U-frame lock problem is repeated with the construction sequence simulated and assuming that the soil behaves according to the hyperbolic stress-strain model described in section 4.7. In addition, interface elements (Goodman, Taylor and Brekke, 1968) are used to allow for relative movement between different material regions. These elements are placed along the interface between the lock and foundation soil, the lock and embankment, and the foundation soil and embankment.

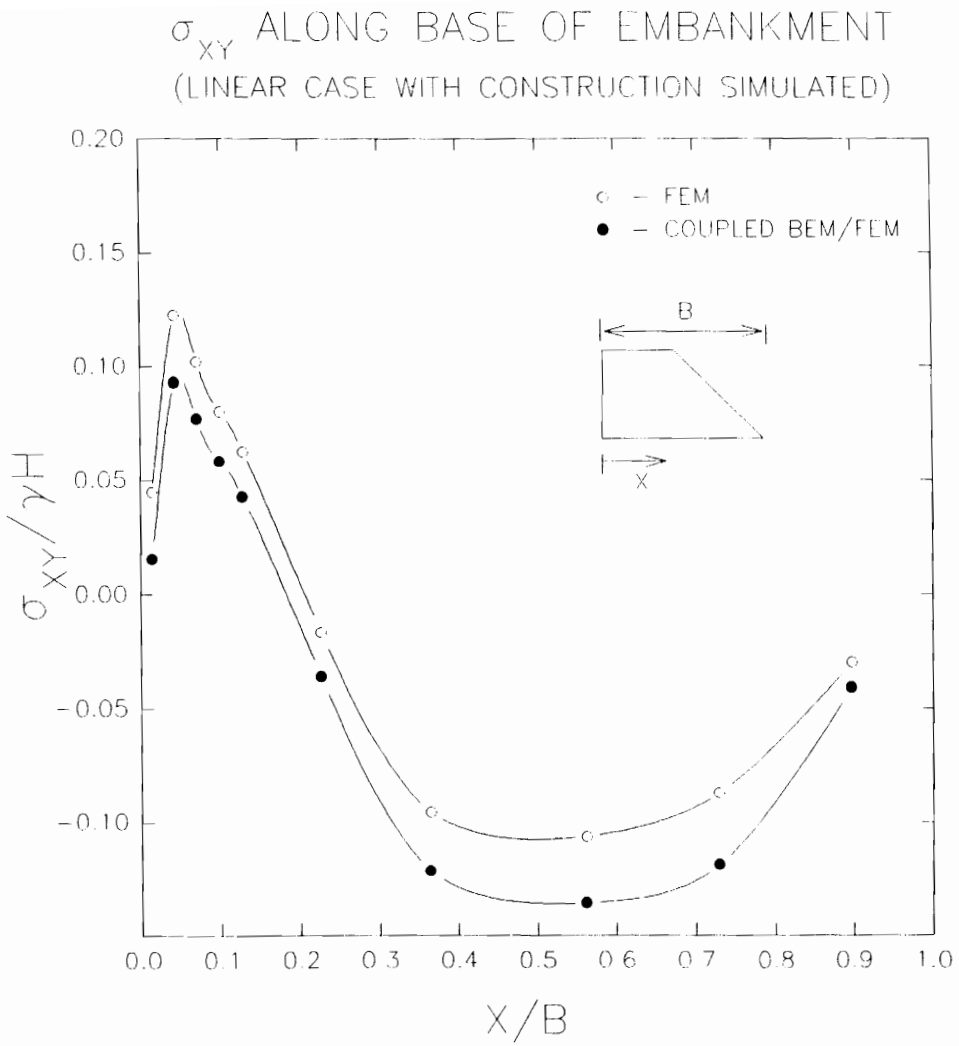

Figure 5.14. σ_{xy} Along Base of Embankment (Linear analysis with construction sequence simulation)

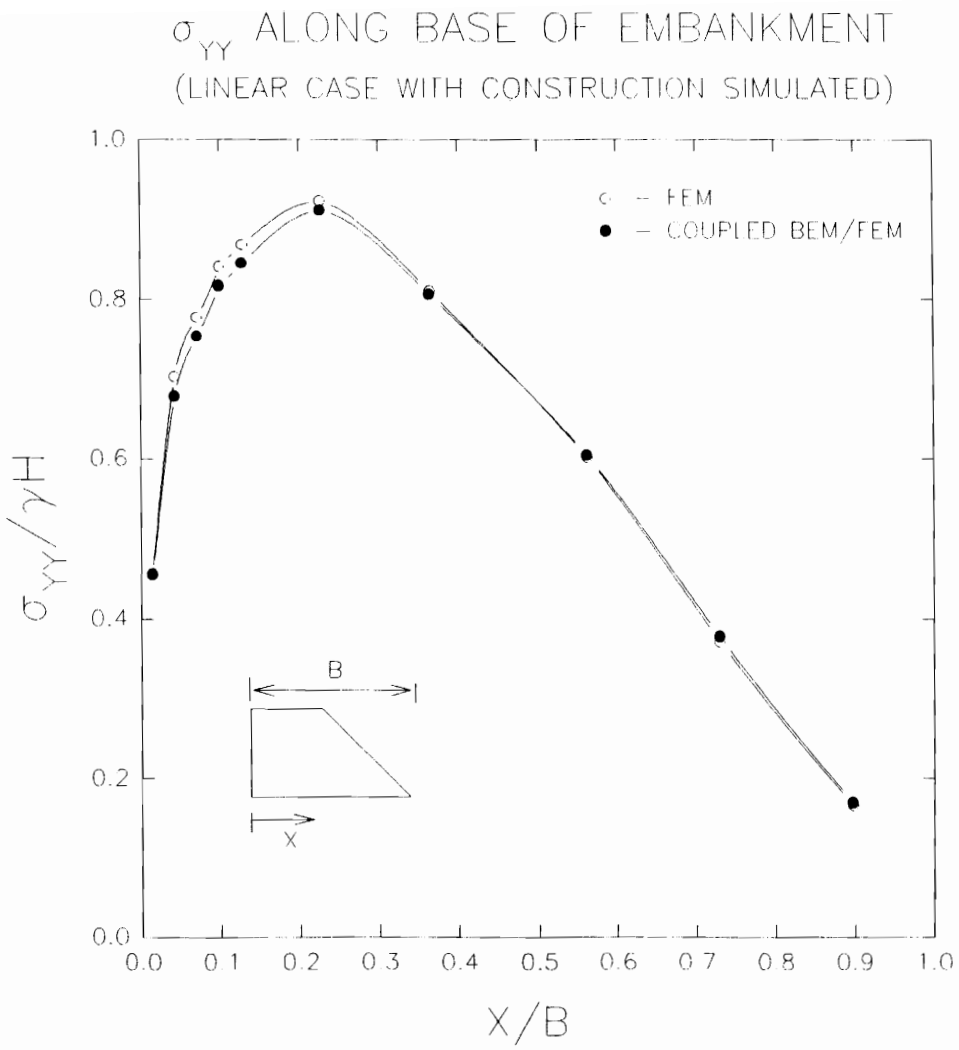

Figure 5.15. σ_{yy} Along Base of Embankment (Linear analysis with construction sequence simulation)

As was done in the previous sections, two analysis are performed. In the first analysis, the U-frame lock problem is solved using only the finite element method. In the second analysis, the same problem is solved using the coupled BEM-FEM method. Figures (5.16) and (5.17) show the mesh used in the first and second analysis respectively. In both meshes, a total of 460 two dimensional elements and 34 interface elements are used. For the mesh used in the coupled BEM-FEM analysis, 36 boundary elements, located along the bottom and right-handside boundary of the boundary, are used. Prior to the analysis, the initial stresses at the centroid of each element in the foundation are computed assuming at rest conditions in the subroutine INITAL. These stresses are used to compute the initial tangent moduli for each element using the hyperbolic model.

The material parameters assumed for the soils in the foundation and embankment are given in table 5.2.

Table 5.2

Material Parameters for soils in U-Frame lock Problem (Non-linear case)

Material Parameter	**Clay**	**Sand**
Modulus number, K	340	300
Modulus exponent, n	0.011	0.5
Failure Ratio, R_f	0.8	0.8
Cohesion Intercept, c	1000 psf	400.0 psf
Friction Angle, ϕ	0.0	37.0°
Unit Weight, γ	125 pcf	125 pcf
Coefficient of lateral earth pressure at rest K_0	1.0	0.5
Poison's Ratio, ν	0.49	0.3

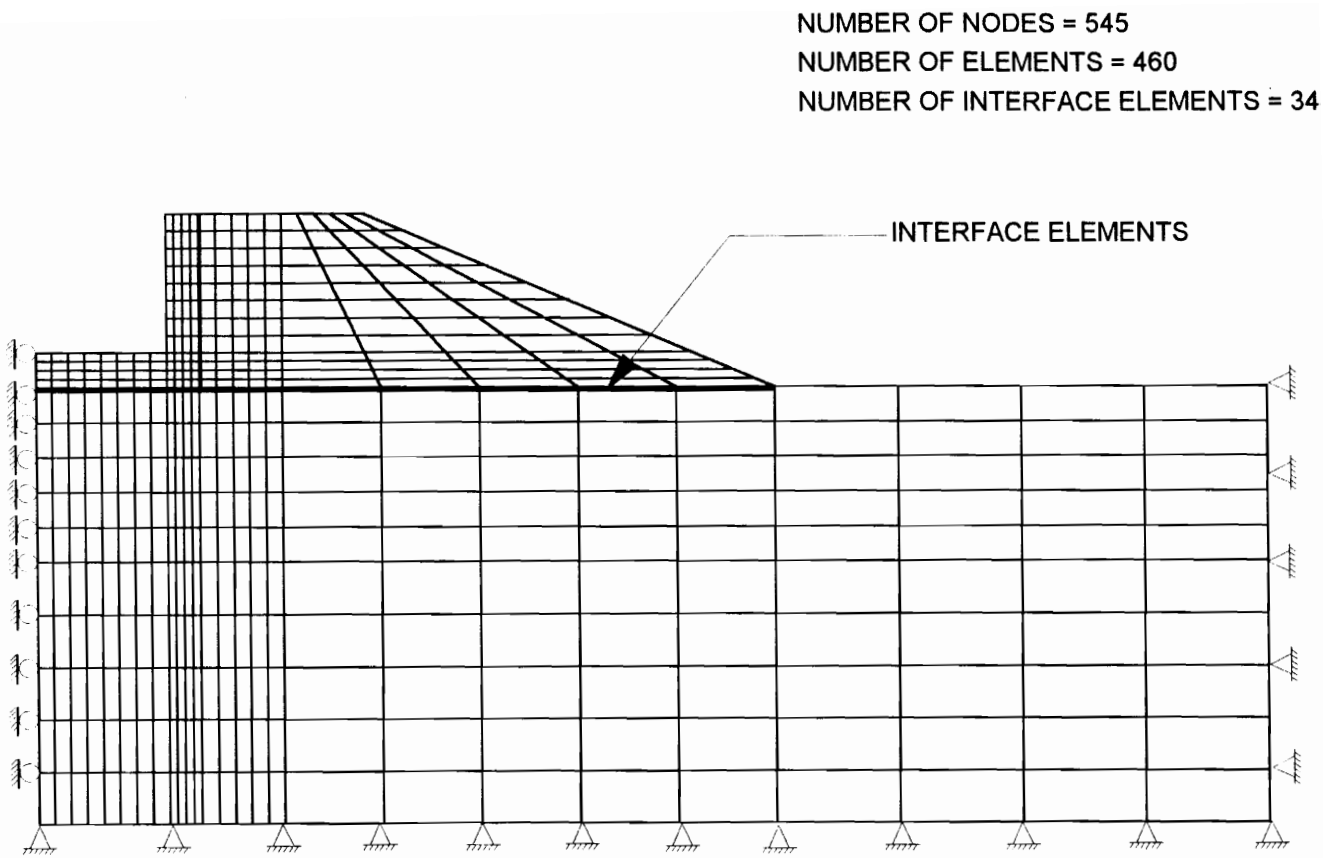

Figure 5.16 Finite Element Mesh with interface elements used in nonlinear analysis.

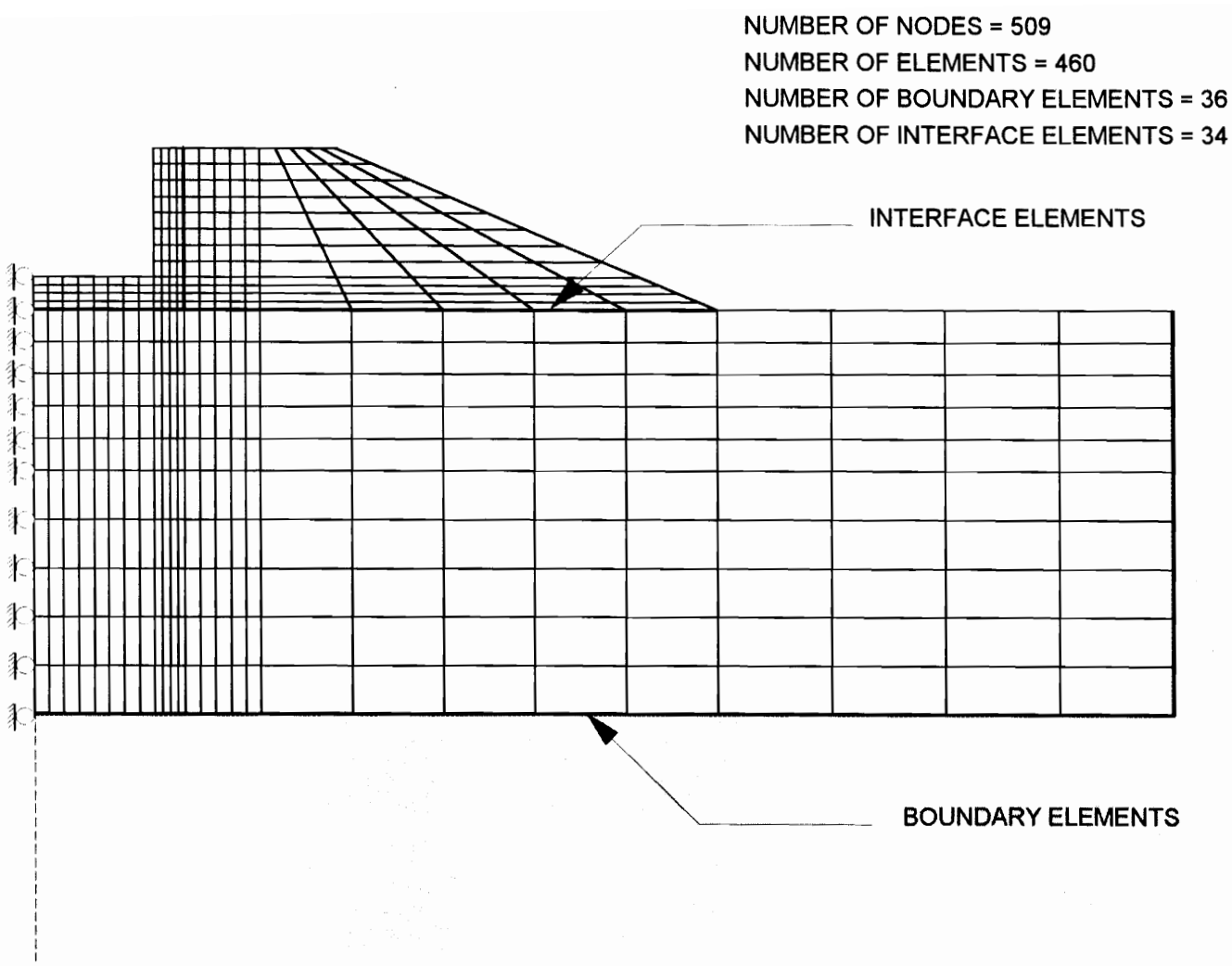

Figure 5.17 Finite Element - Boundary Element Mesh with interface elements used in nonlinear analysis.

The soil in the foundation is assumed to be clay, while the soil in the embankment is assumed to be sand. For the concrete in the lock, $E = 4.5 \times 10^8$ psf, $\nu = 0.2$ and $\gamma = 150.0$ pcf. In the coupled solution, it was assumed that $E = 1.5 \times 10^6$ psf and $\nu = 0.49$. This value of E was approximated by averaging the tangent moduli along bottom boundary of the foundation based on the initial stress analysis. For the interface elements, a bilinear material behavior was assumed.

Table (5.3) gives the material parameters assumed for the interface elements in the U-frame lock problem.

Table 5.3.
Material Parameters for Interface Elements in Nonlinear U-Frame Lock problem

Material Parameter	**Concrete-Clay**	**Concrete - Sand**	**Clay - Sand**
Shear Stiffness, K_s (psf)	36.0×10^3	6.0×10^3	36.0×10^3
Normal Stiffness, K_s (psf)	1.0×10^8	1.0×10^8	1.0×10^8
Minimum Shear Stiffness, K_s (psf)	100.0	100.0	100.0
Minimum Normal Stiffness, K_s (psf)	100.0	100.0	100.0
Cohesion, c (psf)	1000.0	0.0	1000.0
Friction Angle, ϕ (degrees)	0°	17.0°	0°

In this analysis, the construction of the lock and embankment are simulated using the same technique used in the previous section except that the soil moduli of the elements in a lift after placement are computed in succeeding load steps using the hyperbolic model.

Vertical Displacements: In this analysis, all vertical displacements are measured relative to a point on the surface of the foundation located at a distance of L=150.0 ft.

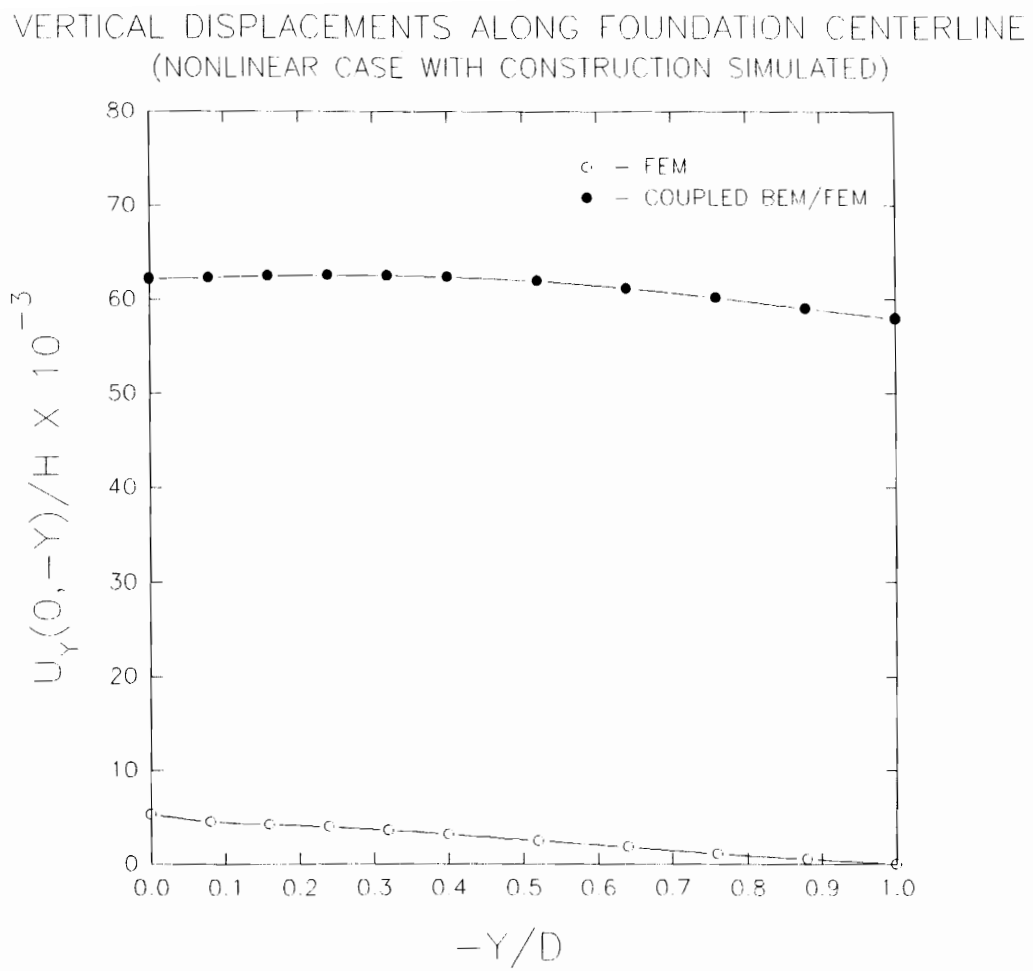

Figure 5.18. Vertical Displacements Along Foundation Centerline (Nonlinear analysis with construction sequence simulation).

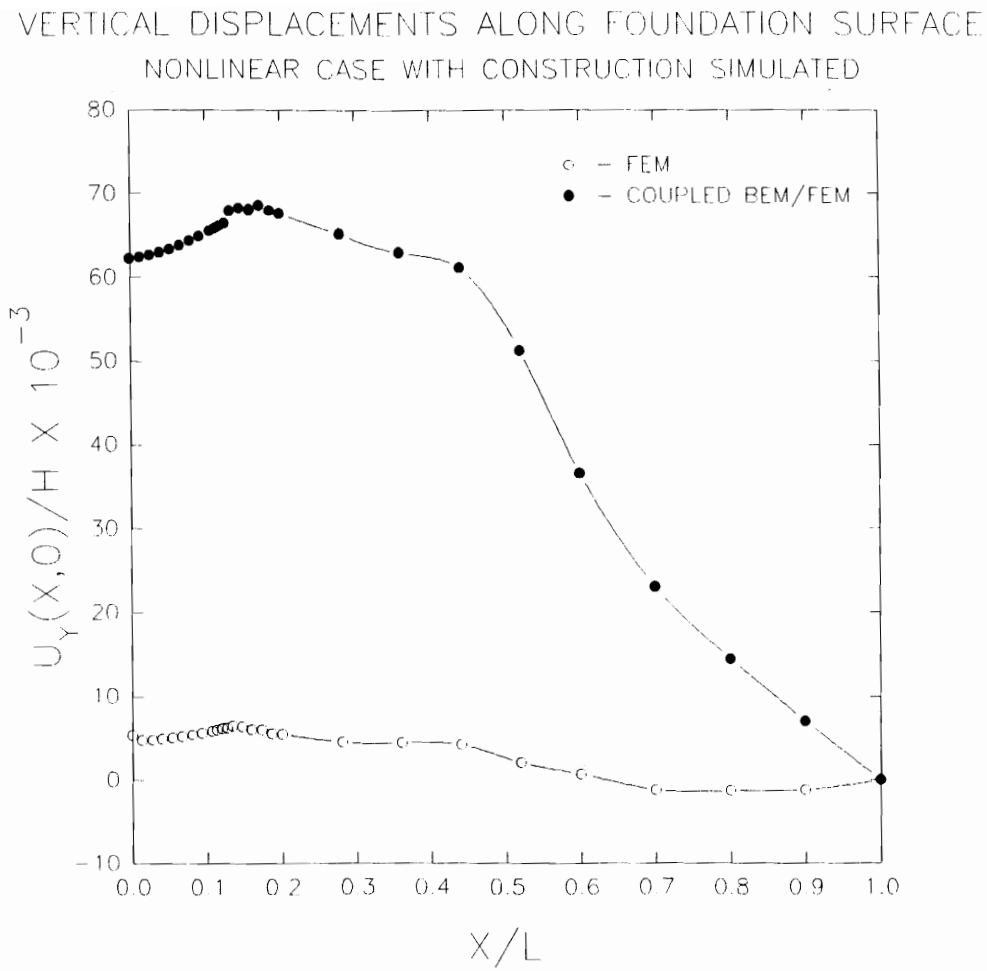

Figure 5.19. Vertical Displacements Along Foundation Surface (Nonlinear analysis with construction sequence simulation).

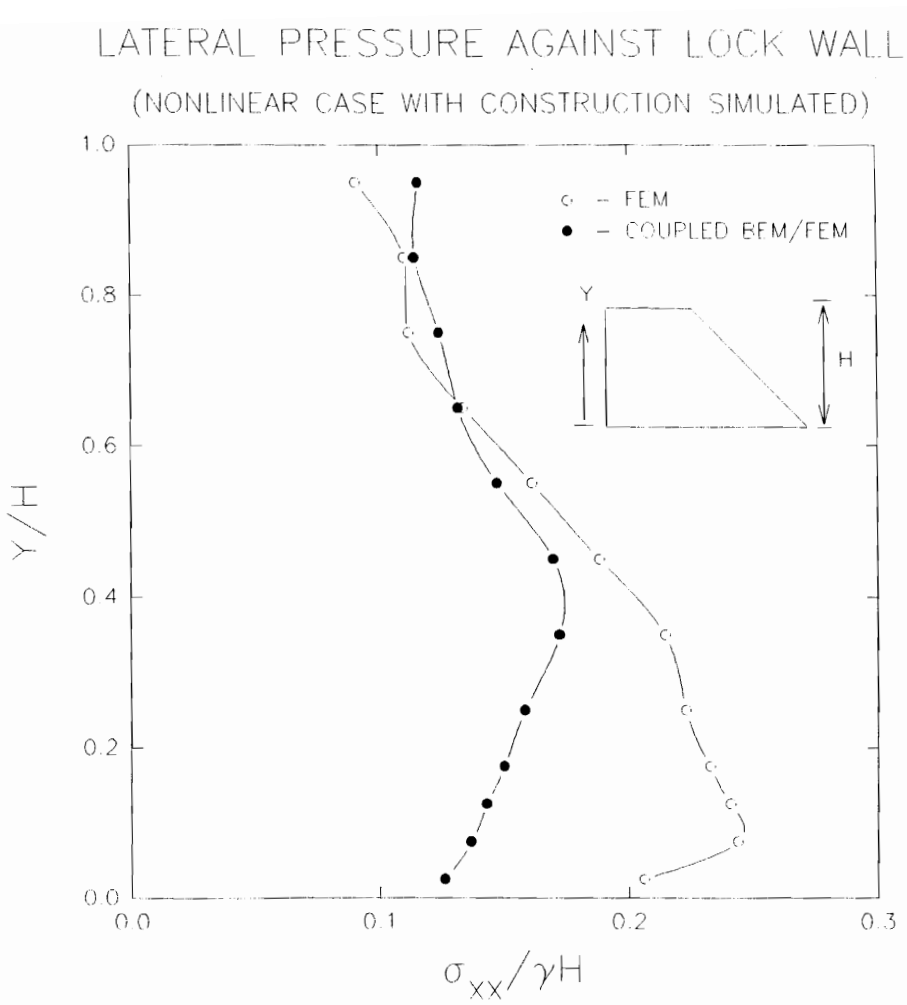

Figure 5.20. Lateral Pressure Against Lock Wall (Nonlinear Analysis with construction sequence simulation).

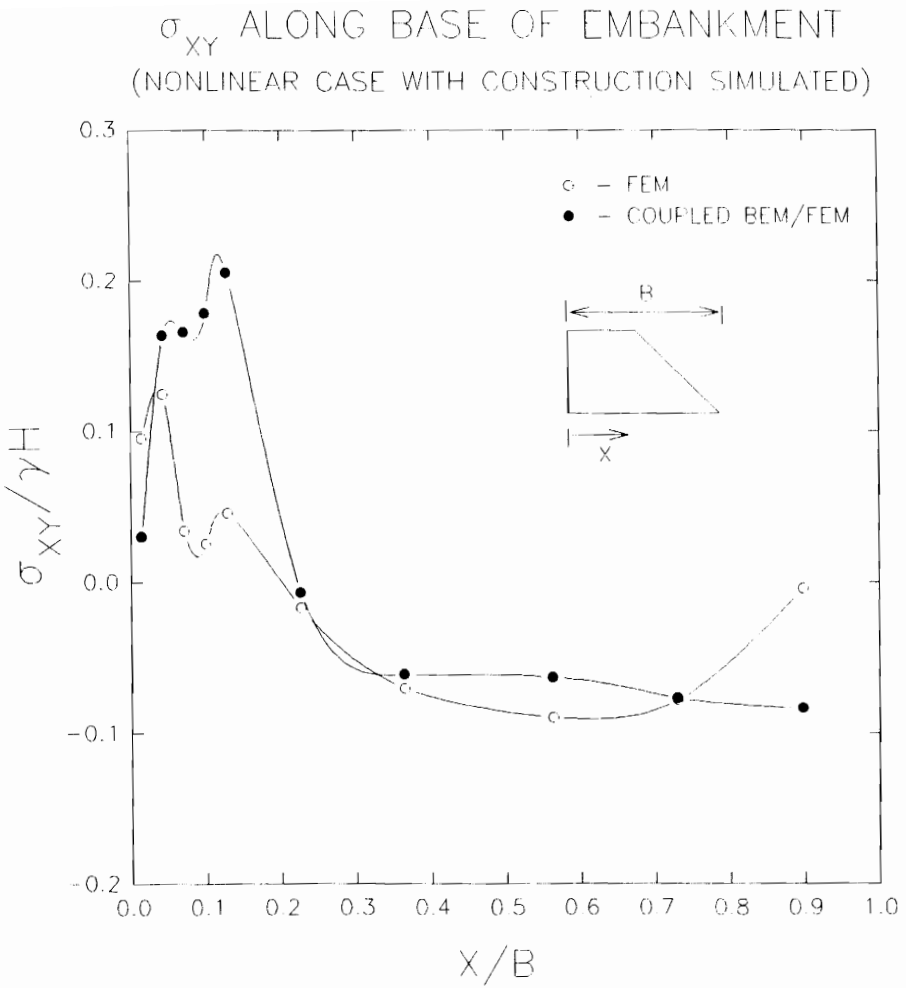

Figure 5.21. σ_{xy} Along Base of Embankment (Nonlinear analysis with construction sequence simulation)

from the centerline. Figure (5.18) shows the vertical displacements along the centerline normalized with respect to the embankment height H and plotted versus the normalized coordinates y/D. This figure shows the vertical displacement at the foundation surface obtained using the coupled BEM-FEM solution to be 10 times the vertical displacement at the same point obtained using the finite element method alone. On the average this disparity is constant along the centerline.

Figure (5.19) shows the vertical displacements along the foundation surface normalized with respect to the embankment height H and plotted versus the normalized coordinates x/L. This figure shows that the vertical displacements obtained using the coupled BEM-FEM method are significantly larger than those obtained using the finite element method only. Specifically, for values of $x/L \leq 0.5$ corresponding to the points beneath the lock and part of the embankment, the displacements obtained using the coupled BEM-FEM are on the average 10 times those obtained using the finite element method alone.

Lateral Earth Pressures: Figure (5.20) shows the lateral pressures exerted by the embankment on the lock wall. In this figure, the pressures are normalized with respect to the quantity γH and plotted versus the normalized coordinates y/H. Within the first 8.0 ft from the top of the embankment corresponding to $0.6 \leq y/H \leq 1.0$, the coupled BEM-FEM solution gives values of lateral pressure which are slightly higher than those obtained using the finite element method alone. Below this level, the lateral pressures obtained using the coupled BEM-FEM method are significantly lower than those obtained using the finite element method. The disparity is greatest for y/H between 0.0 and 0.2 where the lateral pressures from the coupled BEM-FEM method are half those obtained from the finite element method.

Stresses Along the Base of Embankment: Figure (5.21) shows the shear stress distribution along the base of the embankment. In this figure the shear stresses are

normalized versus the quantity γH and plotted versus the normalized coordinates x/B. Within the region near the lock wall corresponding to value of x/B between 0.0 and 0.2, the shear stresses obtained using the coupled BEM-FEM method are significantly larger than those obtained using the finite element method. The largest disparity occurs at x/B = 0.1 where shear stress obtained using the coupled BEM-FEM method is 5 times shear stress obtained from the finite element method. Within this region, both solution procedures give positive values of shear stress. For $x/B \geq 0.2$, both solution procedures give negative values of shear stress. On the average the values of shear stress obtained using the two solution procedures do not significantly differ except for the point x/B = 0.9 where the shear stress obtained using the coupled BEM-FEM method is 10 times the shear stress obtained using the finite element method.

Figure (5.22) shows the variation in the normal stress σ_{yy} along the base of the embankment. Similar to the previous figure, σ_{yy} are normalized with respect to the quantity γH and plotted versus the normalized coordinates σ_{yy}. Along the base of the embankment, the coupled BEM-FEM method gives values of σ_{yy} which are on the average 15% above those obtained using the finite element method. The largest difference in the values of σ_{yy} obtained using the two solution procedures occurs at the point x/B = 0.7 where σ_{yy} obtained from the coupled BEM-FEM method is 30% greater than the value obtained from the finite element method.

5.7 Summary

In this chapter, the proposed substructure method for coupling the boundary element and finite element method was applied to the solution of a U-frame lock problem to investigate the effects of the infinite boundary to the solution of the problem. Three different cases were considered in this chapter namely: one-step linear analysis, linear analysis with construction simulation, and nonlinear analysis with construction simulation and interface elements. In all three cases, two analysis were performed. The first analysis

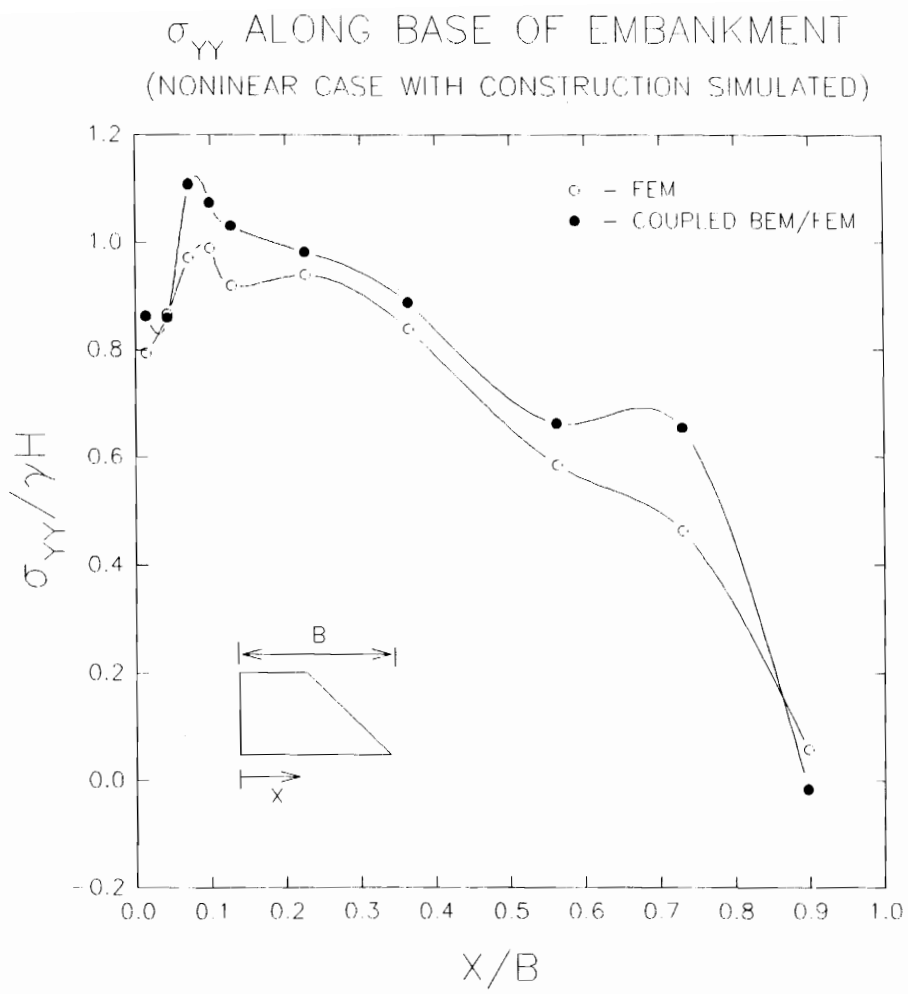

Figure 5.22. σ_{yy} Along Base of Embankment (Nonlinear analysis with construction sequence simulation)

involved solving the problem using only the finite element method. In the second analysis, the problem was solved using the coupled BEM-FEM method to account for the effects of the infinite boundary.

It was observed that infinite boundary had a very significant effect on the vertical displacements obtained. For the linear case, both in the one-step analysis and when the construction sequence was simulated, taking into consideration the effects of the infinite boundary resulted in vertical displacements which were three times those obtained when the infinite boundary was neglected. For the nonlinear case, the disparity was more pronounced. In this case the effects of the infinite boundary resulted in displacements which were ten times greater than those obtained when the infinite boundary was neglected.

For the linear case, both in the one-step analysis and with the construction sequence simulated, the infinite boundary resulted in larger lateral pressures along the lock wall as compared when the infinite boundary was neglected. The difference was greatest near the base of the embankment where the infinite boundary resulted in lateral pressures which were four time those obtained neglecting the infinite boundary. In the nonlinear case, the taking into consideration the infinite boundary resulted in lateral pressures against the lock which were smaller than those obtained neglecting the infinite boundary. In particular, near the base of the embankment, the infinite boundary resulted in lateral pressures which were half those obtained neglecting the infinite boundary.

Similarly, the infinite boundary had significant effects on the shear stresses along the base of the embankment. For the one-step linear analysis, the BEM-FEM method yielded positive shear stresses which at certain points along the base of the embankment were double those obtained using only the finite element method. For the linear case with the construction sequence simulation, the coupled BEM-FEM method yielded positive shear stresses which were 15% less compared to those obtained using the finite element method. For the negative shear stresses, the coupled BEM-FEM method yielded shear

stresses which were double those obtained using the finite element method. In the nonlinear case, the shear stresses obtained using the coupled BEM-FEM solution were as large as five times greater than those obtained using the finite element method.

It was observed that the infinite boundary does not have a very significant effect on the distribution of the normal stress σ_{yy} along the base of the embankment for all cases considered. Based on the results of the analyses, the values of σ_{yy} along the base of the embankment obtained using the two solution procedures differed by at most 15%.

Chapter 6

SOLUTION OF ELASTO-PLASTIC PROBLEMS

6.1 INTRODUCTION

This chapter investigates the effects of the infinite boundary on the finite element solution of elasto-plastic soil-structure interaction problems. The effects of the infinite boundary are incorporated into the solution using the proposed substructure method for coupling the boundary element method to finite element method. Comparisons are made between the displacements and stresses obtained using the coupled boundary element-finite element method with those obtained using the finite element method alone. Problems solved include the bearing capacity of strip footings on elasto-plastic soils and the Rankine earth pressure problem.

6.2 BEARING CAPACITY OF STRIP FOOTINGS

In this section, the analysis of the strip footing problem presented in chapter 4 is repeated here assuming the soil behaves as an elastic-perfectly plastic material. The non-associated Drucker-Prager model presented in chapter 3 is used to describe the plastic behavior of the soil at yielding. The Drucker-Prager strength parameters α and κ are obtained from Mohr-Coulomb strength parameters c and ϕ using the relationships:

$$\alpha = \frac{2\sin\phi}{\sqrt{3}(3-\sin\phi)} \tag{6.1}$$

(6.2)

The elastic properties assigned to the soil prior to yielding are chosen to be E = 600 ksf and $\nu = 0.3$. The strength parameters c and ϕ, and consequently α and κ, as well

as the unit weight of the soil γ_m are varied so as to investigate their effects on the solution. In this study, three different cases are considered namely: (a) weightless soil with cohesion, (b) weightless soil with cohesion and friction, and (c) soil with cohesion, friction and self weight.

The soil domain is modeled using a 50 ft. × 50 ft. finite domain. A uniformly distributed load of magnitude w is applied to the surface over a half-width of a = 5.0 ft. To study the effects of the infinite boundary on the finite element solution of the problem, two analyses are performed for each case. In the first analysis, the effects of the infinite boundary are neglected and the problem is solved using only the finite element method. In the second analysis, the effects of the infinite boundary are modeled using boundary elements based on the Melan fundamental solution. In this analysis, the proposed substructure method is used to couple the boundary element method with the finite element method. Figure (6.1) illustrates the mesh consisting of 100 four-node quadrilateral elements used in all analyses involving only the finite element method. This figure also shows the support conditions assumed along the side and bottom boundaries. Figure (6.2) illustrates the mesh used in the coupled boundary element finite element solution. In addition to the 100 four-node quadrilateral elements used, 20 linear boundary elements are added to the right-handside and bottom boundary to model the effects of the infinite boundary.

6.3 PROBLEM 1: Weightless Soils with $\phi = 0$.

In this problem, the soil is assumed to be both weightless (γ_m = 0.0) and frictionless (ϕ = 0.0°) with a cohesion of c = 1.0 kips/ft^2. The uniformly distributed load, w, is applied in increments of Δw = 1.0 kips/ft^2 until w = 4.0 kips/ft^2 After this point, load increments of Δw = 0.2 kips/ft^2 are applied until w = 5.0 kips/ft^2, after which w is increased in increments of Δw = 0.05 kips/ft^2 until bearing failure occurrs at w/c = 5.2 in

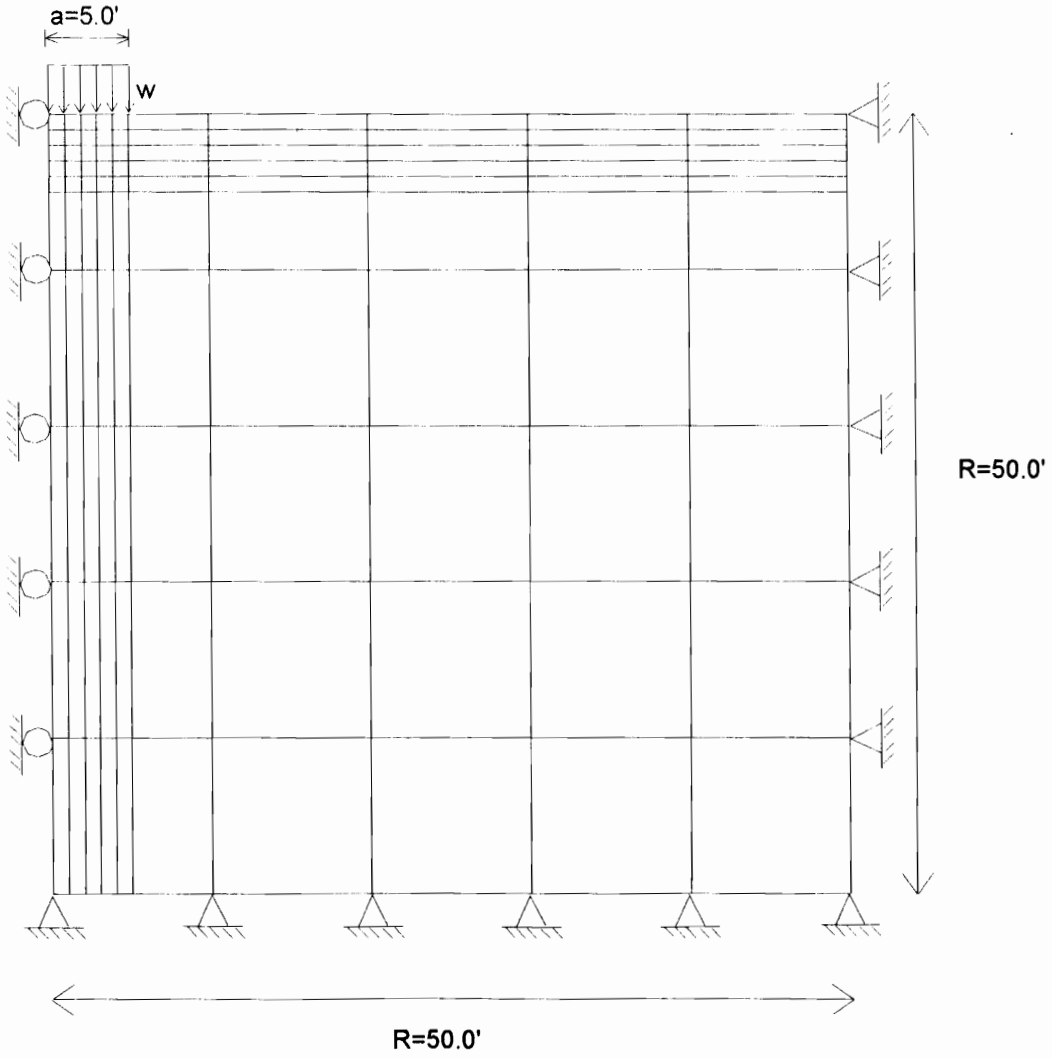

Figure 6.1. Finite element mesh for elasto-plastic footing problem.

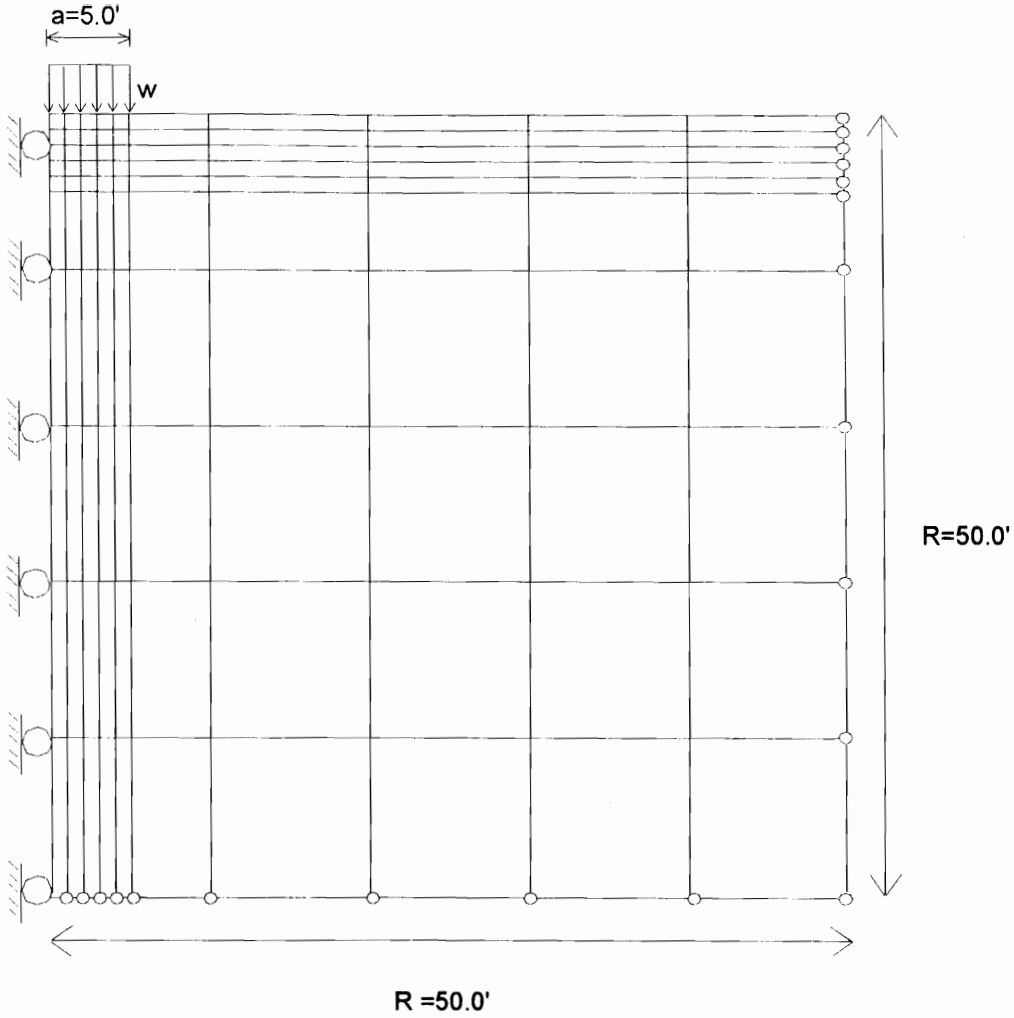

Figure 6.2. Coupled finite element - boundary element mesh for elasto-plastic footing problem.

both the finite element solution and the coupled BEM-FEM method. An error tolerance in the residual norm of $\varepsilon_{tol} = 10^{-5}$ is adopted. Failure is said to have occurred when the residual norm $\|\mathbf{R}\| \geq \varepsilon_{tol}$ after 25 iterations. With $\phi = 0°$, the Drucker-Prager yield condition simplifies to the Von-Mises yield condition and theoretical limit load to this problem is given by Prandtl (1921) as:

$$w / c = 5.14 \tag{6.3}$$

Figure (6.3) shows the normalized load (w/c) plotted versus the normalized vertical displacement at point A measured relative to point B on the surface at a distance $R = 50.0$ ft. from the centerline. This figure shows that the soil in the foundation is elastic in both the finite element solution as well as the coupled BEM-FEM method until $w/c = 3.0$. Within this level of loading, while the behavior of the soil is still elastic, the coupled BEM-FEM method gives displacements which are consistently 20% greater than those obtained using the finite element method only. For values of w/c greater than 3.0, yielding in the soil begins to occur in both solutions. During the initial stages of yielding, when w/c is between 4.0 and 4.4, the displacements obtained from the finite element solution increase at a much faster rate as compared to the coupled BEM-FEM method. Because of this, the disparity in the vertical displacement between the two solution procedures becomes smaller. In particular, at $w/c = 4.2$, the displacement obtained at point A from the finite element method is 5% greater as compared to that obtained using the coupled BEM-FEM method. For values of w/c greater than 4.4, the displacements obtained using the coupled BEM-FEM method increase at a much faster rate as compared to the finite element solution. As this happens, the disparity in the displacements obtained using the two solution technique increases. Both solutions fail to converge after $w/c = 5.2$. At this point the vertical displacement at point A obtained using the coupled BEM-FEM method is 20% greater than that obtained using the finite element method alone.

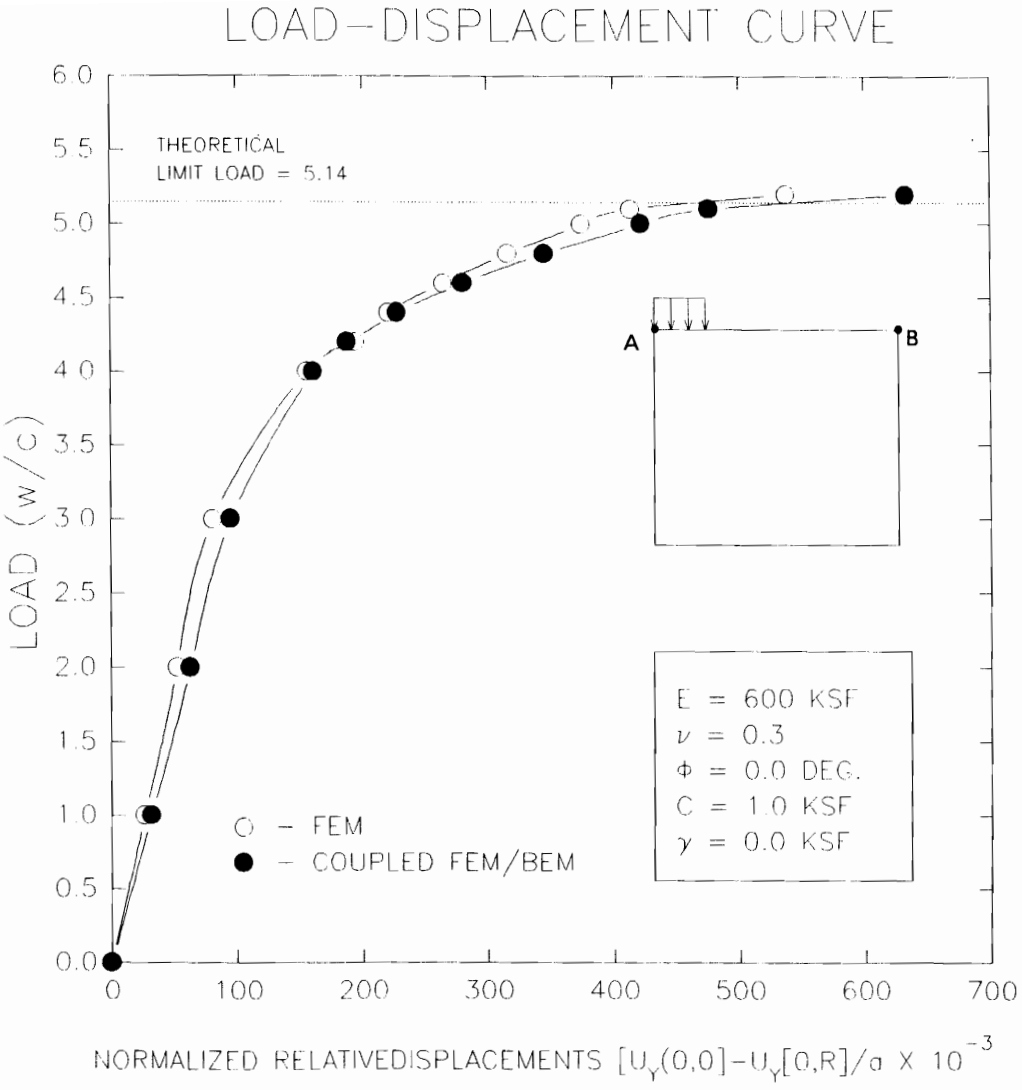

Figure 6.3. Load-Displacement Curve for elasto-plastic footing problem 1.

Vertical Displacements at *w/c* = 4.0: Figure (6.4) shows the vertical displacements along the centerline of the soil mass plotted versus the normalized coordinates *Y/R*, where R = 50.0 is the depth and height of the soil domain. The vertical displacements are measured relative to the point B as described in Figure (6.3) and normalized with respect to the footing half-width a = 5.0 ft. This figure shows that the variation in the vertical displacement along the centerline in the elasto-plastic case is significantly different from that observed in the purely elastic case described in chapter 4. In the elastic case, it is observed that the vertical displacements varied linearly with depth. In the elasto-plastic case, the vertical displacement vary nonlinearly along the centerline. This is particularly evident for values of $-Y/R < 0.4$ corresponding to points near the surface. This can be attributed to the occurrence of large displacements resulting from the plastic yielding of the element within this region in addition to the elastic displacements. For points corresponding to values of $-Y/R \geq 0.4$, the variation in the vertical displacements along the centerline with depth becomes more linear due to the fact that no yielding has yet taken place in this region and the displacements are solely due the elastic deformation of the elements in this region.

Throughout the entire centerline, the coupled BEM-FEM method gives larger vertical displacements as compared to the finite element solution. For points corresponding to values of $-Y/R < 0.4$, the difference between the displacement obtained using the two solution procedures varies by at most 8%. However, for points beneath this level, the displacements resulting from the coupled BEM-FEM method are significantly larger compared to those obtained using the finite element method. A difference of as large as 100% occurs at $-Y/R = 1.0$.

Figure (6.5) shows the vertical displacement along the surface of the soil domain plotted versus the normalized coordinates *X/R*. This figure shows that along the surface,

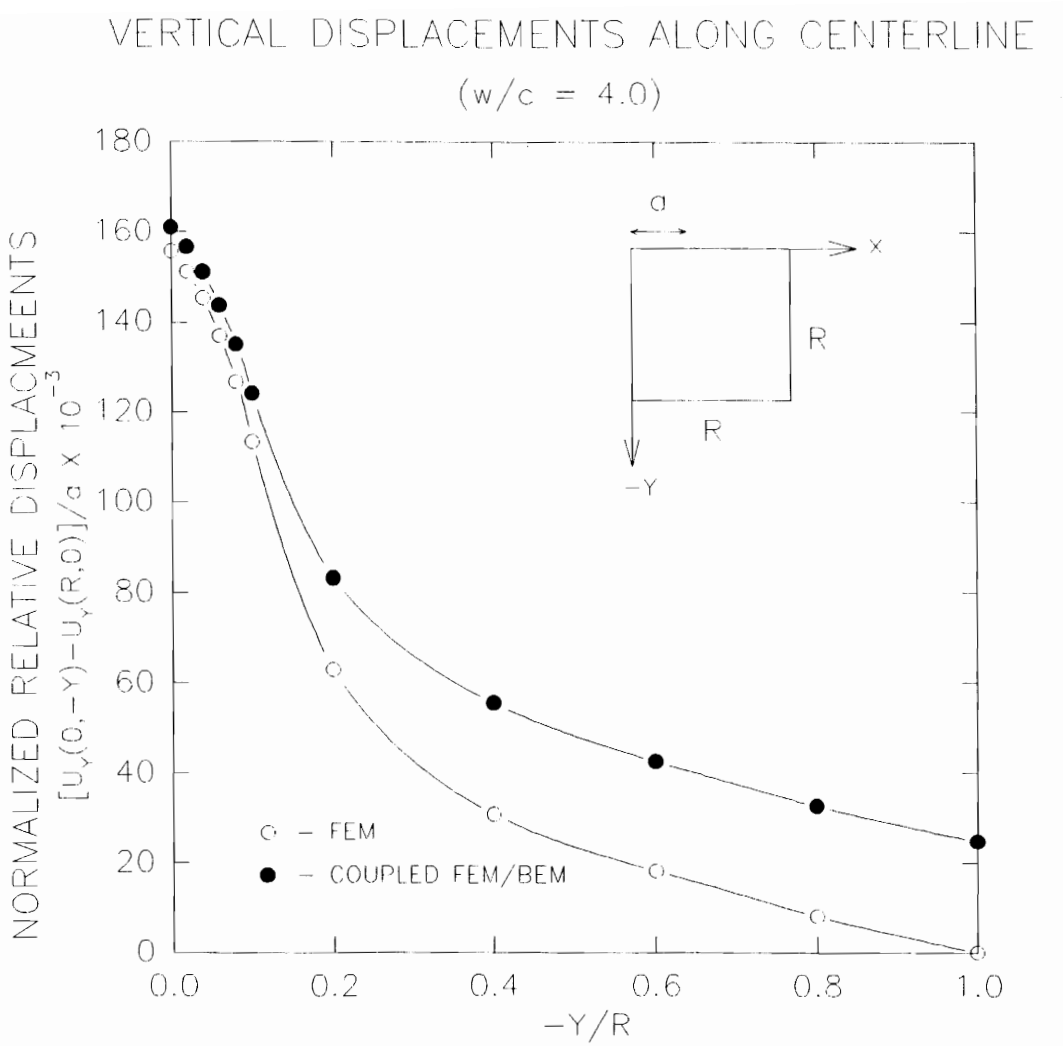

Figure 6.4. Vertical displacements along centerline with w/c = 4.0 for elasto-plastic footing problem 1.

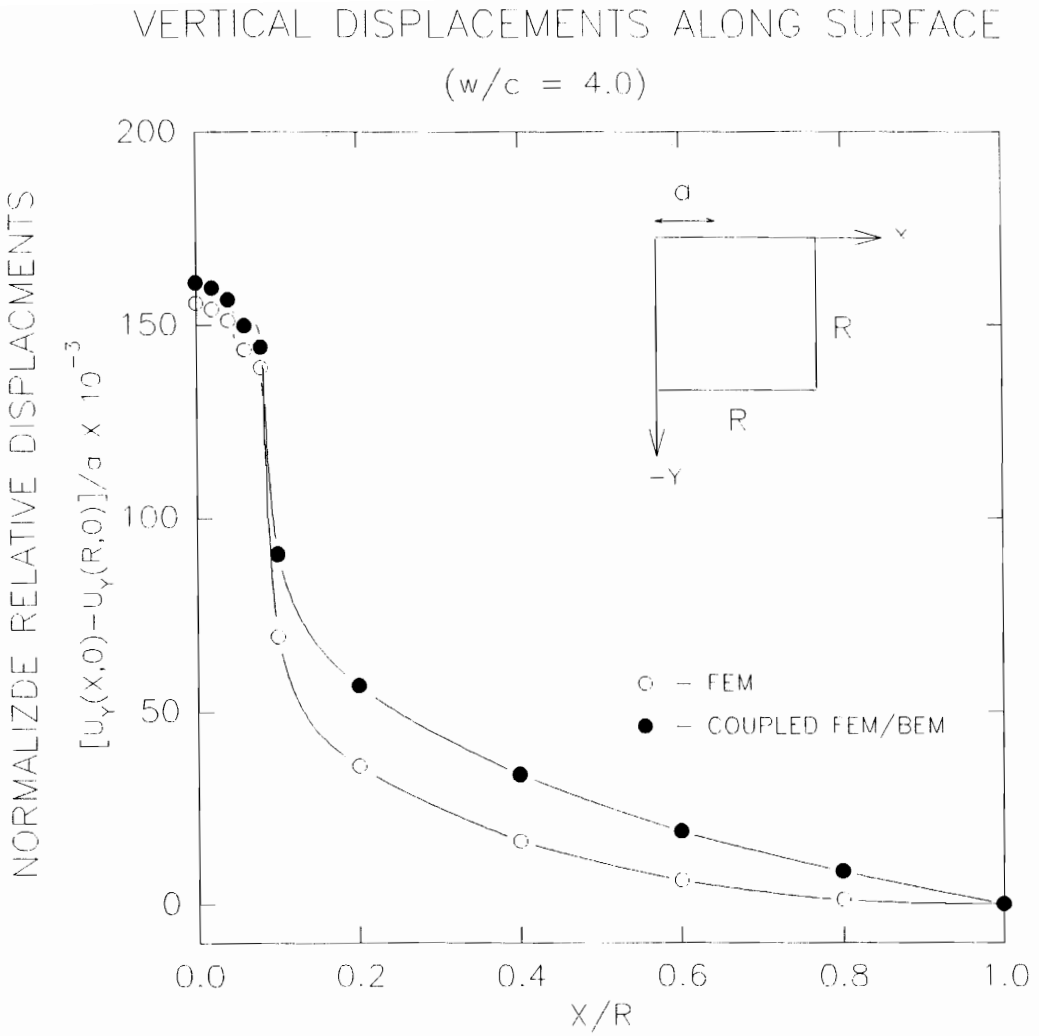

Figure 6.5. Vertical displacements along surface with w/c = 4.0 for elasto-plastic footing problem 1.

the coupled BEM-FEM method results in larger displacements as compared to the finite element method. Underneath the footing corresponding to values of $X/R \leq 0.1$, the difference in displacements obtained using the two solution procedure is at most 8%. Compared to the vertical displacements for larger values of X/R, the vertical displacement underneath and within the proximity of the footing are significantly larger as compared to those corresponding to points distant from the footing. These larger displacements are a result of the plastic yielding which occurs within this region in addition to the elastic deformation.

For values of $X/R > 0.1$, the coupled BEM-FEM method resulting in significantly larger displacements as compared to the finite element solution. This disparity in the vertical displacements is greatest at $X/R = 0.4$ where the displacements obtained using the coupled BEM-FEM method are 40% greater than those obtained using the finite element method. As the value of X/R approaches 1.0, the difference in the displacement obtained using the two solution procedures vanishes. This is due to the fact that the point located at which $X/R = 1.0$ is used as a reference for measuring all vertical displacements. Thus, as points closer to $X/R = 1.0$ are considered, the vertical displacements in both solution procedures approaches zero.

Stresses Along Diagonal Elements at *w/c* = 4.0: Figure (6.6) shows the difference in σ_{xx} for elements lying along the diagonal of the mesh plotted versus the normalized coordinates X/R. Within the proximity of the footing corresponding to value of $X/R < 0.2$, the difference in the values of σ_{xx} obtained using the two solution techniques is within 5%. However for values of $X/R \geq 0.2$, the difference in the value of σ_{xx} obtained using the two solution procedures ranges between 10% at $X/R = 0.3$ to 28% at $X/R = 0.7$.

Figure (6.7) shows the difference in σ_{xy} for elements lying along the diagonal of the mesh plotted versus the normalized coordinates X/R. For values of $X/R \leq 0.3$, the

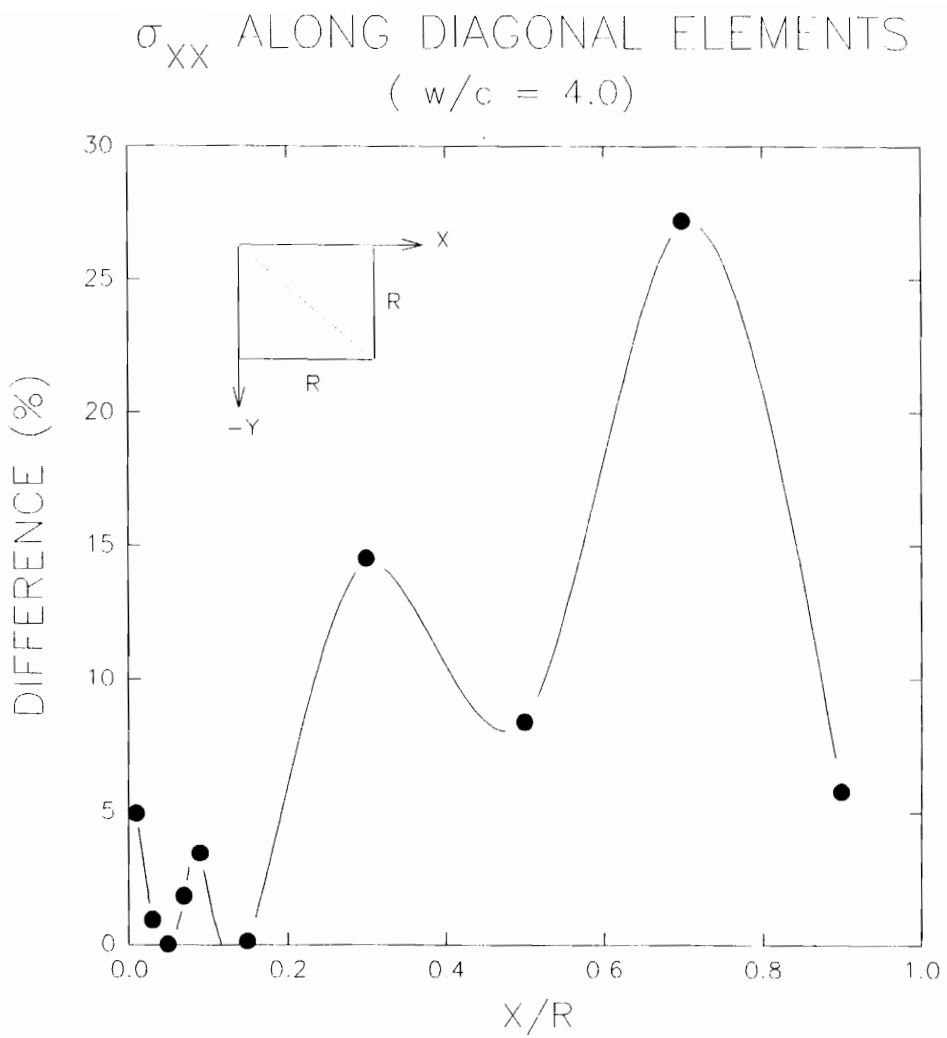

Figure 6.6. σ_{xx} along diagonal elements with w/c = 4.0 for elasto-plastic footing problem 1.

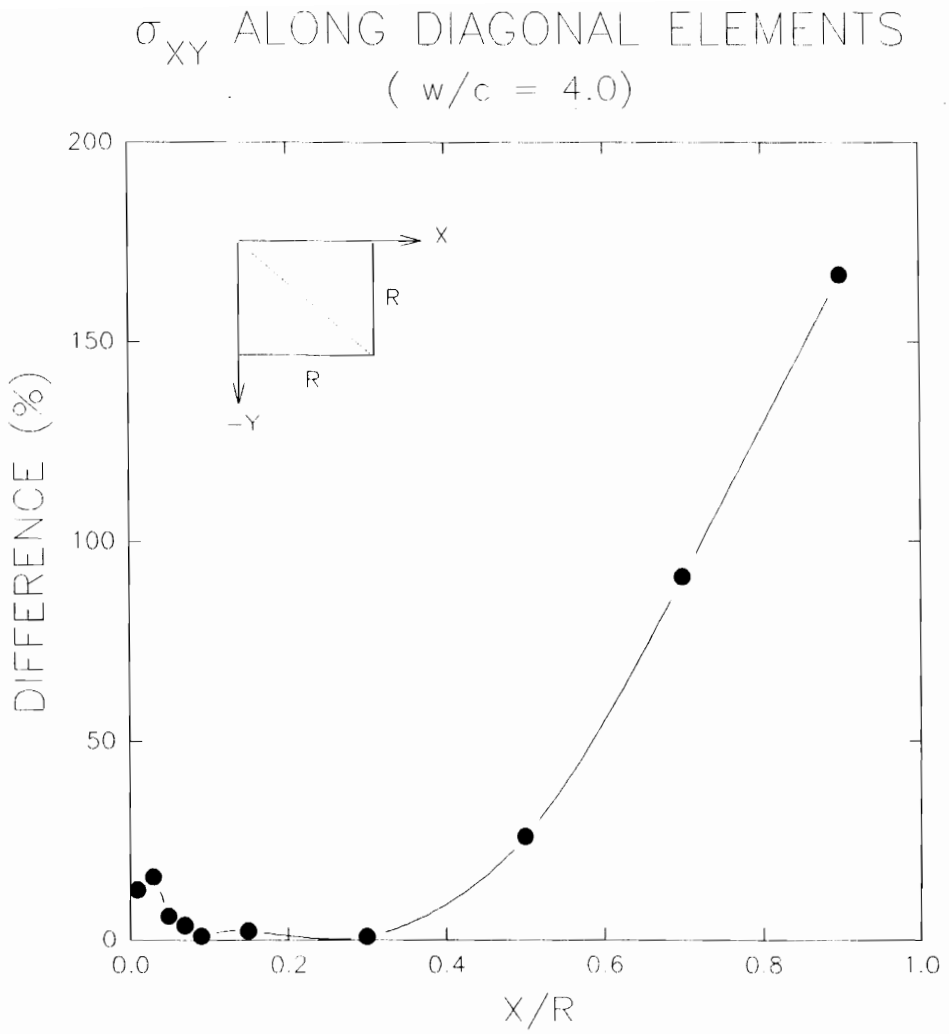

Figure 6.7. σ_{xy} along diagonal elements with w/c = 4.0 for elasto-plastic footing problem 1.

difference in the values of σ_{xy} obtained using the two solution techniques is within 10%. However for values of $X/R > 0.3$, the difference in the value of σ_{xx} obtained using the two solution procedures is significantly larger and steadily increases from 25% at $X/R = 0.5$ to 170% at $X/R = 0.9$.

Figure (6.8) shows the difference in σ_{yy} for elements lying along the diagonal of the mesh plotted versus the normalized coordinates X/R. With the exception of $X/R = 0.9$, the difference in σ_{yy} obtained between the two solution procedures is within 10%. At X/R, the difference is 19%.

Vertical Displacements at *w/c* = 5.2: Figure (6.9) shows the vertical displacement along the centerline of the soil mass plotted versus the normalized coordinates Y/R. The vertical displacements are measured relative to the point B as described in Figure (6.3) and normalized with respect to the footing half-width $a = 5.0$ ft. This figures show that the vertical displacements obtained using the coupled BEM-FEM method are greater than those obtained using the finite element along the entire centerline. With respect to the magnitude, the difference in the vertical displacements obtained using the two solution procedures is largest at the surface ($-Y/R=0.0$) where the displacement obtained using the coupled BEM-FEM solution is 20% greater as compared to that obtained using the finite element method only. For points corresponding to $-Y/R \leq 0.2$, the coupled BEM-FEM method gives displacements which are on the average 25% greater than those obtained using the finite element method alone. For increasing values of $-Y/R$, the magnitude of the difference in the displacement along the centerline obtained using the two solution procedures decreases until $-Y/R = 0.6$ after which the difference remains constant indicating elastic behavior for values of $-Y/R \geq 0.6$. This pattern is very different from that observed for $w/c = 4.0$ where the magnitude of the difference in the vertical

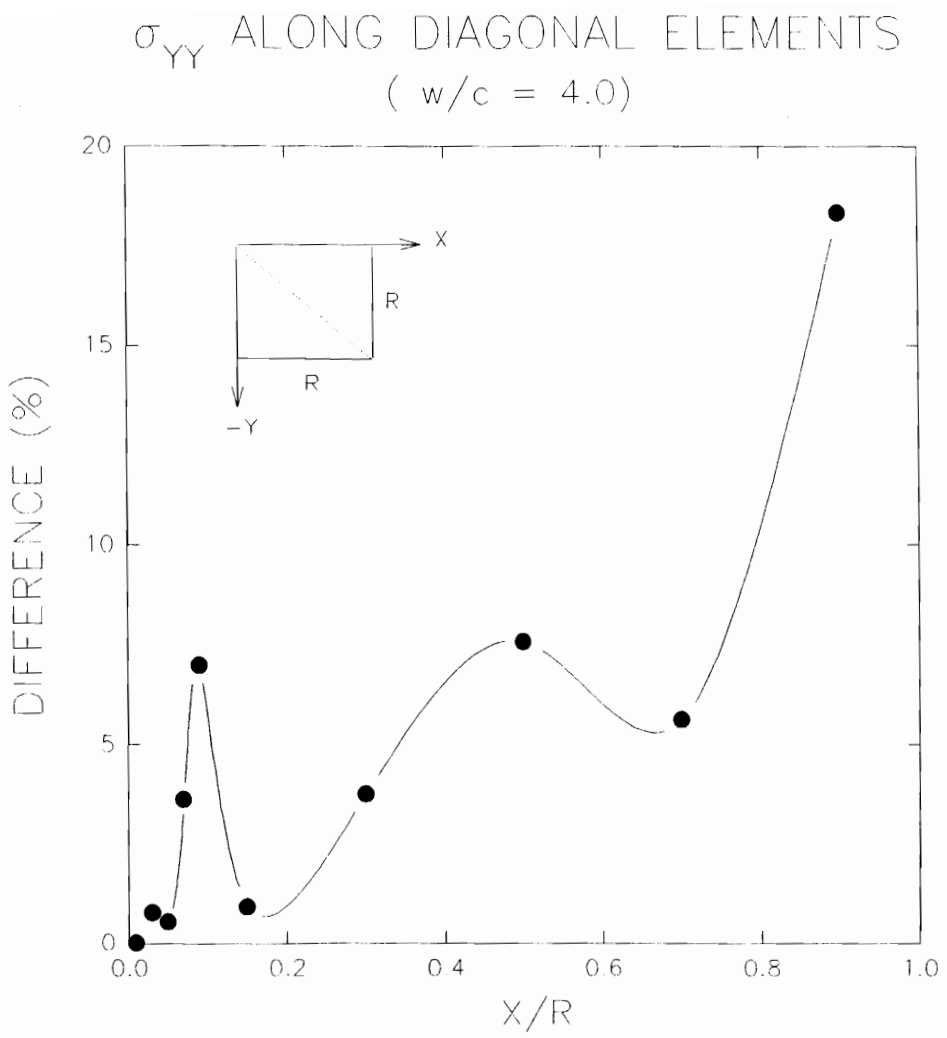

Figure 6.8. σ_{yy} along diagonal elements with w/c = 4.0 for elasto-plastic footing problem 1.

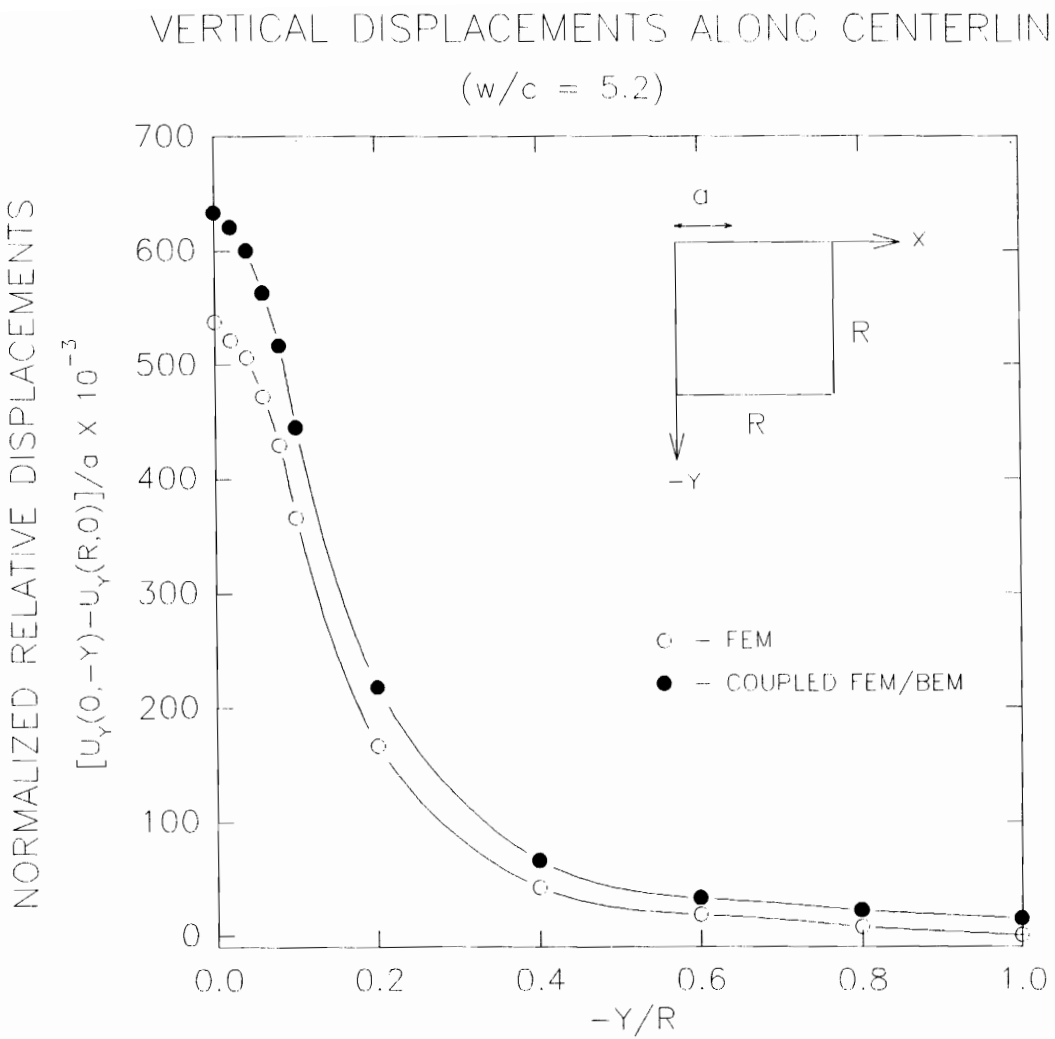

Figure 6.9. Vertical displacements along centerline with w/c = 5.2 for elasto-plastic footing problem 1.

displacements obtained using the two solution procedures is small for values of $-Y/R \leq 0.2$ and increased significantly for larger values of $-Y/R$..

It is also noted that the vertical displacements along the centerline for values of $-Y/R \leq 0.2$ are much larger than those for values of $-Y/R > 0.2$. for both the coupled BEM-FEM method and the finite element solution. As previously mention, this behavior can be attributed to the large plastic deformation that occur in the proximity of the applied load.

Figure (6.10) shows the vertical displacements along the surface of the soil domain plotted versus the normalized coordinates X/R.. This figure shows that coupled BEM-FEM method results in displacements underneath the footing ($X/R \leq 0.1$) which are 20% greater than those obtained using the finite element method. For points not lying underneath the footing ($X/R > 0.1$), the difference in the displacement obtained using the two solution procedures is negligible as compared to the difference in the displacements underneath the footing.

These results indicate that for frictionless soils where the effect of self-weight are neglected, taking into consideration the infinite boundary results in larger displacement at failure. However, the limit load is unaffected by the infinite boundary.

Stresses Along Diagonal Elements at *w/c* = 5.2: Figure (6.11) shows the difference in σ_{xx} for elements lying along the diagonal of the mesh plotted versus the normalized coordinates X/R. Within the proximity of the footing corresponding to value of $X/R < 0.2$, the difference in the values of σ_{xx} obtained using the two solution techniques is within 2%. However for values of $X/R \geq 0.2$, the difference in the value of σ_{xx} obtained using the two solution procedures ranges between 10% at $X/R = 0.3$ to 60% at $X/R = 0.7$.

Figure (6.12) shows the difference in σ_{xy} for elements lying along the diagonal of the mesh plotted versus the normalized coordinates X/R. For values of $X/R \leq 0.3$, the

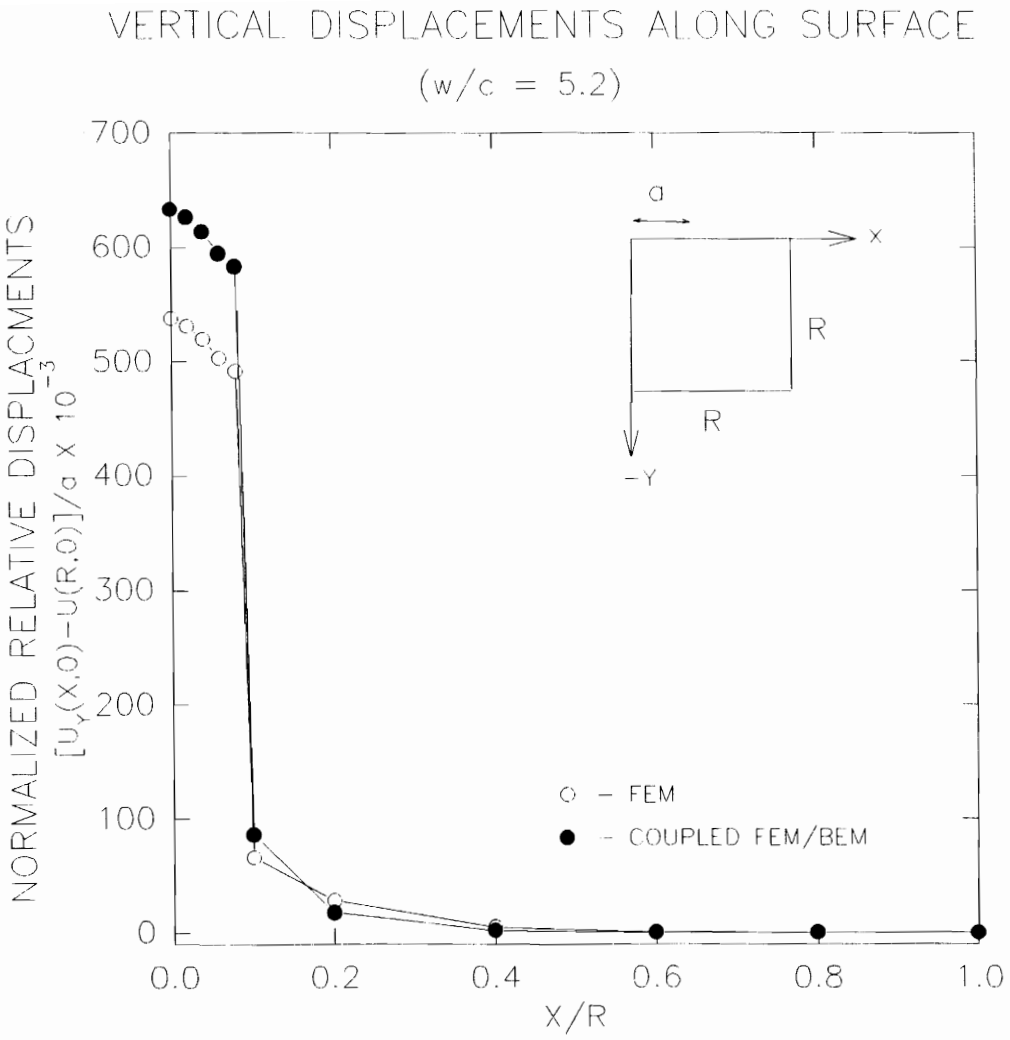

Figure 6.10. Vertical displacements along surface with w/c =5.2 for elasto-plastic footing problem 1.

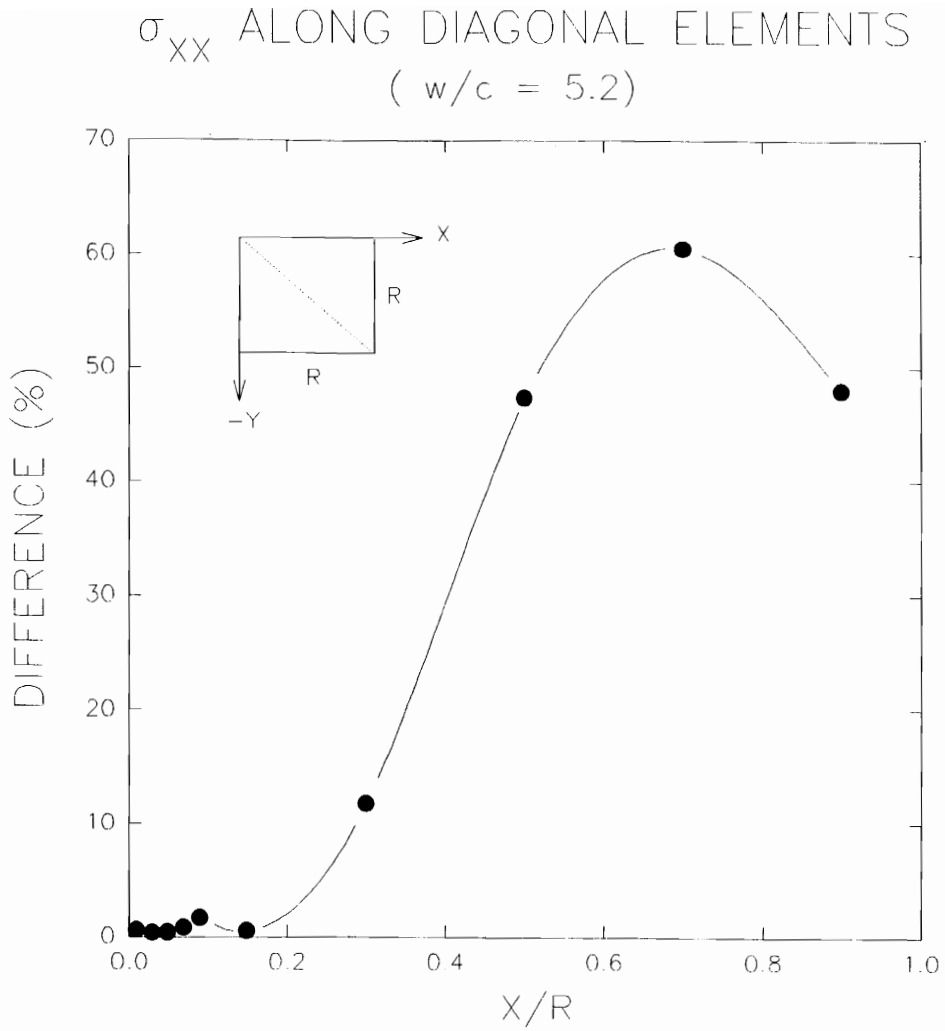

Figure 6.11. σ_{xx} along diagonal elements with w/c = 5.2 for elasto-plastic footing problem 1.

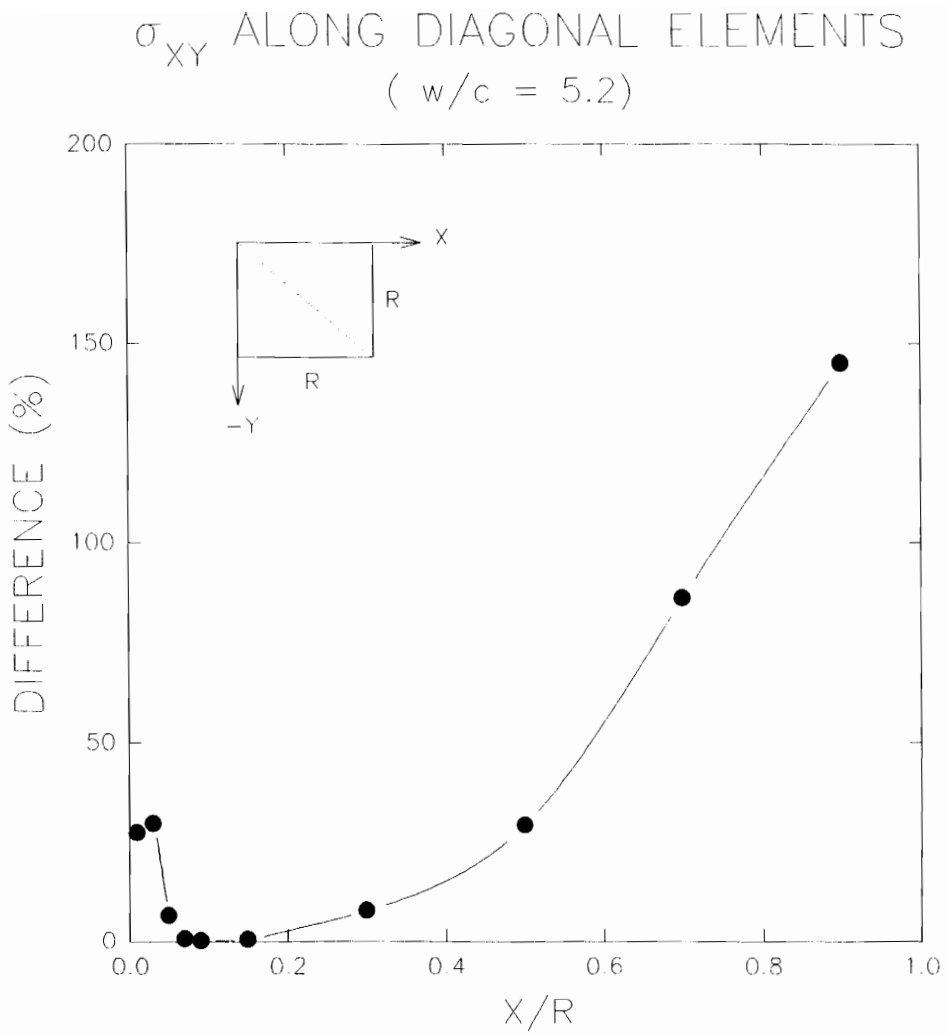

Figure 6.12. σ_{xy} along diagonal elements with w/c = 5.2 for elasto-plastic footing problem 1.

difference in the values of σ_{xy} obtained using the two solution techniques is within 25%. However for values of $X/R > 0.3$, the difference in the value of σ_{xx} obtained using the two solution procedures is significantly larger and steadily increases from 25% at $X/R = 0.5$ to 150% at $X/R = 0.9$.

Figure (6.13) shows the difference in σ_{yy} for elements lying along the diagonal of the mesh plotted versus the normalized coordinates X/R. With the exception of $X/R = 0.9$, the difference in σ_{yy} obtained between the two solution procedures is within 10%. At X/R, the difference is 19%.

Figure (6.14) shows spread of the plastic zones in the finite element solution. The spread of the plastic zones in the coupled BEM-FEM solution is shown in Figure (6.15). For $w/c = 4.0$, the plastic zone formed in the coupled BEM-FEM solution is not very different from that formed in the finite element solution. For $w/c = 5.2$, the coupled BEM-FEM solution results in a plastic zone which reaches a slightly greater depth than that formed in the finite element solution. However, other than this difference, the plastic zones formed using the two solution procedure are not significantly different. This observation is consistent with the fact that stresses within plastic zones do not differ significantly between the two solution procedures.

6.4 PROBLEM 2: Weightless Soils with $\phi > 0$.

In this problem, the soil is assumed to be weightless ($\gamma_m = 0.0$) with an angle of internal friction $\phi = 20.0°$ and cohesion of $c = 1.0$ kips/ft^2. The uniformly distributed load, w, is applied in increments of $\Delta w = 1.0$ kips/ft^2 until $w = 8.0$ kips/ft^2. After this point, load increments of $\Delta w = 1.0$ kips/ft^2 are applied until $w = 14.0$ kips/ft^2, after which w is increased in increments of $\Delta w = 0.1$ kips/ft^2 until bearing failure occurrs. An error tolerance in the residual norm of $\varepsilon_{tol} = 10^{-5}$ is adopted. Failure is said to have occurred

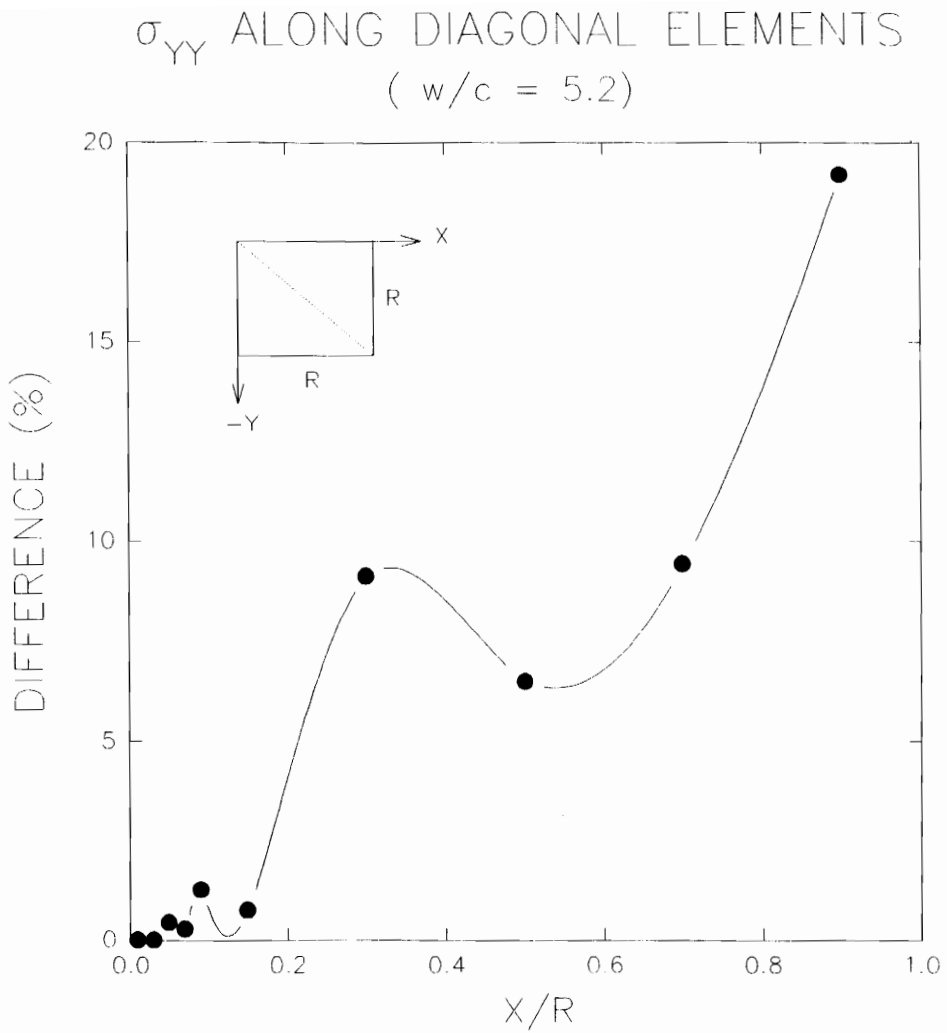

Figure 6.13. σ_{yy} along diagonal elements with w/c = 5.2 for elasto-plastic footing problem 1.

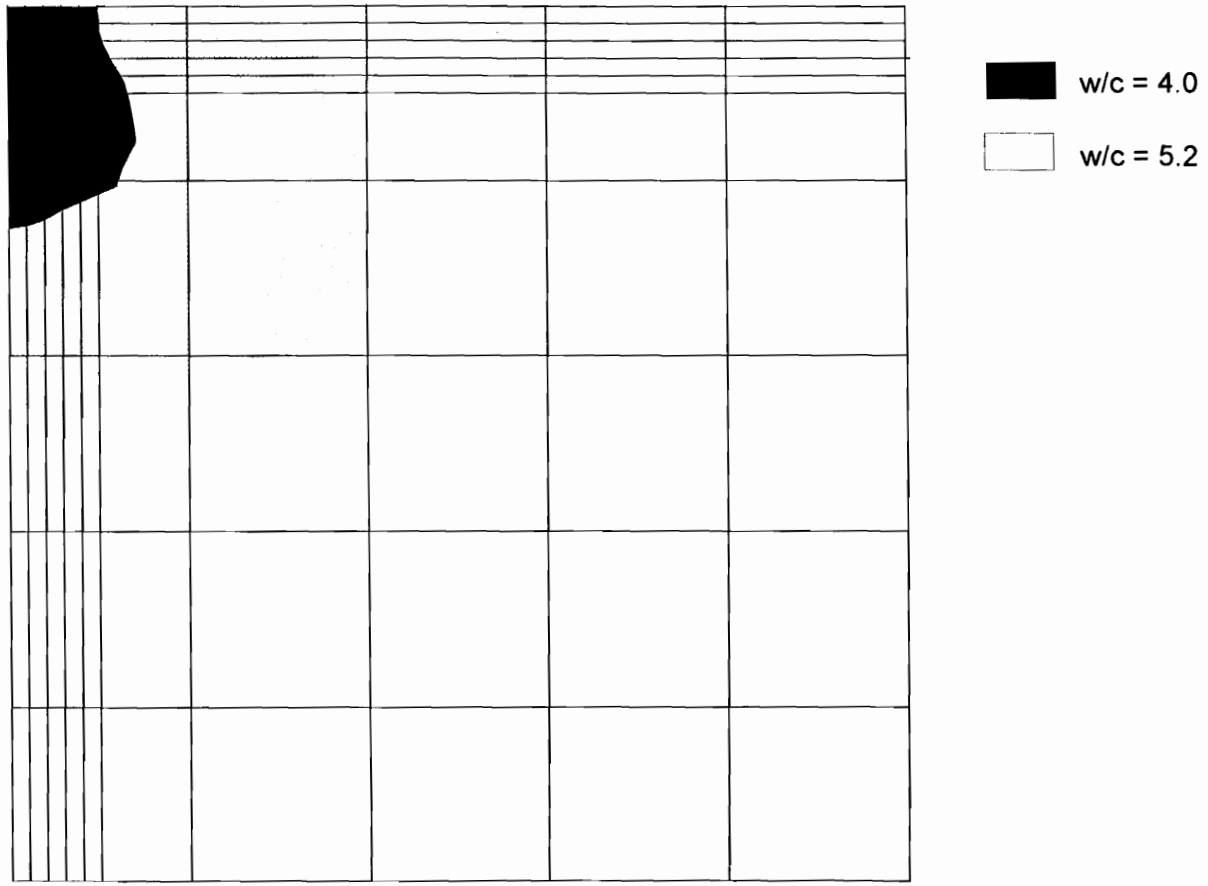

Figure 6.14. Spread of plastic zones for elasto-plastic footing problem 1 using the finite element method alone.

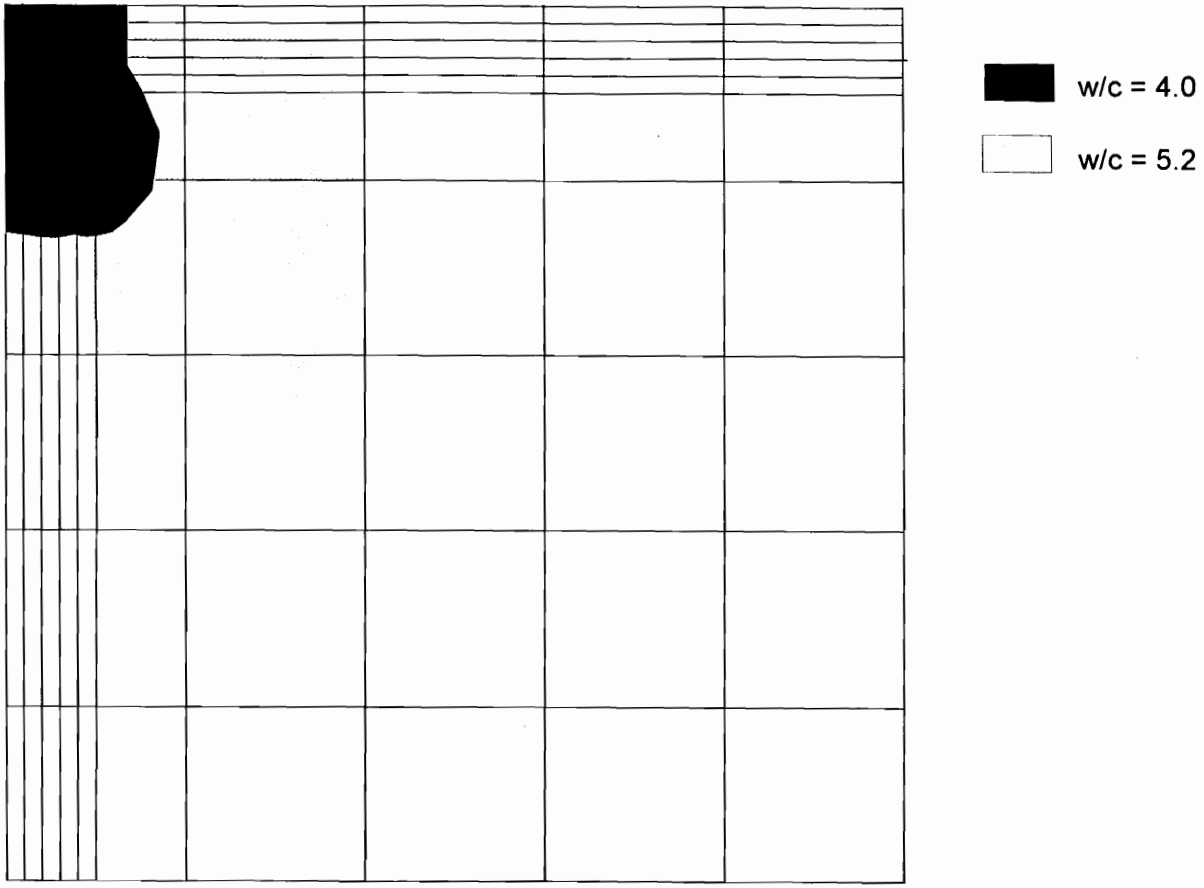

Figure 6.15. Spread of plastic zones for elasto-plastic footing problem 1 using the coupled finite element - boundary element solution.

when the residual norm $\|\mathbf{R}\| \geq \varepsilon_{tol}$ after 25 iterations. Hill (1950) extended Prandtl's solution to weightless soils with both cohesion and friction. This solution is given by:

$$w/c = \cot\phi\left[\exp(\pi\tan\phi)\tan^2\left(\frac{\pi}{4}+\frac{\phi}{2}\right)-1\right] \tag{6.4}$$

For this problem where $\phi = 20.0°$, the corresponding bearing capacity is w/c =14.9.

Figure (6.16) shows the normalized load w/c plotted versus the normalized vertical displacement at point A measured relative to point B on the surface at a distance R = 50.0 ft. from the centerline. This figure shows that the soil in the foundation is elastic in the finite element solution until w/c = 7.0 while for the coupled BEM-FEM method, yielding does not occur until w/c = 8.0. For w/c < 7.0, where behavior of the soil is still elastic, the coupled BEM-FEM method gives displacements which are consistently 20% greater than those obtained using the finite element method only. For values of w/c greater than 8.0, the difference in the vertical displacements obtained using the two solution procedures decreases with increase load levels. In the finite element solution, the solution failed to converge at w/c = 14.4. In the solution involving the coupled BEM-FEM method, the solution failed to converge after w/c = 14.8. This same problem is solved by Zienkiewicz et al. (1975) using 121 quadratic isoparametric elements, and Telles (1981) using boundary elements based on the Kelvin fundamental solution. In both of these solutions, a non-associated Mohr-Coulomb plasticity model was used. The ultimate load predicted by the Zienkiewicz and Telles solution was w/c =15.1 and w/c = 14.9 respectively. Both Zienkiewicz and Telles obtained a load-displacement very similar that shown in Figure (6.16).

Unlike the previous problem, near the ultimate load, no rapid increase in the vertical displacement at point A is observed.

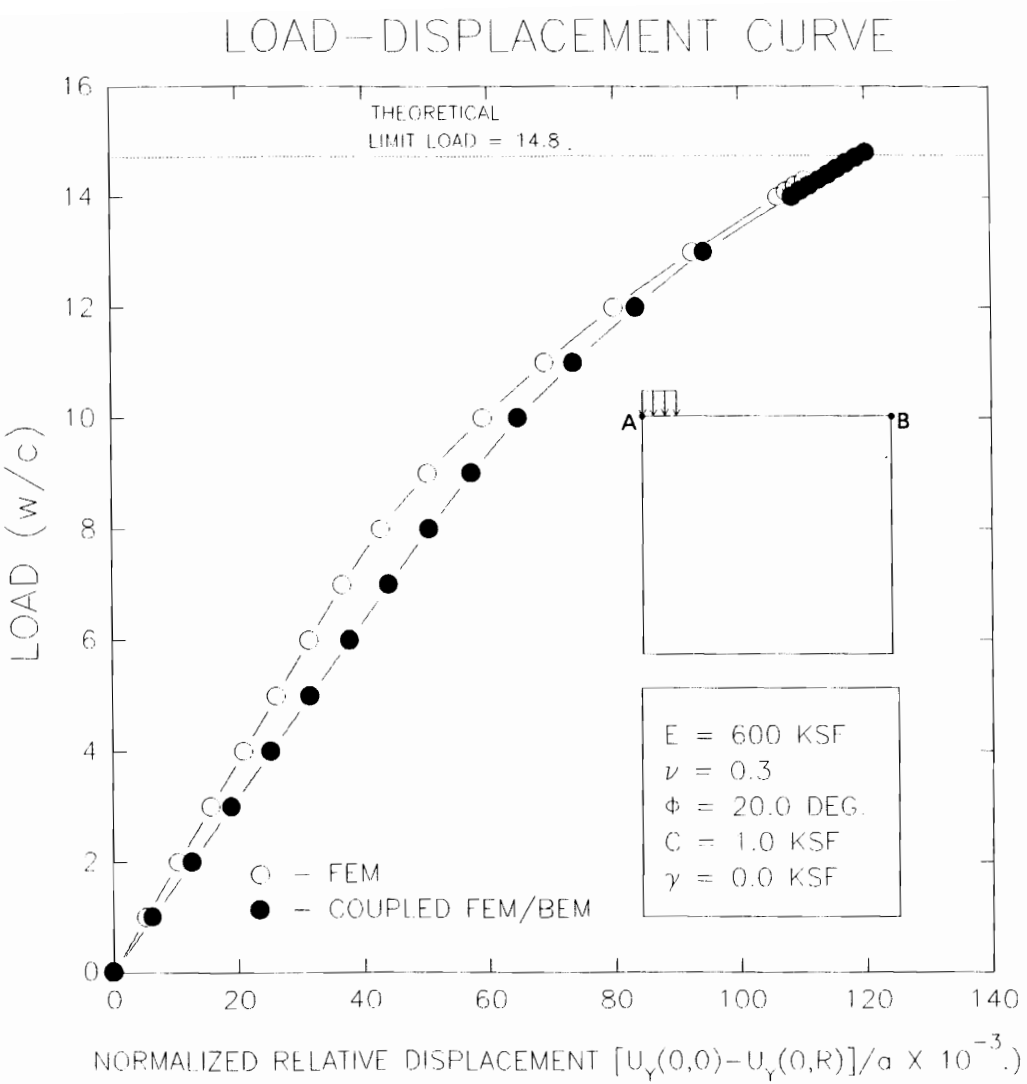

Figure 6.16. Load-Displacement Curve for elasto-plastic footing problem 2.

Vertical Displacements at *w/c* = 8.0: Figure (6.17) shows the vertical displacement along the centerline of the soil mass plotted versus the normalized coordinates *Y/R*, where R = 50.0 is the depth and height of the soil domain. The vertical displacements are measured relative to the point B as described in Figure (6.16) and normalized with respect to the footing half-width a = 5.0 ft. This figure shows that coupled BEM-FEM method gives vertical displacements which are greater than those obtained using the finite element method. The difference in the displacements obtained using the two solution procedure increases with depth. This is unlike the linear case where the difference is constant along the centerline. At the surface ($-Y/R = 0$), the coupled BEM-FEM solution gives displacements which are 20% greater than those obtained using the finite element method. Near the bottom of the mesh, at $-Y/R = 0.8$, the vertical displacement obtained using the coupled BEM-FEM method is four times that of the displacement obtained using the finite element method.

Figure (6.18) shows the vertical displacement along the surface of the soil domain plotted versus the normalized coordinates *X/R*.. With the exception of $X/R = 1.0$, the vertical displacements along the surface obtained using the coupled BEM-FEM method are significantly higher than those obtained using the finite element method. At $X/R = 1.0$, the vertical displacement is zero for both the coupled BEM-FEM solution and the finite element solution. This is due to the fact all vertical displacements are measured relative to this point. The difference in the vertical displacements obtained using the two solution procedures seems to be constant along the surface for values of *X/R* between 0.0 and 0.6 after which the difference decreases to zero as *X/R* approaches 1.0. This difference is equal to 20% of the vertical displacement at point A ($X/R = 0.0$) obtained using the finite element solution.

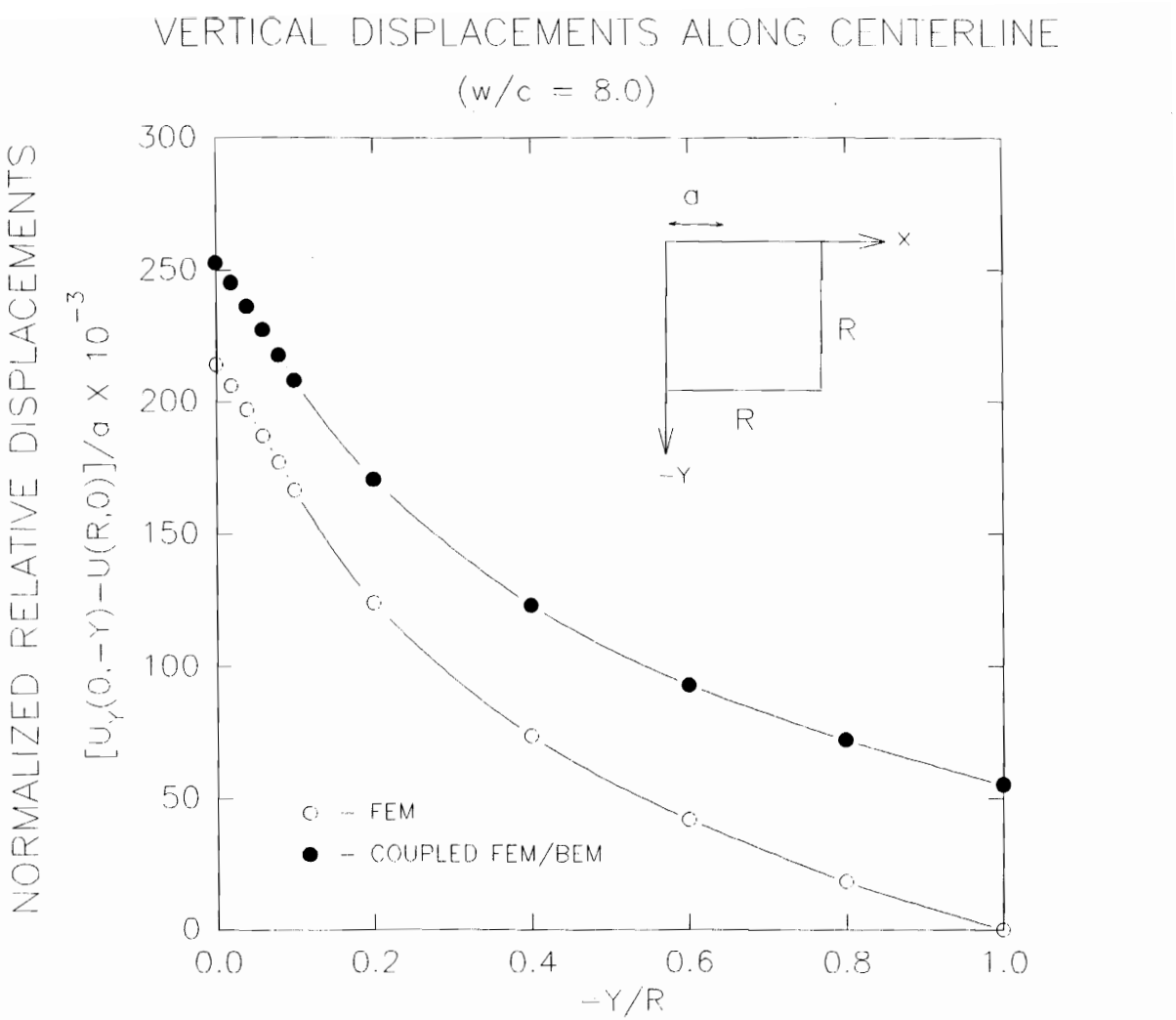

Figure 6.17. Vertical displacements along centerline with w/c = 8.0 for elasto-plastic footing problem 2.

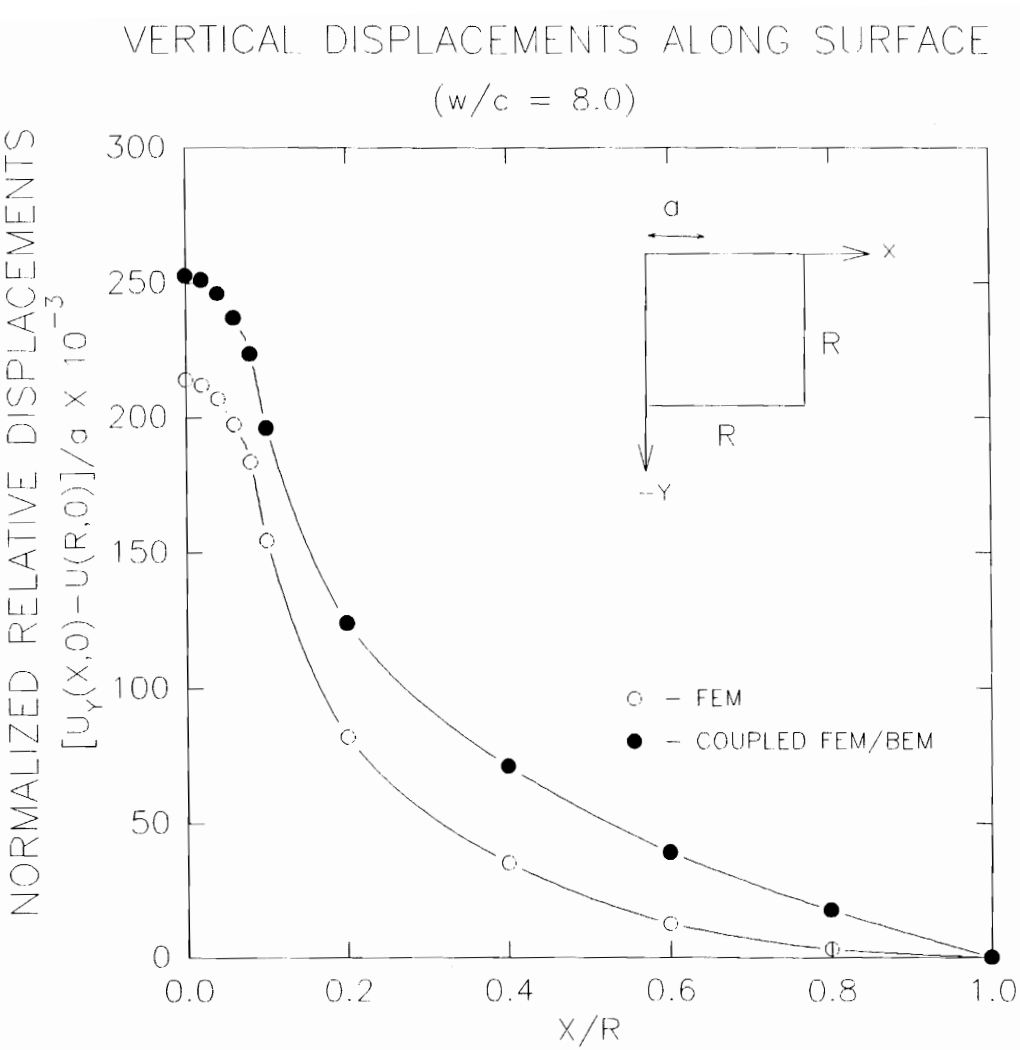

Figure 6.18. Vertical displacements along surface with w/c = 8.0 for elasto-plastic footing problem 2.

Stresses Along Diagonal Elements at *w/c* = 8.0: Figure (6.19) shows the difference in σ_{xx} for elements lying along the diagonal of the mesh plotted versus the normalized coordinates *X/R*. Unlike the previous problem, the value of σ_{xx} obtained using the two solution procedures vary significantly within the proximity of the footing. For values of $X/R \leq 0.1$, the values of σ_{xx} obtained using the two solution procedures differ by as much 26% which occurs a $X/R = 0.03$. For values of $X/R > 0.1$, the values of σ_{xx} differ by as much as 20%. This difference occurs at two points: $X/R = 0.3$ and $X/R = 0.7$. As is observed with the elastic case, the difference in σ_{xx} between the two solution procedures tends to oscillate.

Figure (6.20) shows the difference in σ_{xy} for elements lying along the diagonal of the mesh plotted versus the normalized coordinates *X/R*. For values of $X/R \leq 0.3$, the difference in the values of σ_{xy} obtained using the two solution techniques is within 10%. However for values of $X/R > 0.3$, the difference in the value of σ_{xx} obtained using the two solution procedures is significantly larger and steadily increases from 25% at $X/R = 0.5$ to 170% at $X/R = 0.9$.

Figure (6.21) shows the difference in σ_{yy} for elements lying along the diagonal of the mesh plotted versus the normalized coordinates *X/R*. With the exception of $X/R = 0.9$, the difference in σ_{yy} obtained between the two solution procedures is within 10%. At *X/R*, the difference is 19%.

Vertical Displacements at *w/c* = 14.0: Figure (6.22) shows the vertical displacement along the centerline of the soil mass plotted versus the normalized coordinates *Y/R*, where R = 50.0 is the depth and height of the soil domain. The vertical displacements are measured relative to the point B as described in Figure (6.16) and normalized with respect to the footing half-width $a = 5.0$ ft. This figure shows that the for

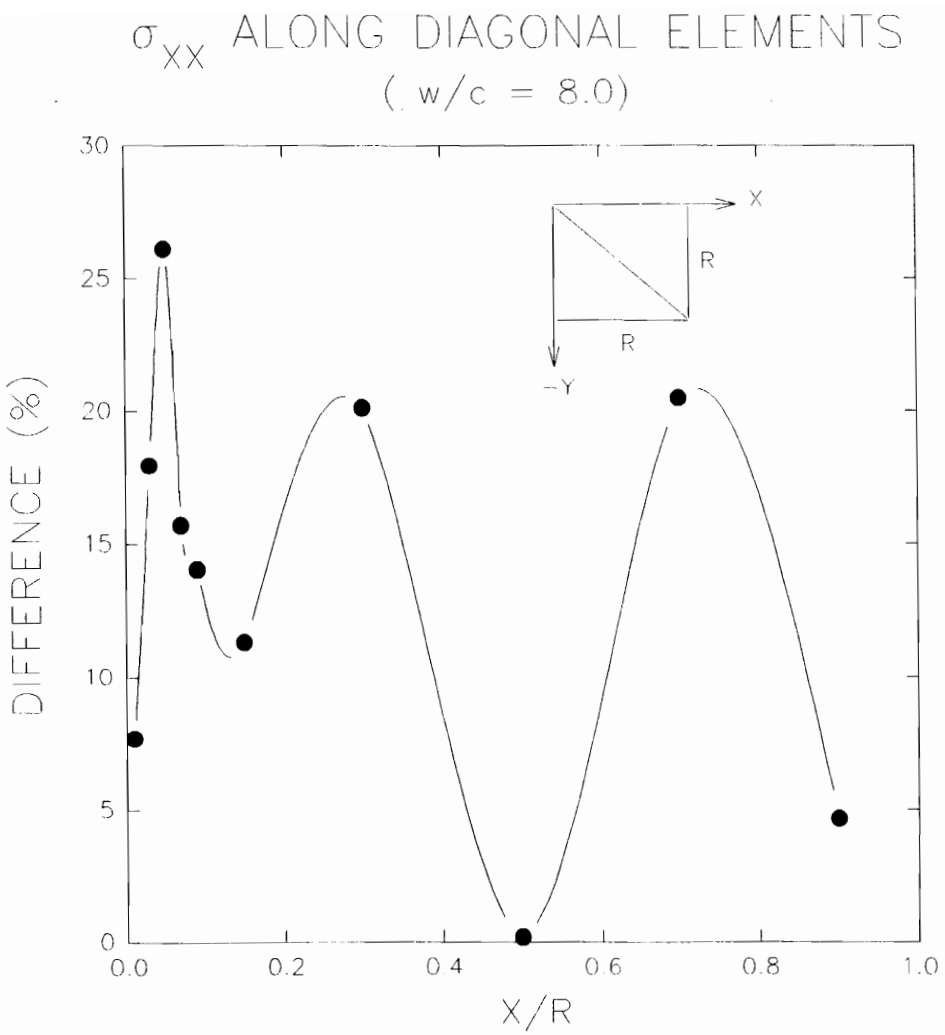

Figure 6.19. σ_{xx} along diagonal elements with w/c = 8.0 for elasto-plastic footing problem 2.

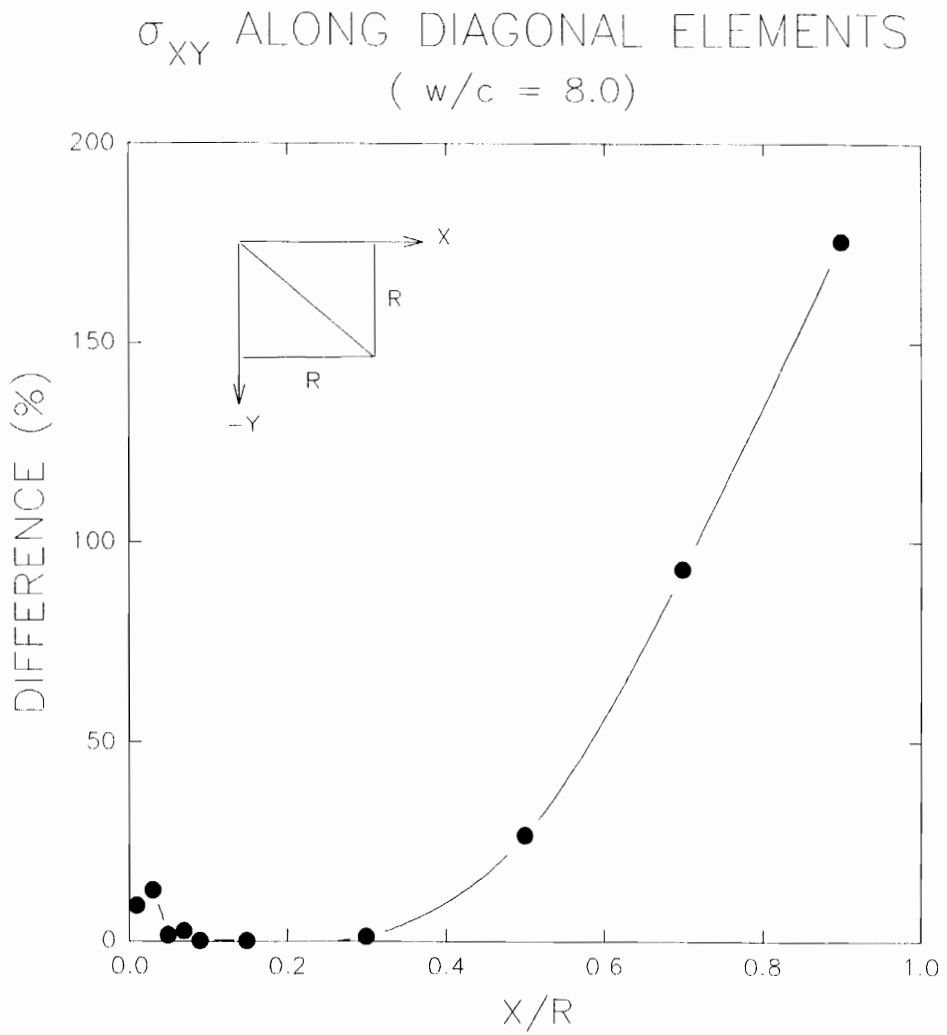

Figure 6.20. σ_{xy} along diagonal elements with w/c = 8.0 for elasto-plastic footing problem 2.

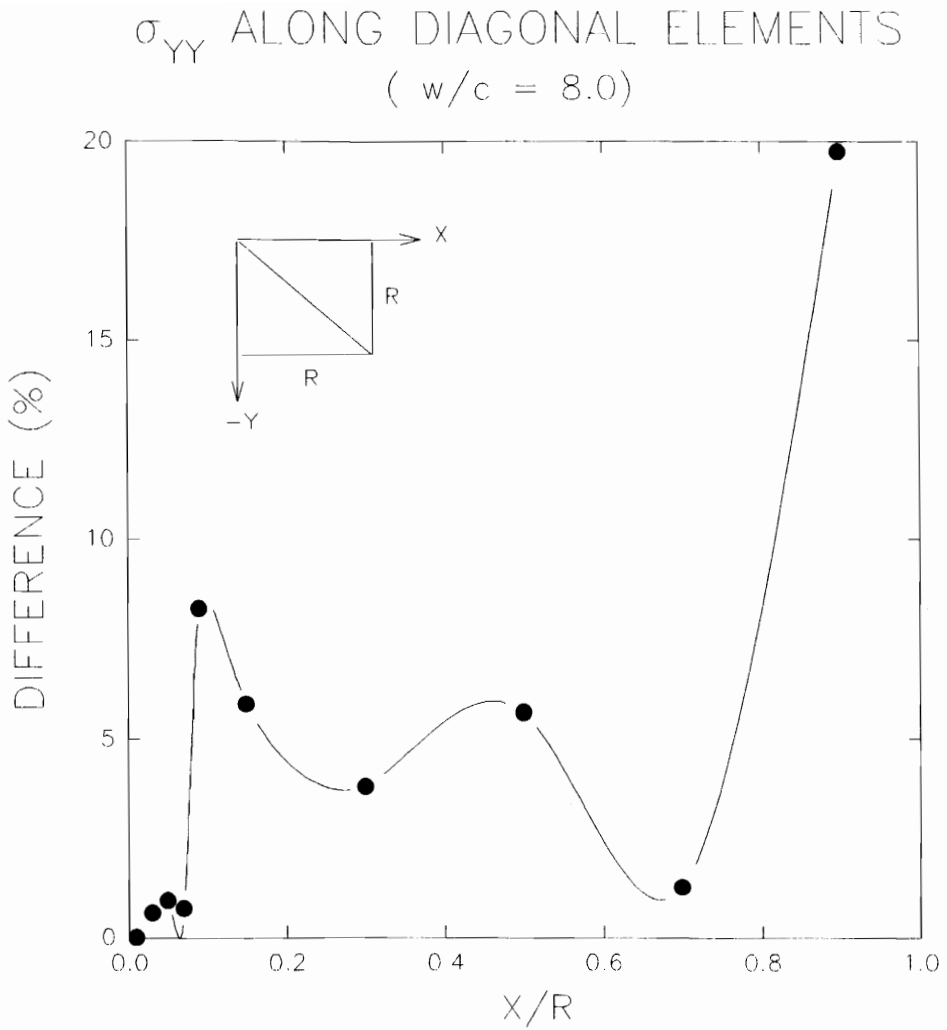

Figure 6.21. σ_{yy} along diagonal elements with w/c = 8.0 for elasto-plastic footing problem 2.

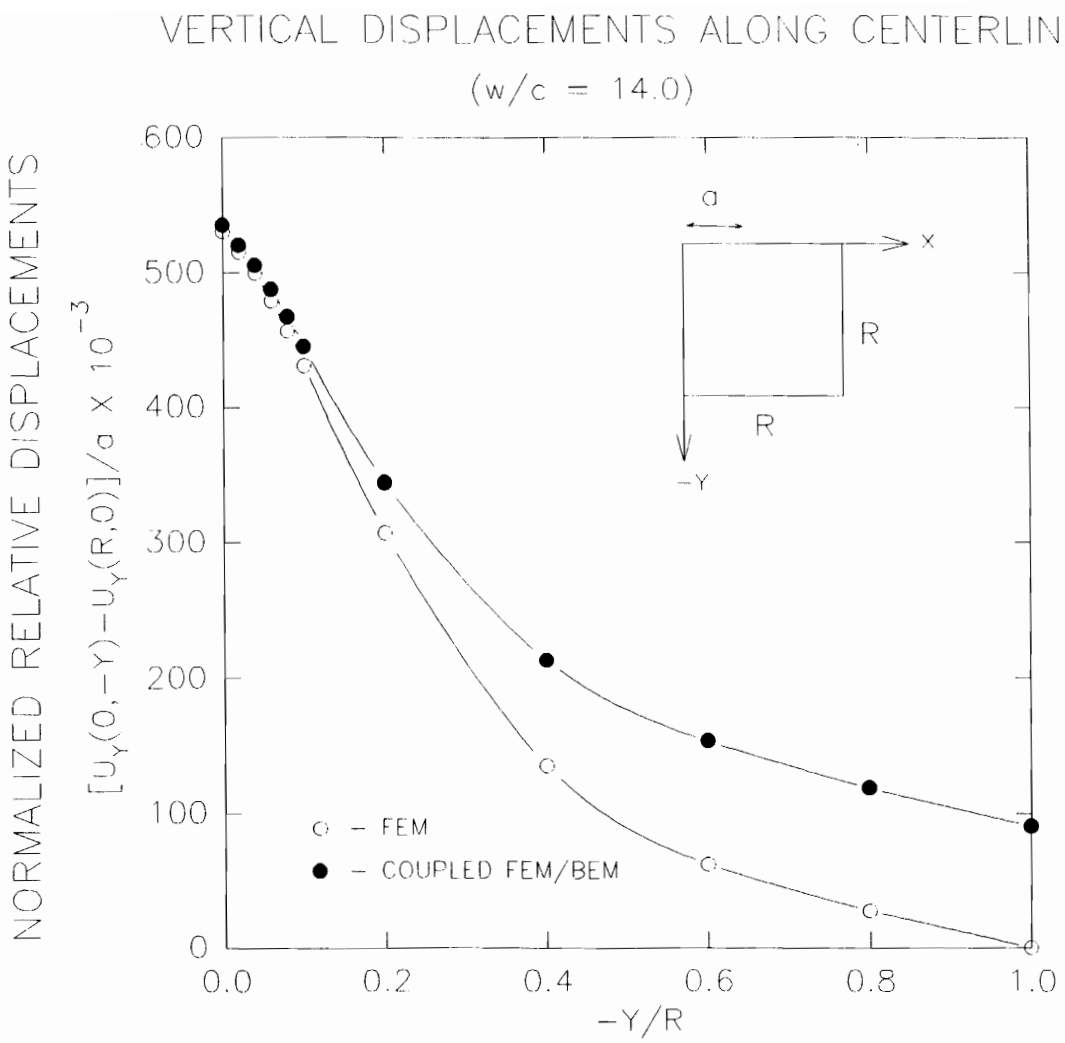

Figure 6.22. Vertical displacements along centerline with w/c = 14.0 for elasto-plastic footing problem 2.

values of $-Y/R \leq 0.1$, vertical displacement obtained using the two solution procedure differ by at most 5%. For values of $-Y/R > 0.1$, the displacements obtained using the coupled BEM-FEM method are between 10% at $-Y/R = 0.2$ to 100% at $-Y/R = 1.0$ higher than those obtained using the finite element solution.

Figure (6.23) shows the vertical displacement along the surface of the soil domain plotted versus the normalized coordinates X/R. This figure shows that underneath the footing ($X/R \leq 0.08$), the vertical displacement obtained using the two solution procedures do not differ by more than 2%. For values of $X/R > 0.08$, the coupled BEM-FEM gives vertical displacements which are between 10%, at $X/R = 0.1$, to 60%, at $X/R = 0.6$, greater than those obtained using the finite element method.

From these observations, it can be concluded that for weightless soils where $\phi > 0.0°$, the vertical displacements that occur within the proximity of the footing are not affected significantly by the infinite boundary. As previously mentioned, the coupled BEM-FEM method gives larger elastic displacements as compared to the finite element solution. However, from the load-displacement curve, yield starts at a lower load level in the finite element solution as compared to the coupled BEM-FEM method. Thus, for a given load level beyond initial yielding, the plastic deformations in the finite element solution are larger than those in the coupled BEM-FEM method. For the finite element solution, the larger plastic deformations offset the smaller elastic displacements and give total displacements which are approximately equal to those obtained using the coupled BEM-FEM solution.

Stresses Along Diagonal Elements at *w/c* = 14.0: Figure (6.24) shows the difference in σ_{xx} for elements lying along the diagonal of the mesh plotted versus the normalized coordinates X/R. For values of $X/R \leq 0.03$, the values of σ_{xx} obtained using the

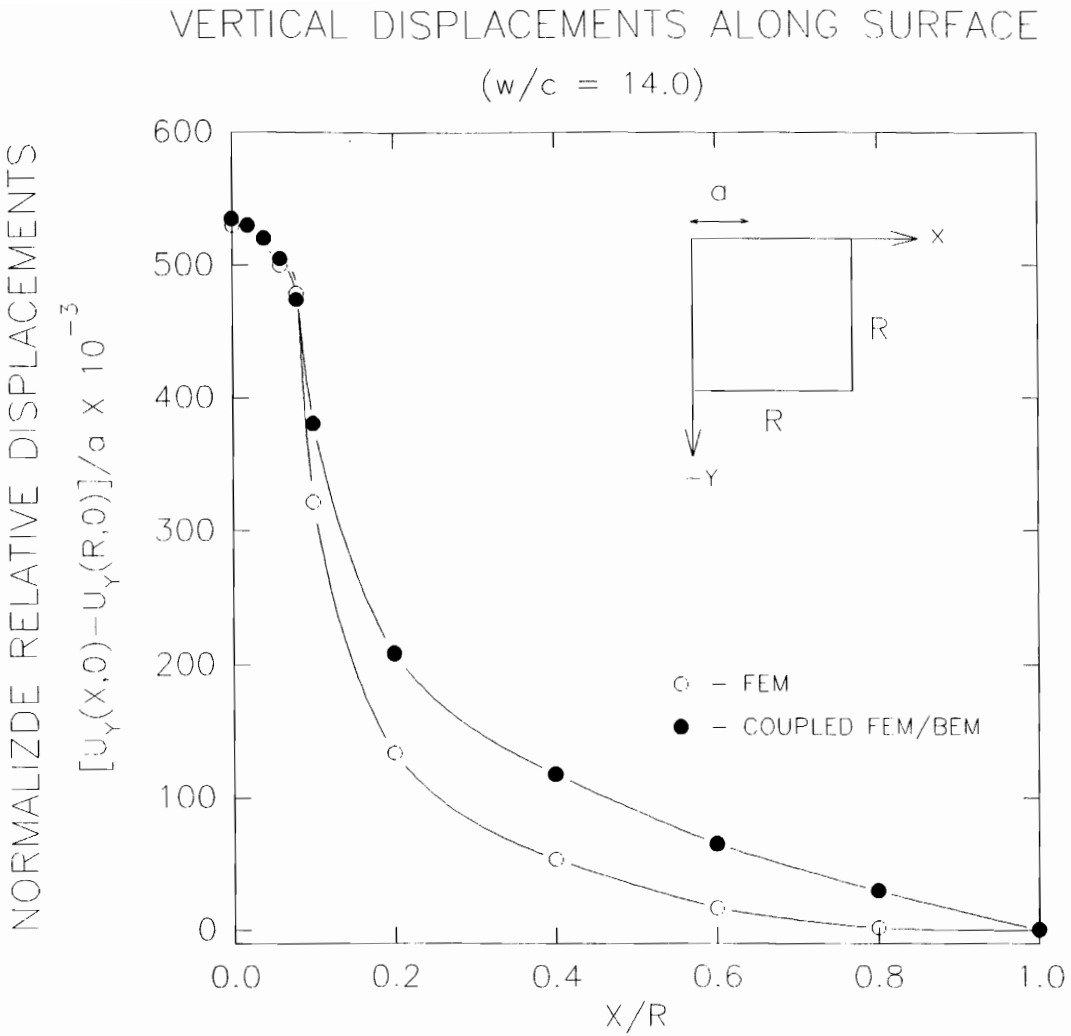

Figure 6.23. Vertical displacements along surface with w/c =14.0 for elasto-plastic footing problem 2.

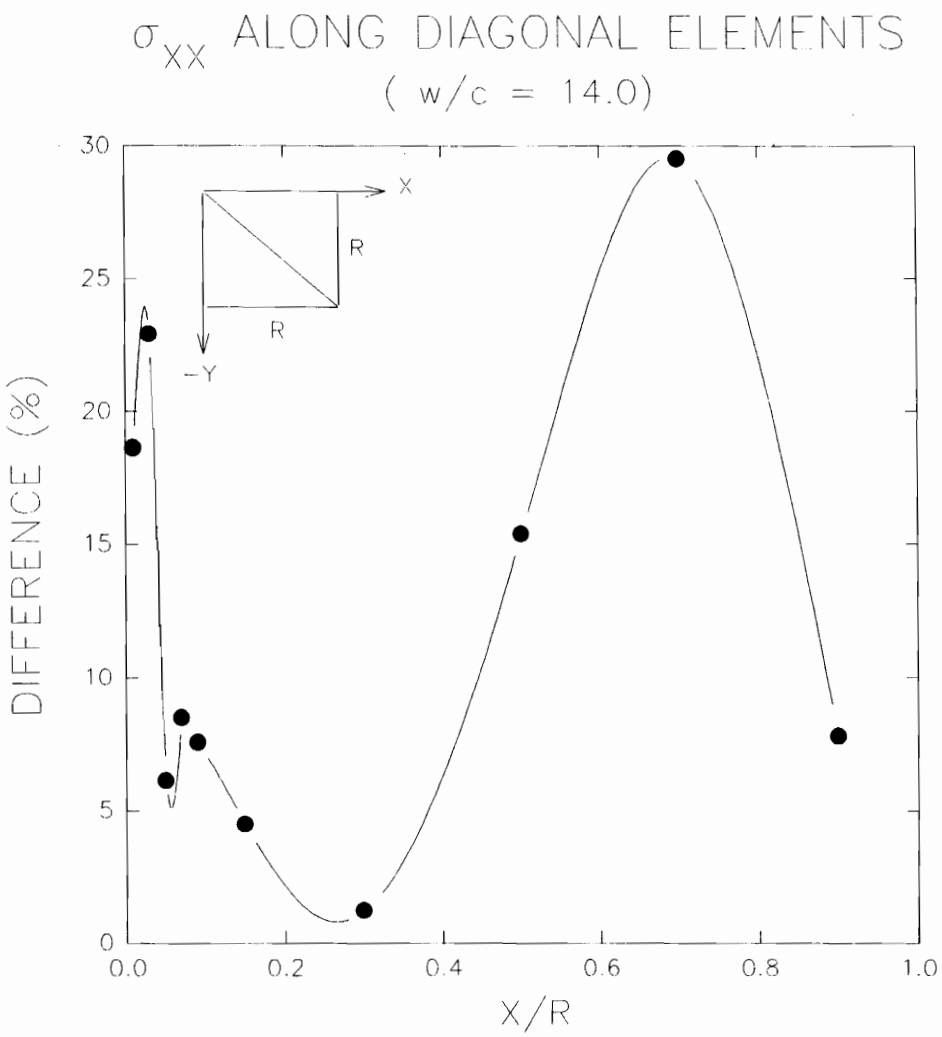

Figure 6.24. σ_{xx} along diagonal elements with w/c = 14.0 for elasto-plastic footing problem 2.

two solution procedure differ by an average of 20%. For values of X/R between 0.05 and 0.3, the difference in the values of σ_{xx} obtained using the two solution procedures are within 8%. Differences of as large as 30%, at X/R = 0.7, in the computed values of σ_{xx} between the two solution procedures occur for values of $X/R \geq 0.5$.

Figure (6.25) shows the difference in σ_{xy} for elements lying along the diagonal of the mesh plotted versus the normalized coordinates X/R. For values of $X/R \leq 0.3$, the difference in the values of σ_{xy} obtained using the two solution techniques is within 35%. However for values of $X/R > 0.3$, the difference in the value of σ_{xx} obtained using the two solution procedures is significantly larger and steadily increases from 25% at $X/R = 0.5$ to 160% at $X/R = 0.9$.

Figure (6.26) shows the difference in σ_{yy} for elements lying along the diagonal of the mesh plotted versus the normalized coordinates X/R. With the exception of X/R = 0.09, the difference in σ_{yy} obtained between the two solution procedures is within 10%. At $X/R = 0.09$, the difference is 26%.

Figure (6.27) shows spread of the plastic zones in the finite element solution. The spread of the plastic zones in the coupled BEM-FEM method is shown in Figure (6.28). For w/c = 8.0, the plastic zone formed in the finite element solution reaches a slightly greater depth as compared to that formed in the coupled BEM-FEM method. For w/c =14.0, the plastic zones formed in both the coupled BEM-FEM and finite element solution extend to approximately the same depth. However, the plastic zone formed in the finite element solution is extends further laterally as compared to the coupled BEM-FEM method. This is consistent with the observation that yielding in the finite element solution takes place at a lower load level as compared to the coupled BEM-FEM method. Thus for a given load level after initial yielding has taken place, the plastic zone formed in the finite element solution is larger as compared to that formed in the coupled BEM-FEM method.

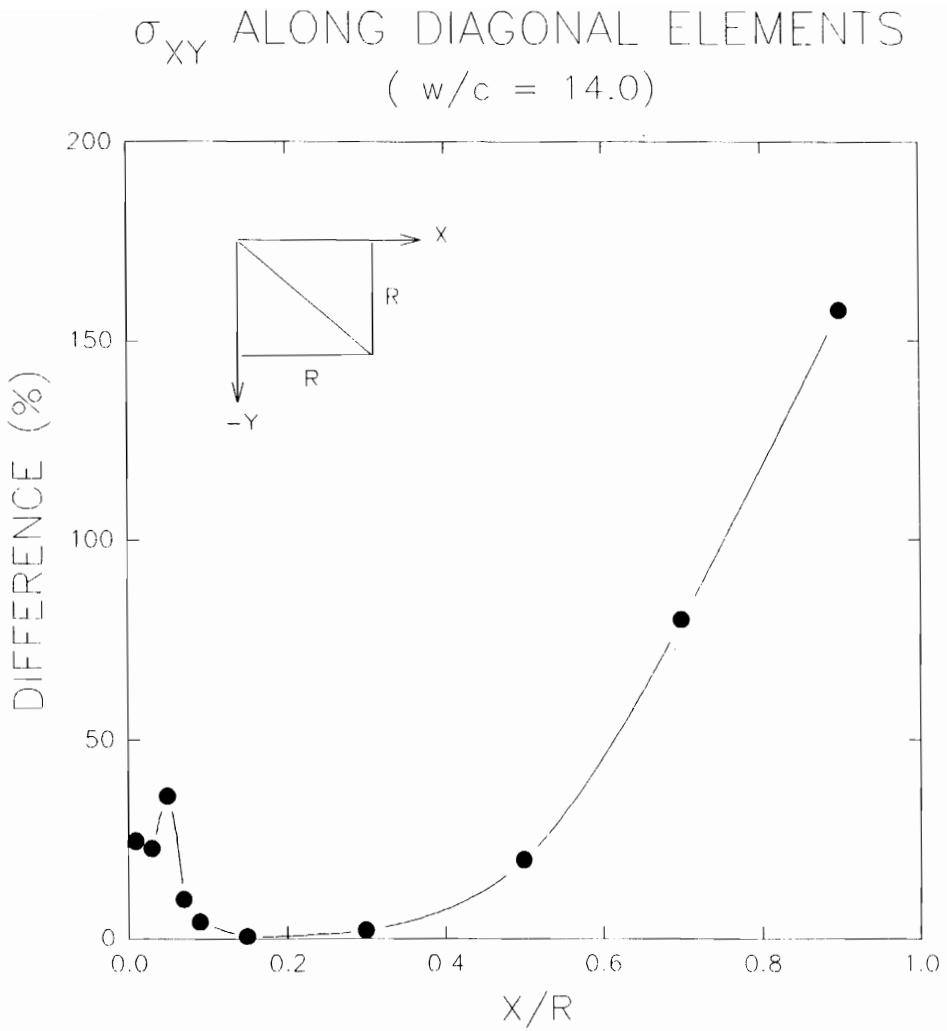

Figure 6.25. σ_{xy} along diagonal elements with w/c = 14.0 for elasto-plastic footing problem 2.

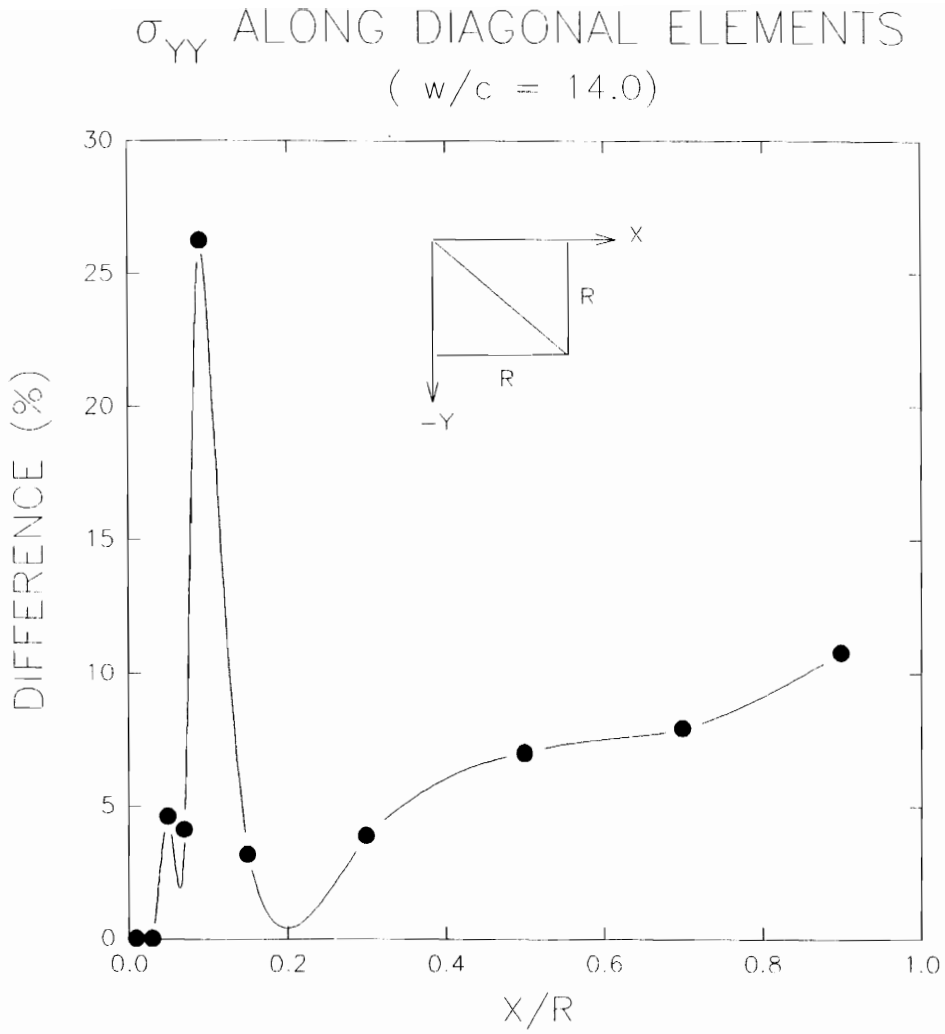

Figure 6.26. σ_{yy} along diagonal elements with w/c = 14.0 for elasto-plastic footing problem 2.

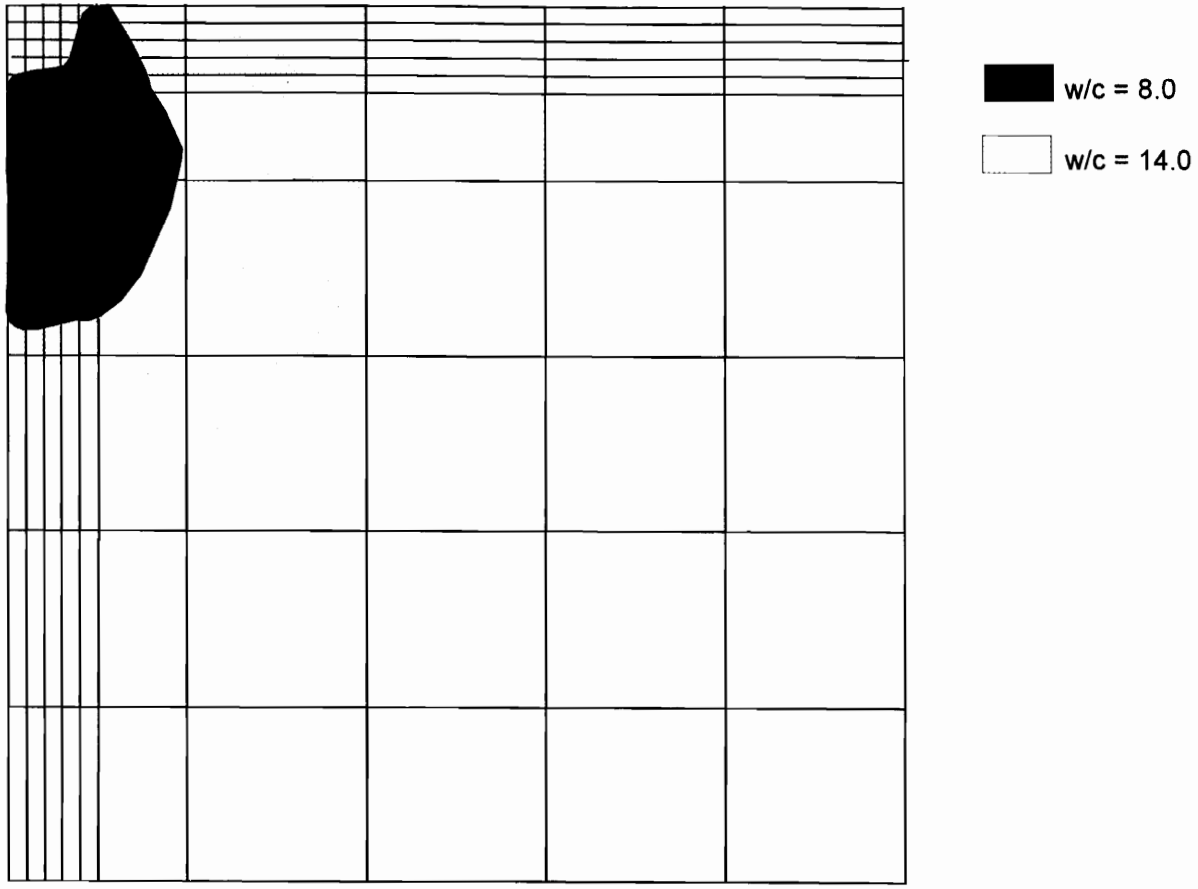

Figure 6.27. Spread of plastic zones for elasto-plastic footing problem 2 using the finite element method alone.

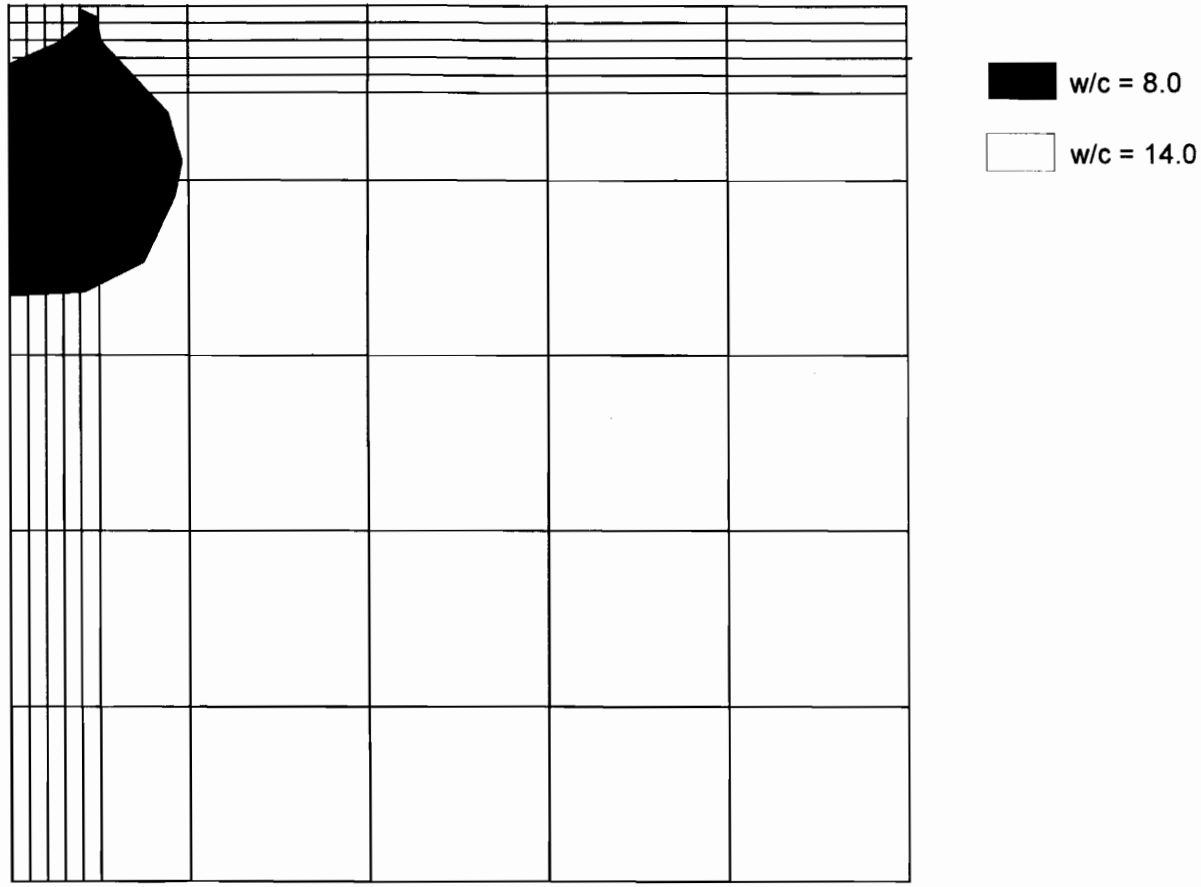

Figure 6.28. Spread of plastic zones for elasto-plastic footing problem 2 using the coupled finite element-boundary element solution.

6.5 PROBLEM 3: Soils with $\phi > 0$ and Self-Weight.

In this problem, the soil is assumed to have an angle of internal friction $\phi = 20.0°$ and a cohesion $c = 1.0$ kips/ft^2. The unit weight of the soil is assumed to be $\gamma_m = 125$ lbs./ft^3. The uniformly distributed load, w, is applied in increments of $\Delta w = 1.0$ kips/ft^2 until $w = 10.0$ kips/ft^2 After this point, load increments of $\Delta w = 1.0$ kips/ft^2 are applied until $w = 16.0$ kips/ft^2, after which w is increased in increments of $\Delta w = 0.1$ kips/ft^2 until bearing failure occurrs. An error tolerance in the residual norm of $\varepsilon_{tol} = 10^{-5}$ is adopted. Failure is said to have occurred when the residual norm $\|\mathbf{R}\| \geq \varepsilon_{tol}$ after 25 iterations. The initial stresses resulting from the weight of the soil are assumed to be in an at-rest state :

$$\sigma_{yy} = \gamma_m y \qquad \sigma_{xx} = \sigma_{zz} = K_0 \sigma_{yy} \qquad \tau_{xy} = 0 \tag{6.5}$$

where y is the distance from the surface of the soil domain. The coefficient of at rest earth pressure K_0 is obtained from Poison's ratio using the relationship

$$K_0 = \frac{\nu}{1-\nu} \tag{6.6}$$

For bearing capacity problems involving the effect of the self-weight of the soil, no closed form solution is readily available (Chen, 1975). However, a number of researchers have proposed approximate solutions to this class of problems. These include those proposed by Terzaghi (1943), Meyerhoff (1963), Hansen (1970) and Vesic (1973). Using the method by Meyerhoff method, the predicted bearing capacity is:

$$w = 16.5 \text{ ksf} \tag{6.7}$$

Figure (6.29) shows the normalized load w/c plotted versus the normalized vertical displacement at point A measured relative to point B on the surface at a distance $R = 50.0$ ft. from the centerline. This figure shows that for the finite element solution, yielding in the soil begins at $w/c = 8.0$. In the solution using the coupled BEM-FEM solution, yielding begins at $w/c = 10.0$. Prior to yielding, the displacement at point A computed using the

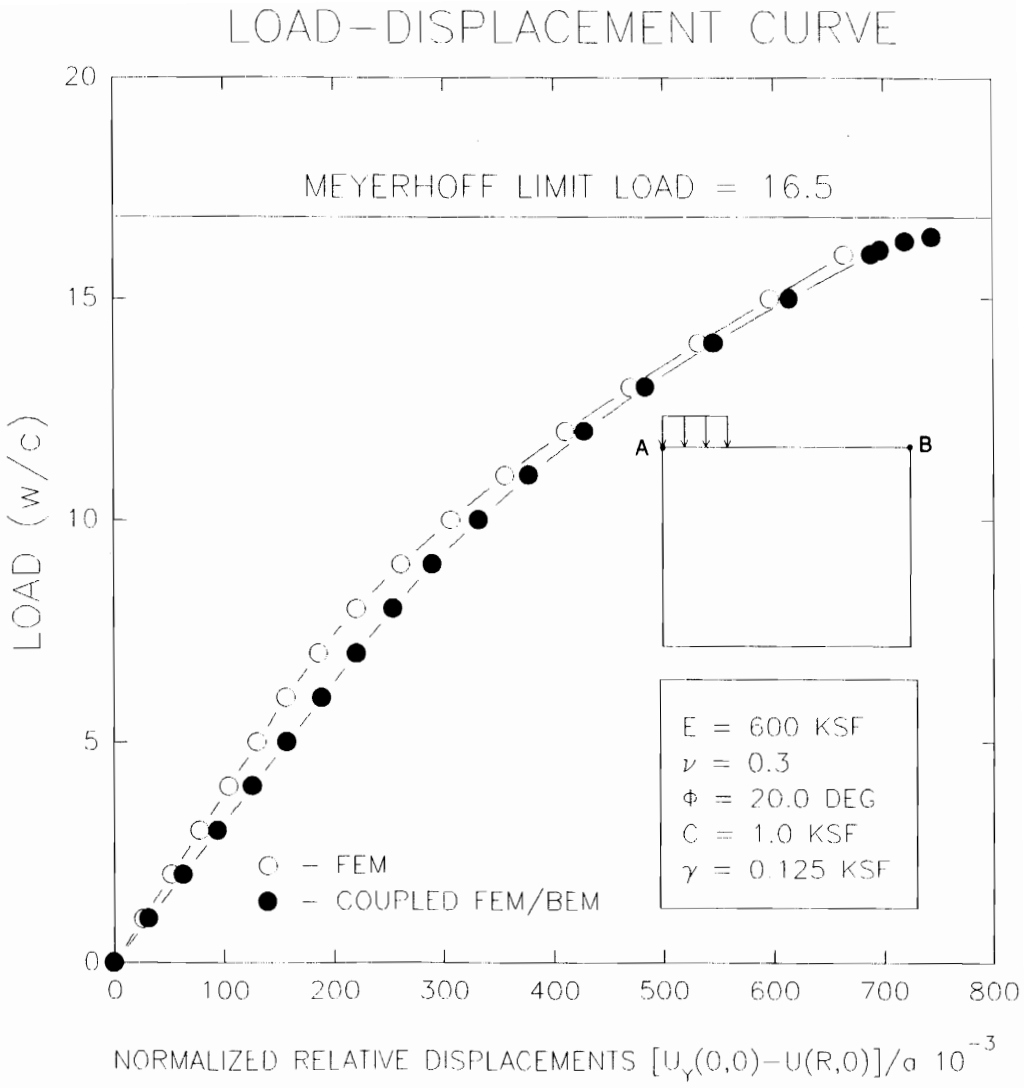

Figure 6.29. Load-Displacement Curve for elasto-plastic footing problem 3.

coupled BEM-FEM method is 20% greater than that computed using the finite element method. After yielding the difference in the displacement at point A computed using the two solution techniques decreases with increasing *w/c*. At *w/c* = 16.0, the difference between the two solution procedures computed displacement at point A is 5%. The ultimate bearing capacity computed by the finite element method is *w/c* =16.0 while the coupled BEM-FEM solution gives an ultimate bearing capacity of *w/c* = 16.3.

Vertical Displacements at *w/c* = 10.0: Figure (6.30) shows the vertical displacement along the centerline of the soil mass plotted versus the normalized coordinates *Y/R*, where R = 50.0 is the depth and height of the soil domain. The vertical displacements are measured relative to the point B as described in Figure (6.29) and normalized with respect to the footing half-width a = 5.0 ft. For values of $-Y/R \leq 0.1$, the difference in the computed displacements between the two solution procedures ranges between 10%, at $-Y/R = 0.0$, to 14% occurring at $-Y/R = 0.1$. For values of $-Y/R > 1.0$, the displacements obtained using the coupled BEM-FEM method are significantly greater than those obtained using only the finite element method. The difference in the computed displacements ranges from 22% at $-Y/R = 0.2$, to 100% at $-Y/R = 1.0$.

Figure (6.31) shows the vertical displacement along the surface of the soil domain plotted versus the normalized coordinates *X/R*. This figure shows that along the surface, the coupled BEM-FEM method results in larger displacements as compared to the finite element method. Underneath the footing corresponding to values of $X/R \leq 0.1$, the difference in displacements obtained using the two solution procedure ranges between 10%, at $X/R = 0.0$, to 20% occurring at $X/R = 0.1$. For values of $X/R > 0.1$, the displacement obtain using the coupled BEM-FEM method are significantly greater. The difference ranges from 33% at $X/R = 0.2$, to 60% at $X/R = 0.8$.

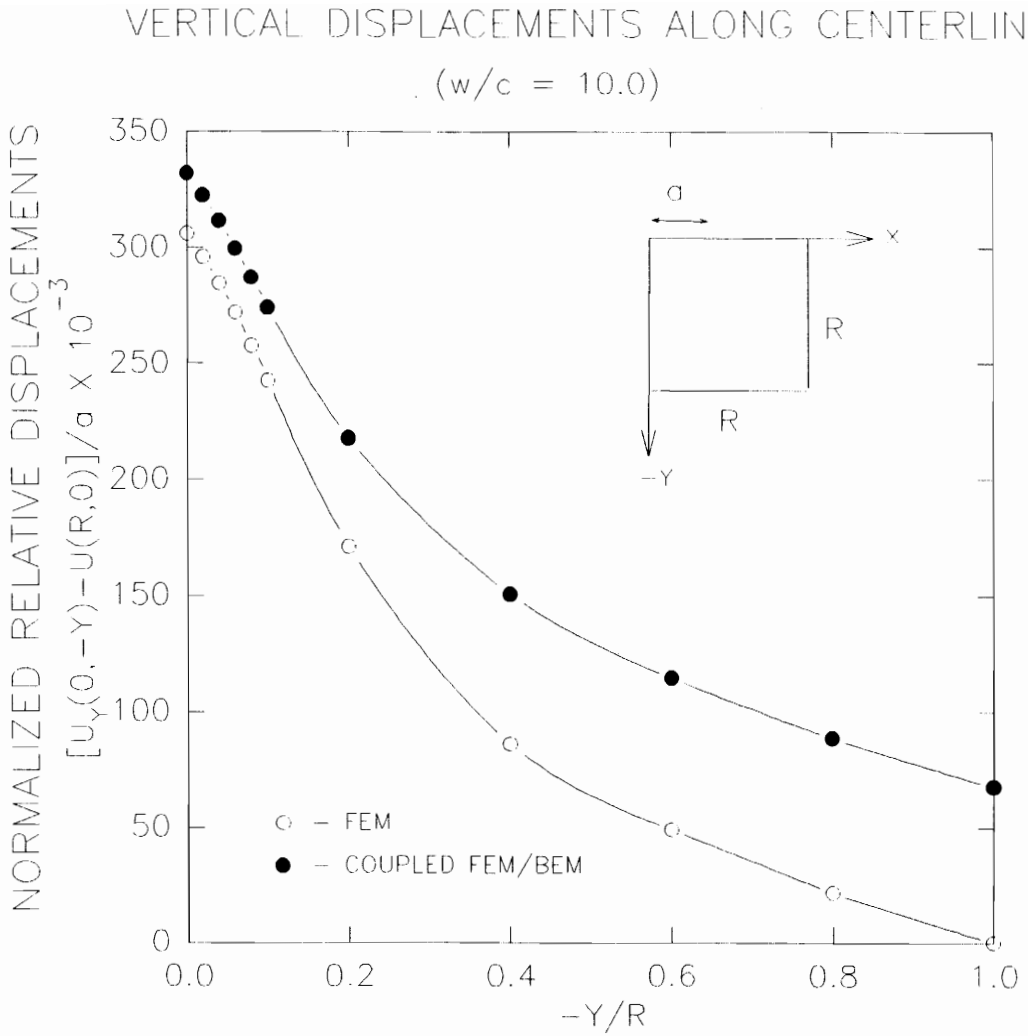

Figure 6.30. Vertical displacements along centerline with w/c = 10.0 for elasto-plastic footing problem 3.

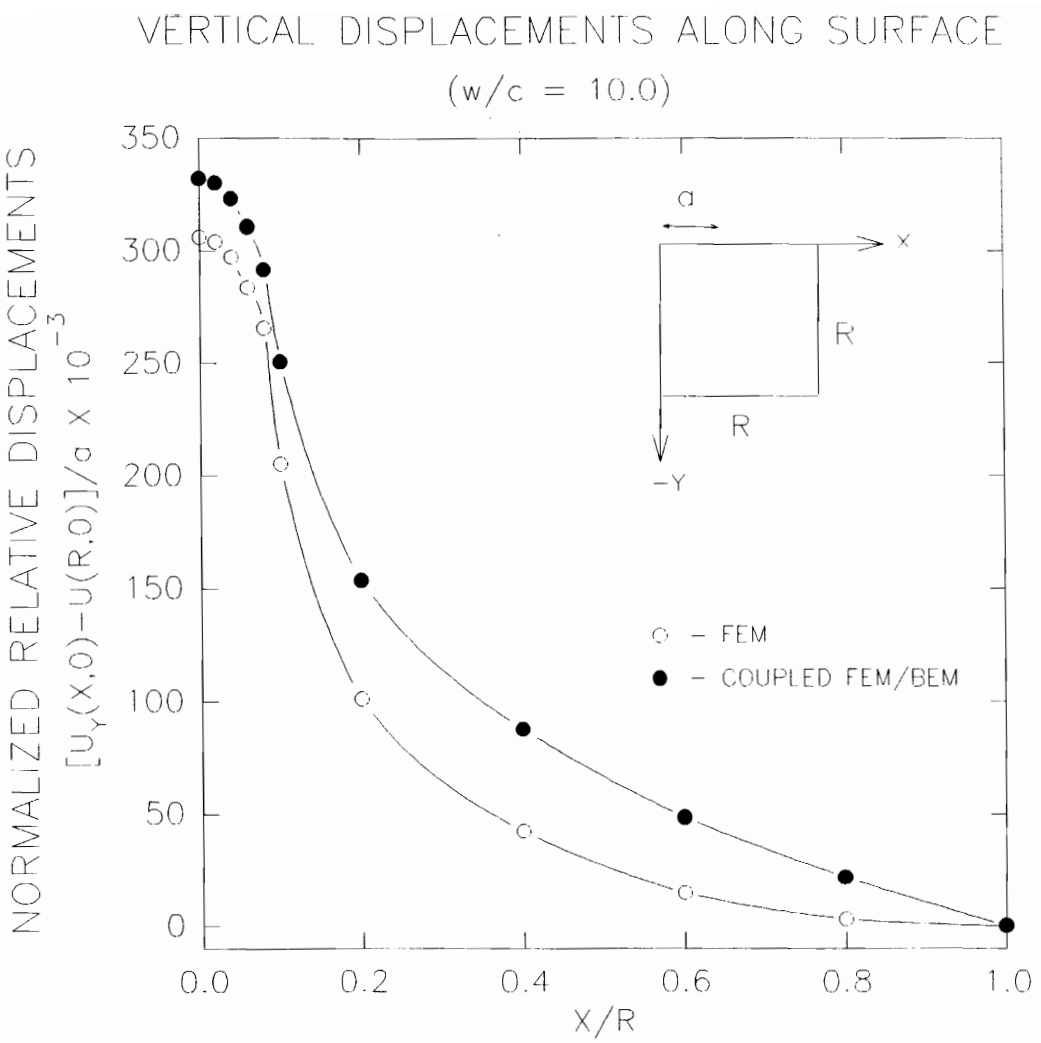

Figure 6.31. Vertical displacements along surface with w/c = 10.0 for elasto-plastic footing problem 3.

Stress Along Diagonal Elements at *w/c* = 10.0: Figure (6.32) shows the difference in σ_{xx} for elements lying along the diagonal of the mesh plotted versus the normalized coordinates *X/R*. With the exception of *X/R* = 0.03, the difference in values of σ_{xx} computed using the two solution procedures is within 14%. At *X/R* = 0.03, the difference is 19%. Unlike the previous problems studied, the difference in σ_{xx} decreases with increasing values of *X/R*.

Figure (6.33) shows the difference in σ_{xy} for elements lying along the diagonal of the mesh plotted versus the normalized coordinates *X/R*. For values of *X/R* ≤0.3, the difference in the values of σ_{xy} obtained using the two solution techniques is within 25%. However for values of *X/R* > 0.3, the difference in the value of σ_{xx} obtained using the two solution procedures is significantly larger and steadily increases from 25% at *X/R* = 0.5 to 170% at *X/R* = 0.9.

Figure (6.34) shows the difference in σ_{yy} for elements lying along the diagonal of the mesh plotted versus the normalized coordinates *X/R*. With the exception of *X/R* = 0.09, the difference in σ_{yy} obtained between the two solution procedures is within 5%. At *X/R*, the difference is 11%.

Vertical Displacements at *w/c* = 16.0: Figure (6.35) shows the vertical displacement along the centerline of the soil mass plotted versus the normalized coordinates *Y/R*, where R = 50.0 is the depth and height of the soil domain. The vertical displacements are measured relative to the point B as described in Figure (6.29) and normalized with respect to the footing half-width *a* = 5.0 ft. For values of -*Y/R* ≤ 0.1, the difference in the computed displacements between the two solution procedures ranges between 5%, at -*Y/R* = 0.0, to 8% occurring at -*Y/R* = 0.1. For values of -*Y/R* > 1.0, the displacements obtained using the coupled BEM-FEM method are significantly greater than

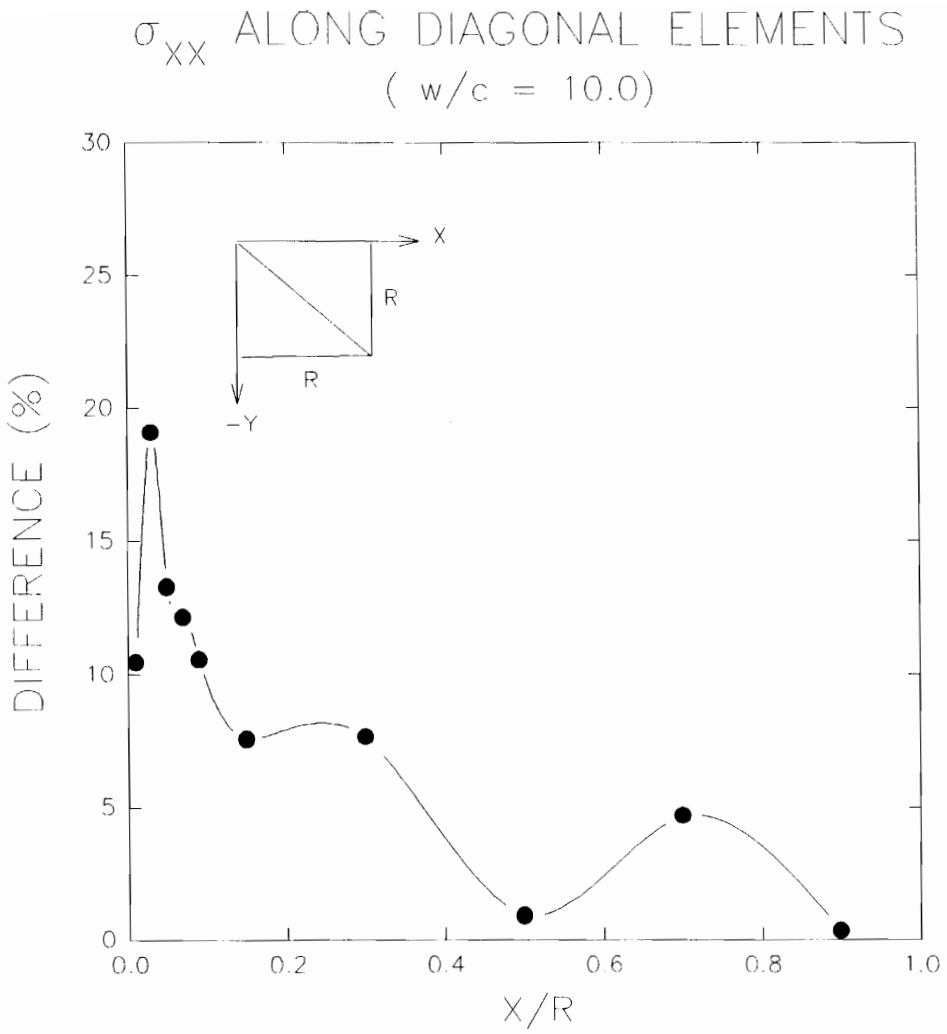

Figure 6.32. σ_{xx} along diagonal elements with w/c = 10.0 for elasto-plastic footing problem 3.

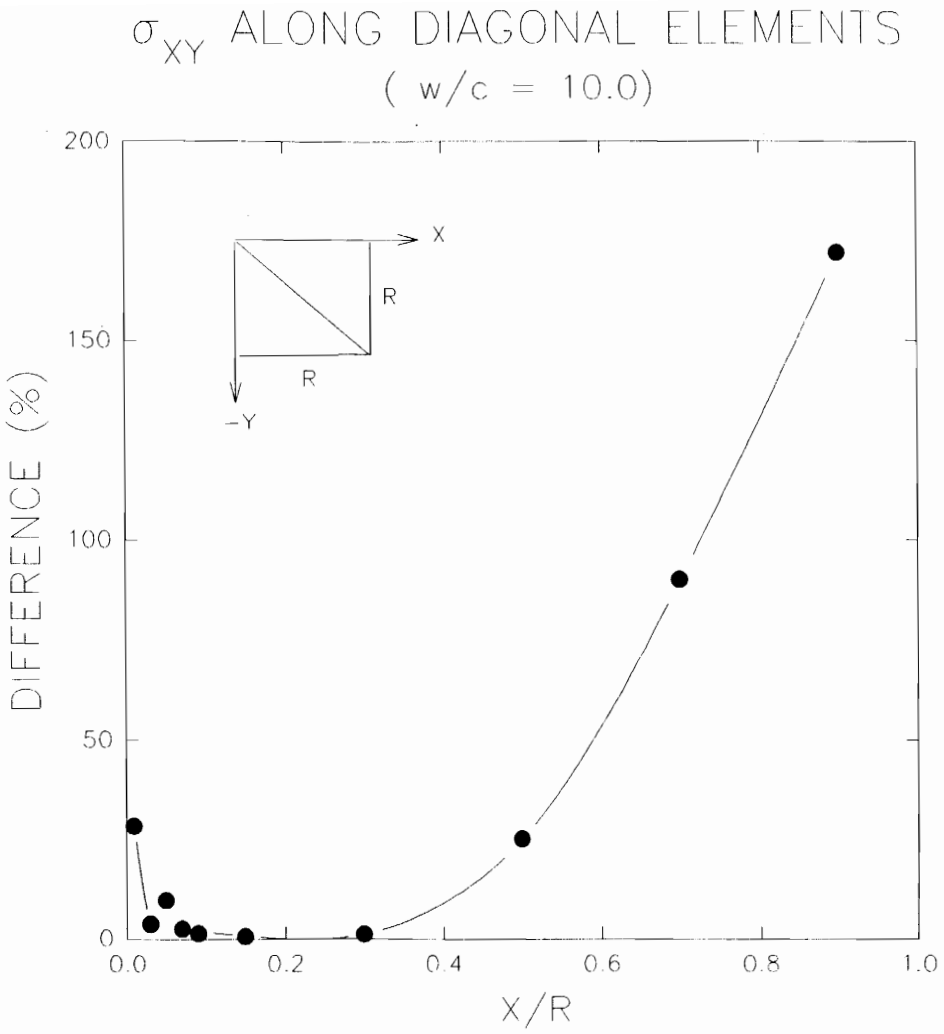

Figure 6.33. σ_{xy} along diagonal elements with w/c = 10.0 for elasto-plastic footing problem 3.

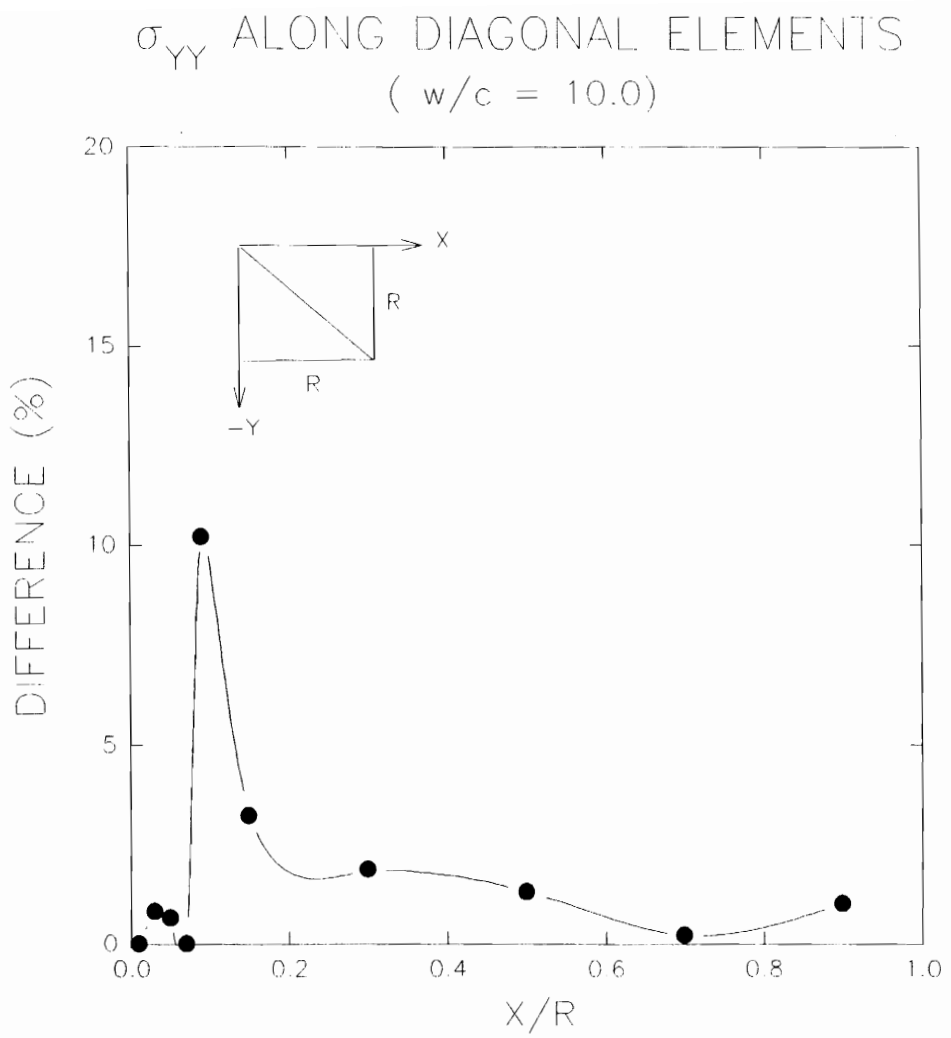

Figure 6.34. σ_{yy} along diagonal elements with w/c = 10.0 for elasto-plastic footing problem 3.

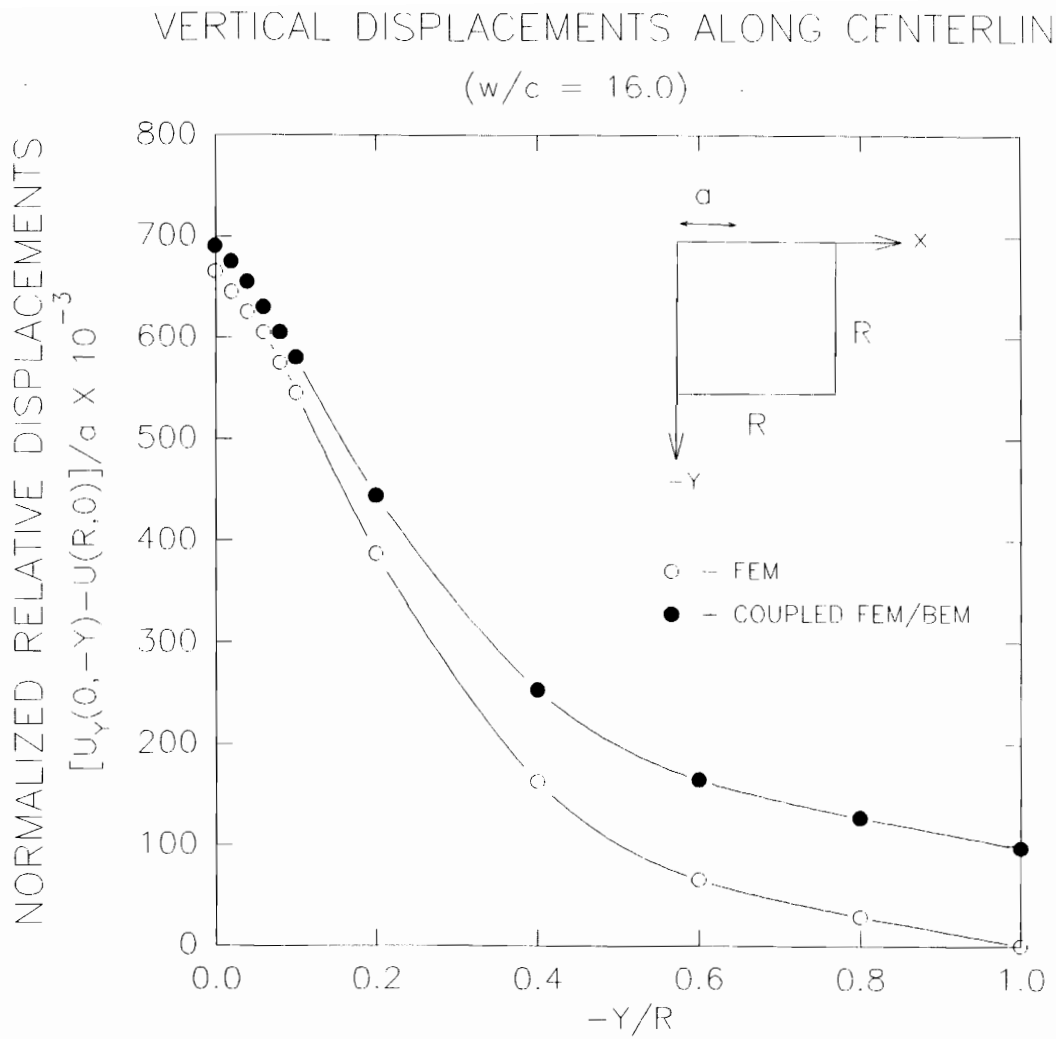

Figure 6.35. Vertical displacements along centerline with w/c = 16.0 for elasto-plastic footing problem 3.

those obtained using only the finite element method. The difference in the computed displacements ranges from 12% at $-Y/R = 0.2$, to 100% at $-Y/R = 1.0$.

Figure (6.36) shows the vertical displacement along the surface of the soil domain plotted versus the normalized coordinates X/R. This figure shows that along the surface, the coupled BEM-FEM method results in larger displacements as compared to the finite element method. Underneath the footing corresponding to values of $X/R < 0.1$, the difference in displacements obtained using the two solution procedure are within 5%. For values of $X/R \geq 0.1$, the displacement obtain using the coupled BEM-FEM method are significantly greater than those obtained from the finite element solution. The difference ranges from 20% at $X/R = 0.1$, to 60% at $X/R = 0.8$.

These results together with those presented for $w/c = 10.0$ show that the difference in the vertical displacements within the proximity of the applied load is smaller as compared to the elastic case. This is due to the fact that in the finite element solution, yielding takes place at a lower load w/c. Thus for a given load w/c, the finite element solution is in the later stages of yielding and has developed larger plastic displacements as compared to the solution obtained from the coupled BEM-FEM solution. As the yielding progresses, the difference in the plastic displacements between the two methods increases. This offsets the effect of the larger elastic displacements resulting from the coupled BEM-FEM method are gives smaller differences in the computed vertical displacements.

Stress Along Diagonal Elements at w/c = 16.0: Figure (6.37) shows the difference in σ_{xx} for elements lying along the diagonal of the mesh plotted versus the normalized coordinates X/R. Near the centerline ($X/R \leq 0.03$), the solution procedures result in values of σ_{xx} which differ by at most 16%. For values of $X/R > 0.03$ the difference in σ_{xx} computed using the two solution procedures is within 10%.

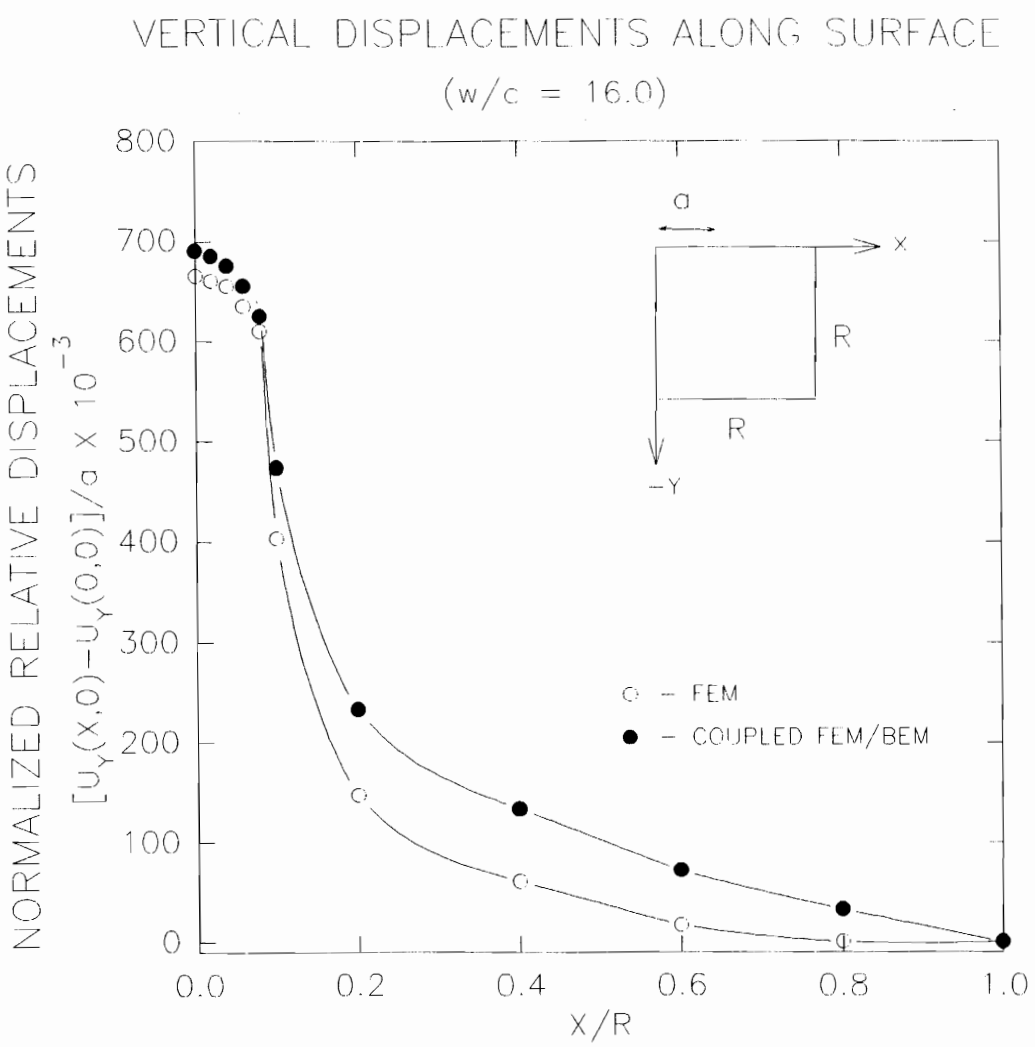

Figure 6.36. Vertical displacements along surface with w/c =16.0 for elasto-plastic footing problem 3.

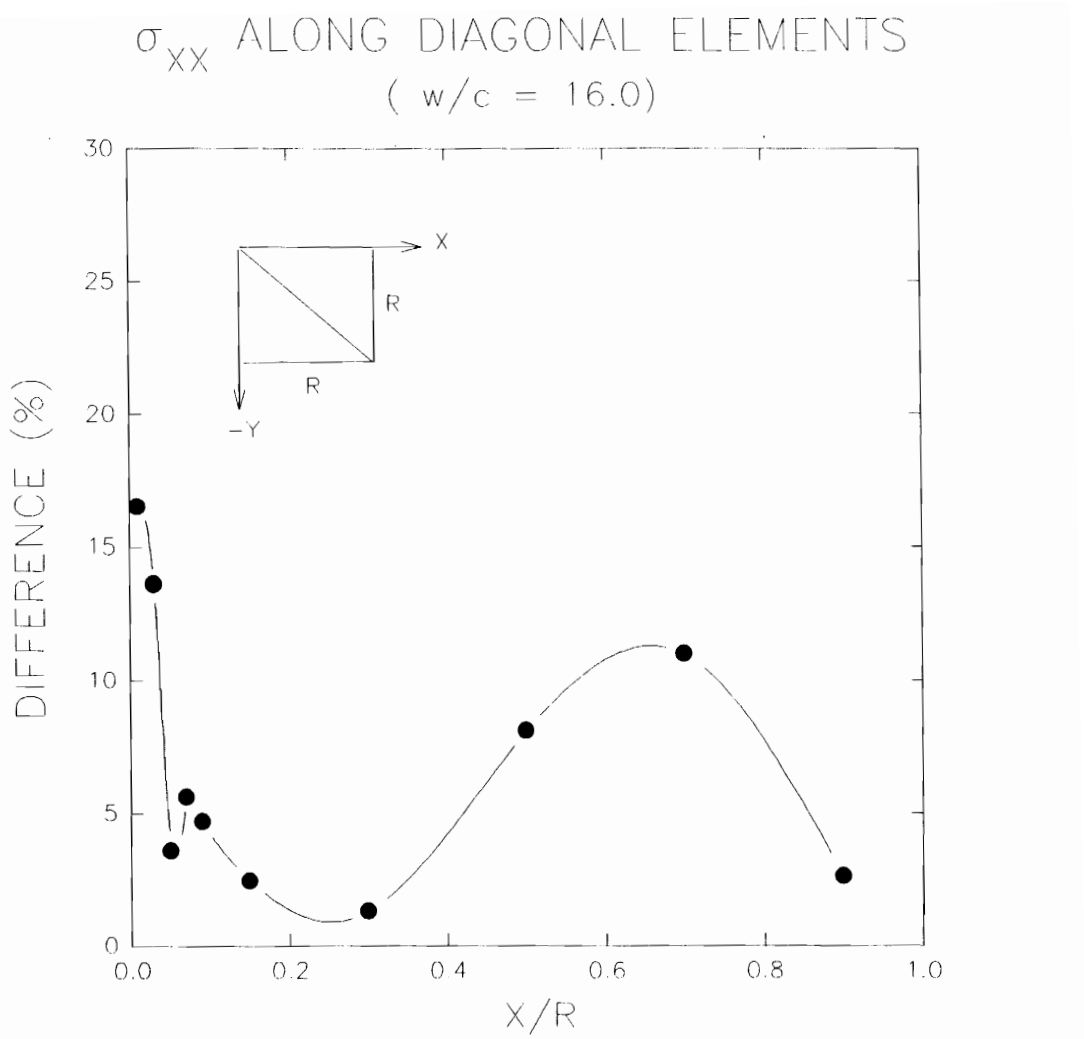

Figure 6.37. σ_{xx} along diagonal elements with w/c = 16.0 for elasto-plastic footing problem 3.

Figure (6.38) shows the difference in σ_{xy} for elements lying along the diagonal of the mesh plotted versus the normalized coordinates *X/R*. For values of *X/R* ≤0.3, the difference in the values of σ_{xy} obtained using the two solution techniques is within 50%. However for values of *X/R* > 0.3, the difference in the value of σ_{xx} obtained using the two solution procedures is significantly larger and steadily increases from 25% at *X/R* = 0.5 to 160% at *X/R* = 0.9.

Figure (6.39) shows the difference in σ_{yy} for elements lying along the diagonal of the mesh plotted versus the normalized coordinates *X/R*. With the exception of *X/R* = 0.09, the difference in σ_{yy} obtained between the two solution procedures is within 3%. At *X/R*, the difference is 11%.

Figure (6.40) shows spread of the plastic zones in the finite element solution. The spread of the plastic zones in the coupled BEM-FEM method is shown in Figure (6.41). For *w/c* = 10.0, the plastic zone formed in the finite element solution extend to a depth 25% more as compared to that formed in the coupled BEM-FEM method. The lateral extent of the plastic zones form in both solution is roughly the same For *w/c* =16.0, the plastic zone formed in both the coupled BEM-FEM and finite element solution extend to approximately the same with respect to the lateral extent and depth. This observation is consistent with the fact that the stresses, particularly, values of σ_{xx} and σ_{yy} in plastic zone do not differ significantly between the two solution techniques.

It is observed in this particular problem that the differences in the values of σ_{xx} and σ_{yy} obtained using the two solution procedures are smaller than those observed in the elastic case even at point where the stresses are still in the elastic range.

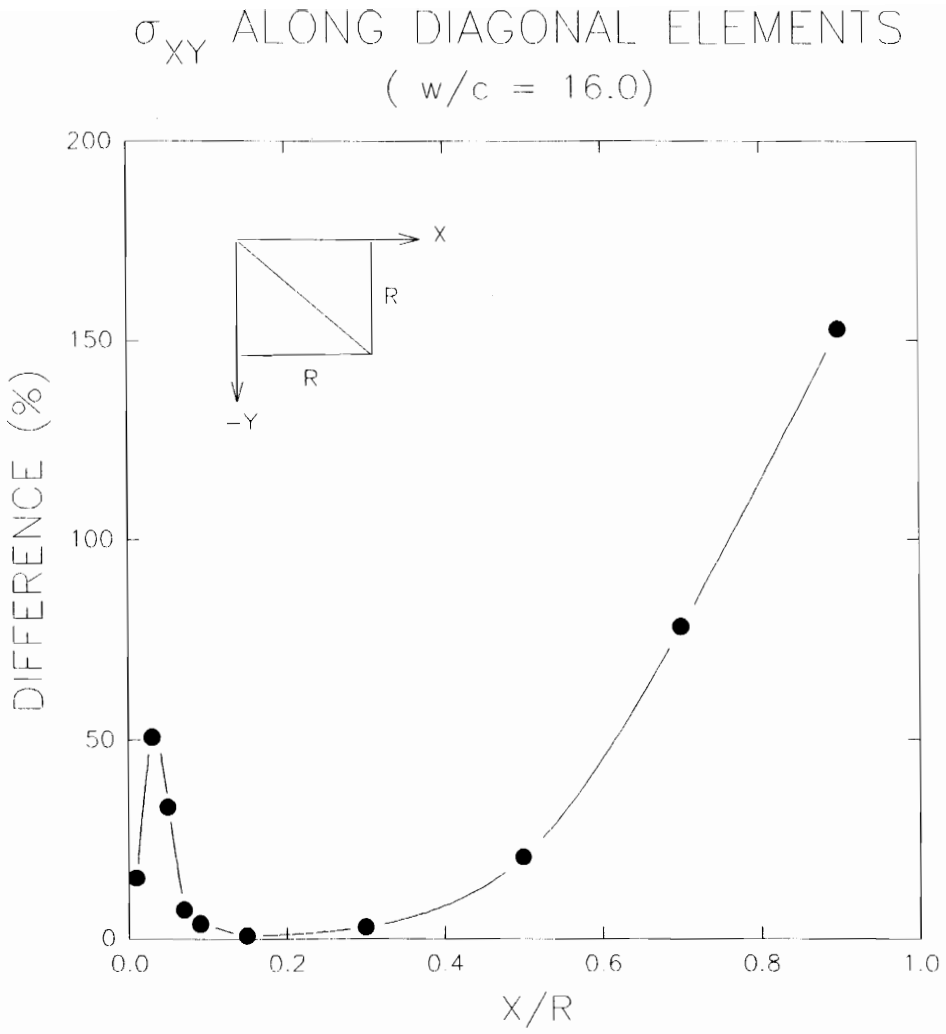

Figure 6.38. σ_{xy} along diagonal elements with w/c = 16.0 for elasto-plastic footing problem 3.

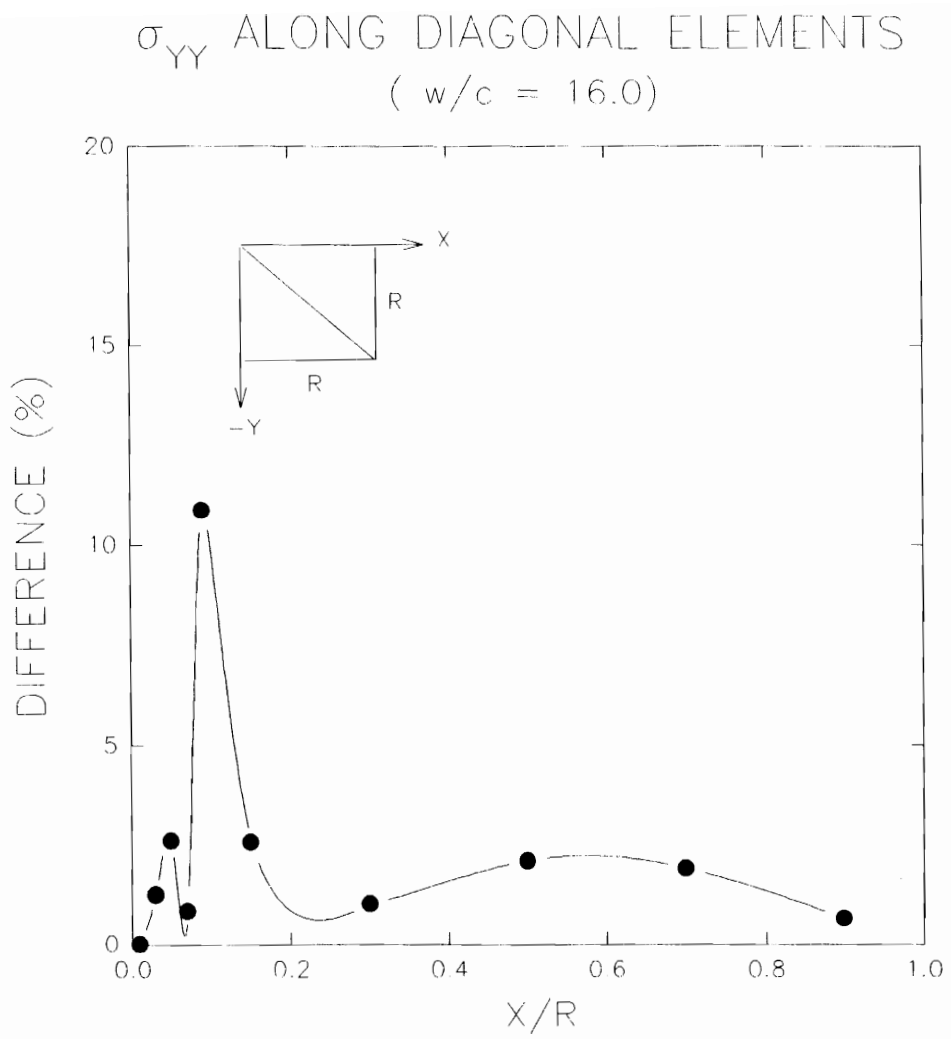

Figure 6.39. σ_{yy} along diagonal elements with w/c = 16.0 for elasto-plastic footing problem 3.

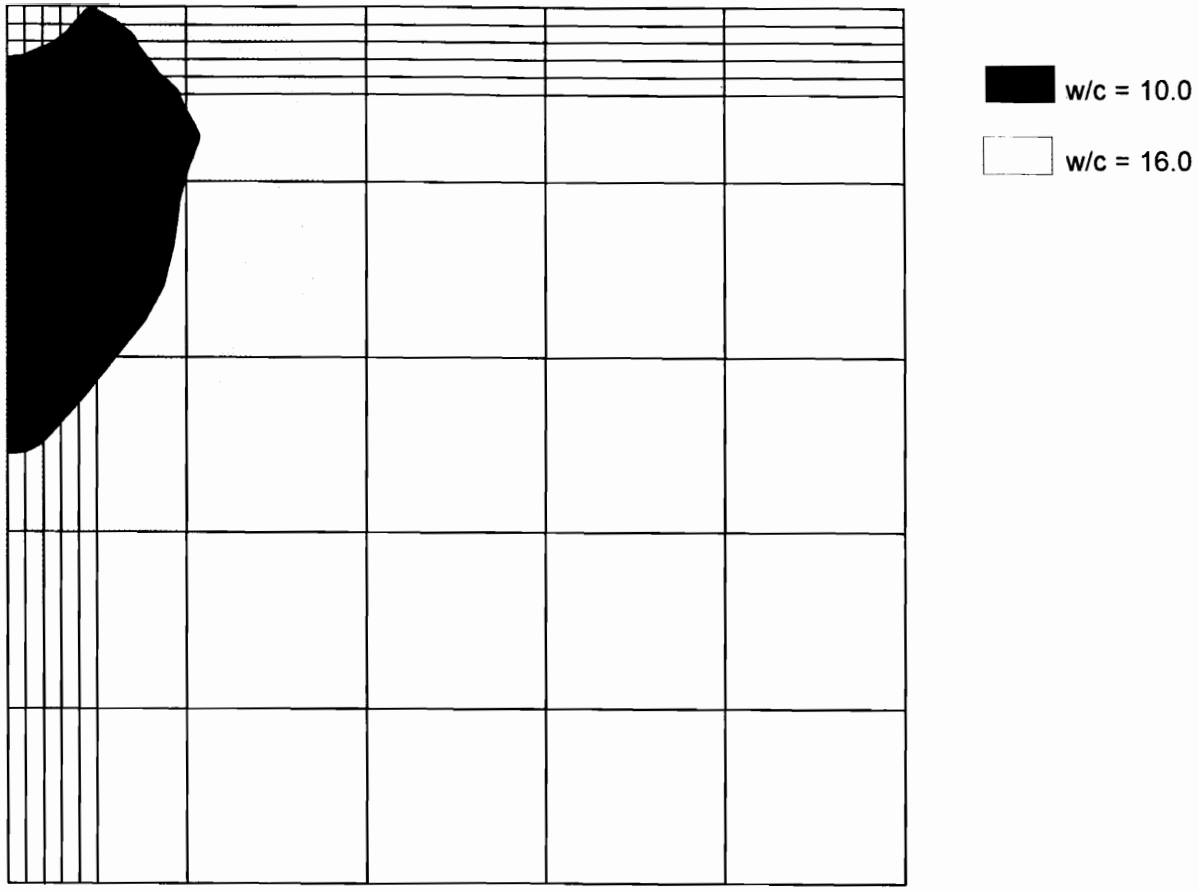

Figure 6.40. Spread of plastic zones for elasto-plastic footing problem 3 using the finite element method alone.

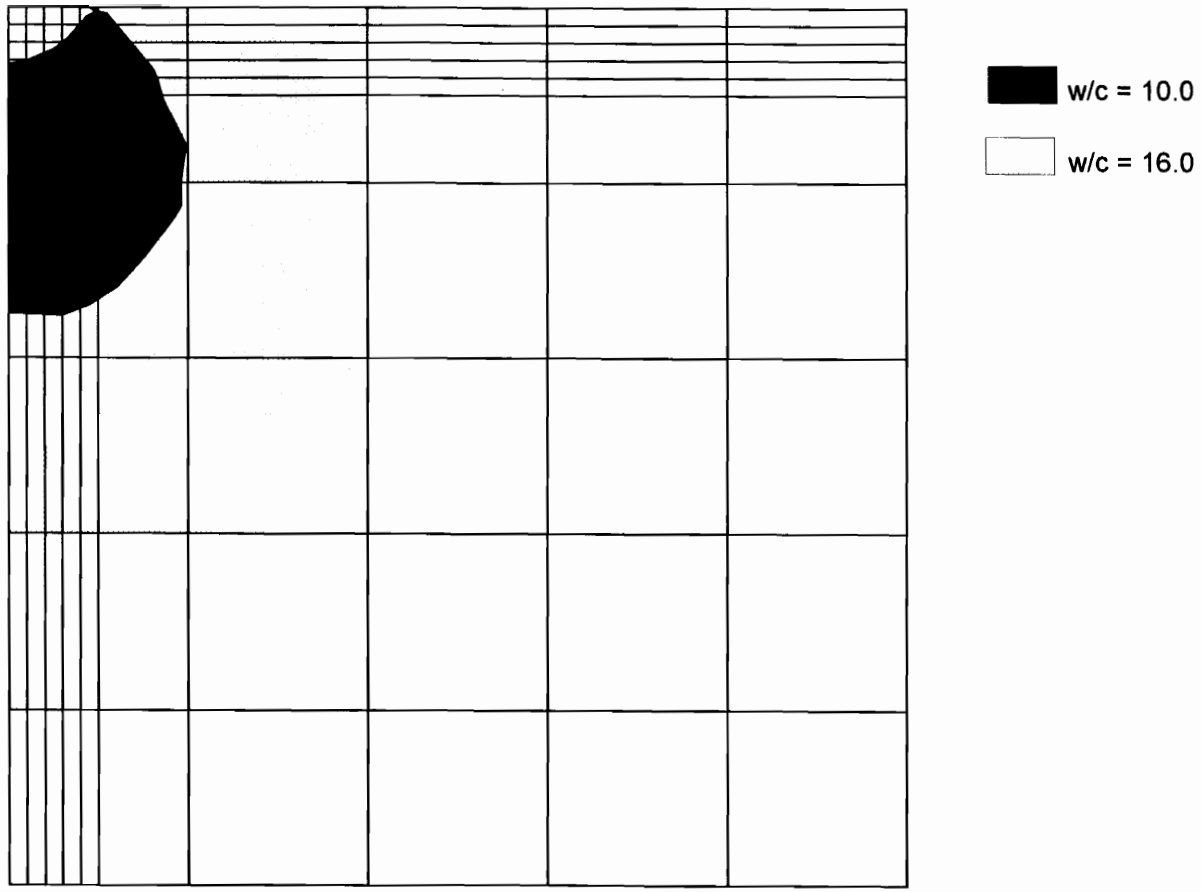

Figure 6.41. Spread of plastic zones for elasto-plastic footing problem 3 using the coupled finite element-boundary element method.

6.6 RANKINE PASSIVE PRESSURE PROBLEM

This problem consists of a smooth wall which is allowed to translate horizontally into a mass of sand. For the passive case, the wall is moved into the soil mass. For the problem solved in this section, as well as the succeeding section, the sand is assumed to have the following elastic parameters: $E = 10^5$ kN/m^2 and $\nu = 0.3$. The dry unit weight of the soil γ is assumed to be equal to 20 kN/m^3. The sand is assumed to be cohesionless with a angle of internal friction equal to $\phi = 30°$. The geometry of the problem as well as the finite element mesh used in the solution are shown in Figure (6.42).In this figure, the soil is assumed to be 5.0 m. long and 2.0 m. deep, while the height of the wall used is 1 m. To examine the effects of the infinite the boundary, two analysis are performed. In the first analysis, the problem is solved using only the finite element method. In this solution, 196 quadrilateral elements are used to model the soil domain. In the second analysis, the coupled BEM-FEM method is used. The location of the boundary elements in the mesh used in this analysis are shown in Figure (6.43). This same problem was solved by Griffith (1988) using quadratic elements and assuming a non-associated Mohr-Coulomb plasticity model. In both analysis performed, the non-associated Drucker Prager model is used. The Drucker-Prager parameters are obtained from the strength parameter using equations (6.1) and (6.2). An error tolerance of in the residual norm of $\varepsilon_{tol} = 10^{-5}$ is adopted. The solution procedure terminated when the residual norm a $\|\mathbf{R}\| \geq \varepsilon_{tol}$ occurred after 25 iterations. Following the application of each displacement increment, the solution converged within 5 iterations. In both analyses, the initial stresses in the sand mass are computed prior to the application of the load using equations (6.5) and (6.6) assuming an at-rest stress state.

The load is applied by displacing horizontally the wall in increments of $\delta = 2.0 \times 10^{-5}$. As the displacements are incrementally applied, the passive force P_p by taking the average horizontal normal stress σ_{xx} along the gauss points adjacent to the wall, and

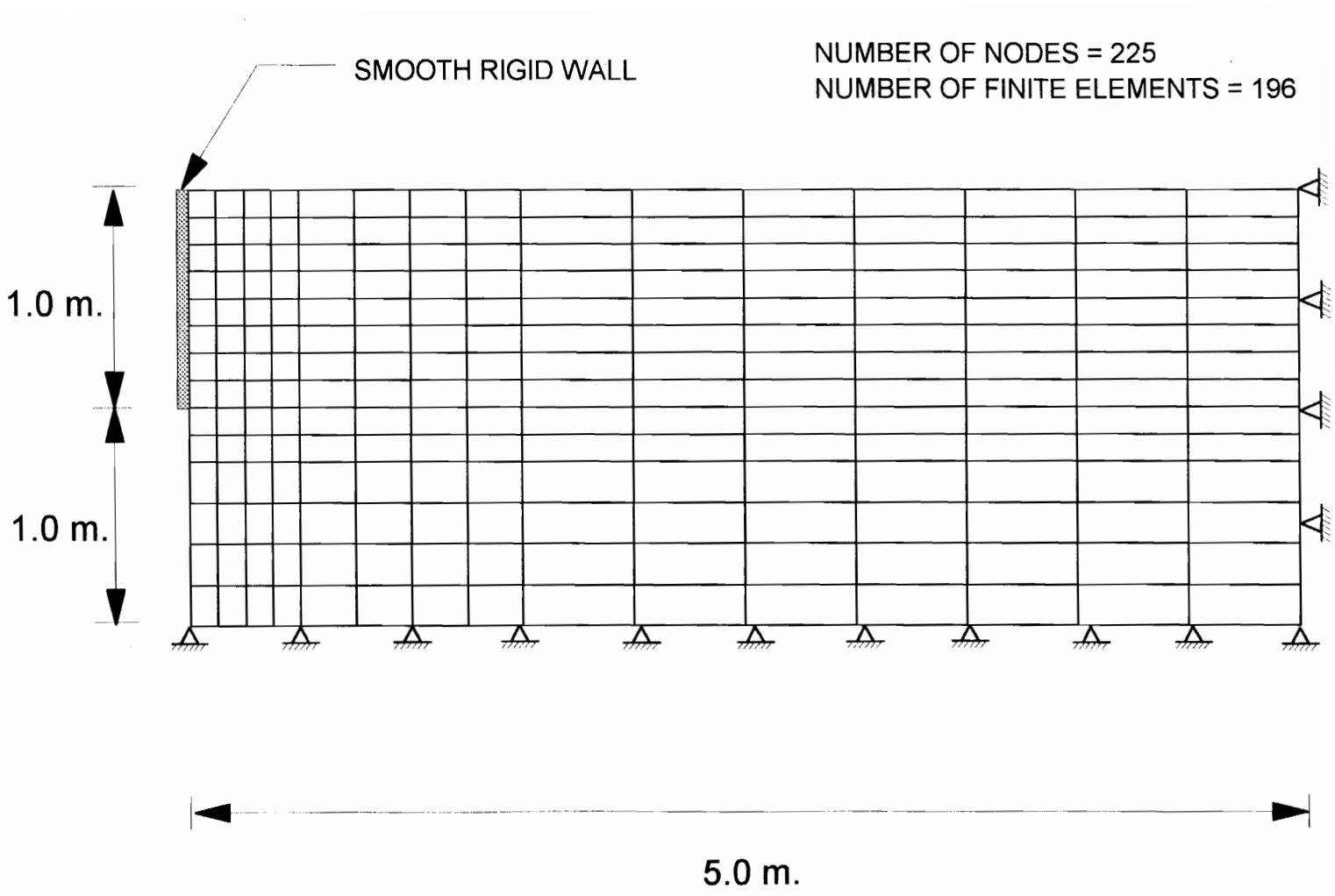

Figure 6.42. Finite element mesh used in Passive Rankine Analysis.

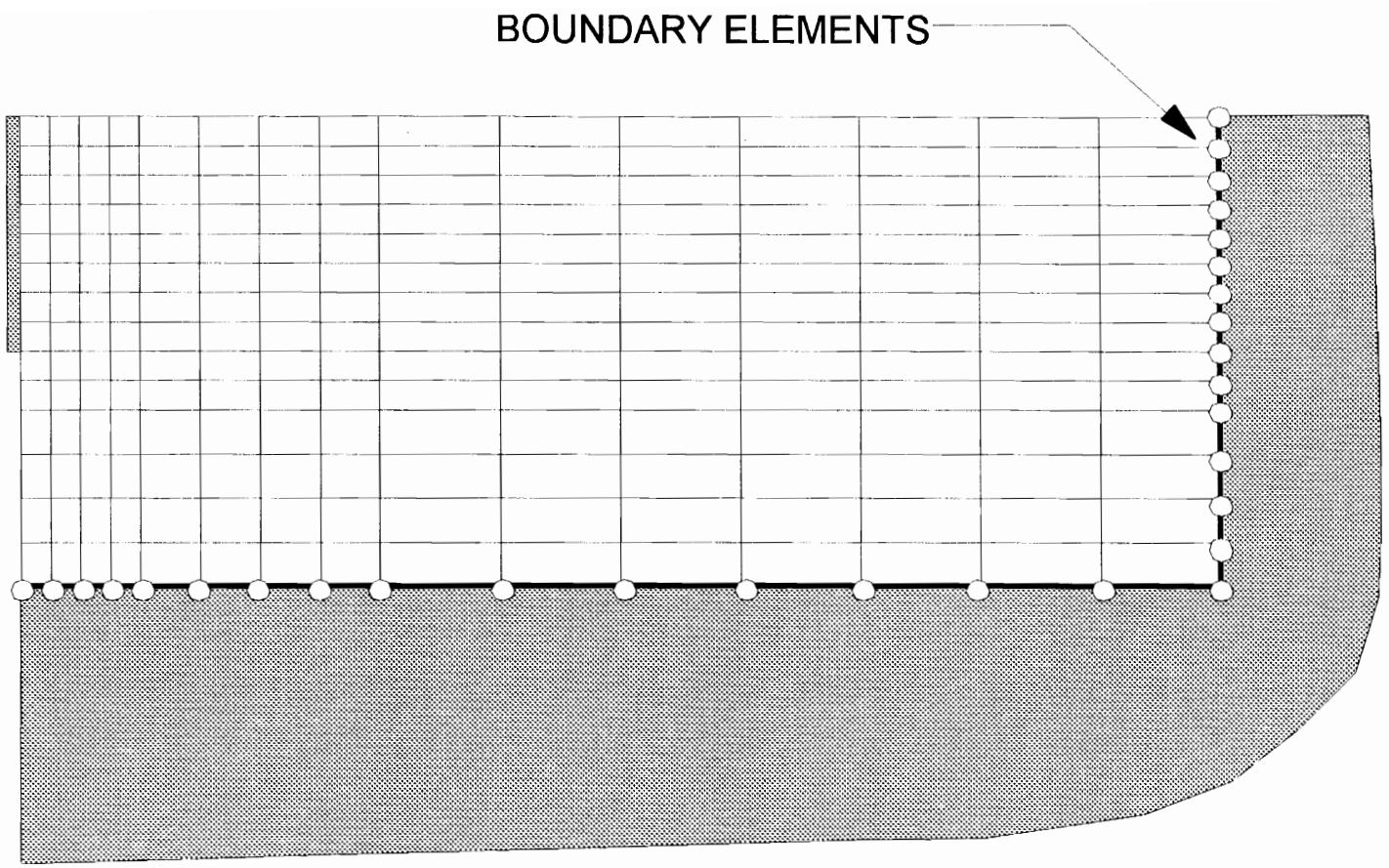

Figure 6.43. Coupled boundary element - finite element mesh used in Passive Rankine Analysis.

multiplying this average value by the wall height H = 1 m. The limit load given by the Rankine earth pressures theory (Bowles, 1988) is:

$$P_p = \frac{1}{2}\gamma H^2 K_p \tag{6.8}$$

where K_p is the passive earth pressure coefficient. For a flat backfill with no cohesion and an angle of internal fiction ϕ = 30°, K_p = 3.0, and thus for the given problem, P_p = 30.0 kN/m.

Figure (6.44) shows the variation in passive force P_p plotted versus the normalized horizontal movement of the wall Δ/H. This figure shows that in the finite element solution, the passive earth pressure state is reached at $\Delta/H = 7.0 \times 10^{-4}$. The passive force computed using the finite element solution is equal to P_p = 30.16 kN/m. For the coupled BEM-FEM method, the passive earth pressure state is reached at $\Delta/H = 1.0 \times 10^{-3}$. The increased horizontal movement required to mobilized the passive stress state is due to the additional flexibility resulting from the infinite boundary. In the coupled BEM-FEM method, the computed passive force is P_p = 30.24 kN/m. In this finite element solution obtained by Griffith, a value of P_p = 30.6 kN/m was computed.

Figure (6.45) shows the normalized passive earth pressure at failure along the face of the wall plotted with respect to the normalized coordinates Z/H, where Z is the distance from the base of the wall, and H = 1.0 is the wall height. The pressure distribution obtained using the finite element method varies linearly with depth. The coupled BEM-FEM method, the lateral pressures gives larger values of lateral earth pressure for values of $Z/H <$ 0.2. The difference is greatest at Z/H = 0.0625 where the pressure obtained using the coupled BEM-FEM method is 10% greater than that obtained using only the finite element method. For values of $Z/H >$ 0.2, the coupled BEM-FEM method gives

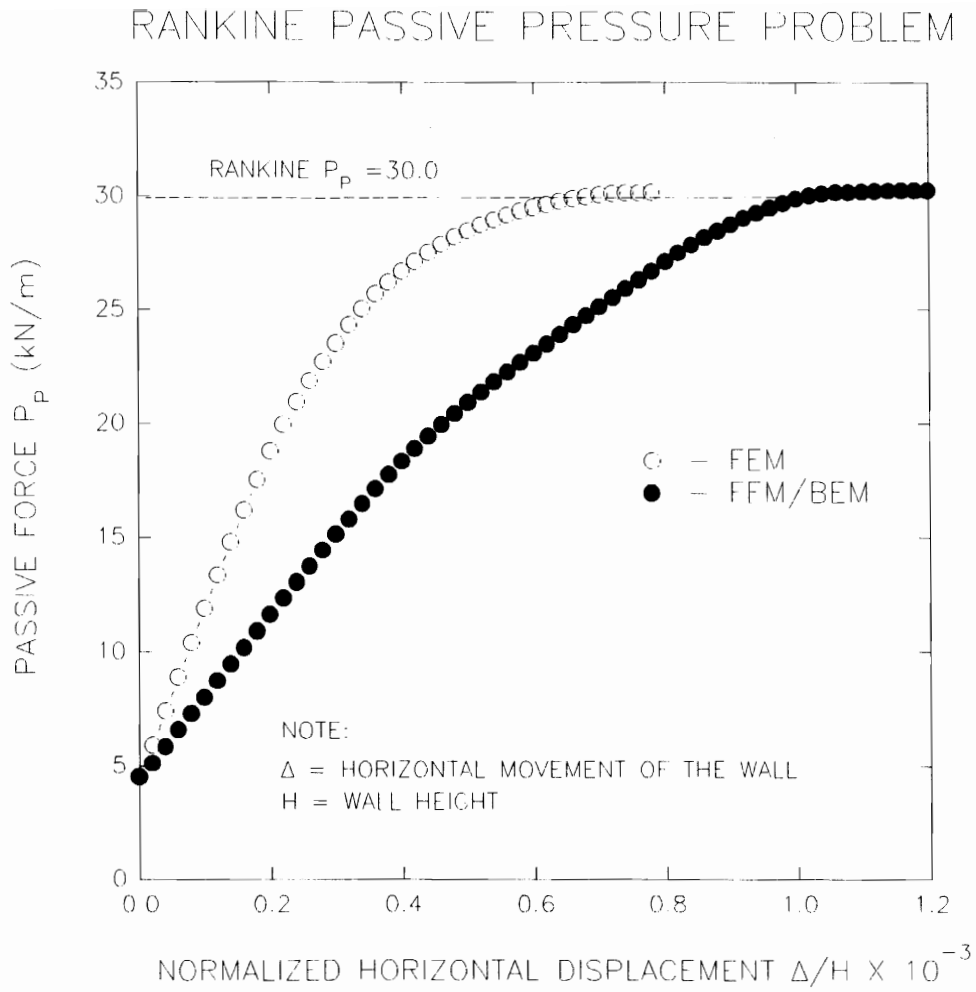

Figure 6.44. Passive force in Rankine Passive Pressure Problem.

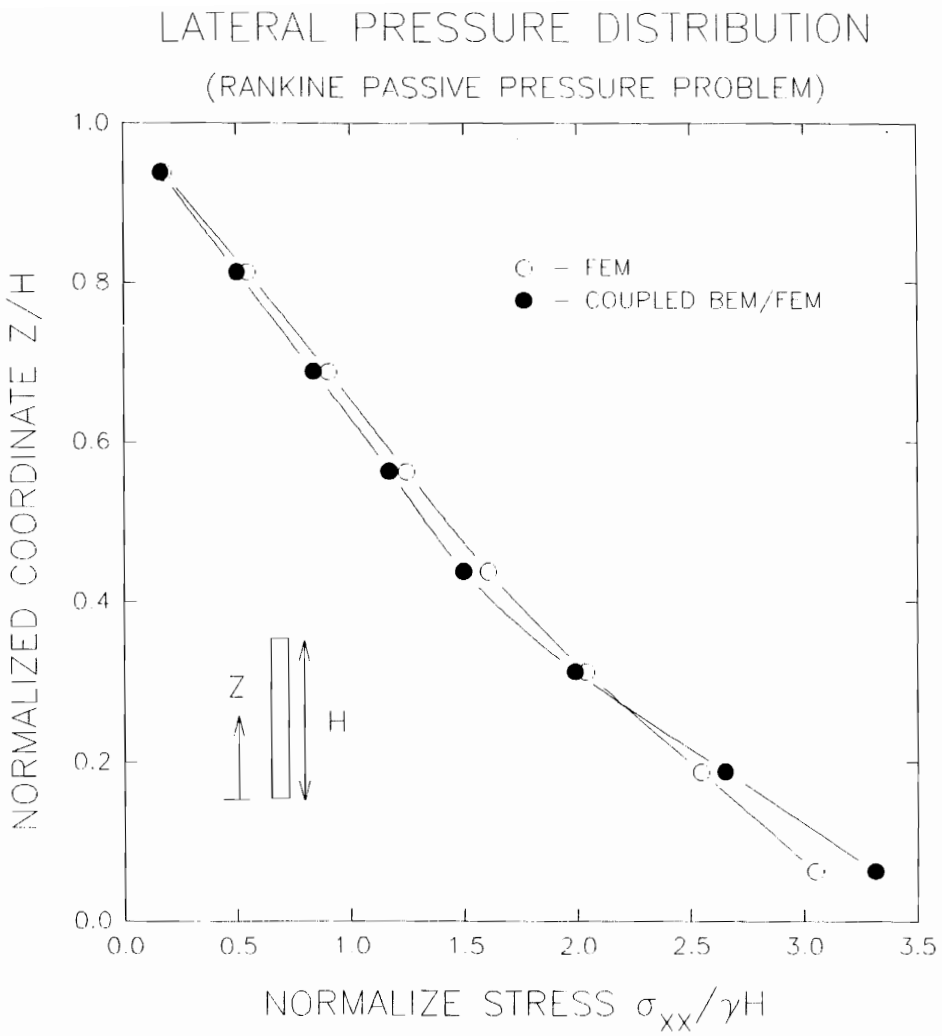

Figure 6.45. Lateral earth pressure distribution at failure for Rankine Passive Pressure Problem.

lower values of lateral earth pressures. However, the difference between the lateral pressures obtained using the two solution techniques is at most 4%.

Figures (6.46) and (6.47) show the plastic zones formed at failure in the finite element solution and coupled BEM-FEM solution. An element is said to fail if failure occurred at three of more gauss points within the element. Based on the Rankine earth pressure theory, the failure in this problem occurs along a plane inclined at an angle of 45° -ϕ/2 with the horizontal. In both cases, the plastic zones formed fall slightly outside the predicted failure plane. For the coupled BEM-FEM solution, plastic zone formed extends slightly further passed the predicted failure plane near the base of the wall as compared to the finite element solution. Aside from this, no other differences are observed in the plastic zones formed between the two solution procedures used.

6.7 RANKINE ACTIVE PRESSURE PROBLEM

The analyses performed on the lateral earth pressure problem described in the previous section is repeated assuming an active state of stress. This moving the wall away from the soil mass. The same material properties, geometry, meshes and convergence criteria used in the previous section are also used in solving the active pressure problem in this section.

The load is applied by displacing horizontally the wall in increments of $\delta = 2.0 \times 10^{-6}$. As the displacements are incrementally applied, the active force P_a by taking the average horizontal normal stress σ_{xx} along the gauss points adjacent to the wall, and multiplying this average value by the wall height H = 1 m. The limit load given by the Rankine earth pressures theory (Bowles, 1988) is:

$$P_a = \frac{1}{2}\gamma H^2 K_a \tag{6.9}$$

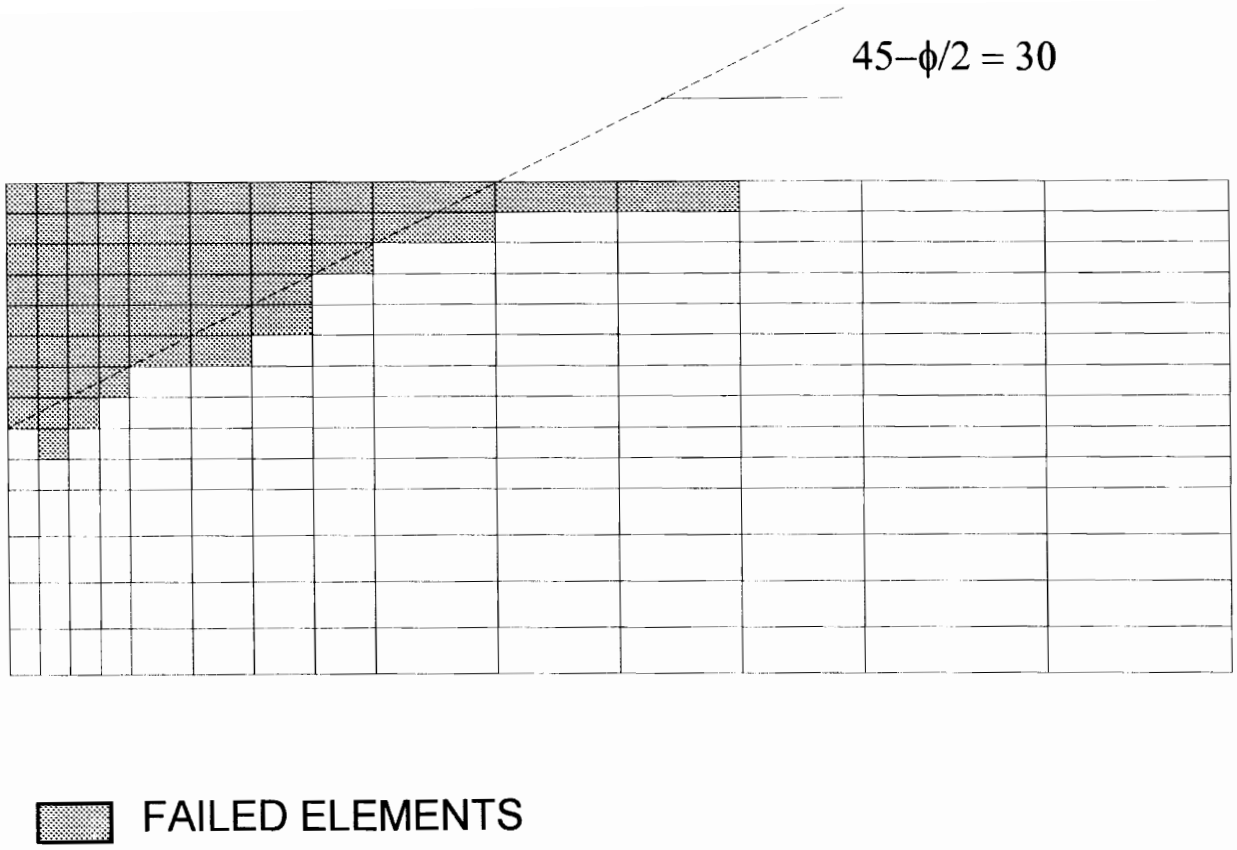

Figure 6.46. Plastic zone at failure in finite element solution for Rankine Passive Pressure Problem.

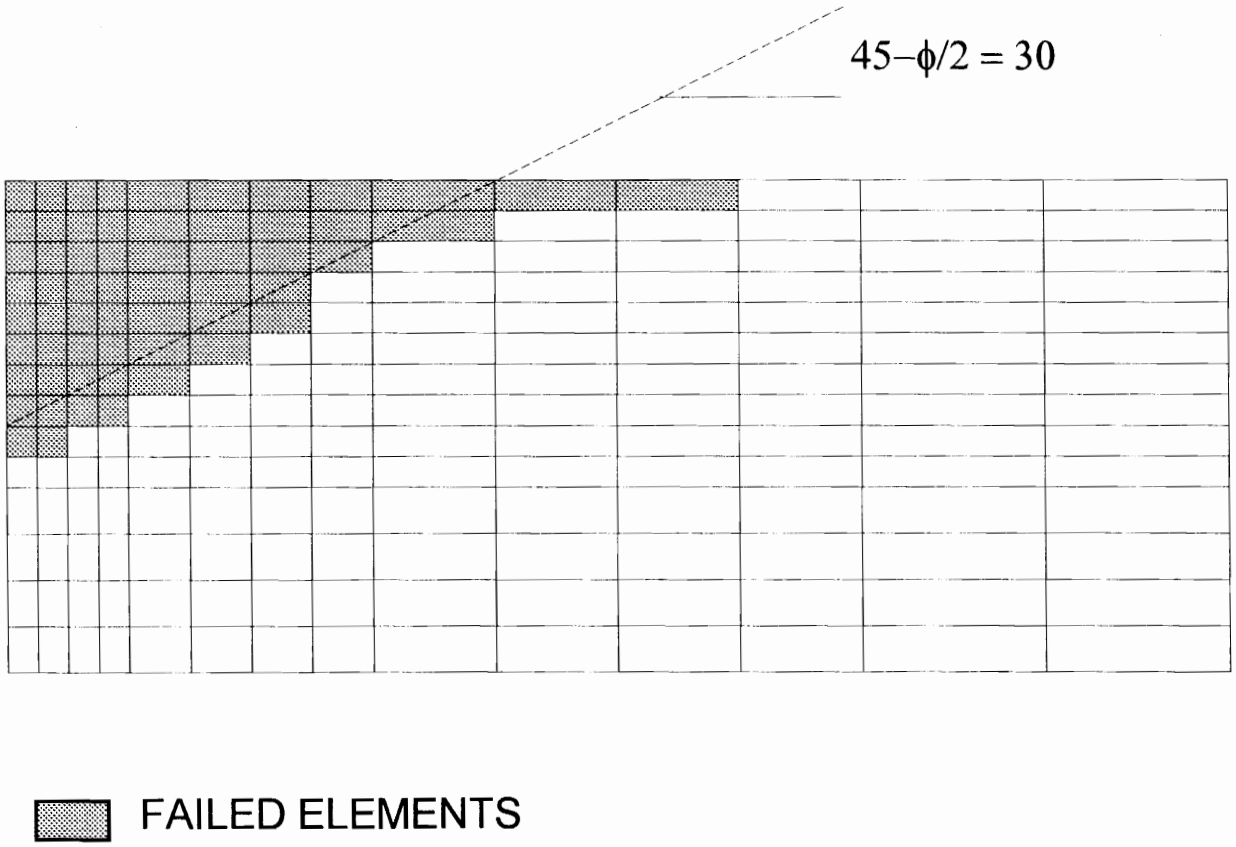

Figure 6.47. Plastic zone at failure in coupled BEM-FEM solution for Rankine Passive Pressure Problem.

where K_p is the active earth pressure coefficient. For a flat backfill with no cohesion and an angle of internal fiction $\phi = 30°$, $K_a = 3.0$, and thus for the given problem, $P_a = 3.333$ kN/m.

Figure (6.48) shows the variation in passive force P_a plotted versus the normalized horizontal movement of the wall Δ/H. This figure shows that in the finite element solution, the active earth pressure state is reached at $\Delta/H = 1.0 \times 10^{-4}$. The active force computed using the finite element solution is equal to $P_a = 3.34$ kN/m. For the coupled BEM-FEM method, the active earth pressure state is reached at $\Delta/H = 2.0 \times 10^{-4}$. The increased horizontal movement required to mobilized the active stress state is due to the additional flexibility resulting from the infinite boundary. In the coupled BEM-FEM method, the computed passive force is $P_a = 3.35$ kN/m.

Figure (6.49) shows the normalized active earth pressure at failure along the face of the wall plotted with respect to the normalized coordinates Z/H, where Z is the distance from the base of the wall, and $H = 1.0$ is the wall height. The coupled BEM-FEM method, the lateral pressures gives slightly larger values of lateral earth pressure for values of $Z/H < 0.2$. The difference is greatest at $Z/H = 0.0625$ where the pressure obtained using the coupled BEM-FEM method is 2% greater than that obtained using only the finite element method. For values of $Z/H > 0.2$, the coupled BEM-FEM method gives values of lateral earth pressures which the same as those obtained using the finite element solution.

Figures (6.50) and (6.51) show the plastic zones formed at failure in the finite element solution and coupled BEM-FEM solution. An element is said to fail if failure occurred at three of more gauss points within the element. Based on the Rankine earth pressure theory, the failure in this problem occurs along a plane inclined at an angle of $45° + \phi/2$ with the horizontal. Comparing these two figures reveals that the plastic zones

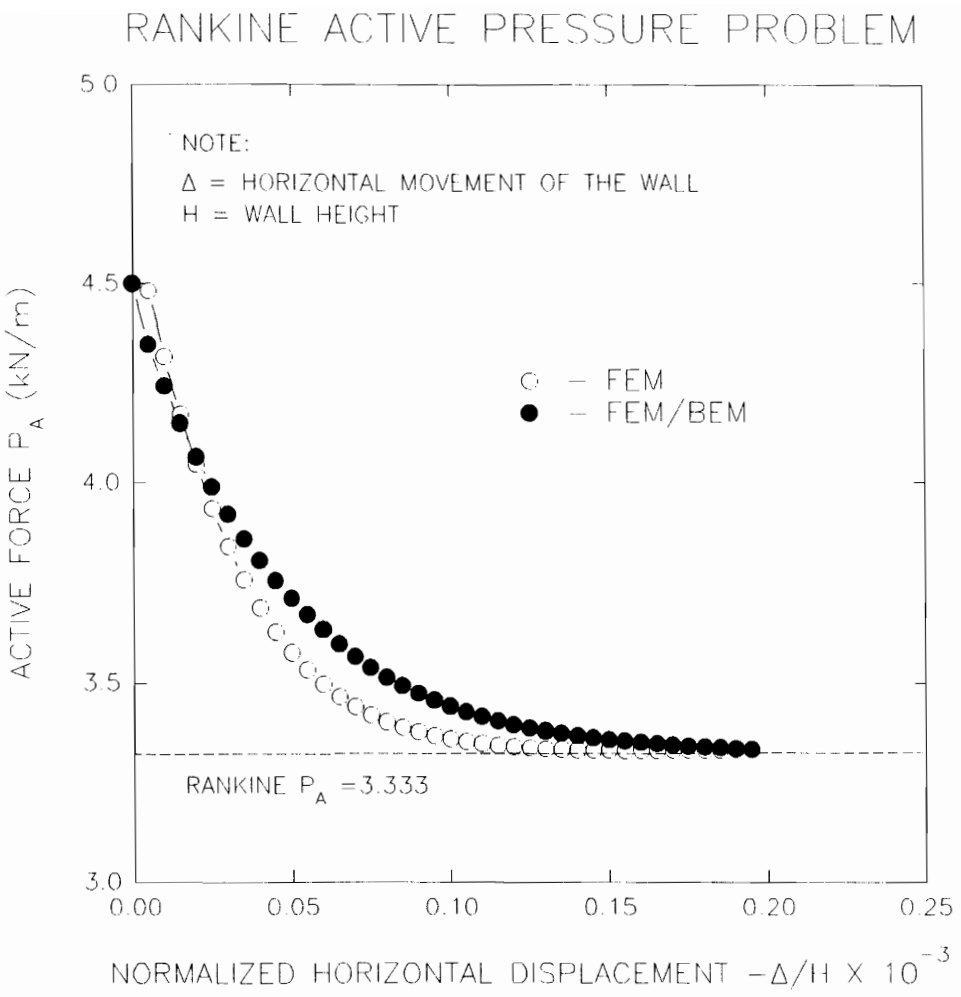

Figure 6.48. Active force in Rankine Active Pressure Problem.

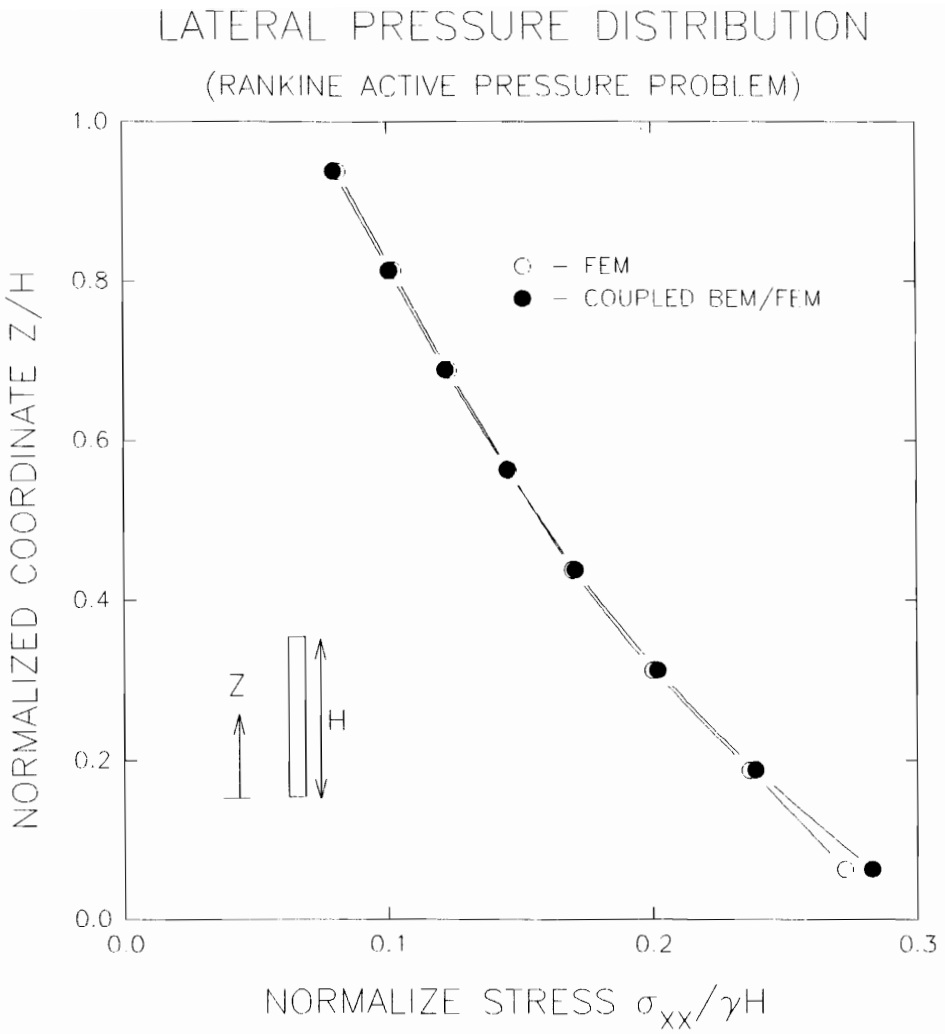

Figure 6.49. Lateral pressure distribution in Rankine Active Pressure Problem.

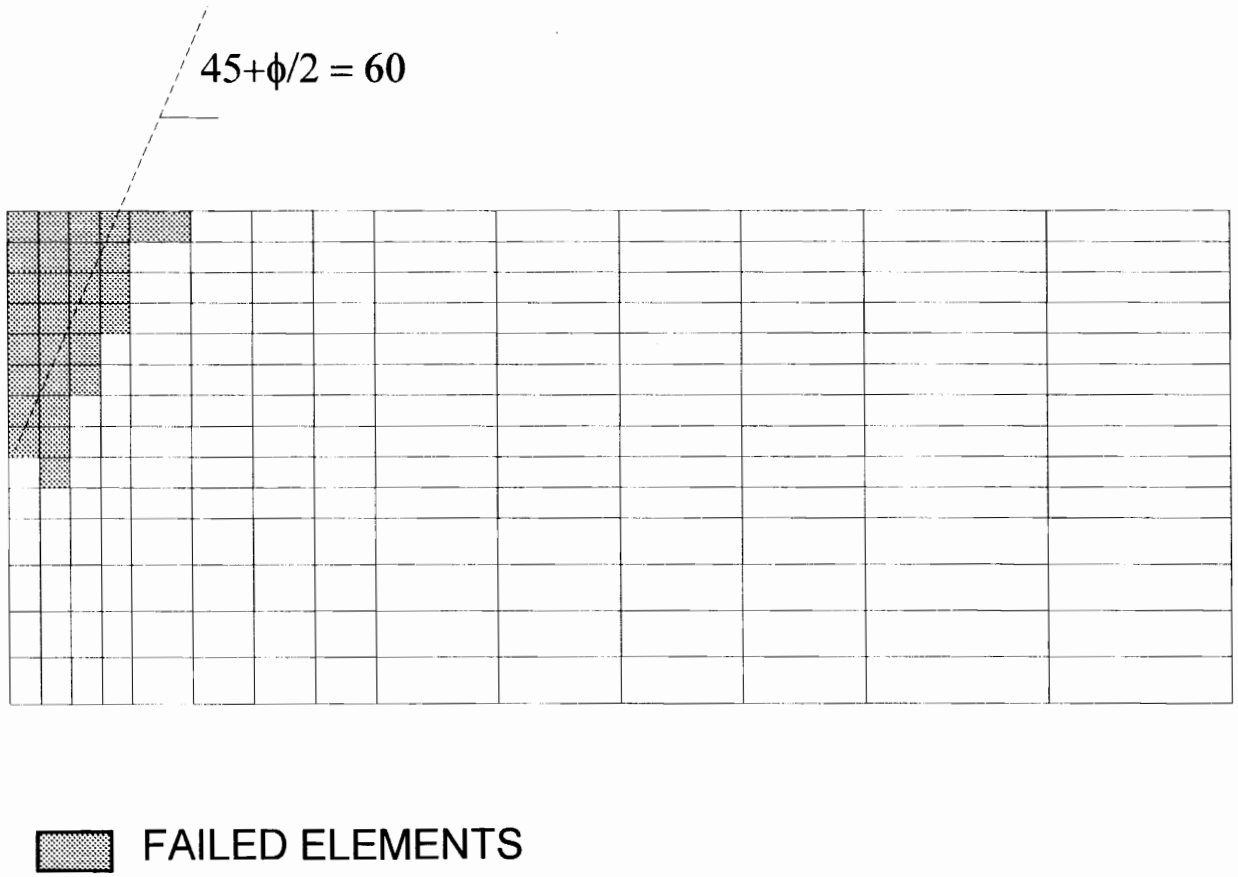

Figure 6.50. Plastic zone at failure in finite element solution for Ranking ActivePressure Problem.

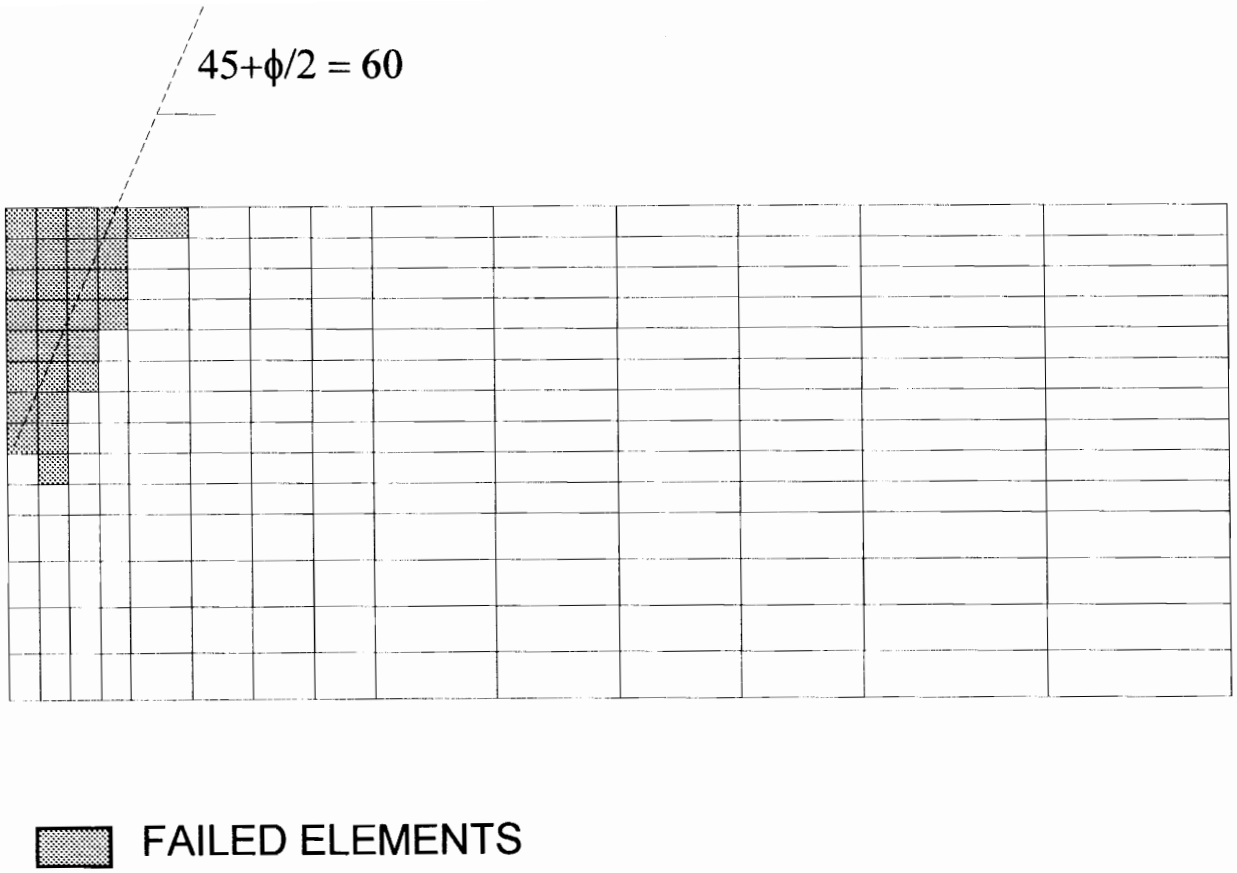

Figure 6.51. Plastic zone at failure in coupled BEM-FEM solution for Ranking ActivePressure Problem.

formed in each of the solution procedures is the same. In both cases, the plastic zone extends slightly outside of the predicted failure plane.

6.8 SUMMARY

In this chapter, the effects of the infinite boundary on the solution of elasto-plastic bearing capacity problems were studied. The effects of the infinite boundary were accounted for in the finite element solution using the coupled BEM-FEM method.

For frictionless soils, where the effects of weight of the soil were neglected, the infinite boundary did not significantly affect the computed bearing capacity. As with the elastic case, the infinite boundary resulted in larger elastic displacements. However, at the load level at which initial yielding occurrs, the infinite boundary resulted in smaller plastic displacements for points located near the applied load. Thus for these points, the combination of the larger elastic displacement together with the smaller plastic displacements results in total displacements which were approximately the same as those obtained when the infinite boundary was neglected. Near the limit load, the infinite boundary resulted in both larger elastic and plastic displacements. The resulting total displacements were 20% greater than those obtained when the infinite boundary is neglected.

For soils with friction, taking into consideration the infinite boundary results in bearing capacities which were slightly larger than those obtained neglecting the infinite boundary. Also, taking into consideration the infinite boundary resulted in a higher load level at which yielding took place. Because of this, the solution where the infinite boundary was neglected was in a later stage of yielding and had greater plastic displacements as compared to the solution where the infinite boundary was accounted for. This effect slightly offset the larger elastic displacements resulting from the infinite boundary. Thus, for points where plastic yielding occurrs, taking into account the infinite

boundary resulted in vertical displacements which were between 5% and 10% greater than those obtained when the infinite boundary was neglected.

For the case where the effects of the self-weight of the soil were neglected, the effect of the infinite boundary on the computed stresses was similar to that observed in the elastic case. When the effect of the soil's self-weight was taken into consideration, the effects of the infinite boundary on the computed values of σ_{xx} and σ_{yy} became less pronounced even for points where the stresses were still in the elastic range.

In the analysis of the Rankine pressure problems, it was noted the wall movements when the infinite boundary was taken into accounted needed to reach both the passive and active states were respectively 45% and 100% greater than those required when the infinite boundary was neglected However, both the passive and active Rankine force computed are unaffected by the infinite boundary. Taking into consideration the effects of the infinite boundary results in lateral pressures along the wall face which differ by as much as 10% in the passive case and as well as a slight larger plastic zone at failure. These differences occurred at the base of the wall. For the active case, both the lateral pressure distribution and the plastic zones formed at failure are unaffected by the infinite boundary.

Chapter 7

CONCLUSIONS AND RECOMMENDATIONS

Conclusions

The main objective of this research is to develop a numerical method for solving soil-structure interaction problems in which both the near and far-field are considered. In this research, the nonlinear near field was modeled using finite elements while the far field was modeled using linear boundary elements based on the Melan fundamental solution. A technique for coupling the boundary element and finite method, called the *substructure method*, was developed. The advantage of this method over those previously developed is that it preserves the bandedness of the system of equations resulting from the finite element method. To solve linear elastic and elasto-plastic plane strain problem, the *substructure method* was implemented into a computer program BEFEC. The *substructure method* was also incorporated into an existing computer program, SOILSTRUCT to solve soil-structure interaction problems with nonlinear stress-strain behavior and construction simulation.

Parametric studies were performed to asses the effects of domain size, boundary conditions, element type as well as other methods using analog spring and infinite elements for incorporating the effects of the infinite boundary into the finite element method, on the solution of linear elastic strip footing problems. These studies reveal that depending upon the domain size considered, the errors resulting in both the computed displacements and stress predictions may be very large compared to the closed form solution. The boundary conditions assumed as well as the type of finite element used had very little effect on the magnitude of the error. While the use of analog spring elements and infinite elements reduced the errors that occurred in the displacements, the errors in the stresses remained

very large. The coupled boundary element-finite element method proposed in this research resulted in displacements and stresses which were within 2% of the closed form solution. It was also discovered that when the skew-symmetric portion of the boundary element stiffness matrix was discarded, the resulting displacement and stresses did not differ significantly from those obtained using the full stiffness matrix.

The analysis of the footing problem was repeated assuming the soil modulus varied linearly with depth. Errors in the displacements and stress predictions of as large as 80% were observed when the far field domain was neglected. Using the coupled BEM-FEM method, the displacements and stress obtained were within 5% and 20% respectively of the closed form solution. The analysis of the strip footing problem was also repeated assuming a hyperbolic stress-strain behavior for the soil. It was observed that the displacements obtained using the coupled BEM-FEM solution were as much as 60% greater than those obtained using only the finite element method. Also, the values of the stresses σ_{xx} and σ_{xy} obtained using the coupled BEM-FEM method differed by as much as 80% from those obtained using only the finite element method.

In the analyses performed on the U-frame lock problem, three different cases were considered namely: one-step linear analysis, linear analysis with construction simulation, and nonlinear analysis with construction simulation. In the nonlinear analysis, a hyperbolic stress-strain behavior was assumed for the soil in the foundation and embankment. The interfaces between the lock, foundation and embankment were modeled using interface elements. In all three cases, the vertical displacements both along the centerline and surface of the foundation obtained using the coupled BEM-FEM method were significantly greater than those obtained using the finite element method alone. In the linear cases, the coupled BEM-FEM method results in displacements which were three times those obtained using the finite element method only. For the nonlinear case, the

displacement obtained using the coupled BEM-FEM method were greater than those obtained using the finite element method only by a factor of 10. The coupled BEM-FEM method also resulted in lateral pressures against the lock wall which at much as four times those obtained using only the finite element method. In the nonlinear case, the coupled BEM-FEM method resulted in lateral pressures which were as much as 50% less as compared to those obtained using the finite element solution. In all three cases, the coupled BEM-FEM method resulted in shear stresses along the base of the embankment which were as much as double those obtained using the finite element method only. It was noted however, that the infinite boundary did not significantly affect that computed values of σ_{yy}.

In the bearing capacity analysis of strip footing on elasto-plastic soils, incorporating the effects of the infinite boundary resulted in load levels at which yielding took place which were 10% higher than those in the solution where the infinite boundary was neglected. Because of this, the plastic deformations in the finite element solution were greater than those occurring the coupled BEM-FEM method for a given load level. This effect tended to offset the larger elastic displacements resulting from the effects of the infinite boundary. Incorporating the effects of the infinite boundary also resulted in values of σ_{xx} and σ_{xy} which differed from those obtained using the finite element method only by as much as 25% and 170% respectively. However, when the effects of self-weight was taken into account, the computed values of σ_{xx} between the two solution techniques differed by at most 15%. It was noted that the values of σ_{yy} computed using the two solution techniques did not significantly differ. On the average, the bearing capacities obtained using the coupled BEM-FEM method 3% greater as compared to those obtained using the finite element solution.

In the analysis of the Rankine pressures problem, it was noted that the infinite boundary did not have any significant effect on the computed Rankine forces, lateral pressure distribution and extent of the plastic zone formed both in the passive and active cases. However, the wall movements in the coupled BEM-FEM method needed to reach the passive and active states were respectively 45% and 100% greater than those required in the finite element solution.

Recommendations

In view of these conclusions presented, the following recommendations are made:

1. The formulation in this study which couples linear finite elements to linear boundary elements should be extended to the coupling of higher order elements. In particular, the current formulation can easily be extended to the coupling of quadratic finite elements with quadratic boundary elements. Such a formulation should prove useful in the solution of nonlinear problems.

2. Currently, BEFEC minimizes the profile of the system of equations by simply rearranging the system equations such that degrees of freedom common to both the finite element and boundary element system are isolated. The profile can further be reduced if an algorithm for profile reduction is used instead. Examples of such algorithm are those proposed by Cuthill and McKee (1969), and Sloan (1986).

3. The current boundary element formulation limits the far field to a homogenous half-plane. In view of this, the possibility of developing a boundary element formulation which allows for more general type of far field should be investigated. Such a far field might included a sloping surface, modulus varying with depth or layering in the soil.

REFERENCES

Bathe, K. J., *Finite Element Procedures in Engineering Analysis*, Prentice Hall, Inc., Englewood Ciffs, New Jersey, 1982.

Beer, C., and Meek, J. L., "Infinite Domain Elements," *Internation Journal of Numerical Methods in Engineering*, 11, pp. 53-64, 1977

Bowles, J. E., *Foundation Analysis and Design* (4th ed.), Chap. 11, McGraww-Hill, New York, 1004 pp., 1988.

Brebbia, C. A., Telles, J. C. F., and Wrobel, L. C., *Boundary Element Techniques: Theory and Applications in Engineering*, Spring-Verlag, New York, 1984.

Brebbia, C. A., *The Boundary Element Method for Engineers*, Pentech Press, London, 1978.

Brebbia, C. A., and Georgiou, P., "Combiniation of Boundary and Finite Elements in Elastostatics," *Appl. Math. Modelling*, Vol. 3, pp. 212 - 220, June 1979.

Chen, W. F., *Limit Analysis and Soil Plasticity,* Chapter 6, Elsevier, Amsterdam, 1975.

Clough, G. W., and Duncan, J. M., "Finite Element Analysis of Port Allen and Old River Locks," Report No. TE 69-3, College of Engineering, Office of Research Services, University of California, Berkely, CA., Sep. 1969.

Cristescu, M., and Loubignac, G., "Gaussian Quadrature Formulas for Functions with Singularities in 1/r Over Triangles and Quadrangles," *Recent Advances in Boundary Element Methods*, Eds. C. A. Brebbia, pp. 375-390, Pentech Press, London, 1978.

Crouch, S. L. and Starfield, A. M., *Boundary Element Methods in Solid Mechanics*, George Allen and Unwin, London, 1983.

Cuthill, E., and McKee, J. "Reducing the Bandwidth of Sparse Symmetric Matrices," *Proc. ACM Nat. Conf.*, Assoc. of Computing Machinery, New York, 1969.

Doherty, W. P., E. L. Wilson, and Taylor, R. L., *Stress Analysis of Axisymmetric Solids Utilizing Higher Order Quadrilateral Finite Elements*, Report No. SESM 69-3, Structural Engineering Laboratory, University of California, Berkely, CA., 1969.

Duncan, J. M., and Chang, C. Y., "Nonlinear Analysis of Stress and Strains in Soils," *Journal of the Soil Mechanics and Foundations Division, ASCE*, Vol. 96, No. SM5, Proc. Paper 7513, pp. 1629-1653, Sep. 1970.

Gibson, R. E., "Some Results Concerning Displacements and Stress in a Non-Homogenous Elastic Half-Space," *Geotechnique*, Vol. 17, pp. 58-67, 1967. Also, Correspondence, Vol. 18, No.2 pp. 275-276, 1968, and Vol. 19, No. 1, pp. 160-161, 1969.

Goodman, R. E., Taylor, R. L., and Breeke, T. L., "A Model for the Mechanics of Jointed Rock," *Journal of the Soil Mechanics and Foundation Division, ASCE*, No. SM3., 1968.

Greenspan, D. and Werner, P., "A Numerical Method for the Exterior Dirichlet Problem for the Related Wave Equation," *Arch. Rational Mech. Anal*, Vol. 23, pp. 288-316, 1966.

Griffiths, D. V., *Finite Element Analyses of Walls, Footing and Slopes,* Ph.D. Dissertation, University of Manchester, 1981.

Hansen, J. B., "A Revised and Extended Formula for Bearing Capacity," *Danish Geotechnical Institute Bulletin,* No. 28, Copenhagen, 21 pp., 1970.

Hill, R., *The Mathematical Theory of Plasticity,* Claredon, Oxford, 1950.

Hughes, T. R. J., *The Finite Element Method: Linear Static and Dynamic Finite Element Analysis*, Prentice Hall, Inc., Englewood Cliffs, New Jersey, 1987.

Irons, B. M., "Engineering Application of Numerical Integration in Stiffness Method," *Journal of the American Institute of Aeronautics and Astronautics*, 14, pp. 2035-2037, 1966.

James, M. L., et. al., *Applied Numerical Methods for Digital Computation with FORTRAN*, International Textbook, Scranton, 1967.

Johnston, C. and Nedelec, J. C., "On Coupling the Boundary Integral and Finite Element Methods," *Math. Comp.*, Vol. 35, pp. 1063-1079, 1980.

Lachat, J. C., and Watson, J. O., "Effective Numerical Treatment of Boundary-Integral Equation Formulation for Three-Dimensional Elastostatics," *Internation Journal for Numerical Methods in Engineering*, Vol. 10, 1976.

Loret, B., and Prevost, J. H., "Accurate Numerical Solutions for Drucker-Prager Elastic-Plastic Models," *Comp. Meth. App. Mech. and Engg.*, Vol. 54, pp. 259-277, 1986.

Melan, E., "Der Spannungszustand der durch eine Einselkraft im Innern beanspruchten Halbscheibe," *Z. Angew. Math Mech.*, 12, pp. 323-346, 1932.

Meyerhoff, G. G., "Some Recent Research on Bearing Capacity of Foundations," *Canadian Geotechnical Journal*, Ottawa, Vol. 1, No. 1, pp. 16-26, Sept. 1963.

Nagtegaal, J. C., Parks, D. M., and Rice, J. R., "On Numerically Accurate Finite Element Solutions in the Fully Plastic Range," *Comp. Meth. App. Mech. and Engg.*, Vol. 4., pp.153-177, 1974.

Owen, D. R. J., and Hinton, E., *Finite Elements in Plasticity: Theory and Practice*, Pineridge Press, Swansea, U.K., 1980.

Pian, T. H. H., and Tong, P., "Derivation of Element Stiffness Matrices by Assumed Stress Distribution," *Journal of the American Institute of Aeronautics and Astronautics*, Vol. 2, pp. 1333-1336., July, 1969.

Prandtl, L. "Eindringungsfestigkeit und Festigket von Schneiden," *Z. Angew Math. Mech.* Vol. 1, No. 5, pp. 15, 1921.

Reddy, J. N., *Introduction to the Finite Element Method*, McGraw-Hill Book Company, New York, 1984.

Richart, F. E., Woods, R. D., and Hall, J. R., *Vibration of Soils and Foundations*, Prentice Hall, Inc., Englewood Ciffs, New Jersey, 1970.

Simo, J. C., and Taylor, R. L., "Consitent Tangent Operators for Rater-Independent Elastoplasticity," *Comp. Meth. App. Mech. and Engg.*, Vol. 48, pp 101-118, 1985.

Sloan, S. W., "An Algorithim for Profile and Wavefront Reduction of Sparse Matrices," *International Journal for Numerical Methods in Engineering*, Vol. 23, pp. 239-252, 1986.

Stroud, A. H., and Secrest, D., *Gaussian Quadrature Formulas*, Prentice Hall, Inc., Englewood Ciffs, New Jersey, 1966.

Taig, I. C., *Structural Analysis by the Matrix Displacement Method*, English Electric Aviation Report No. S017, 1961.

Telles, J. C. F., and Brebbia, C. A., "Boundary Element Solution of Half-Plane Problems," *International Journal of Solids and Structures*, 18, pp. 1149-1158, 1981.

Telles, J. C. F., *The Boundary Element Method Applied to Inelastic Problems*, Lecture Notes in Engineering, Spring-Verlag, Berlin, 243 pp., 1981.

Terzaghi, K., *Theoretical Soil Mechanics*, John Wiley and Sons, New York, 510 pp., 1943.

Timoshenko, S., and Goodier, J. N., *Theory of Elasticity* (3rd. ed.), McGraw-Hill, New York, 1970.

Vallabhan, C. V. G., Sivakumar, J., and Radhakrishnan, N. "Appications of Boundary Element Method for Soil-Structure Interaction Problems," *Proc. 6th International Conference on Boundary Element Methods,* Vol 6., pp. 67-39, Springer-Verlag, Berlin, 1986.

Vesic, A. S., "Analysis of Ultimate Loads of Shallow Foundations," *Journal of the Soil Mechanics and Foundation Division, ASCE,* Vol. 99, SM1, pp. 45-73, Jan. 1973.

Wilkins, M. L., "Calculations of Elastic-Plastic Flow," *Methods of Computational Physics,* Vol. 3., Academic Press, New York, 1964.

Wilson, E. L., "Static Condensation Algorithim," *Internation Journal of Numerical Methods in Engineering,* Vol. 8, pp. 199-203, 1974.

Zienkiewicz, O. C., Kelly, D. W., and Bettess, P., "The Coupling of the Finite Element Method and Boundary Solution Procedures," *Internation Journal for Numerical Methods in Engineering,* Vol. 11, pp. 355-375, 1977.

Zienkiewicz, O. C., Humpheson, C. and Lewis, R. H., "Associated and Non-Associated Visco-Plasticity and Plasticity in Soil Mechanics," *Geotechnique,* No. 25, pp. 671-689, 1975.

Appendix A

FUNDAMENTAL SOLUTIONS

In this appendix, the complete solution to the Kelvin and Melan problems are presented. The Melan solution consists of two parts namely: (1) the Kelvin solution representing the solution to a point load applied inside an infinite plane, and (2) the complementary solution which when added to the Kelvin solution gives the solution to a point load applied inside a half-plane. Thus the complete solution can be written as follows:

$$u_{ij}^{*} = u_{ij}^{k} + u_{ij}^{c} \tag{A.1}$$

$$\sigma_{ijk}^{*} = \sigma_{ijk}^{k} + \sigma_{ijk}^{c} \tag{A.2}$$

where u_{ij}^{*} is the displacement in the *i*th direction due to a unit load applied in the *j*th direction and σ_{ijk}^{*} is the *ij*th component of stress due to a unit load applied in the *k*th direction.

A.1 Kelvin Solution

Figure (A.1) illustrates the Kelvin problem, The displacements corresponding to the solution of this problem are given by:

$$u_{xx}^{k} = \frac{1}{8\pi G(1-\nu)}\left[(3-4\nu)\ln\left(\frac{1}{r}\right)+\frac{x^2}{r^2}\right] \tag{A.3}$$

$$u_{xy}^{k} = \frac{1}{8\pi G(1-\nu)}\left[\frac{xy}{r^2}\right] \tag{A.4}$$

$$u_{yx}^{k} = \frac{1}{8\pi G(1-\nu)}\left[\frac{xy}{r^2}\right] \tag{A.5}$$

$$u_{yy}^{k} = \frac{1}{8\pi G(1-\nu)}\left[(3-4\nu)\ln\left(\frac{1}{r}\right)+\frac{y^2}{r^2}\right] \tag{A.6}$$

while the stresses are given by

$$\sigma_{xxx}^{k} = \frac{1}{4\pi(1-\nu)r}\left[(1-2\nu)\left(\frac{x}{r}\right)+\frac{x^3}{r^3}\right] \tag{A.7}$$

$$\sigma_{xyx}^{k} = \frac{1}{4\pi(1-\nu)r}\left[(1-2\nu)\left(\frac{y}{r}\right)+\frac{x^2y}{r^3}\right] \tag{A.8}$$

$$\sigma_{yyx}^{k} = \frac{1}{4\pi(1-\nu)r}\left[(1-2\nu)\left(\frac{x}{r}\right)+\frac{xy^2}{r^3}\right] \tag{A.9}$$

$$\sigma_{xxy}^{k} = \frac{1}{4\pi(1-\nu)r}\left[(1-2\nu)\left(\frac{y}{r}\right)+\frac{x^2y}{r^3}\right] \tag{A.10}$$

$$\sigma_{xyy}^{k} = \frac{1}{4\pi(1-\nu)r}\left[(1-2\nu)\left(\frac{x}{r}\right)+\frac{xy^2}{r^3}\right] \tag{A.11}$$

$$\sigma_{yyy}^{k} = \frac{1}{4\pi(1-\nu)r}\left[(1-2\nu)\left(\frac{y}{r}\right)+\frac{y^3}{r^3}\right] \tag{A.12}$$

where

$$r = \sqrt{x^2+y^2} \tag{A.13}$$

A.2 Complementary Solution

The Melan problem is illustrated in Figure (A.2). The displacement corresponding to the solution of this problem are given by:

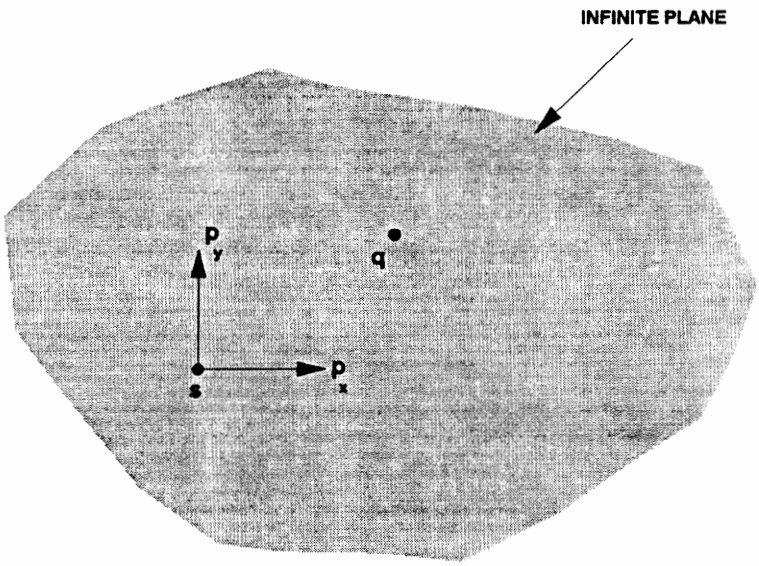

Figure A.1. Kelvin Fundamental Solution.

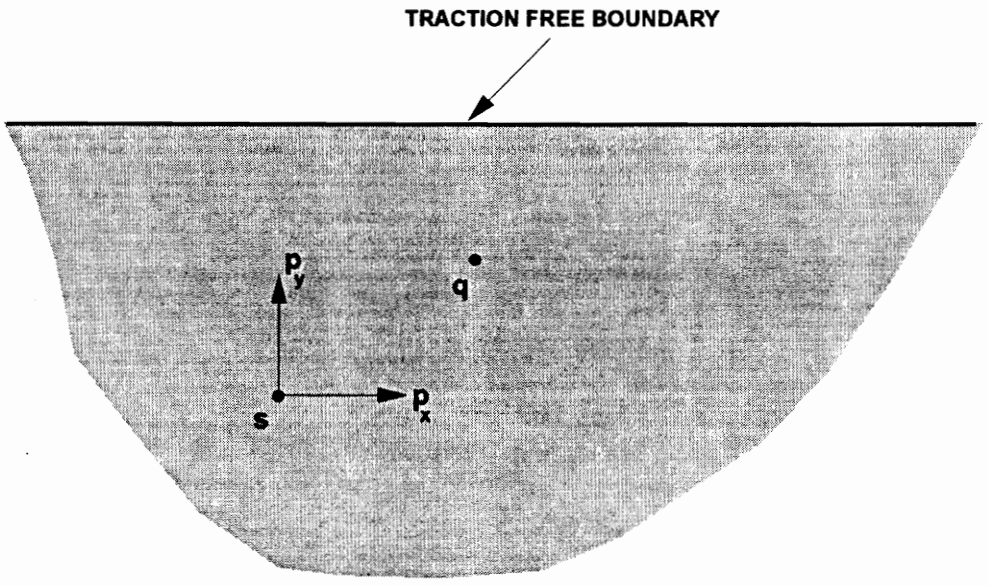

Figure A.2 Melan Fundamental Solution

$$u_{xx}^{c} = K_d\left\{-\left[8(1-\nu)^2-(3-4\nu)\right]\ln R+\frac{\left[(3-4\nu)R_1^2-2c\underline{x}\right]}{R^2} + \frac{4c\underline{x}R_1^2}{R^4}\right\} \tag{A.14}$$

$$u_{xy}^{c} = K_d\left\{\frac{(3-4\nu)r_1r_2}{R^2}+\frac{4c\underline{x}R_1r_2}{R^4}-4(1-\nu)(1-2\nu)\theta\right\} \tag{A.15}$$

$$u_{xy}^{c} = K_d\left\{\frac{(3-4\nu)r_1r_2}{R^2}+\frac{4c\underline{x}R_1r_2}{R^4}+4(1-\nu)(1-2\nu)\theta\right\} \tag{A.16}$$

$$u_{yy}^{c} = K_d\left\{-\left[8(1-\nu)^2-(3-4\nu)\right]\ln R+\frac{\left[(3-4\nu)r_2^2-2c\underline{x}\right]}{R^2} + \frac{4c\underline{x}r_2^2}{R^4}\right\} \tag{A.17}$$

while the stresses are given by:

$$\sigma_{xxx}^{c} = -K_s\left\{-\frac{(3\underline{x}+c)(1-2\nu)}{R^2}+\frac{2R_1\left(R_1^2+2c\underline{x}\right)-\left(4\underline{x}r_2^2\right)(1-2\nu)}{R^4} - \frac{16c\underline{x}R_1r_2^2}{R^6}\right\} \tag{A.18}$$

$$\sigma_{xyx}^{c} = -K_sr_2\left\{-\frac{(1-2\nu)}{R^2}+\frac{2\left[c^2-2c\underline{x}-\underline{x}^2+2cR_1(1-2\nu)\right]}{R^4} + \frac{16c\underline{x}R_1^{\,2}}{R^6}\right\} \tag{A.19}$$

$$\sigma^{c}_{yyx} = -K_s\left\{-\frac{(3\underline{x}+c)(1-2\nu)}{R^2}+\frac{2\left[R_1\left(r_2^2+2\underline{x}^2\right)-2\underline{x}r_2^2+2cr_2^2(1-2\nu)\right]}{R^4}\right.$$
$$\left.-\frac{16c\underline{x}R_1^2}{R^6}\right\} \tag{A.20}$$

$$\sigma^{c}_{xxy} = -K_s r_2\left\{\frac{(1-2\nu)}{R^2}+\frac{2\left[\underline{x}^2-c^2+6c\underline{x}-2cR_1(1-2\nu)\right]}{R^4}\right.$$
$$\left.+\frac{16c\underline{x}r_2^{\,2}}{R^6}\right\} \tag{A.21}$$

$$\sigma^{c}_{xxy} = -K_s\left\{-\frac{(3\underline{x}+c)(1-2\nu)}{R^2}+\frac{2\left[\left(2c\underline{x}+r_2^2\right)R_1-2cR_1^2(1-2\nu)\right]}{R^4}\right.$$
$$\left.-\frac{16c\underline{x}R_1r_2^2}{R^6}\right\} \tag{A.22}$$

$$\sigma^{c}_{yyy} = -K_s r_2\left\{\frac{3(1-2\nu)}{R^2}+\frac{2\left[r_2^2-4c\underline{x}-2\underline{x}-2cR_1(1-2\nu)\right]}{R^4}\right.$$
$$\left.+\frac{16c\underline{x}R_1^{\,2}}{R^6}\right\} \tag{A.23}$$

where

$$\theta = \arctan\left(\frac{r_2}{R_1}\right) \tag{A.24}$$

$$K_d = \frac{1}{[8\pi(1-\nu)G]} \tag{A.25}$$

$$K_s = \frac{1}{[4\pi(1-\nu)]} \tag{A.26}$$

The geometry of the various quantities used in the Melan complementary solution are illustrated in figure (A.3)

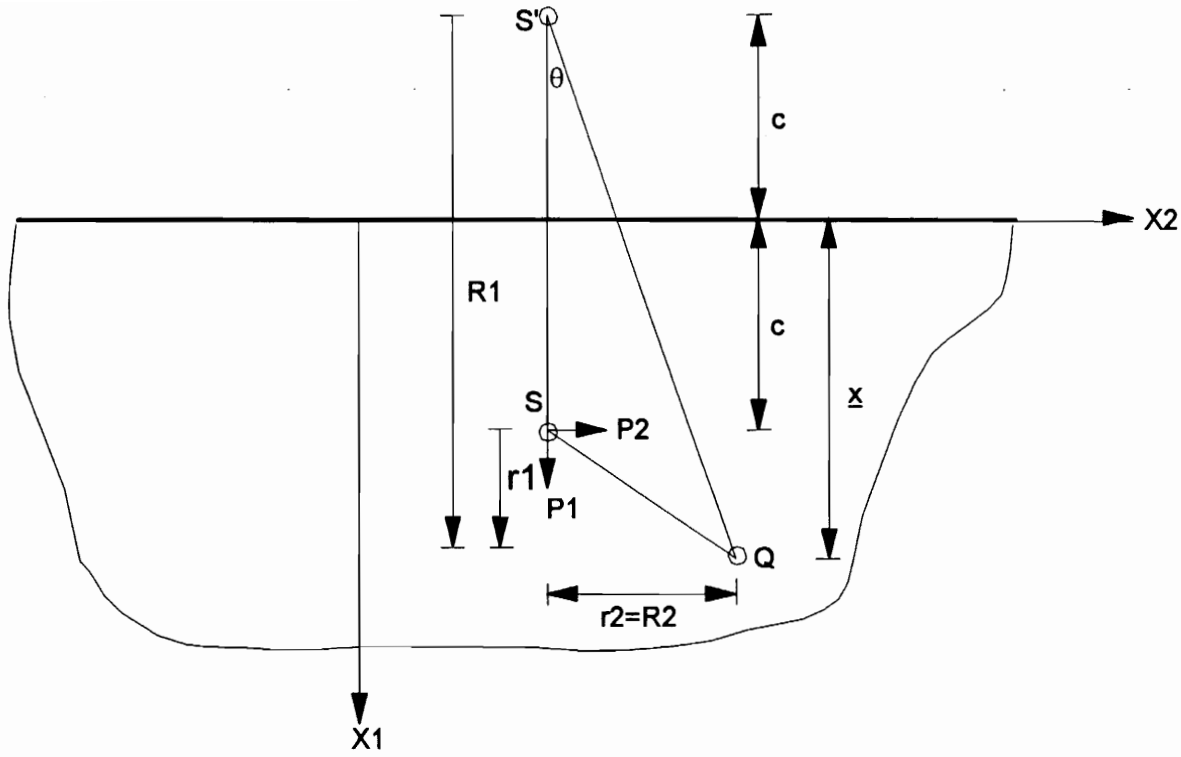

Figure A.3. Geometry of quantities used in the complementary part of the Melan solution.

Appendix B

BEFEC USER'S GUIDE

1. TITLE CARD

Variable	Description
TITLE	Job title for heading the output.

2. EXECUTION CONTROL CARD

Variable	Description
IEXEC	Execution code EQ. 0, data check only EQ. 1, execution
IPRNT	Input data print code EQ. 0, print nodal and element input data EQ. 1, do not print nodal and element input data
IREAD	Read restart file code EQ. 0, do not read restart file EQ. 1, read restart file
IWRITE	Write restart file code EQ. 0, do not write restart file EQ. 1, write restart file
ISYMM	Symmetry code EQ. 0, symmetric system of equations EQ. 1, fully unsymmetric system of equations EQ. 2, partially unsymmetric system of equations
IOPT	Analysis Option EQ. 0, Axisymmetric case EQ. 1, Plane Strain case
IBBAR	Strain-displacement option EQ. 0, standard formulation EQ. 1, mean-dilitational (B-Bar) formulation

2. EXECUTION CONTROL CARD (Continued)

Variable	Description
INIT	Initial stress option EQ. 0, zero out initial stresses EQ. 1, read initial stresses from file EQ. 2, horizontal Ko analysis EQ. 3, elastic FEM analysis EQ. 4, Ko FEM analysis
IPLOT	Plotting option EQ. 0, do not generate plotting file EQ. 1, generate plotting file

3. MESH DATA CARD

Variable	Description
NUMNP	Number of nodal points in mesh.
NUMAT	Number of materials
NUMEL	Number of finite elements
NUMBEL	Number of boundary elements
NUMLDS	Number of loading steps
NITER	Maximum allowable number of iterations
ETOL	Error tolerance

4.1 NODAL COORDINATE CARD

Variable	Description
N	Node number; GE. 1 and LE. NUMNP Terminate input with 0
NUMGP	Number of generation points; EQ. 0, no generation, skip next two cards EQ. 4, 2-D linear isoparametric generation EQ. 8, 2-D quadratic isoparametric generation

4.1 NODAL COORDINATE CARD (Continued)

X(1,N)	X - coordinate of node N
X(1,N)	Y - coordinate of node N

Note: Generation of nodal coordinates in two dimensions may be defined using four or eight generation points.

In the case of NUMGP = 4, bilinear interpolation is employed, resulting in equally spaced nodal points along generating lines as shown in figure (B.1)

In the case of NUMGP=8, biquadratic serendipity interpolation is employed, and graded nodal spacing may be achieved by placing generation points 5 - 8 off center as shown in figure (B.2). Note that generation point 5 - 8 do not generally coincide with any nodal points. The spacing of the nodal points may be determined from the serendipity mapping.

4.2 GENERATION POINT COORDINATE CARDS

Variable	Description
TEMP(1,J)	X - coordinate of generation point J
TEMP(2,J)	Y - coordinate of generation point J

Note: The coordinates of each generation point are defined by a generation point coordinate card. This card must be read in order (J = 2, 3, ..., NUMGP) following the nodal coordinate card which initiated the generation sequence (J = 1). A nodal increment card follows the last generation point card (J = NUMGP)

4.3 NODAL INCREMENT CARD

Variable	Description
NINC(1)	Number of node increments in X-direction; GE. 0
INC(1)	Node number increment in X-direction.
NINC(2)	Number of node increments in Y-direction; GE. 0
INC(2)	Node number increment in Y-direction.

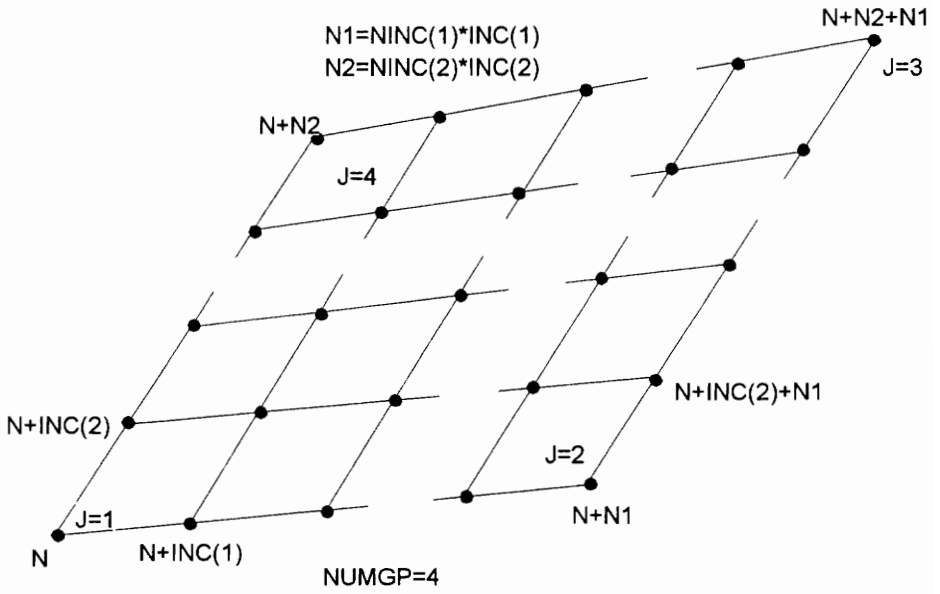

Figure B.1. Bilinear generation of nodal coordinate data.

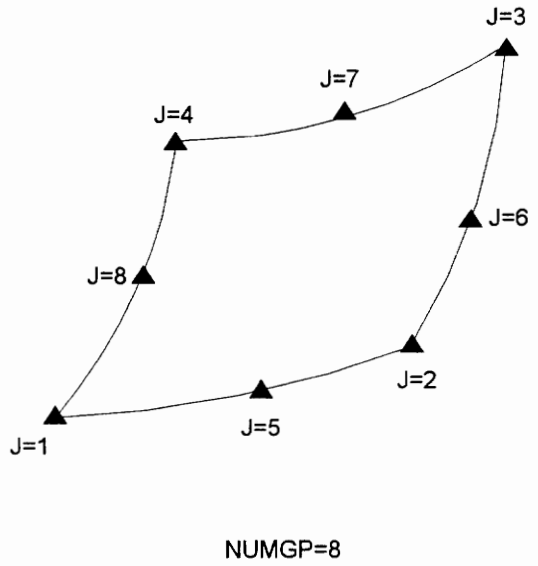

Figure B.2. Biquadratic serendipity generation of nodal coordinate data.

5. MATERIAL PROPERTIES CARD

LINEAR ELASTIC MATERIAL

Variable	Description
M	Material type number for material N, EQ. 1 for linear elastic
SPAR(N,1)	Young's Modulus for material N
SPAR(N,2)	Poisson's ratio for material N
SPAR(N,5)	Unit weight for material N
SPAR(N,6)	Coefficient of at-rest lateral earth pressure for material N

ELASTO-PLASTIC (DRUCKER-PRAGER) MATERIAL

Variable	Description
M	Material type number for material N, EQ. 2 for elasto-plastic (Drucker-Pragger)
SPAR(N,1)	Young's Modulus for material N
SPAR(N,2)	Poisson's ratio for material N
SPAR(N,3)	Angle of friction for material N
SPAR(N,4)	Cohesion intercept for material N
SPAR(N,5)	Unit weight for material N
SPAR(N,6)	Coefficient of at-rest lateral earth pressure for material N

Note: The material properites of each material are defined by a material properties card. This card must be read in order (J = 1, 2, ..., NUMAT) following the numbering assigned to the materials.

6.1 ELEMENT NODAL DATA CARD

Variable	Description
N	Element number, terminate input with 0

6.1 ELEMENT NODAL DATA CARD (Continued)

Variable	Description
M	Element material number
IEN(1,N)	Node number of first node
IEN(2,N)	Node number of second node
IEN(3,N)	Node number of third node
IEN(4,N)	Node number of fourth node
NG	Generation parameter EQ. 0, no generation, skip next card EQ. 1, generate data

Note: See Figure (B.3) for a schematic representation of the generation algorithim.

6.2 ELEMENT GENERATION DATA CARD

Variable	Description
NEL(1)	Number of elements in the X-direction If EQ.0, set internally to 1.
INCEL(1)	Element number increment in the X-direction If EQ.0, set internally to 1.
INC(1)	Node number increment in the X-direction If EQ.0, set internally to 1.
NEL(2)	Number of elements in the Y-direction If EQ.0, set internally to 1.
INCEL(2)	Element number increment in the Y-direction If EQ.0, set internally to 1.
NEL(2)	Node number increment in the Y-direction If EQ.0, set internally to 1.

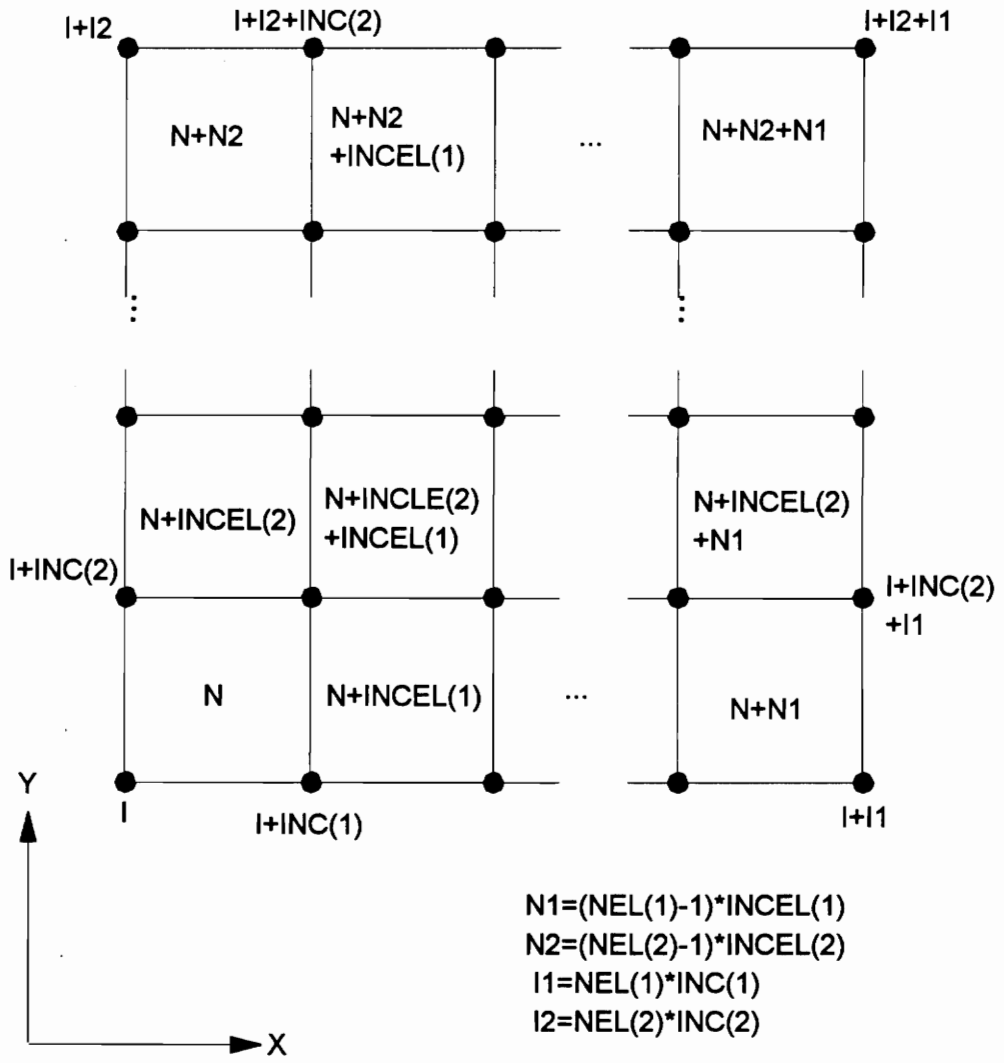

Figure B.3. Schematic representation of the generation algorithm for element nodal data.

7.1 BOUNDARY ELEMENT NODAL DATA CARD

Variable	Description
IX(1)	Node number corresponding to first node in boundary element system
IX(2)	Node number corresponding to second node in boundary element system
:	:
IX(NUMBEL+1)	Node number corresponding to the last node in the boundary element system

NOTE: All node numbers in the boundary element system are defined in the boundary element nodal data card. Node numbers must be specified in the order IX(J), J = 1, NUMBEL+1 following the confluency condition of the boundary element system.

7.2 BOUNDARY ELEMENT SYMMETRY CARD

Variable	Description
NUMSYM	Number of nodes lying on the line of symmetry. If EQ. 0, ignore the remainder of this card.
ISYM(1)	Local node number of first node in boundary element system lying on line of symmtery.
:	:
ISYM(NUMSYM)	Local node number of last node in boundary element system lying on line of symmetry.

7.3 BOUNDARY ELEMENT MATERIAL PROPERTIES CARD

Variable	Description
E	Young's Modulus of boundary element system
PO	Poisson's ration of boundary element system

8.1 BOUNDARY CONDITION CODE CARD (X-DIRECTION)

Variable	Description
NUMX	Number of nodes with displacements prescribed in the X-direction
ITEMP(1)	Node number of first node with prescribed displacement in X-direction
ITEMP(2)	Node number of second node with prescribed displacement in X-direction
:	:
ITEMP(NUMX)	Node number of last node with prescribed displacement in X-direction

Note: Node numbers can be prescribed in any order.

8.2 BOUNDARY CONDITION CODE CARD (Y-DIRECTION)

Variable	Description
NUMY	Number of nodes with displacements prescribed in the Y-direction
ITEMP(1)	Node number of first node with prescribed displacement in Y-direction
ITEMP(2)	Node number of second node with prescribed displacement in Y-direction
:	:
ITEMP(NUMX)	Node number of last node with prescribed displacement in Y-direction

Note: Node numbers can be prescribed in any order.

9.1 INITIAL STRESS ELEMENT CARD

Variable	Description
N	Element number of which the initial stresses are being specified. Terminate input with 0.

Note: This and the succeeding card are only specified if INIT = 1.

9.2 INITIAL STRESS DATA CARD

Variable	Description
STR0(1,J,N)	σ_{xx} for gauss point J of element N
STR(2,J,N)	σ_{yy} for gauss point J of element N
STR(3,J,N)	σ_{xy} for gauss point J of element N
STR(4,J,N)	σ_{zz} for gauss point J of element N

Note: The initial stresses for each gauss point J = 1 to 4 are specified using a initial stress data card. Cards must be read in the order corresponding to the numbering of the gauss points.

10.1 LOAD STEP CARD

Variable	Description
NUMSSTP	Number of substeps in current load step

Note: This and the succeeding set of cards is specified for every load step J = 1 to NLOAD.

10.2 LOAD DATA CARD

Variable	Description
N	Node number of applied force/displacement. Input terminated by 0.
BC(N,1)	Prescribed value of applied force/displacement in X-direction
BC(N,2)	Prescribed value of applied force/displacement in Y-direction

Note: The prescibed boundary conditions for each node are specified using a load data card. Data can be specified in any order.

Appendix C

ANALYTICAL SOLUTION TO FOOTING PROBLEM

In this appendix, the complete analytical solution to the strip footing problem consisting of a uniformly distributed load applied to the surface of an elastic half-plane is presented. The displacements corresponding to this problem are given by

$$u_x(x,y) = -\frac{w}{2\pi G}\left[(1-2\nu)\{(x-a)\theta_1 - (x+a)\theta_2 - \pi a\} + (1-\nu)y\ln\left(\frac{r_1^2}{r_2^2}\right)\right] \tag{C.1}$$

$$u_y(x,y) - u_y(L,0) = \frac{w}{2\pi G}\left[(1-\nu)y(\theta_1-\theta_2) + (1-\nu)\{(x-a)\ln r_1^2 - (x-a)\ln r_2^2 + (L+a)\ln(L+a)^2 - (L-a)\ln(L-a)^2\}\right] \tag{C.2}$$

and the stresses are given by

$$\sigma_{xx} = -\frac{w}{\pi}\left[\theta_1 - \theta_2 + y\left\{\frac{(x-a)}{r_1^2} - \frac{(x+a)}{r_2^2}\right\}\right] \tag{C.3}$$

$$\sigma_{yy} = -\frac{w}{\pi}\left[\theta_1 - \theta_2 - y\left\{\frac{(x-a)}{r_1^2} - \frac{(x+a)}{r_2^2}\right\}\right] \tag{C.4}$$

$$\sigma_{xy} = -\frac{w}{\pi}y^2\left(\frac{1}{r_1^2} - \frac{1}{r_2^2}\right) \tag{C.5}$$

In these expressions, the following abbreviation are used

$$\theta_1 = \arctan\frac{y}{x-a} \tag{C.6}$$

$$\theta_2 = \arctan\frac{y}{x+a} \tag{C.7}$$

$$r_1^2 = (x-a)^2 + y^2 \tag{C.8}$$

$$r_1^2 = (x+a)^2 + y^2 \tag{C.9}$$

where the distributed load w is applied from point $(-a,0)$ to $(a,0)$, while the displacements and stresses evaluated at the point (x,y) and r is the distance from the origin to the point (x,y) such that

$$r = \sqrt{x^2 + y^2} \tag{C.10}$$

The constant G is the shear modulus, ν is poisson's ratio, and L is an arbitraryy constant chosen so that at the point $(L,0)$, $u_y = 0$. Figure (C.1) describes the geometry of the problem, and the distances and angles from the endpoints of the strip to the point (x,y).

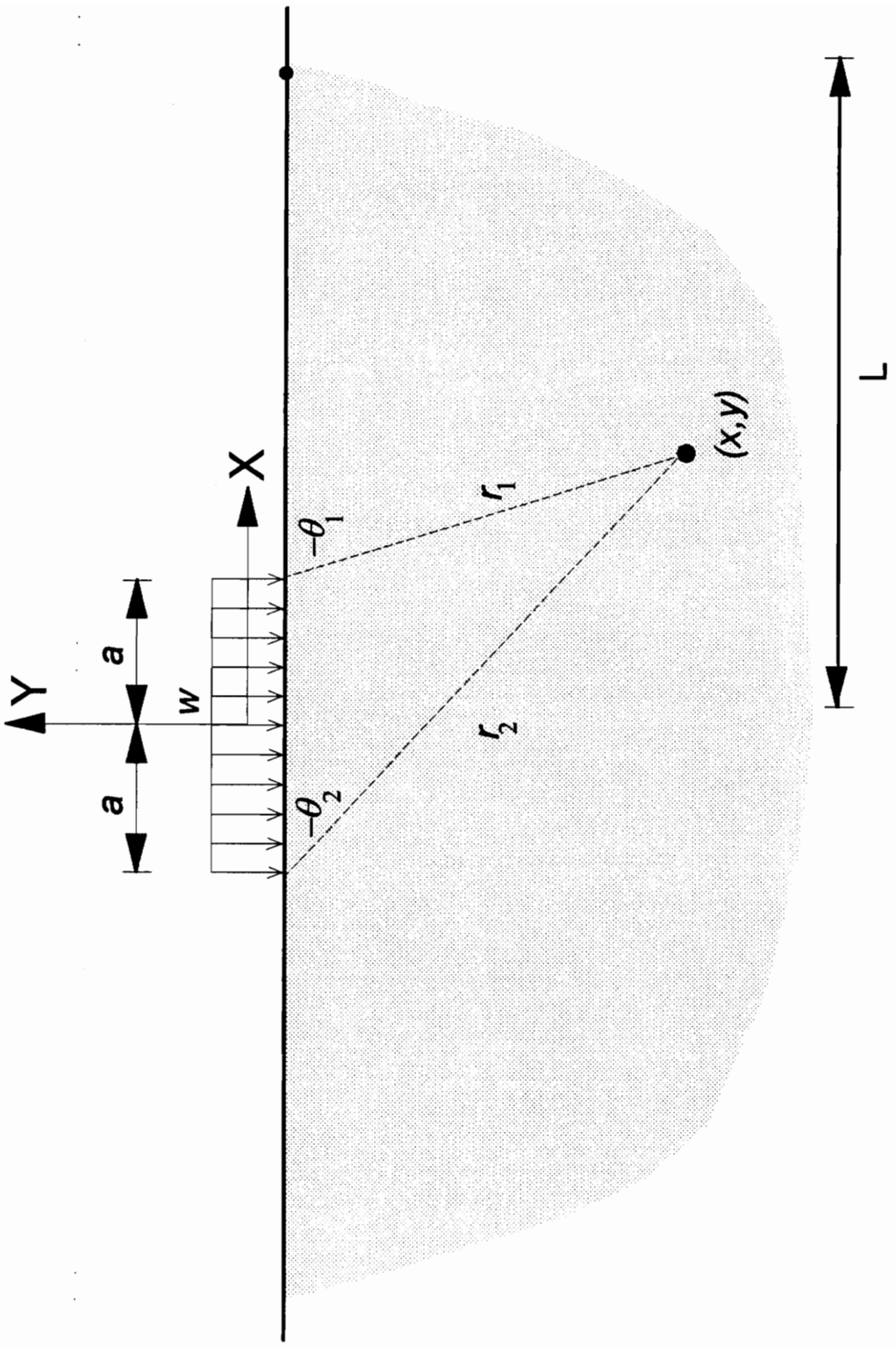

Figure C.1 Distances and angles from endpoints of strip.

VITA

Mark Albert Zarco was born on November 10, 1963 in Manila, the Philippines, He received his Bachelor of Science in Civil Engineering in April of 1985 from the University of the Philippines, graduating with honors. In April of 1987, he received his Masters of Science in Civil Engineering from the same university. In June of 1987, he joined the faculty of Department of Engineering Sciences of the same University.

In August of 1989, he entered graduate program in Civil Engineering at Virginia Polytechnic Institute and State University, under the Fulbright-Hayes Program, to pursue a doctorate in Civil Engineering, with emphasis in geotechnical engineering. He was later employed by the Department of Civil Engineering as a graduate research assistant. His Ph.D. research was supervised by Professor T. Kuppusamy.

Upon finishing, he will be returning back to the University of the Philippines to resume his teaching career.